

**Measurement of the neutrino-oxygen
neutral-current quasielastic cross section
and study of nucleon-nucleus interaction model
using atmospheric neutrino data in the SK-Gd experiment**

March 15, 2024

Seiya Sakai

Graduate School of
Natural Science and Technology
(Doctor's Course)
OKAYAMA UNIVERSITY

ABSTRACT

In July 2020, 0.011% by mass of gadolinium (Gd) was loaded in the Super-Kamiokande (SK) detector to improve the neutron-tagging efficiency, and the SK-Gd experiment started. The SK-Gd experiment is aiming to achieve the world's first observation of the diffuse supernova neutrino background (DSNB). One of the main backgrounds in the SK-Gd DSNB search is the atmospheric neutrino-oxygen neutral-current quasielastic scattering (NCQE) reactions. In order to estimate the NCQE events precisely, we must understand the number and energy of deexcitation gamma-rays and the number of neutrons by the nucleon-nucleus interactions in water (secondary interactions). So far, the secondary interaction model based on the Bertini Cascade model (BERT) was the only choice in the SK detector simulation. However, now other secondary interaction models like the Binary Cascade model (BIC) and the Liège Intranuclear Cascade model (INCL++) are available.

Using 552.2 days of data from August 2020 to June 2022, we performed the comparison of secondary interaction models using atmospheric neutrino events and the measurement of the atmospheric neutrino-oxygen NCQE cross section in the energy range from 160 MeV to 10 GeV. First, we compared the distributions of reconstructed Cherenkov angle, visible energy, and the number of delayed signals for the three secondary interaction models. The results suggest that the evaporation model used in BIC and INCL++ reproduces the observed data better than that used in BERT for all distributions. Moreover, we measure the NCQE cross section to be $0.74 \pm 0.22(\text{stat.})^{+0.85}_{-0.15}(\text{syst.}) \times 10^{-38} \text{ cm}^2/\text{oxygen}$ in the energy range from 160 MeV to 10 GeV, which is consistent with the atmospheric neutrino-flux-averaged theoretical NCQE cross section and the measurement in the SK pure-water phase within the uncertainties.

Now we continue the observation with a 0.03% Gd-loaded SK detector, the phase known as SK-VII. By combining about three years of data in SK-VII, the statistical uncertainty will be half of this work, and the secondary interaction models will be able to be verified more precisely. Furthermore, the evaporation model can be determined at 5σ by combining about four years of data in SK-VII. Once the evaporation model is determined, the systematic uncertainty of measured NCQE cross section is significantly reduced.

ACKNOWLEDGMENTS

I would like to express my gratitude to many people for their guidance and encouragement as I carried out this study.

My supervisor, Prof. Yusuke Koshio, was very encouraging to me. Even though he was busy, he was always concerned about my study and gave me a lot of advice on how to proceed with my study smoothly. He also taught me the importance of having a strong own will and not being influenced by other people's opinions. I have been able to come this far because of his support, and I would like to apply what I have learned so far to my life in the future. If we have a chance, let's go for a drink again!

I would also like to express my gratitude to my co-researchers for their help on various situations. Prof. Masayuki Nakahata, Prof. Hiroyuki Sekiya, Dr. Motoyasu Ikeda, Dr. Kei Ieki, and Dr. Keishi Hosokawa were very helpful during the gadolinium-loading work. Prof. Yoshinari Hayato and Dr. Seisho Abe were very kind to teach me about the simulation for neutrino interactions. Dr. Takatomi Yano and Dr. Yuuki Nakano helped me with the Super-Kamiokande detector simulation development and data analysis. Prof. Teppei Katoh, Prof. Yasuhiro Nakajima, Dr. Volodymyr Takhistov, Dr. Linyan Wan, Prof. Mark Vagins, Prof. Kate Scholberg, Prof. Luis Labarga, Dr. Ryosuke Akutsu, Dr. Yosuke Ashida, and Dr. Hiroshi Ito gave me a lot of comments and advice when I was writing my paper (S. Sakai *et al.*, Phys. Rev. D **109**, L011101 (2024)). My colleagues, Shota Izumiya, Masataka Shinoki, and Seungho Han, gave me great inspiration as I proceeded my study.

I would also like to thank the members of the Particle Physics Laboratory at Okayama University for their help and support. My seniors, Dr. Yota Hino and Dr. Masayuki Harada, helped me in various aspects of my study. Thanks to my juniors, Fumi Nakanishi, Yuki Shiraishi, Tomoaki Tada, Tomohiro Tano, Koyo Takeya, Kouki Hamaguchi, Akinori Higashi, Mei Homma, and Nozomu Meguro, my research life has become more enjoyable. The office manager, Rie Yamamoto, helped me with business trips and paperwork. I would also like to express my gratitude to the alumni of the Particle Physics Laboratory at Okayama University. In particular, my colleagues, Ryo Okada and Wenjie Ma, gave me emotional support as I pursued my study.

In addition to that, I have been indebted to many people throughout my life. I believe that the reason I am able to spend such a meaningful time now is because of the encounters I have had with each and every one of you.

Finally, I would like to thank my family from the bottom of my heart for supporting me.

This work was supported by JSPS KAKENHI Grant Number JP22KJ2301.

Contents

1	Introduction	1
1.1	Neutrino	1
1.2	Neutrino oscillation	1
1.3	Neutrinos from core-collapse supernovae	5
1.3.1	Neutrinos from SN1987A	5
1.3.2	Diffuse supernova neutrino background	6
1.4	DSNB search	6
1.5	NCQE background in SK-Gd DSNB search	9
1.6	Measurements of NCQE cross section	11
1.6.1	Measurements using accelerator neutrinos	11
1.6.2	Measurements using atmospheric neutrinos	12
1.6.3	Issues in previous measurements	13
2	Super-Kamiokande	14
2.1	Super-Kamiokande	14
2.2	ID PMT and OD PMT	15
2.3	Helmholtz coils	17
2.4	Observation phase	18
2.5	Detection principle	21
2.6	Water purification system	22
2.7	Air purification system	23
2.8	Data acquisition system	24
3	Simulation	27
3.1	Atmospheric neutrino flux	27
3.2	Neutirno interaction	27
3.3	Simulation for the IBD-like event	36
3.3.1	Spallation events	36
3.3.2	Reactor neutrino events	37
3.3.3	DSNB events	38
3.4	Detector simulation	38
4	Event reconstruction	41
4.1	Vertex reconstruction	41
4.2	Direction reconstruction	42
4.3	Energy reconstruction	44
5	Detector calibration	48
5.1	ID detector calibration	48
5.1.1	High-Voltage determiniation	48
5.1.2	Relative gain measurement	49
5.1.3	Absolute gain measurement	50

5.1.4	Relative QE measurement	51
5.1.5	Timing response calibration	51
5.2	Photon tracking	54
5.2.1	Water transparency measurement	54
5.2.2	Top-Bottom Asymmetry	54
5.2.3	Photon reflection on the material surface	56
5.3	LINAC	57
6	Event selection	59
6.1	First reduction: Pre-cut	60
6.1.1	Non-SHE-triggered event and noise event cut	60
6.1.2	Cosmic ray muon-induced event cut	60
6.1.3	Fiducial volume cut	60
6.1.4	Fit quality cut	60
6.1.5	Trigger requirement	61
6.2	Second reduction: Spallation cut	61
6.2.1	1 ms cut	61
6.2.2	Multiple spallation cut	62
6.2.3	Neutron cloud cut	62
6.2.4	Spallation likelihood cut	63
6.2.5	Spallation box cut	70
6.2.6	Spallation cut efficiency	70
6.3	Third reduction	71
6.3.1	Effective wall distance cut	71
6.3.2	Pre-activity cut and post-activity cut	71
6.3.3	Ring cleanliness cut	71
6.3.4	Charge over hit cut	74
6.4	Cherenkov angle cut and neutron tagging	74
6.4.1	Reconstructed Cherenkov angle of the prompt signal	74
6.4.2	Number of delayed signals per event	74
6.4.3	Difference between this study and the DSNB search in SK-VI	75
6.5	Observed and expected number of events	75
7	Comparison of secondary interaction models	81
7.1	Features of secondary interaction models	81
7.2	Differences of secondary interaction models	86
7.2.1	Intranuclear-cascade model	86
7.2.2	Pre-compound model and evaporation model	88
7.3	Comparison with the observed data	92
8	Measurement of NCQE cross section in SK-Gd	95
8.1	Measured NCQE cross section	95
8.2	Systematic uncertainties of the expected events	96
8.3	Systematic uncertainty of the measured NCQE cross section	102

9 Future prospects and conclusion	106
9.1 Future prospects	106
9.2 Conclusion	109
A Chi-square using the Poisson-likelihood	110
B Other distributions	111
B.1 Simulation	111
B.2 Event selection	117
B.3 Comparison of secondary interaction models	146
B.4 Measurement of NCQE cross section in SK-Gd	162

List of Figures

1.1	Neutrino events from SN1987A observed in Kamiokande II and IMB	5
1.2	Predictions of DSNB $\bar{\nu}_e$ flux	7
1.3	Neutrino interaction cross sections	7
1.4	Upper limits of $\bar{\nu}_e$ flux in recent DSNB searches	8
1.5	Schematic view of a DSNB event in SK	8
1.6	Schematic view of a DSNB event and a NCQE event in SK-Gd	9
1.7	Kinetic energy of neutrons in DSNB events and NCQE events	10
1.8	Detailed schematic view of a NCQE event	10
1.9	Reconstructed energy spectra of the observed data and the expected backgrounds in the SK-Gd DSNB search	11
1.10	Reconstructed Cherenkov angle (θ_C) distributions from the FHC (neutrino-mode) sample and the RHC (antineutrino-mode) sample in T2K NCQE cross section measurement	12
1.11	The measured NCQE cross section, the theoretical NCQE cross section, and the atmospheric neutrino flux measured in SK	13
2.1	Overview of the Super-Kamiokande detector	14
2.2	Cross section of the SK detector and overview of supermodule frames	15
2.3	Schematic view of the ID PMT	16
2.4	Quantum efficiency of the ID PMT photocathode as a function of wavelength	16
2.5	Single photoelectron pulse height distribution of the ID PMT	16
2.6	Relative transit time distribution for a typical ID PMT tested using 410 nm wavelength light at the single photoelectron intensity level	17
2.7	Positional relationship of ID PMTs and OD PMTs in a supermodule frame	17
2.8	Schematic view of Helmholtz coils	18
2.9	Picture of a shockwave prevention case	19
2.10	Neutron capture rate on Gd	20
2.11	Schematic view of Cherenkov radiation	21
2.12	Schematic view of water purification system	23
2.13	Typical radon concentration in the air at the SK over a year	24
2.14	Schematic view of air purification system	24
2.15	Schematic view of the data acquisition system	25
2.16	Block diagram of the QTC and its surroundings	26
2.17	Software trigger threshold for recording PMT hits of each trigger type in SK-IV	26
2.18	Software trigger threshold for recording PMT hits of each trigger type in SK-V, SK-VI, and SK-VII	26
3.1	Schematic view of atmospheric neutrino production	27
3.2	Atmospheric neutrino flux predicted by the HKKM11 model for the Kamioka site	28
3.3	Atmospheric neutrino/antineutrino ratio and atmospheric neutrino flux of $\nu_e + \nu_\mu$ ($\bar{\nu}_e + \bar{\nu}_\mu$), ν_e ($\bar{\nu}_e$), and ν_μ ($\bar{\nu}_\mu$) predicted by the HKKM11 model for the Kamioka site	28
3.4	Cross sections of charged-current interactions to nucleon for ν_μ and $\bar{\nu}_\mu$ used in NEUT (version 5.4.0.1)	29
3.5	Cross sections of charged-current interactions to nucleon for ν_e and $\bar{\nu}_e$ used in NEUT (version 5.4.0.1)	29

3.6	Schematic view of neutrino-oxygen NCQE scattering	30
3.7	NCQE cross section on nucleon and on oxygen nucleus as a function of neutrino energy	31
3.8	The ratio of the BBBA05 vector form factors to G_d	32
3.9	Schematic view of a spallation event	36
3.10	Energy spectrum of electrons from ${}^9\text{Li}$ decays modeled by the BESTIOLE code	36
3.11	Activities of Japanese reactors from April 2018	37
3.12	Expected reactor neutrino flux at the SK	37
3.13	IBD cross section of Strumia-Vissani model	38
3.14	Final state models of neutron inelastic scattering	39
3.15	Final state models of proton inelastic scattering	39
3.16	Final state models of charged pion inelastic scattering	39
3.17	Cross sections of charged pion inelastic scattering	40
3.18	Ratio of data from the ANNRI experiment by MC with the ANNRI-Gd model for the single gamma-ray events	40
4.1	Definition of the SK detector coordinate system	41
4.2	Probability density function for $t_{\text{res},i}$	42
4.3	Vertex resolution for SK-I, II, III, and IV	42
4.4	Probability density function for $\cos \Theta_i$ depending on the energy E	43
4.5	Angular resolution for SK-I and SK-III	43
4.6	Definition of the incident angle	45
4.7	Distributions of correction function $S(\theta_i, \phi_i)$ for barrel PMTs and top and bottom PMTs	45
4.8	Probability density function for wavelength λ of Cherenkov photons	46
5.1	Location of standard PMTs in ID and schematic view of the grouping of nearby PMTs	49
5.2	Picture of the Ni-Cf source	50
5.3	Charge distribution of the Ni-Cf source data in SK-III	51
5.4	Hit rate distribution of data and MC	52
5.5	Schematic view of the timing response calibration system and cross section of the diffuser ball	53
5.6	2D distribution of timing and charge for one readout channel	53
5.7	Schematic view of the laser calibration system and TOF-subtracted hit timing distributions of the laser calibration data and MC	55
5.8	Time variation of TBA in SK-V and SK-VI	56
5.9	Schematic view of the black sheet reflectivity measurement	57
5.10	Schematic view of LINAC	58
6.1	Schematic view of an atmospheric neutrino NC event with single meson	59
6.2	Schematic view of atmospheric neutrino CC events	59
6.3	Schematic view of multiple spallation cut	62
6.4	Definition of the variables used in the neutron cloud cut	63
6.5	Definition of the muon spallation sample and the random sample	64
6.6	Definition of l_t and l_l used in the spallation likelihood cut	65
6.7	Schematic view of a single-through going muon, a stopping muon, and multiple muons	65
6.8	PDFs of the muon spallation sample and the random sample for single-through going muons ($dt: 0\text{--}0.05\text{ s}, l_t: 0\text{--}300\text{ cm}$)	66
6.9	$\mathcal{L}_{\text{spall}}$ distributions ($E_{\text{vis}}: 7.49\text{--}9.49\text{ MeV}$)	69
6.10	Definition of d_{eff}	71

6.11	Schematic view of atmospheric neutrino events with two hit peaks	72
6.12	Definition of θ	73
6.13	Histogram of θ for all three hits combinations and the hit map	73
6.14	Histogram of θ for all three hits combinations	74
6.15	Schematic view of neutron candidate search	75
6.16	Vertex distribution of prompt signals and delayed signals for the data	76
6.17	θ_C distribution in BERT	77
6.18	E_{vis} distribution in BERT	78
6.19	N_{delayed} distribution in BERT	78
6.20	NCQE cumulative signal efficiencies as a function of E_{vis}	79
7.1	The number of generated neutrons per process after primary interactions	82
7.2	The number of neutrons generated after primary interactions	83
7.3	The total number of neutrons	83
7.4	The number of neutron captures	83
7.5	The number of neutron inelastic scattering reactions	84
7.6	The number of generated gamma-rays per neutron inelastic scattering reaction	84
7.7	The number of gamma-rays generated by neutron inelastic scattering reactions	85
7.8	Energy of gamma-rays generated by neutron inelastic scattering reactions	85
7.9	Total energy of gamma-rays generated by neutron inelastic scattering reactions	85
7.10	Nucleon-density distributions of ^{65}Cu	87
7.11	Time variation of four physical quantities obtained by collisions of 1-GeV protons with Pb nuclei in INCL++	88
7.12	The number of generated gamma-rays per neutron inelastic scattering reaction	89
7.13	The number of gamma-rays generated by neutron inelastic scattering reactions	89
7.14	Energy of gamma-rays generated by neutron inelastic scattering reactions	89
7.15	Total energy of gamma-rays generated by neutron inelastic scattering reactions	90
7.16	θ_C distribution	93
7.17	E_{vis} distribution	94
7.18	N_{delayed} distribution	94
8.1	Uncertainty of the measured atmospheric neutrino flux in SK	98
8.2	Ratio of atmospheric neutrino flux	98
8.3	Pictures and schematic views of Am/Be source and BGO scintillator crystals	101
8.4	Result of the toy-MC	104
8.5	The measured neutrino-oxygen NCQE cross section, the theoretical neutrino-oxygen NCQE cross section, and the atmospheric neutrino flux predicted using the HKKM11 model	104
8.6	Comparison of f_{NCQE} with previous measurements in SK and T2K	105
8.7	Comparison of the measured neutrino-oxygen NCQE cross section with previous measurements in SK and T2K	105
9.1	Expected N_{delayed} distributions in SK-VII	107
9.2	Expectation of the observed number of events as a function of SK-VII live time	107
9.3	Expectation of the statistical uncertainty as a function of SK-VII live time	108
9.4	Expectation of the difference between the observed and expected number of events in $\theta_C \in [78, 90]$ degrees as a function of SK-VII live time	108
B.1	Energy of atmospheric neutrinos that induced neutrino-nucleus interactions	111

B.2	The number of gamma-rays generated by neutrino-nucleus interactions	112
B.3	Energy of gamma-rays generated by neutrino-nucleus interactions	113
B.4	The number of neutrons generated by neutrino-nucleus interactions	114
B.5	Kinetic energy of neutrons generated by neutrino-nucleus interactions	115
B.6	2D distribution of the number of neutrons generated by neutrino-nucleus interactions and energy of atmospheric neutrinos that induced neutrino-nucleus interactions	116
B.7	Timing of delayed signals	117
B.8	NCQE cumulative signal efficiencies as a function of neutrino energy	117
B.9	Singal-to-background ratio	118
B.10	Singal-to-background ratio	118
B.11	Distance from the ID wall for the data and accidental coincidence events	119
B.12	Distance from the ID wall for atmospheric neutrino events	120
B.13	Distance from the ID wall for spallation, reactor neutrino, and DSNB events	121
B.14	d_{eff} for the data and accidental coincidence events	122
B.15	d_{eff} for atmospheric neutrino events	123
B.16	d_{eff} for spallation, reactor neutrino, and DSNB events	124
B.17	$N_{\text{decay-e}}$ for the data and accidental coincidence events	125
B.18	$N_{\text{decay-e}}$ for atmospheric neutrino events	126
B.19	$N_{\text{decay-e}}$ for spallation, reactor neutrino, and DSNB events	127
B.20	L_{cle} for the data and accidental coincidence events	128
B.21	L_{cle} for atmospheric neutrino events	129
B.22	L_{cle} for spallation, reactor neutrino, and DSNB events	130
B.23	Q_{50}/N_{50} for the data and accidental coincidence events	131
B.24	Q_{50}/N_{50} for atmospheric neutrino events	132
B.25	Q_{50}/N_{50} for spallation, reactor neutrino, and DSNB events	133
B.26	θ_{C} for the data and accidental coincidence events	134
B.27	θ_{C} for atmospheric neutrino events	135
B.28	θ_{C} for spallation, reactor neutrino, and DSNB events	136
B.29	E_{vis} for the data and accidental coincidence events	137
B.30	E_{vis} for atmospheric neutrino events	138
B.31	E_{vis} for spallation, reactor neutrino, and DSNB events	139
B.32	N_{delayed} for the data and accidental coincidence events	140
B.33	N_{delayed} for atmospheric neutrino events	141
B.34	N_{delayed} for spallation, reactor neutrino, and DSNB events	142
B.35	Distance from prompt signal to delayed signal ($N_{\text{delayed}} = 1$) for the data and accidental coincidence events	143
B.36	Distance from prompt signal to delayed signal ($N_{\text{delayed}} = 1$) for atmospheric neutrino events	144
B.37	Distance from prompt signal to delayed signal ($N_{\text{delayed}} = 1$) for spallation, reactor neutrino, and DSNB events	145
B.38	The number of generated neutrons per process after neutrino-proton NCQE reactions	146
B.39	The number of generated neutrons per process after neutrino-neutron NCQE reactions	147
B.40	The number of generated neutrons per process after antineutrino-proton NCQE reactions . .	148
B.41	The number of generated neutrons per process after antineutrino-neutron NCQE reactions .	149
B.42	The number of neutrons generated after NCQE reactions	150

B.43 The total number of neutrons	151
B.44 The number of neutron captures	152
B.45 The number of neutron inelastic scattering reactions	153
B.46 The number of generated gamma-rays per neutron inelastic scattering reaction	154
B.47 The number of gamma-rays generated by neutron inelastic scattering reactions	155
B.48 Energy of gamma-rays generated by neutron inelastic scattering reactions	156
B.49 Total energy of gamma-rays generated by neutron inelastic scattering reactions	157
B.50 The comparison of the number of gamma-rays generated by neutrino-nucleus interaction . .	162
B.51 The comparison of energy of gamma-rays generated by neutrino-nucleus interaction . . .	163
B.52 The comparison of the number of neutrons generated by neutrino-nucleus interaction . . .	164
B.53 The comparison of energy of neutrons generated by neutrino-nucleus interaction	165

List of Tables

1.1	Three-neutrino mixing parameters and δ_{CP}	5
1.2	Systematic uncertainty on the NCQE events in the SK-Gd DSNB search	11
2.1	Thermal neutron capture cross sections	19
2.2	Information of each observation phase	20
2.3	Cherenkov threshold of main charged particles	22
3.1	Spectroscopic strengths of the ^{16}O hole states and probabilities that a nucleon in the state is knocked out	32
3.2	De-excitation modes of $(p_{3/2})^{-1}$ state for ^{15}O implemented in NEUT	33
3.3	De-excitation modes of $(p_{3/2})^{-1}$ state for ^{15}N implemented in NEUT	33
3.4	De-excitation modes of $(s_{1/2})^{-1}$ state for ^{15}O implemented in NEUT	34
3.5	De-excitation modes of $(s_{1/2})^{-1}$ state for ^{15}N implemented in NEUT	35
4.1	Values of p_i and N_{thr}	47
5.1	Values of P_0 to P_8	56
6.1	AFT trigger efficiency considering the whole period of SK-VI	61
6.2	Cut criteria of neutron cloud cut	63
6.3	Cut criteria of spallation likelihood cut for single-through going muons	67
6.4	Cut criteria of spallation likelihood cut for stopping muons	67
6.5	Cut criteria of spallation likelihood cut for multiple muons	68
6.6	Cut criteria of spallation likelihood cut for misfit muons	68
6.7	Cut criteria of spallation box cut	70
6.8	Spallation cut efficiency for random and ^9Li events	70
6.9	The expected number of events in each secondary interaction model	77
6.10	NCQE cumulative signal efficiencies at each event reduction	80
7.1	The number of neutrons generated by each process, the total number of neutrons and neutron captures, and the number of gamma-rays	91
7.2	Values of the chi-square for θ_C , E_{vis} , and N_{delayed} distributions	92
7.3	The observed and expected number of events in $\theta_C \in [78, 90]$ degrees and $E_{\text{vis}} \in [7.49, 29.49]$ MeV in this study and T2K	93
8.1	Systematic uncertainties of the expected NCQE, NC non-QE, and CC events	96
8.2	Measured atmospheric neutrino flux using SK-I to SK-IV data	97
8.3	Production probabilities of $(p_{1/2})^{-1}$, $(p_{3/2})^{-1}$, and $(s_{1/2})^{-1}$ state and the expected number of NCQE, NC non-QE, and CC events in each condition of the primary interaction uncertainty estimation	99
8.4	The expected number of NCQE, NC non-QE, and CC events in each condition of the secondary interaction uncertainty estimation	100
8.5	The expected number of NCQE, NC non-QE, and CC events in each condition of the energy cutoff uncertainty estimation	100
8.6	Systematic uncertainties for the reduction cuts	101
B.1	The number of neutrons generated by each process, the total number of neutrons and neutron captures, and the number of gamma-rays in the case of neutrino-proton NCQE reactions	158
B.2	The number of neutrons generated by each process, the total number of neutrons and neutron captures, and the number of gamma-rays in the case of neutrino-neutron NCQE reactions	159

- B.3 The number of neutrons generated by each process, the total number of neutrons and neutron captures, and the number of gamma-rays in the case of antineutrino-proton NCQE reactions 160
- B.4 The number of neutrons generated by each process, the total number of neutrons and neutron captures, and the number of gamma-rays in the case of antineutrino-neutron NCQE reactions 161

1 Introduction

1.1 Neutrino

Neutrinos, which are Fermions with spin of 1/2, are classified as leptons that do not participate in the strong interaction in the Standard Model (SM) of the particle physics. Moreover, neutrinos do not have charge. Therefore, neutrinos interact with other particles only via the weak interaction¹, and are difficult to observe. The name "neutrino" was named by E. Fermi in 1933 [2]. The name comes from the "neutral" that means the zero charge, and "ino" that means small in Italian. Currently, we know that there are three flavors of neutrinos: electron neutrino, muon neutrino, and tau neutrino.

The existence of neutrinos was suggested by W. Pauli in 1930 [2]. Once, the energy spectrum of the electron emitted by the beta decay was expected to be the line spectrum. However, in 1914, J. Chadwick found that the energy spectrum was not the line spectrum but the continuous spectrum [3]. To explain the continuous spectrum of the electron reported by Chadwick, Pauli claimed that an unknown particle with spin of 1/2 and zero charge is emitted in the beta decay in addition to an electron. In 1956, more than 20 years after Pauli proposed the existence of neutrinos, (electron anti)neutrinos produced in nuclear reactors were discovered by F. Reines and C. Cowan [4]. In 1962, muon neutrinos were discovered in the accelerator experiment by L. Lederman, M. Schwartz, and J. Steinberger [5]. In 2001, tau neutrinos were discovered in the DONUT (Direct Observation of NU Tau) experiment [6].

1.2 Neutrino oscillation

In the SM, the neutrino mass was assumed to be zero [1]. However, in 1998, the evidence for the neutrino oscillation was discovered in the Super-Kamiokande and it was proved that the neutrino mass is not zero [7]. Neutrino oscillation is a phenomenon that the flavor of neutrino changes while the neutrino passes through a space.

Here, the neutrino oscillation in vacuum is considered. The flavor eigenstate $|\nu_\alpha\rangle$ is represented by the superposition of the mass eigenstate $|\nu_i\rangle$,

$$|\nu_\alpha\rangle = \sum_{i=1}^n U_{\alpha i}^* |\nu_i\rangle, \quad (1.1)$$

where $n (= 3)$ is the number of neutrino species and U is a 3×3 unitary matrix, called the Pontecorvo-Maki-Nakagawa-Sakata (PMNS) mixing matrix. This matrix consists of four independent parameters (three

¹Gravitational interaction can be ignored because gravitational constant (magnitude of the gravitational interaction) is so tiny. Gravitational constant, Fermi coupling constant (magnitude of the weak interaction), fine-structure constant (magnitude of the electromagnetic interaction), and strong coupling constant (magnitude of the strong interaction) are $6.708\,83(15) \times 10^{-39} \hbar c (\text{GeV}/c^2)^{-2}$, $1.166\,378\,8(6) \times 10^{-5} \text{GeV}^{-2}$, $7.297\,352\,5693(11) \times 10^{-3}$, and $0.1180(9)$, respectively [1].

mixing angles, θ_{12} , θ_{23} , and θ_{13} , and one phase angle δ_{CP}),

$$\begin{aligned} U &= \begin{pmatrix} 1 & 0 & 0 \\ 0 & c_{23} & s_{23} \\ 0 & -s_{23} & c_{23} \end{pmatrix} \begin{pmatrix} c_{13} & 0 & s_{13}e^{-i\delta_{\text{CP}}} \\ 0 & 1 & 0 \\ -s_{13}e^{i\delta_{\text{CP}}} & 0 & c_{13} \end{pmatrix} \begin{pmatrix} c_{12} & s_{12} & 0 \\ -s_{12} & c_{12} & 0 \\ 0 & 0 & 1 \end{pmatrix} \\ &= \begin{pmatrix} c_{12}c_{13} & s_{12}c_{13} & s_{13}e^{-i\delta_{\text{CP}}} \\ -s_{12}c_{23} - c_{12}s_{23}s_{13}e^{i\delta_{\text{CP}}} & c_{12}c_{23} - s_{12}s_{23}s_{13}e^{i\delta_{\text{CP}}} & s_{23}c_{13} \\ s_{12}s_{23} - c_{12}c_{23}s_{13}e^{i\delta_{\text{CP}}} & -c_{12}s_{23} - s_{12}c_{23}s_{13}e^{i\delta_{\text{CP}}} & c_{23}c_{13} \end{pmatrix}, \end{aligned} \quad (1.2)$$

where $c_{ij} \equiv \cos \theta_{ij}$ and $s_{ij} \equiv \sin \theta_{ij}$. After traveling a distance L ($\simeq ct$ for relativistic neutrinos), the flavor eigenstate evolves as

$$|\nu_\alpha(t)\rangle = \sum_{i=1}^n U_{\alpha i}^* |\nu_i(t)\rangle, \quad (1.3)$$

where $|\nu_i(t)\rangle = e^{-iE_i t} |\nu_i(0)\rangle$ (E_i is the energy of the neutrino mass eigenstate ν_i). At that time, the probability of being observed as the flavor eigenstate $|\nu_\beta\rangle$ is

$$P_{\alpha\beta} = |\langle \nu_\beta | \nu_\alpha(t) \rangle|^2 = \left| \sum_{i=1}^n \sum_{j=1}^n U_{\alpha i}^* U_{\beta j} \langle \nu_j | \nu_i(t) \rangle \right|^2. \quad (1.4)$$

Here, neutrinos are relativistic, thus $p_i \simeq p_j \equiv p \simeq E$. Therefore, E_i can be approximated as

$$E_i = \sqrt{p_i^2 + m_i^2} = p_i \sqrt{1 + \frac{m_i^2}{p_i^2}} \simeq p_i \left(1 + \frac{m_i^2}{2p_i^2} \right) \simeq E + \frac{m_i^2}{2E}. \quad (1.5)$$

Using Equation (1.5) and the orthogonality of the mass eigenstates, $\langle \nu_j | \nu_i \rangle = \delta_{ij}$, Equation (1.4) can be expressed as

$$P_{\alpha\beta} = \delta_{\alpha\beta} - 4 \sum_{i < j} \text{Re}[U_{\alpha i} U_{\beta i}^* U_{\alpha j}^* U_{\beta j}] \sin^2 X_{ij} + 2 \sum_{i < j} \text{Im}[U_{\alpha i} U_{\beta i}^* U_{\alpha j}^* U_{\beta j}] \sin 2X_{ij}, \quad (1.6)$$

where

$$X_{ij} = \frac{(m_i^2 - m_j^2)L}{4E} \equiv \frac{\Delta m_{ij}^2 L}{4E} = 1.267 \frac{\Delta m_{ij}^2}{\text{eV}^2} \frac{L/E}{\text{m/MeV}}. \quad (1.7)$$

For a simpler example, the neutrino oscillation between two neutrino species in vacuum is considered. The relationship between flavor eigenstates and mass eigenstates can be expressed as

$$\begin{pmatrix} |\nu_\alpha\rangle \\ |\nu_\beta\rangle \end{pmatrix} = \begin{pmatrix} \cos \theta & \sin \theta \\ -\sin \theta & \cos \theta \end{pmatrix} \begin{pmatrix} |\nu_1\rangle \\ |\nu_2\rangle \end{pmatrix} = \begin{pmatrix} \cos \theta |\nu_1\rangle + \sin \theta |\nu_2\rangle \\ -\sin \theta |\nu_1\rangle + \cos \theta |\nu_2\rangle \end{pmatrix}. \quad (1.8)$$

From Equation (1.8),

$$\begin{pmatrix} |\nu_1\rangle \\ |\nu_2\rangle \end{pmatrix} = \begin{pmatrix} \cos \theta |\nu_\alpha\rangle - \sin \theta |\nu_\beta\rangle \\ \sin \theta |\nu_\alpha\rangle + \cos \theta |\nu_\beta\rangle \end{pmatrix}. \quad (1.9)$$

Assuming that $|\nu_\alpha(0)\rangle = 1$ and $|\nu_\beta(0)\rangle = 0$, after traveling a distance L ($\simeq ct$ for relativistic neutrinos), the flavor eigenstates evolve as

$$\begin{aligned} |\nu_\alpha(t)\rangle &= \cos\theta|\nu_1(t)\rangle + \sin\theta|\nu_2(t)\rangle \\ &= \cos\theta \times e^{-iE_1t/\hbar}|\nu_1(0)\rangle + \sin\theta \times e^{-iE_2t/\hbar}|\nu_2(0)\rangle \\ &= e^{-iE_1t/\hbar}\cos\theta\{\cos\theta|\nu_\alpha(0)\rangle - \sin\theta|\nu_\beta(0)\rangle\} + e^{-iE_2t/\hbar}\sin\theta\{\sin\theta|\nu_\alpha(0)\rangle + \cos\theta|\nu_\beta(0)\rangle\} \\ &= e^{-iE_1t/\hbar}\cos^2\theta + e^{-iE_2t/\hbar}\sin^2\theta, \end{aligned} \quad (1.10)$$

$$\begin{aligned} |\nu_\beta(t)\rangle &= -\sin\theta|\nu_1(t)\rangle + \cos\theta|\nu_2(t)\rangle \\ &= -\sin\theta \times e^{-iE_1t/\hbar}|\nu_1(0)\rangle + \cos\theta \times e^{-iE_2t/\hbar}|\nu_2(0)\rangle \\ &= -e^{-iE_1t/\hbar}\sin\theta\{\cos\theta|\nu_\alpha(0)\rangle - \sin\theta|\nu_\beta(0)\rangle\} + e^{-iE_2t/\hbar}\cos\theta\{\sin\theta|\nu_\alpha(0)\rangle + \cos\theta|\nu_\beta(0)\rangle\} \\ &= -e^{-iE_1t/\hbar}\sin\theta\cos\theta + e^{-iE_2t/\hbar}\cos\theta\sin\theta \\ &= \sin\theta\cos\theta(-e^{-iE_1t/\hbar} + e^{-iE_2t/\hbar}). \end{aligned} \quad (1.11)$$

At that time, the probability of being observed as the flavor eigenstate $|\nu_\beta\rangle$ is

$$\begin{aligned} P_{\alpha\beta} &= |\langle\nu_\beta(t)|\nu_\alpha(0)\rangle|^2 \\ &= |\sin\theta\cos\theta(-e^{iE_1t/\hbar} + e^{iE_2t/\hbar})(\cos^2\theta + \sin^2\theta)|^2 \\ &= (\sin\theta\cos\theta)^2(-e^{iE_1t/\hbar} + e^{iE_2t/\hbar})(-e^{-iE_1t/\hbar} + e^{-iE_2t/\hbar}) \\ &= \left(\frac{1}{2}\sin 2\theta\right)^2 [2 - \{e^{i(E_2-E_1)t/\hbar} + e^{-i(E_2-E_1)t/\hbar}\}] \\ &= \frac{1}{4}\sin^2 2\theta \left\{2 - 2\cos\frac{(E_2-E_1)t}{\hbar}\right\} \\ &= \frac{1}{4}\sin^2 2\theta \times 4\sin^2\frac{(E_2-E_1)t}{2\hbar} \\ &\quad \left(\because 2 - 2\cos\frac{(E_2-E_1)t}{\hbar} = 2 - 2\left\{\cos^2\frac{(E_2-E_1)t}{2\hbar} - \sin^2\frac{(E_2-E_1)t}{2\hbar}\right\}\right) \\ &= 2 - 2\left\{1 - 2\sin^2\frac{(E_2-E_1)t}{2\hbar}\right\} = 4\sin^2\frac{(E_2-E_1)t}{2\hbar} \\ &= \sin^2 2\theta \sin^2\frac{(E_2-E_1)t}{2\hbar} \\ &= \sin^2 2\theta \sin^2\left(\frac{m_2^2 - m_1^2}{2E}\frac{ct}{2\hbar c}\right) \quad (\because \text{Equation (1.5)}) \\ &= \sin^2 2\theta \sin^2\frac{\Delta m_{21}^2 L}{4E\hbar c} \\ &= \sin^2 2\theta \sin^2\left(\frac{\Delta m_{21}^2}{\text{eV}^2}\frac{L/E}{\text{m/eV}}\frac{\text{eV} \times \text{m}}{4 \times 1.9733 \times 10^{-7}}\right) \\ &= \sin^2 2\theta \sin^2\left(1.267\frac{\Delta m_{21}^2}{\text{eV}^2}\frac{L/E}{\text{m/MeV}}\right) \\ &= \sin^2 2\theta \sin^2 X_{21} \quad (\because \text{Equation (1.7)}). \end{aligned} \quad (1.12)$$

While the probability of being observed as the flavor eigenstate $|\nu_\alpha\rangle$ is

$$P_{\alpha\alpha} = 1 - \sin^2 2\theta \sin^2 X_{21}. \quad (1.13)$$

Next, the neutrino oscillation between two neutrino species (ν_e and ν_μ) in matter is considered. In matter, all flavor neutrinos are affected by the potential due to its neutral-current interactions, while only electron

neutrinos are affected by the potential due to its charged-current interactions with electrons. Therefore, Equation (1.8) and Equation (1.9) change as

$$\begin{pmatrix} |\nu_e\rangle \\ |\nu_\mu\rangle \end{pmatrix} = \begin{pmatrix} \cos\theta_M |\nu_1^M\rangle + \sin\theta_M |\nu_2^M\rangle \\ -\sin\theta_M |\nu_1^M\rangle + \cos\theta_M |\nu_2^M\rangle \end{pmatrix}, \quad (1.14)$$

$$\begin{pmatrix} |\nu_1^M\rangle \\ |\nu_2^M\rangle \end{pmatrix} = \begin{pmatrix} \cos\theta_M |\nu_e\rangle - \sin\theta_M |\nu_\mu\rangle \\ \sin\theta_M |\nu_e\rangle + \cos\theta_M |\nu_\mu\rangle \end{pmatrix}. \quad (1.15)$$

Assuming that $|\nu_e(0)\rangle = 1$ and $|\nu_\mu(0)\rangle = 0$, the probability of being observed as the flavor eigenstate $|\nu_\mu\rangle$ after traveling a distance L ($\simeq ct$ for relativistic neutrinos) is

$$P_{e\mu} = \sin^2 2\theta_M \sin^2 X_M. \quad (1.16)$$

While the probability of being observed as the flavor eigenstate $|\nu_e\rangle$ is

$$P_{ee} = 1 - \sin^2 2\theta_M \sin^2 X_M. \quad (1.17)$$

Here,

$$\begin{aligned} M_1^2 &= \frac{m_1^2 + m_2^2}{2} + \sqrt{2}G_F N_e E \\ &\quad - \frac{1}{2}\sqrt{(\Delta m_{21}^2 \sin 2\theta)^2 + (\Delta m_{21}^2 \cos 2\theta - 2\sqrt{2}G_F N_e E)^2}, \end{aligned} \quad (1.18)$$

$$\begin{aligned} M_2^2 &= \frac{m_1^2 + m_2^2}{2} + \sqrt{2}G_F N_e E \\ &\quad + \frac{1}{2}\sqrt{(\Delta m_{21}^2 \sin 2\theta)^2 + (\Delta m_{21}^2 \cos 2\theta - 2\sqrt{2}G_F N_e E)^2}, \end{aligned} \quad (1.19)$$

$$\Delta M_{21}^2 \equiv M_2^2 - M_1^2 = \sqrt{(\Delta m_{21}^2 \sin 2\theta)^2 + (\Delta m_{21}^2 \cos 2\theta - 2\sqrt{2}G_F N_e E)^2}, \quad (1.20)$$

$$\sin^2 2\theta_M = \left(\frac{\Delta m_{21}^2 \sin 2\theta}{\Delta M_{21}^2} \right)^2, \quad (1.21)$$

$$X_M = 1.267 \frac{\Delta M_{21}^2}{\text{eV}^2} \frac{L/E}{\text{m/MeV}}. \quad (1.22)$$

In Equation (1.18) to Equation (1.22), M_1 and M_2 are the effective neutrino masses in matter, G_F is the Fermi coupling constant, and N_e is the electron number density in the medium. In a medium with varying density (N_e), $\sin^2 2\theta_M$ becomes largest when

$$\Delta m_{21}^2 \cos 2\theta = 2\sqrt{2}G_F N_e E. \quad (1.23)$$

The effect that the oscillation probability changes significantly with density is called the Mikheyev-Smirnov-Wolfenstein (MSW) effect. Details about neutrino oscillations in matter are summarized in Ref. [1,8].

From the above calculation, it can be seen that the neutrino oscillation can be described by six parameters (θ_{12} , θ_{23} , θ_{13} , Δm_{21}^2 , Δm_{32}^2 , and δ_{CP}). These parameters can be measured by observing the oscillation phenomena of solar neutrinos, atmospheric neutrinos, reactor neutrinos, and accelerator neutrinos. Table 1.1 shows the three-neutrino mixing parameters and δ_{CP} [9]. Currently, the absolute neutrino masses (m_1 , m_2 , and m_3) and the neutrino mass ordering are not yet known. There are two possibilities of the neutrino mass ordering: Normal Ordering (NO, $m_1 < m_2 < m_3$) or Inverted Ordering (IO, $m_3 < m_1 < m_2$). At this time, NO is a little preferred [10]. Moreover, CP conserving points, $\delta_{\text{CP}} = 0$ and $\delta_{\text{CP}} = \pi$, are rejected at the 95% confidence level [11].

Table 1.1: Three-neutrino mixing parameters and δ_{CP} [9]. Here, $\theta_{ij} \in [0, \pi/2]$ and $\delta_{\text{CP}} \in [0, 2\pi]$.

$\sin^2 \theta_{12}$	0.307 ± 0.013
$\sin^2 \theta_{23}$ (NO)	$0.547^{+0.018}_{-0.024}$
$\sin^2 \theta_{23}$ (IO)	$0.534^{+0.021}_{-0.024}$
$\sin^2 \theta_{13}$	$(2.20 \pm 0.07) \times 10^{-2}$
Δm_{21}^2	$(7.53 \pm 0.18) \times 10^{-5} \text{ eV}^2$
Δm_{32}^2 (NO)	$(2.437 \pm 0.033) \times 10^{-3} \text{ eV}^2$
Δm_{32}^2 (IO)	$(-2.519 \pm 0.033) \times 10^{-3} \text{ eV}^2$
δ_{CP}	$1.23 \pm 0.21 \pi \text{ rad}$

1.3 Neutrinos from core-collapse supernovae

A star with mass more than about eight solar masses causes a huge explosion called "core-collapse supernova" at the end of its life [12, 13]. The released energy is approximately 10^{53} ergs, and about 99% of that energy is carried away by neutrinos [14]. Here, observations of neutrinos from core-collapse supernovae are briefly described.

1.3.1 Neutrinos from SN1987A

On February 23, 1987, Kamiokande II, IMB (Irvine-Michigan-Brookhaven), and Baksan observed a burst of neutrinos from SN1987A², which is a core-collapse supernova that occurred in the Large Magellanic Cloud [16–18]. Here, Kamiokande II and IMB are water Cherenkov detectors and Baksan is a scintillator detector. Figure 1.1 shows the neutrino events from SN1987A observed in Kamiokande II and IMB [12]. This was the world's first observation of neutrinos from a supernova (neutrinos from outside the solar system), and we got a better understanding on supernovae from this observation [15]. To further understand about supernovae, detectors around the world, including Super-Kamiokande, are waiting for the next neutrino burst from nearby supernova.

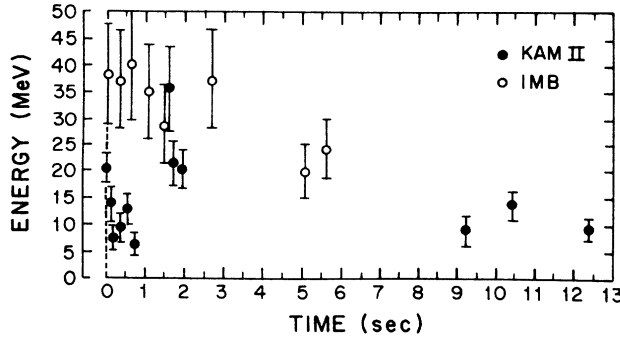


Figure 1.1: Neutrino events from SN1987A observed in Kamiokande II and IMB [12].

²Mont Blanc also reported neutrino signals from SN1987A [15]. However, signals reported in Mont Blanc were unrelated to SN1987A.

1.3.2 Diffuse supernova neutrino background

As described in Section 1.3.1, now we are waiting for the next neutrino burst from nearby supernova. However, according to Ref. [19], a galactic core-collapse supernova rate is only $3.2^{+7.3}_{-2.6}$ per century, and actually bursts of neutrinos from supernovae have not been observed since SN1987A. Nevertheless, there is a way to understand about supernovae without waiting for the neutrino bursts. Neutrinos emitted from all past core-collapse supernovae comprise an integrated flux called the diffuse supernova neutrino background (DSNB) [20]. Detecting the DSNB would contribute to our understanding of the mechanism of supernova explosions and the history of star formation.

According to Ref. [21], the DSNB flux on the Earth can be described as

$$\frac{d\Phi(E_\nu)}{dE_\nu} = c \int_0^{z_{\max}} \frac{dz}{H_0 \sqrt{\Omega_m(1+z)^3 + \Omega_\Lambda}} \times \left[R_{\text{CC}}(z) \int_0^{Z_{\max}} \psi_{\text{ZF}}(z, Z) \left\{ \int_{M_{\min}}^{M_{\max}} \psi_{\text{IMF}}(M) \frac{dN(M, Z, E'_\nu)}{dE'_\nu} dM \right\} dZ \right], \quad (1.24)$$

where c is the velocity of light, $H_0 = 70 \text{ km s}^{-1} \text{ Mpc}^{-1}$, $\Omega_m = 0.3$, $\Omega_\Lambda = 0.7$, Z is the metallicity of progenitors, M is the initial mass of progenitors, and $dN(M, Z, E'_\nu)/dE'_\nu$ is the neutrino number spectrum from the core collapse of a progenitor including the neutrino oscillation effect. The neutrino energy on the Earth E_ν is related to that at the redshift z , E'_ν , as $E'_\nu = (1+z)E_\nu$. The total core-collapse rate $R_{\text{CC}}(z)$ is determined by the cosmic star formation rate density. The metallicity distribution function of progenitors $\psi_{\text{ZF}}(z, Z)$ and the initial mass function of progenitors $\psi_{\text{IMF}}(M)$ are normalized as

$$\int_0^{Z_{\max}} \psi_{\text{ZF}}(z, Z) dZ = 1, \quad (1.25)$$

$$\int_{M_{\min}}^{M_{\max}} \psi_{\text{IMF}}(M) dM = 1. \quad (1.26)$$

Figure 1.2 shows the predictions of DSNB $\bar{\nu}_e$ flux [22]. As shown in this figure, the predicted DSNB $\bar{\nu}_e$ fluxes differ by more than one order of magnitude between the smallest one and the largest one.

1.4 DSNB search

As shown in Figure 1.2, there are many predictions of DSNB $\bar{\nu}_e$ flux. Observation of the DSNB can limit these predictions. Here, the DSNB search method and the current status of DSNB search are explained.

Most of experiments look for the inverse-beta decay (IBD) events by electron antineutrinos ($\bar{\nu}_e + p \rightarrow e^+ + n$) in the DSNB search. It is because its cross section is large in the $\mathcal{O}(10)$ MeV region, as shown in Figure 1.3, where the DSNB flux is large.

Since the 1980s, the DSNB search has been performed in various experiments. The DSNB has not been observed yet, but the upper limits of $\bar{\nu}_e$ flux are approaching and arriving at the predicted DSNB $\bar{\nu}_e$ fluxes. Figure 1.4 shows the upper limits of $\bar{\nu}_e$ flux in recent DSNB searches [38]. Here, we focus on the DSNB search performed in Super-Kamiokande (SK), KamLAND, and Borexino.

SK is a 50-kilotons water Cherenkov detector in Kamioka, Gifu, Japan. Details of the SK are described in Section 2. In 2012, the DSNB search using 2,853 days of data was performed in SK. This search gave the upper limits of $\bar{\nu}_e$ flux in the neutrino energy region above 17.3 MeV [39]. Moreover, in 2008, the data

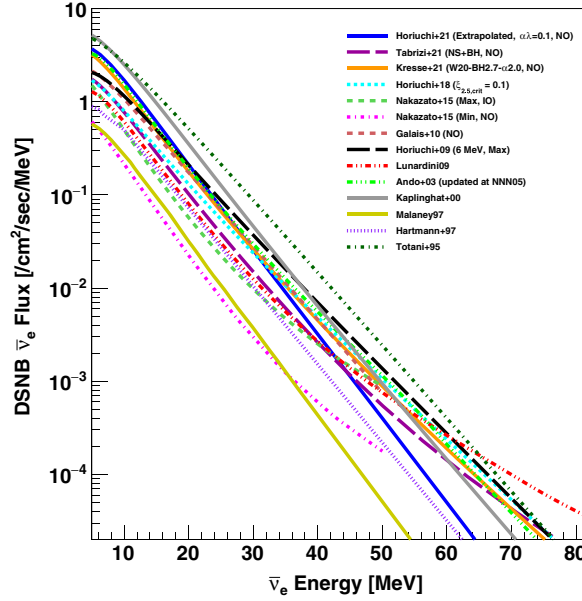


Figure 1.2: Predictions of DSNB $\bar{\nu}_e$ flux [22]. These fluxes are predicted by theoretical models of Horiuchi + 21 [23], Tabrizi + 21 [24], Kresse + 21 [25], Horiuchi + 18 [26], Nakazato + 15 [21], Galais + 10 [27], Horiuchi + 09 [28], Lunardini09 [29], Ando + 03 [30], Kaplinghat + 00 [31], Malaney + 97 [32], Hartmann + 97 [33], and Totani + 95 [34]. Ando + 03 model was updated at the NNN05 conference [35]. Details of each theoretical model are summarized in Ref. [22, 36].

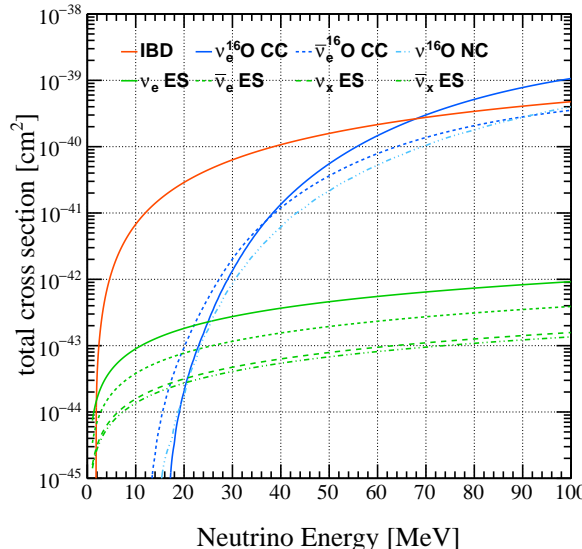


Figure 1.3: Neutrino interaction cross sections [37]. CC, NC, and ES stand for charged-current interactions, neutral-current interactions, and elastic scattering reactions, respectively.

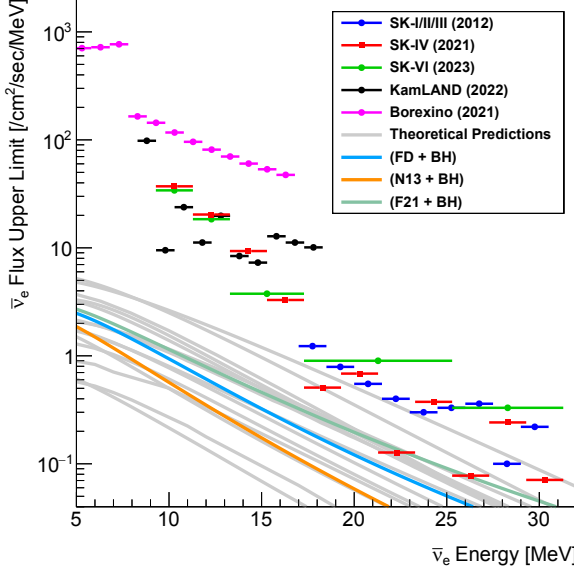


Figure 1.4: Upper limits of $\bar{\nu}_e$ flux in recent DSNB searches [38]. Plots show the 90%-confidence level upper limits for SK-I/II/III (blue) [39], SK-IV (red) [22], SK-VI (green) [40], KamLAND (black) [41], and Borexino (magenta) [42], respectively. Lines show the theoretical predictions of DSNB $\bar{\nu}_e$ flux. FD, BH, N13, and F21 stand for Fermi-Dirac, black hole, Nakazato (2013) [43], and Fornax (2021) [44,45], respectively.

acquisition system was renewed (see Section 2.8). As a result, in addition to the positron signal generated by the IBD reaction, the signal of a 2.2 MeV gamma-ray generated by neutron capture on free proton in water also became available (see Figure 1.5).

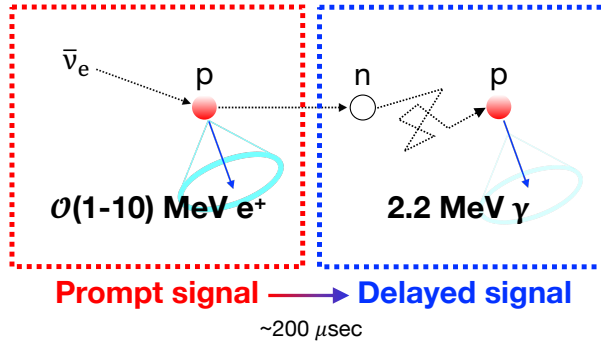


Figure 1.5: Schematic view of a DSNB event in SK. The positron emits Cherenkov photons immediately, while the neutron is thermalized and then captured on free proton in water, emitting a 2.2 MeV gamma-ray. The gamma-ray give their energy to electrons or positrons via Compton scattering or pair production, then Cherenkov photons are emitted.

By detecting the positron signal (prompt signal) and the neutron signal (delayed signal), a large number of backgrounds that do not contain neutrons can be removed, and the DSNB search in the lower energy region became possible. However, the 2.2 MeV gamma-rays are low-energy events in SK. Therefore, the neutron-tagging efficiency is low ($\sim 20\%$), and the statistics become small. In 2021, the DSNB search with the prompt and delayed signals using 2,970 days of data was performed in SK. This search gave the upper limits of $\bar{\nu}_e$ flux in the neutrino energy region above 9.3 MeV [22]. Furthermore, in 2020, 0.011% by mass of gadolinium (Gd) was loaded in the SK detector to improve the neutron-tagging efficiency, and the

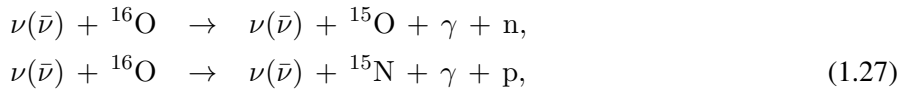
Super-Kamiokande Gadolinium (SK-Gd) experiment started [46, 47]. Details of the SK-Gd experiment are described in Section 2.4. In 2023, the DSNB search using 552.2 days of data with 0.011% gadolinium-loaded water was performed in SK-Gd. The upper limits of $\bar{\nu}_e$ flux in this search is comparable to that in SK DSNB search using 2,970 days of pure-water data [40].

KamLAND is a 1-kilotons liquid scintillator detector in Kamioka, Gifu, Japan. The advantage of KamLAND is that the 2.2 MeV gamma-ray generated by neutron capture on free proton can be detected with an efficiency of about 100%. In 2022, the DSNB search using 4,528.5 days of data was performed in KamLAND. This search gave the upper limits of $\bar{\nu}_e$ flux in the neutrino energy region from 8.3 MeV to 30.8 MeV [41]. Especially, the upper limits are the most stringent below 12.3 MeV.

Borexino is a 278-tons liquid scintillator detector in Gran Sasso, Italy. The strength of Borexino is that the energy threshold is low thanks to the extremely low radiopurity. In 2021, the DSNB search using 2,771 days of data was performed in Borexino. This search gave the upper limits of $\bar{\nu}_e$ flux in the neutrino energy region from 1.8 MeV to 16.8 MeV [42]. The upper limits below 8.3 MeV are given only by Borexino.

1.5 NCQE background in SK-Gd DSNB search

As described in Section 1.4, a large number of backgrounds that do not contain neutrons can be removed by detecting prompt and delayed signals. However, backgrounds that contain neutrons cannot be completely removed. One of the main backgrounds in the SK-Gd DSNB search is caused by the atmospheric neutrino-oxygen neutral-current quasielastic (NCQE) scattering reactions. Figure 1.6 shows the schematic view of a DSNB event and a NCQE event in SK-Gd. NCQE reactions can be expressed as



where the atmospheric neutrino knocks out a nucleon of the oxygen nucleus, and the residual nucleus may emit one or more de-excitation gamma-rays with a few MeV. When a neutron is knocked out, the combination of de-excitation gamma-rays and neutron mimics the DSNB event, making it difficult to distinguish between NCQE and DSNB events. Therefore, the precise estimation of NCQE events is essential for the DSNB discovery in SK-Gd.

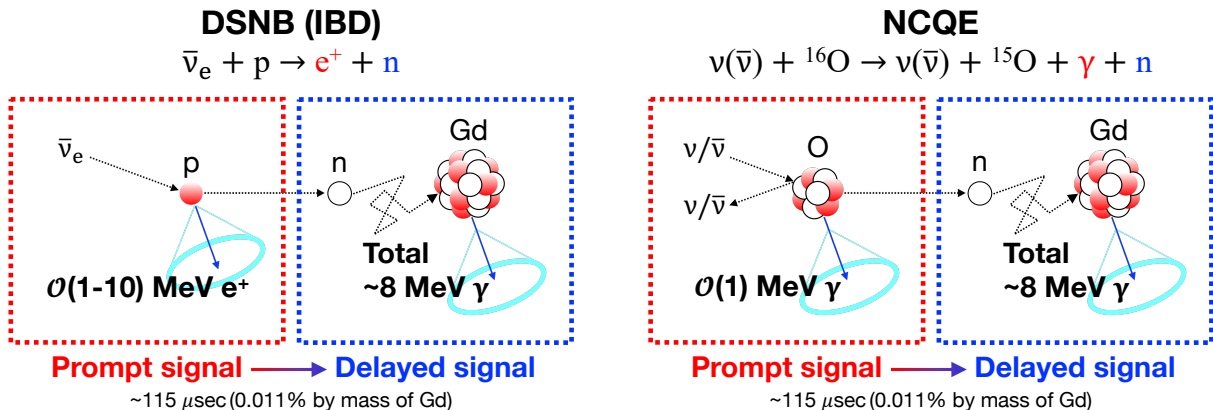


Figure 1.6: Schematic view of a DSNB event (left) and a NCQE event (right) in SK-Gd.

To estimate the NCQE events precisely, the behavior of neutrons in water must be understood. Figure 1.7 shows the kinetic energy of neutrons in DSNB events and NCQE events. In DSNB events, the outgoing neutron has at most a few MeV, while in NCQE events, the knocked-out neutron may have hundreds of MeV. In the latter case, it can knock out other nucleons of oxygen nuclei in water, and additional de-excitation gamma-rays and neutrons are generated. Since the numbers of gamma-rays and neutrons affect the event reconstruction, it is crucial to understand the nucleon-nucleus interactions in water (secondary interactions). Detailed schematic view of a NCQE event is shown in Figure 1.8.

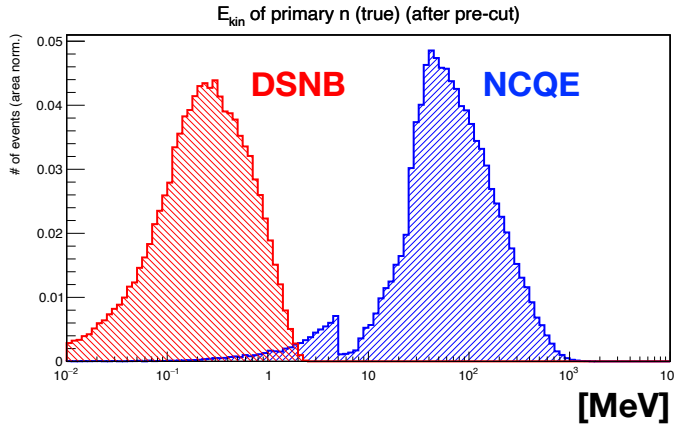


Figure 1.7: Kinetic energy of neutrons in DSNB events and NCQE events. This figure was made by using MC.

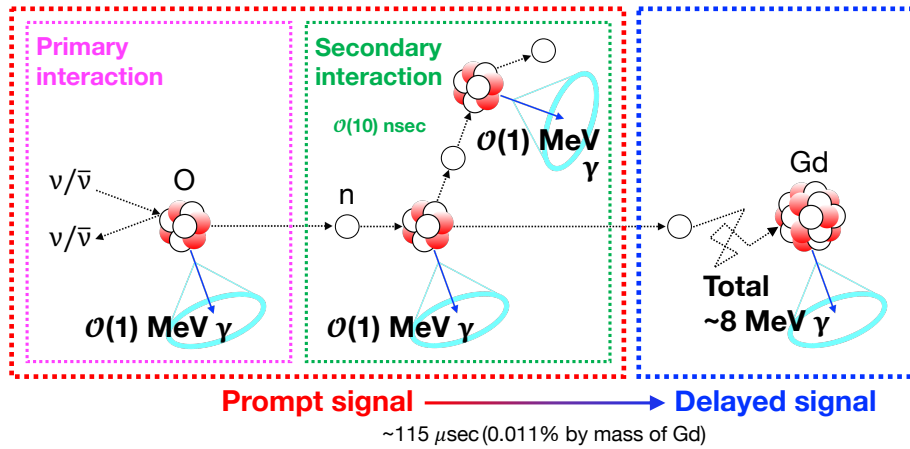


Figure 1.8: Detailed schematic view of a NCQE event. Prompt signal consists of gamma-rays generated by neutrino-nucleus (primary) interaction and nucleon-nucleus (secondary) interaction.

Figure 1.9 shows the reconstructed energy spectra of the observed data and the expected backgrounds in the SK-Gd DSNB search [40]. In this figure, the cyan color-filled histogram shows the expected number of NCQE background events and the hatched areas show the total systematic uncertainty for each bin. In this search, systematic uncertainty on the NCQE events is taken as 68% [36], which is too large to discover the DSNB in the near future. Each component of the systematic uncertainty on the NCQE events in the SK-Gd DSNB search is summarized in Table 1.2 [36]. From this table, we can confirm that uncertainties of T2K cross section, neutron multiplicity, and spectral shape are dominant. Uncertainties of neutron multiplicity and spectral shape are related to the number of neutrons and gamma-rays generated by secondary interactions,

respectively. Moreover, uncertainty of T2K cross section, which is used to scale the number of NCQE events, mainly comes from the gamma-rays by secondary interactions. Figure 1.9 and Table 1.2 show how important it is to understand secondary interactions. Details of T2K cross section are described in Section 1.6.

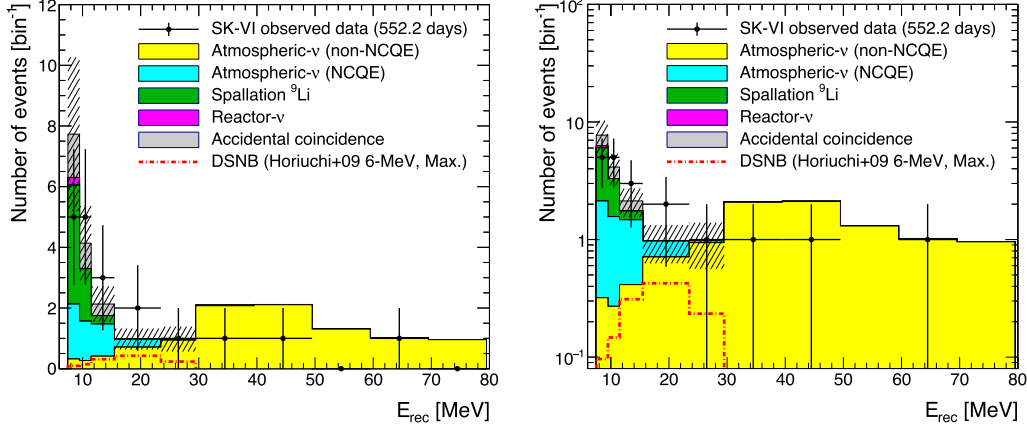


Figure 1.9: Reconstructed energy spectra of the observed data and the expected backgrounds in the SK-Gd DSNB search [40]. Left and right figure shows in a linear and a logarithmic scale for the vertical axis, respectively. These figures include not only the DSNB search window ([7.49, 29.49] MeV) but also the side-band region above 29.49 MeV. Each color-filled histogram shows the expected number of backgrounds, and these background histograms are stacked on the other histograms. Details of these backgrounds are described later. The hatched areas show the total systematic uncertainty for each bin. The red dashed-dot line shows the expected number of DSNB events predicted by the Horiuchi + 09 model [28].

Table 1.2: Systematic uncertainty on the NCQE events in the SK-Gd DSNB search [36]. This table is the same as TABLE 9.2 in Ref. [36].

T2K cross section	44%
Atmospheric neutrino flux	15%
Flux difference	7%
Reductions	2%
Neutron tagging efficiency	9%
Neutron multiplicity	30%
Spectral shape	37%
Total	68%

1.6 Measurements of NCQE cross section

1.6.1 Measurements using accelerator neutrinos

In Table 1.2, uncertainty of T2K cross section is estimated by using the result of accelerator neutrino-oxygen NCQE cross section measurement in the T2K experiment [48]. In this measurement, data from a $14.94(16.35) \times 10^{20}$ protons-on-target exposure of the neutrino (antineutrino) beam was used, and the

flux-averaged NCQE-like cross sections on oxygen nuclei were measured to be

$$\langle \sigma_{\nu\text{-NCQE}} \rangle = 1.70 \pm 0.17(\text{stat.})^{+0.51}_{-0.38}(\text{syst.}) \times 10^{-38} \text{ cm}^2/\text{oxygen}, \quad (1.28)$$

$$\langle \sigma_{\bar{\nu}\text{-NCQE}} \rangle = 0.98 \pm 0.16(\text{stat.})^{+0.26}_{-0.19}(\text{syst.}) \times 10^{-38} \text{ cm}^2/\text{oxygen}, \quad (1.29)$$

where $\langle \sigma_{\nu\text{-NCQE}} \rangle$ is for neutrinos at a flux-averaged energy of 0.82 GeV and $\langle \sigma_{\bar{\nu}\text{-NCQE}} \rangle$ is for antineutrinos at a flux-averaged energy of 0.68 GeV. The result of (1.28) was consistent with that of the previous NCQE cross section measurement in T2K ($\langle \sigma_{\nu\text{-NCQE}} \rangle = 1.55^{+0.71}_{-0.35}(\text{stat.} \oplus \text{syst.}) \times 10^{-38} \text{ cm}^2/\text{oxygen}$), where data from a 3.01×10^{20} protons-on-target exposure of the neutrino beam was used [49]. The 44% T2K cross section uncertainty in Table 1.2 can be estimated by using (1.28) and (1.29),

$$\sqrt{\left\{ \sqrt{\left(\frac{0.17}{1.70} \right)^2 + \left(\frac{0.51}{1.70} \right)^2} \right\}^2 + \left\{ \sqrt{\left(\frac{0.16}{0.98} \right)^2 + \left(\frac{0.26}{0.98} \right)^2} \right\}^2} \sim 44\%. \quad (1.30)$$

The large uncertainty mainly comes from the gamma-rays by secondary interactions. Figure 1.10 shows the reconstructed Cherenkov angle (θ_C) distributions from the FHC (neutrino-mode) sample and the RHC (antineutrino-mode) sample in the T2K NCQE cross section measurement [48]. θ_C is related to the number of gamma-rays, and θ_C becomes larger as the number of gamma-rays by secondary interactions gets larger. In Figure 1.10, we can confirm that, in the case of the FHC sample, there is a large discrepancy between data and MC in high θ_C region where events with multiple gamma-rays are dominant. This means that more gamma-rays are generated by secondary interactions in MC, that is, the agreements of the secondary interaction model used in MC is poor.

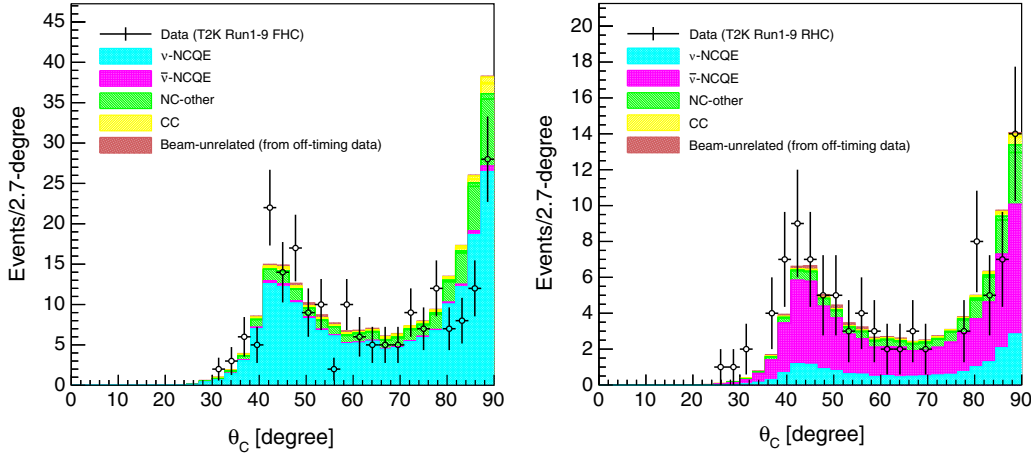


Figure 1.10: Reconstructed Cherenkov angle (θ_C) distributions from the FHC (neutrino-mode) sample (left) and the RHC (antineutrino-mode) sample (right) in the T2K NCQE cross section measurement [48]. In the left figure, there is a large discrepancy between data and MC in high θ_C region where events with multiple gamma-rays are dominant.

1.6.2 Measurements using atmospheric neutrinos

It is important to measure the NCQE cross section using atmospheric neutrinos, which are the source of backgrounds in the DSNB search, and to confirm the consistency with the NCQE cross section measurements using accelerator neutrinos. The first measurement of the atmospheric neutrino-oxygen NCQE cross section

was performed in SK pure water phase [50]. In this measurement, 2,778 days of SK pure water data from October 2008 to October 2017 was used, and the flux-averaged NCQE cross section on oxygen nuclei was measured to be

$$\langle \sigma_{\text{NCQE}} \rangle = 1.01 \pm 0.17(\text{stat.})^{+0.78}_{-0.30}(\text{syst.}) \times 10^{-38} \text{ cm}^2/\text{oxygen}. \quad (1.31)$$

Figure 1.11 shows the measured NCQE cross section [50], the theoretical NCQE cross section [51], and the atmospheric neutrino flux measured in SK [52]. The large uncertainty in this measurement also mainly comes from the gamma-rays and neutrons by secondary interactions.

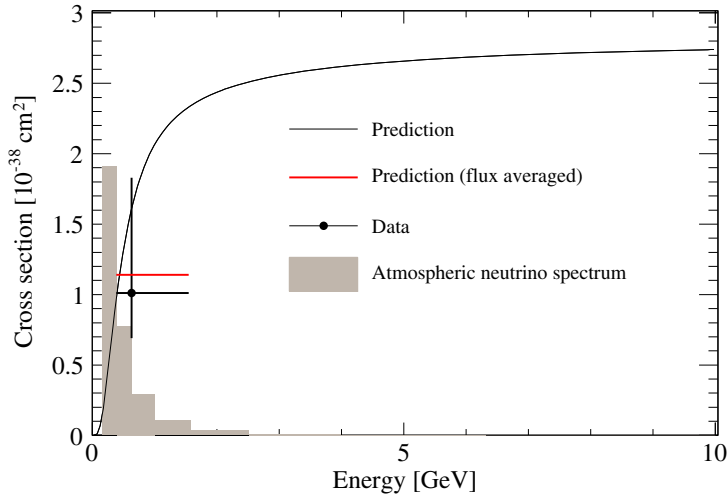


Figure 1.11: The measured NCQE cross section [50], the theoretical neutrino-oxygen NCQE cross section [51], and the atmospheric neutrino flux measured in SK [52].

1.6.3 Issues in previous measurements

In the NCQE cross section measurements described above, the large uncertainty mainly came from secondary interactions. A more precise secondary interaction model is required to reduce the uncertainty, but, so far, the secondary interaction model based on the Bertini Cascade model (BERT) [53] was the only choice in MC. However, now other secondary interaction models like the Binary Cascade model (BIC) [54] and the Liège Intranuclear Cascade model (INCL++) [55] can be employed and compared with data. In Section 7, the reproducibility of the observed data in each secondary interaction model using atmospheric neutrino events is discussed.

Moreover, the measurement of the neutrino-oxygen NCQE cross section had not been performed in SK-Gd. The NCQE cross section measurement in SK-Gd would contribute to our understanding of the behavior of neutrons in water, as well as the performance of the SK-Gd experiment. In Section 8, the first measurement of the atmospheric neutrino-oxygen NCQE cross section in the Gd-loaded SK water Cherenkov detector is reported.

2 Super-Kamiokande

2.1 Super-Kamiokande

The Super-Kamiokande (SK) [56] is the experiment held in Kamioka, Gifu, Japan, with the large water Cherenkov detector placed in 1,000 m underground, 2,700 m water equivalent overburden. The overview of the SK detector is shown in Figure 2.1. The SK stands for “Super-Kamioka Neutrino Detection Experiment” and “Super-Kamioka Nucleon Decay Experiment”. The rate of cosmic ray muon is reduced by a factor of 10^5 compared to that of the ground level.

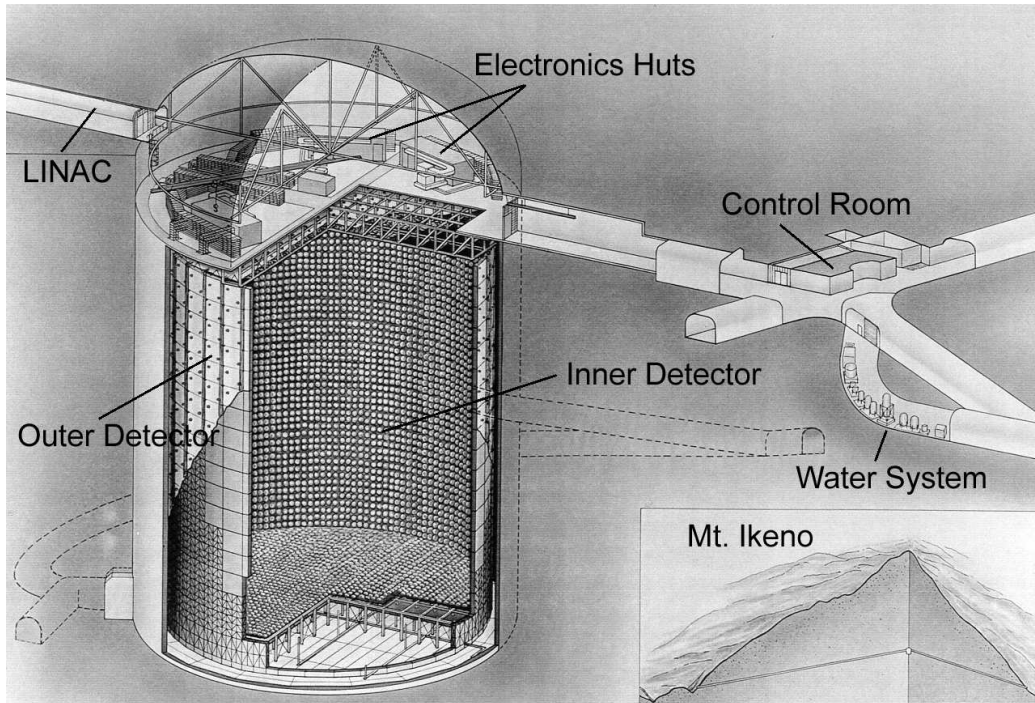


Figure 2.1: Overview of the SK detector [56].

The SK detector consists of the stainless-steel cylindrical tank with a diameter of 39.3 m and a height of 41.4 m and 50 kilotons ultrapure water. The tank is separated into the inner detector (ID) and the outer detector (OD) by stainless-steel frames (supermodule frames). The cross section of the SK detector and the overview of supermodule frames are shown in Figure 2.2. The diameter of ID, the height of ID and the volume of ID (the fiducial volume) is 33.8 m, 36.2 m and 32 kilotons (22.5 kilotons), respectively. In ID, 11,129 20-inch (50 cm) photomultiplier tubes (PMTs) are installed. The gaps between ID PMTs are covered by black polyethylene terephthalate sheets. The sheets separate ID and OD optically and suppress the reflection at the surface of the ID wall. Moreover, the sheets reduce low energy events by radioactive backgrounds occurring behind the PMTs. On the other hand, in OD, 1,885 8-inch (20 cm) PMTs are installed. OD volume is covered by white Tyvek sheets manufactured by DuPont. The Tyvek sheets have high reflectivity and enhance the light collection efficiency in OD.

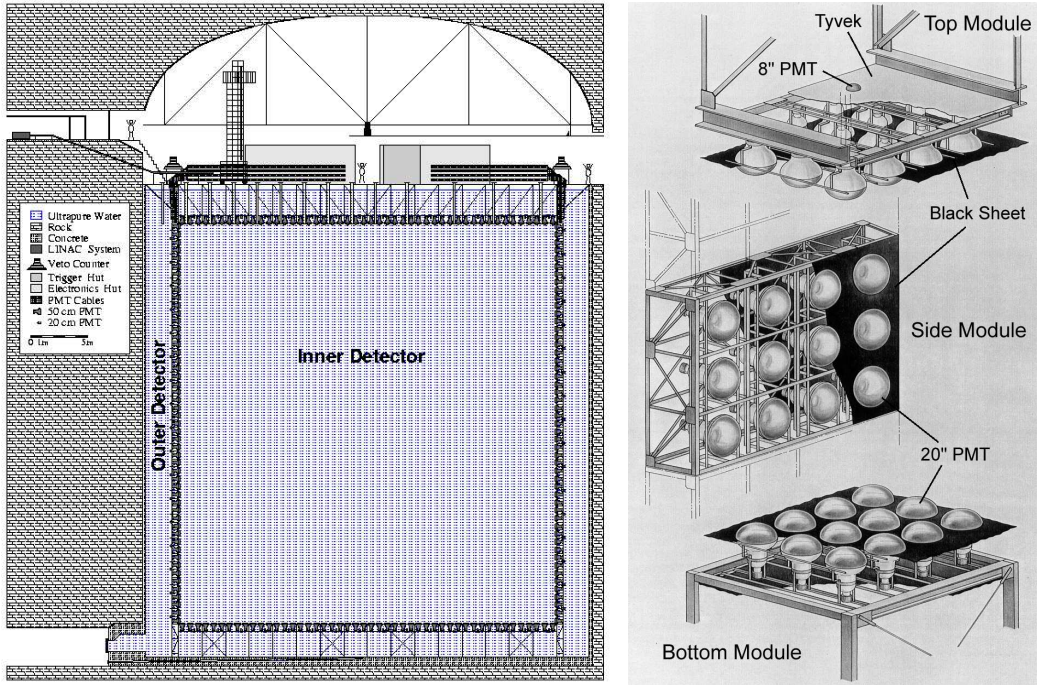


Figure 2.2: Cross section of the SK detector (left) and overview of supermodule frames (right) [56].

2.2 ID PMT and OD PMT

The schematic view of the ID PMT is shown in Figure 2.3. The number of ID PMTs is 7,650 on the barrel (side walls), 1,740 on the top and 1,739 on the bottom, and the effective photocathode coverage of ID is 40%. The role of ID PMTs is to reconstruct the energy, generated position, direction and the kind of the charged particles. Figure 2.4 shows the quantum efficiency of the ID PMT photocathode as a function of wavelength. The material of photocathode is bialkali (Sb-K-Cs) and the quantum efficiency is about 21% at 360 - 400 nm. Figure 2.5 shows the single photoelectron pulse height distribution of the ID PMT. The peak around zero ADC count is caused by PMT dark current. Figure 2.6 shows the relative transit time distribution for a typical ID PMT tested using 410 nm wavelength light at the single photoelectron intensity level. The 1σ of transit time for a single photoelectron signal is 2.16 ns.

The number of OD PMTs is 1,275 on the barrel, 302 on the top and 308 on the bottom. To compensate the small number of OD PMTs, wavelength shifting (WS) plate is attached to each OD PMT. The WS plate is square acrylic panel with a side of 60 cm and a thickness of 1.3 cm, doped with 50 mg/L of bis-MSB ($C_{24}H_{22}$). The WS plate absorbs UV light, and then emit photons in the blue - green. OD PMT with bialkali photocathode is more sensitive to blue - green photons than UV photons. Therefore, the light collection efficiency is improved by about a factor of 1.5 compared to without WS plates. The timing resolution of OD PMTs with WS plates is 15 ns (FWHM), which is poorer than that of ID PMTs. However, OD was optimized as a veto counter and the poorer timing resolution is less important. Figure 2.7 shows the positional relationship of ID PMTs and OD PMTs in a supermodule frame. Basically, in a supermodule frame, 12 ID PMTs and 2 OD PMTs are attached.

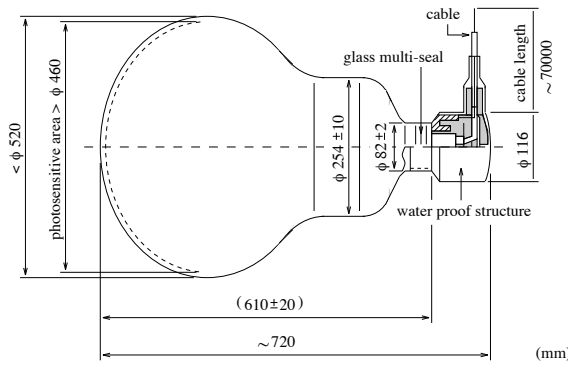


Figure 2.3: Schematic view of the ID PMT [56].

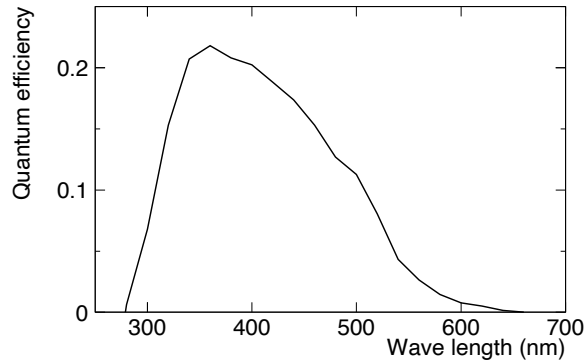


Figure 2.4: Quantum efficiency of the ID PMT photocathode as a function of wavelength [56]. The material of ID PMT photocathode is bialkali (Sb-K-Cs).

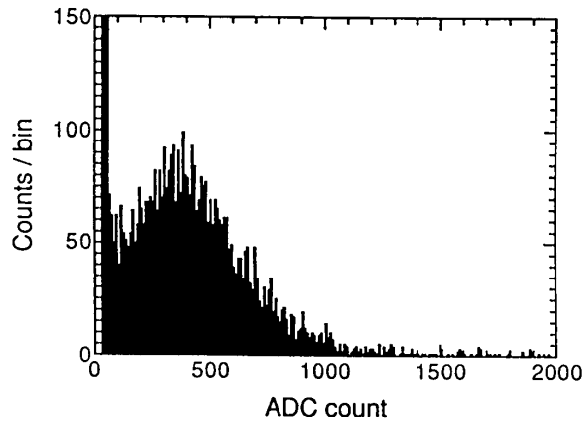


Figure 2.5: Single photoelectron pulse height distribution of the ID PMT [56]. The peak around zero ADC count is caused by PMT dark current.

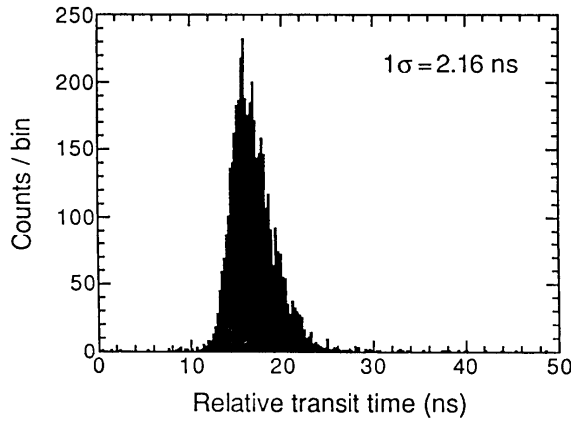


Figure 2.6: Relative transit time distribution for a typical ID PMT tested using 410 nm wavelength light at the single photoelectron intensity level [56].

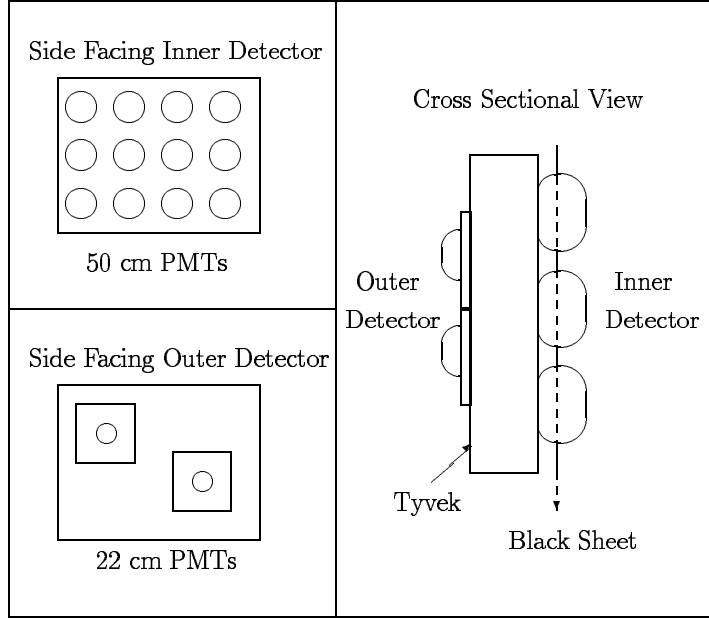


Figure 2.7: Positional relationship of ID PMTs and OD PMTs in a supermodule frame [57]. 12 ID PMTs and 2 OD PMTs are attached in a supermodule frame, basically.

2.3 Helmholtz coils

The geomagnetic field would affect photoelectron trajectories and timing in the PMTs. Therefore, 26 sets of horizontal and vertical Helmholtz coils are deployed around the inner surface of the tank to reduce the geomagnetic field. Figure 2.8 shows the schematic view of Helmholtz coils. The average geomagnetic field intensity without Helmholtz coils is about 450 mG [56]. The average field intensity can be reduced to 32 mG with Helmholtz coils, resulting that the deviation in the collection efficiency of photoelectrons is 2% [58].

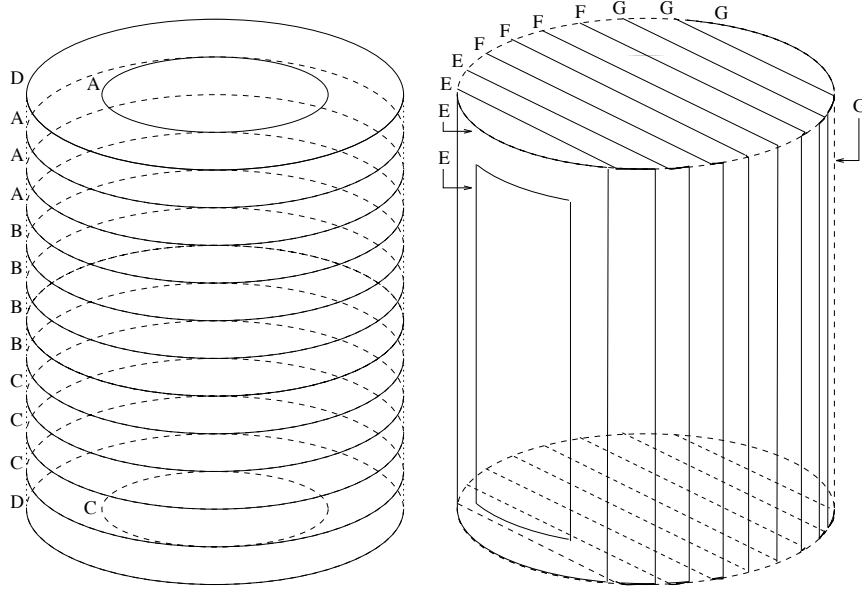


Figure 2.8: Schematic view of Helmholtz coils [59].

2.4 Observation phase

The observation phase of SK is categorized into seven, from SK-I to SK-VII. Each observation phase is described below.

SK-I

SK-I started in April 1996 and ended in July 2001. In ID, 11,146 PMTs were attached and the effective photocathode coverage of ID was 40%. It was during the SK-I that we got the evidence for neutrino oscillation [7].

SK-II

In November 12th, 2001, one bottom PMT broke when ultrapure water was filled into SK detector after finishing the detector maintenance. Due to the shockwave generated at that time, other PMTs were broken in a chain. As a result, it became a serious accident that 6,779 ID PMTs and 1,017 OD PMTs were lost. In SK-II, which started in October 2002 and ended in October 2005, the observation was performed using 5,182 remained and spare ID PMTs and 1,885 remained and new OD PMTs. The effective photocathode coverage of ID was 19%. Since SK-II, each ID PMT has been covered with a shockwave prevention case. The case consists of an acrylic that covers the photocathode and Fiber Reinforced Plastic (FRP) case that covers parts other than the photocathode. The case not only prevents shockwave but also increases the water pressure resistance of the PMT. The picture of a shockwave prevention case is shown in Figure 2.9.

SK-III

SK-III started in July 2006 and ended in August 2008. Since SK-III, the number of ID PMTs has been 11,129 and the effective photocathode coverage of ID has been 40%. The reason why the number of ID PMTs is reduced by 17 compared to SK-I is that ID PMTs cannot be installed at the edge of the detector



Figure 2.9: Picture of a shockwave prevention case [60].

because the size of the shockwave prevention case is large.

SK-IV

In September 2008, the data acquisition system was renewed from Analog Timing Module (ATM) to QTC-Based Electronics with Ethernet (QBEE) and SK-IV started [61]. QTC stands for charge-to-time converter. The renewal of the system allows us to open the data acquisition time window until $535\ \mu\text{s}$ ($385\ \mu\text{s}$ before November 2010 [22]) from the trigger timing and enabled to search neutron signals [62]. SK-IV continued until June 2018 and is longest phase at this time.

SK-V

The tank refurbishment work toward the SK-Gd experiment was conducted between SK-IV and SK-V. The purpose of the work was the water stop reinforcement of the tank, the piping improvement in the tank and the PMT replacement. After finishing the work, SK-V started in January 2019 and ended in July 2020.

SK-VI

In July 2020, we dissolved 13.2 tons of $\text{Gd}_2(\text{SO}_4)_3 \cdot 8\text{H}_2\text{O}$ (we introduced 0.011% of Gd) into the SK tank and SK-VI (the SK-Gd experiment) started. Since Gd has the largest thermal neutron capture cross section among natural elements, neutron capture rate on Gd is high even at low concentrations. Table 2.1 and Figure 2.10 show the thermal neutron capture cross sections [63] and neutron capture rate on Gd [64], respectively. Moreover, when a thermal neutron is captured on Gd, a total of about 8 MeV of gamma-rays are emitted. From these reasons, neutron-tagging efficiency is largely improved in SK-Gd. The time constant of neutron capture at this Gd mass concentration is about $115\ \mu\text{s}$ [46]. SK-VI continued until June 2022.

Table 2.1: Thermal neutron capture cross sections [63].

	H	O	S	Gd
Thermal neutron capture cross section [b]	0.33	0.0002	0.53	49,700

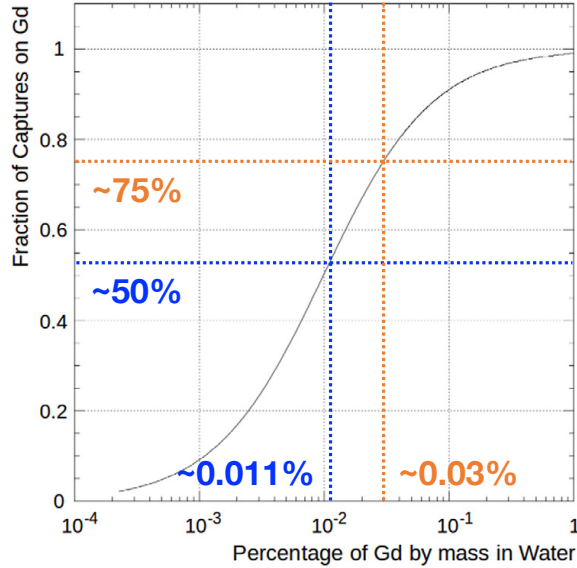


Figure 2.10: Neutron capture rate on Gd [64].

SK-VII

In June 2022, we additionally dissolved 27.3 tons of $\text{Gd}_2(\text{SO}_4)_3 \cdot 8\text{H}_2\text{O}$ into the SK tank and SK-VII started. The Gd mass concentration is comparable to 0.03%. The time constant of neutron capture at this Gd mass concentration is about $62 \mu\text{s}$.

The information of each observation phase is summarized in Table 2.2.

Table 2.2: Information of each observation phase.

Phase	SK-I	SK-II	SK-III
Start	Apr. 1996	Oct. 2002	Jul. 2006
End	Jul. 2001	Oct. 2005	Sep. 2008
# of ID PMTs (Coverage)	11,146 (40%)	5,182 (19%)	11,129 (40%)
# of OD PMTs	1,885	1,885	1,885
Electronics	ATM	ATM	ATM
Gd mass concentration	0%	0%	0%

Phase	SK-IV	SK-V	SK-VI	SK-VII
Start	Sep. 2008	Jan. 2019	Jul. 2020	Jun. 2022
End	Jun. 2018	Jul. 2020	Jun. 2022	-
# of ID PMTs (Coverage)	11,129 (40%)	11,129 (40%)	11,129 (40%)	11,129 (40%)
# of OD PMTs	1,885	1,885	1,885	1,885
Electronics	QBEE	QBEE	QBEE	QBEE
Gd mass concentration	0%	0%	0.011%	0.03%

2.5 Detection principle

When the speed of the charged particle passing through the dielectric medium is faster than the speed of light in the medium, photons are radiated conically along the track of the particle. This phenomenon is called “Cherenkov radiation”, and the radiated photons are called “Cherenkov photons”. Figure 2.11 shows the schematic view of Cherenkov radiation. The Cherenkov photons are projected in a ring as shown in left side of Figure 2.11. The ring is called “Cherenkov ring”. In the SK, the energy, generated position, direction and the kind of the charged particle are reconstructed using the time, quantity of charge and Cherenkov ring pattern information that ID PMTs received. In right side of Figure 2.11, the charged particle with velocity v moves distance $vt = \frac{v}{c}ct = \beta ct$ in time t , where c is the speed of light in vacuum and $\beta = \frac{v}{c}$ is the ratio of v and c . While the Cherenkov photon moves distance $\frac{c}{n}t$ in time t , where n is the refractive index of the dielectric medium. Therefore, when the angle between the direction of charged particle and the direction of Cherenkov photon is defined as θ_C , the next formula is established,

$$\cos \theta_C = \frac{\frac{c}{n}t}{\beta ct} = \frac{1}{n\beta}. \quad (2.1)$$

In Equation (2.1), assuming that $n = 1.34$, which is the refractive index of water, and $\beta = 1$, θ_C becomes about 42 degrees. Therefore, in water, the maximum angle between the direction of charged particle and the direction of Cherenkov angle is about 42 degrees.

The energy E required for the charged particle with rest mass m to emit Cherenkov photons (Cherenkov threshold) is

$$E = \frac{mc^2}{\sqrt{1 - \beta^2}} \geq \frac{mc^2}{\sqrt{1 - \left(\frac{1}{n}\right)^2}} = \frac{nmc^2}{\sqrt{n^2 - 1}}. \quad (2.2)$$

The Cherenkov threshold of main charged particles is summarized in Table 2.3.

Assuming that the wavelength region of Cherenkov photons is from λ_1 to λ_2 , the number of Cherenkov photons N emitted per unit length x when the particle with charge z passes through the medium is

$$\frac{dN}{dx} = 2\pi\alpha z^2 \sin^2 \theta_C \left(\frac{1}{\lambda_1} - \frac{1}{\lambda_2} \right), \quad (2.3)$$

where α is the fine-structure constant.

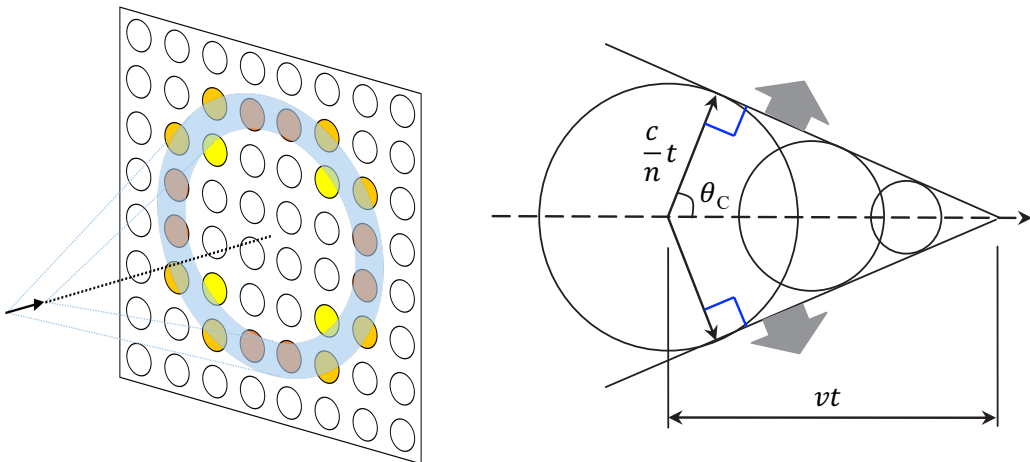


Figure 2.11: Schematic view of Cherenkov radiation [65].

Table 2.3: Cherenkov threshold of main charged particles [1]. m is rest mass and E is Cherenkov threshold. Here $n = 1.34$ is assumed.

Charged particle	e^\pm	μ^\pm	π^\pm	K^\pm	p
m [MeV/ c^2]	0.511	105.658	139.570	493.677	938.272
E [MeV]	0.768	158.730	209.676	741.652	1,409.568

2.6 Water purification system

The 50 kilotons ultrapure water of the SK is made from the underground water of the Kamioka mine. The underground water contains the dust, bacteria and radioactive impurities. These impurities should be removed to avoid decreasing the water transparency and increasing low energy backgrounds. In the SK, these impurities are removed by circulating and purifying the ultrapure water using the water purification system at a flow rate of 120 m³/h. Figure 2.12 shows the schematic view of water purification system. This system consists of three systems: the dissolving system, the pretreatment system and the re-circulation system. The dissolving system and the pretreatment system are used during Gd loading, while the re-circulation system is used during both Gd loading and data taking. Here each component of re-circulation system is described below.

- UV total organic carbon reduction lamp (TOC): TOC lamp oxidatively decomposes carbon and other compounds. These are eventually decomposed into water and carbon dioxide.
- Heat exchanger (HE): High water temperature causes the bacterial growth, the decrease of water transparency and the increase of PMT dark noise. HE keeps the water temperature around 13 °C at a precision better than 0.01 °C.
- Strongly acidic cation exchange resin (C-Ex Resin): C-Ex Resin removes positively charged impurities, and radium ions in particular, while preserving the dissolved gadolinium ions (Gd³⁺).
- Strongly basic anion exchange resin (A-Ex Resin): A-Ex Resin removes negatively charged impurities while preserving the dissolved sulfate ions (SO₄²⁻).
- One micron filter (1 μm): 1 μm filter removes the dusts larger than 1 μm.
- UV sterilizer (UV): UV sterilizer kills the bacteria.
- Ultrafiltration modules (UF): UF modules remove tiny dusts.
- Membrane degasifier (MD): MD removes radon dissolved in the ultrapure water.

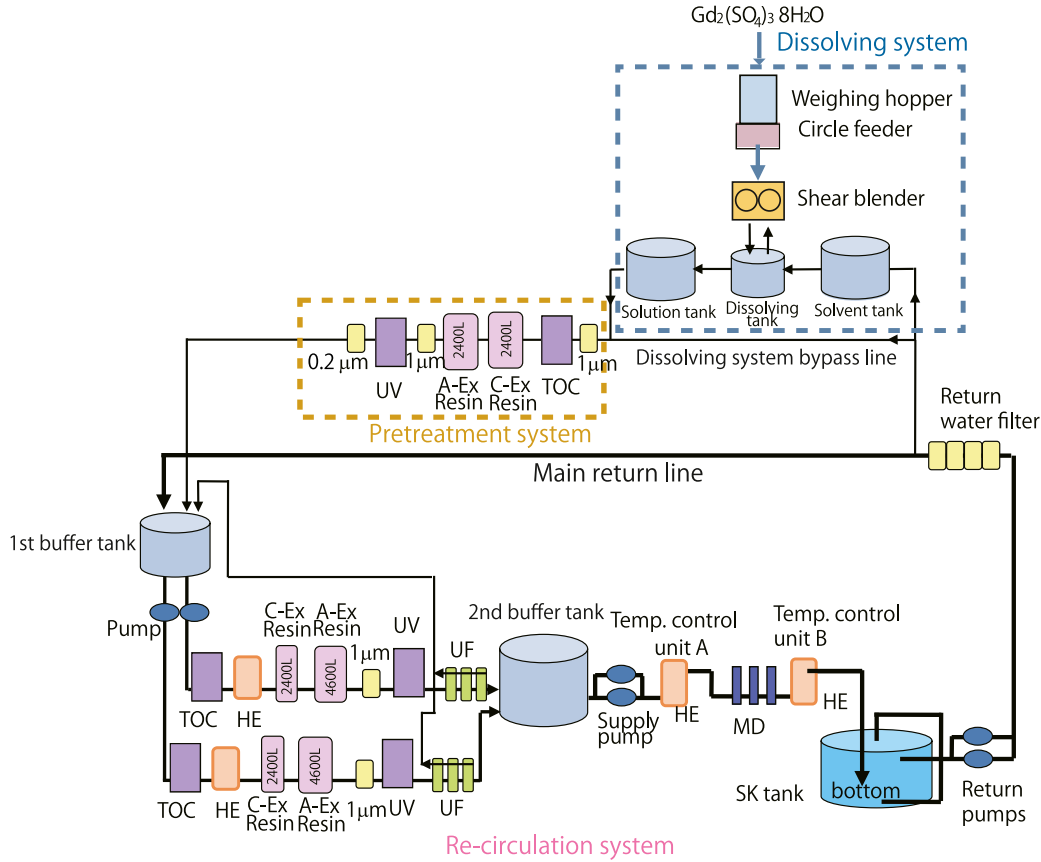


Figure 2.12: Schematic view of water purification system [46]. The dissolving system and the pretreatment system are used during Gd loading, while the re-circulation system is used during both Gd loading and data taking.

2.7 Air purification system

Most of radioactive backgrounds come from radon, which is rich in the rock of the Kamioka mine. To reduce radioactive backgrounds, radon in the air should be reduced as much as possible.

Figure 2.13 shows the typical radon concentration in the air at the SK over a year. Radon concentration in the air of the mine is 2,000 - 3,000 Bq/m³ during the warm season, from May to October, while the concentration is 100 - 300 Bq/m³ in the cold season, from November to April. This is because the airflow inside the mine changes depending on the temperature outside the mine. To keep the concentration below 100 Bq/m³ inside the experimental area, fresh air is continuously blown at a flow rate of 10 m³/min from outside the mine (Radon Hut) to the experimental area through an air duct. The flow rate makes the air pressure inside the experimental area higher than outside, minimizing the entry of the air outside the experimental area. As a result, the concentration inside the experimental area is kept at 30 - 50 Bq/m³ throughout the year, as shown in Figure 2.13.

However, the radon concentration inside the experimental area is still too high for observations with low radioactive backgrounds. Therefore, the fresh air is purified using the air purification system, then the purified air is supplied to the gap between the top of the SK tank and the water surface. Figure 2.14 shows the schematic view of air purification system. Each component of air purification system is described in Ref. [66]. The residual radon concentration in the purified air is a few mBq/m³.

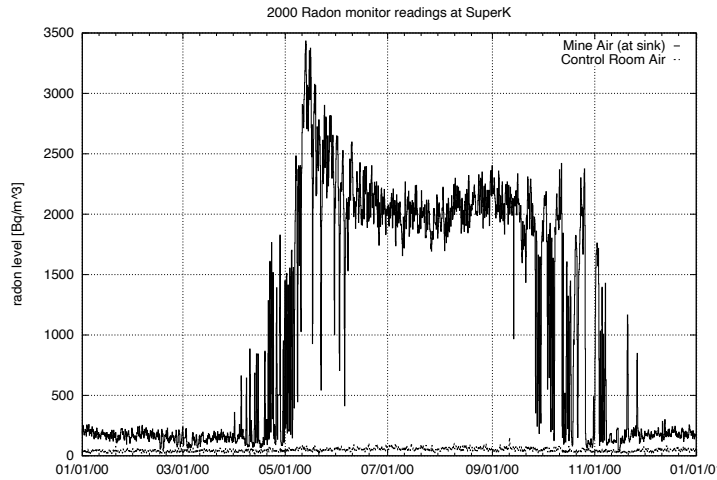


Figure 2.13: Typical radon concentration in the air at the SK over a year [56]. The solid line shows the concentration outside the experimental area. The dashed line shows the concentration inside the experimental area.

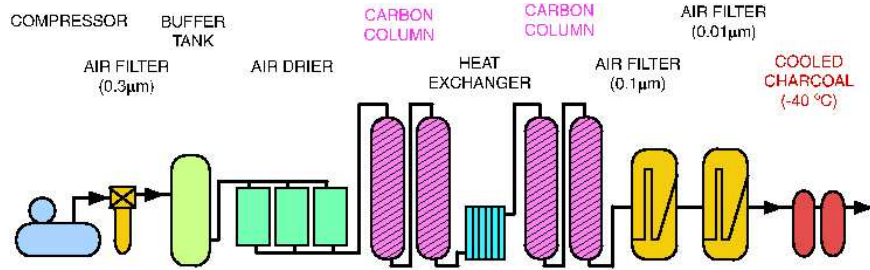


Figure 2.14: Schematic view of air purification system [56]. Each component of air purification system is described in Ref. [66].

2.8 Data acquisition system

As explained in Section 2.4, the data acquisition system was changed from ATM to QBEE in SK-IV. The data used in this thesis was acquired by QBEE. Therefore, the description of ATM is omitted in this thesis.

Figure 2.15 shows the schematic view of the data acquisition system after SK-IV. One QBEE board has 8 QTCs, and one QTC has 3 analog input channels for PMT signals. That is, one QBEE board has 24 analog input channels for PMT signals. Figure 2.16 shows the block diagram of the QTC and its surroundings. Each analog input channel has three gain ranges: small, medium, and large. The gain ratio of small, medium, and large is set to 1, 1/7, and 1/49, respectively. Also, the charge dynamic range of small, medium, and large is 0.2 - 51 pC, 1 - 357 pC, and 5 - 2500 pC, respectively. The gain ratio is optimized to cover a wide charge dynamic range with reasonable resolution. When the charge is sent to a QBEE board, the QTC integrates the charge and generates the output signal with the width proportional to the integrated charge. Then the output signal is digitized by time-to-digital converter (TDC). The digitized signals are transferred to 20 front-end PCs, and sent to 10 merger PCs. In the merger PCs, the signals from all the front-end PCs are merged and the software trigger is applied. Details about the software trigger is described later. From the merger PCs,

signals for triggered events are sent to an organizer PC and then written onto the disk for offline analysis. Details about the front-end PCs, merger in the merger PCs, the organizer PC, and the disk are described in Ref. [67].

The software trigger process scans the signals sent to the merger PCs and searches the events satisfying the trigger conditions. A trigger is applied when the number of ID PMT hits within 200 ns, which corresponds to the time that a Cherenkov photon moves from the edge of the SK tank to other, is a certain value or more. Figure 2.17 and Figure 2.18 show the software trigger threshold for recording PMT hits of each trigger type from SK-IV to SK-VII. There are four trigger types for ID: Super Low Energy (SLE), Low Energy (LE), High Energy (HE), and Super High Energy (SHE). Each trigger threshold changes depending on its trigger rate. Also, OD trigger is applied when the number of OD PMT hits within 200 ns is 22 or more. Basically, when a trigger is applied, all hits from $-5 \mu\text{s}$ to $35 \mu\text{s}$ are recorded, where the trigger timing is $0 \mu\text{s}$. However, in the case of SLE, all hits from $-0.5 \mu\text{s}$ to $1.0 \mu\text{s}$ are recorded due to the high trigger rate.

From SK-IV, a special trigger, AFT, was installed to search delayed neutron capture signals. Previously, AFT trigger was applied when SHE trigger was applied and OD trigger was not applied to avoid events by cosmic ray muons. However, from June 2020, the condition about OD trigger was removed to study spallation events by cosmic ray muons. When AFT trigger is applied, all hits from $35 \mu\text{s}$ to $535 \mu\text{s}$ (from $35 \mu\text{s}$ to $385 \mu\text{s}$ before November 2010 [22]) in addition to from $-5 \mu\text{s}$ to $35 \mu\text{s}$ are recorded.

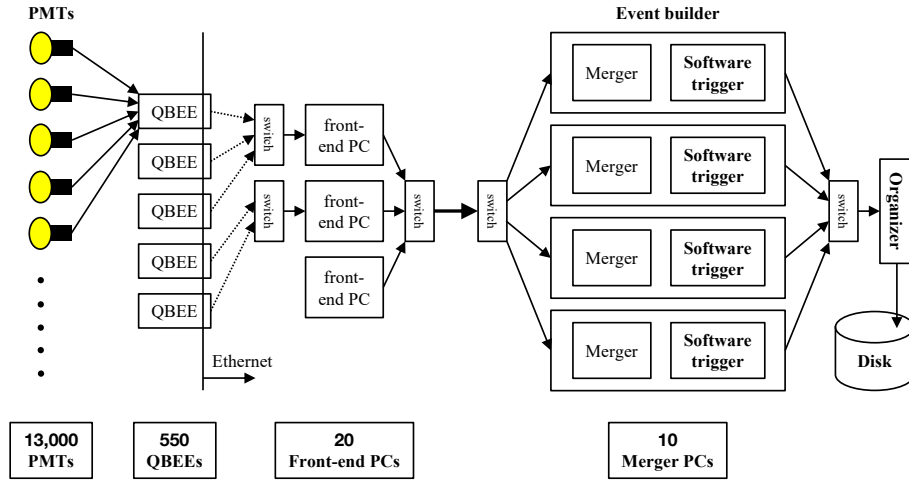


Figure 2.15: Schematic view of the data acquisition system [67].

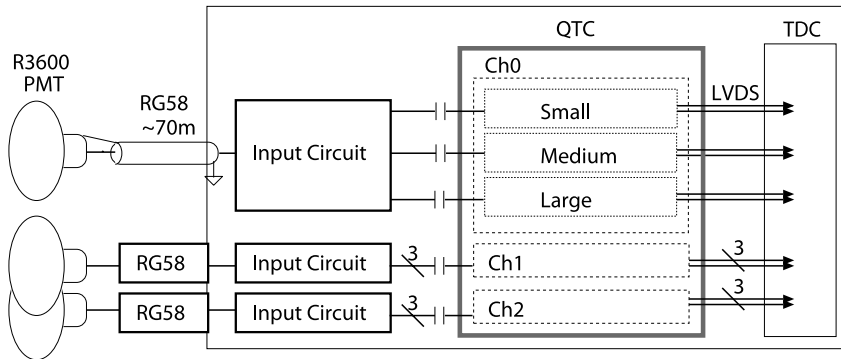


Figure 2.16: Block diagram of the QTC and its surroundings [61]. The output signal of each range (small, medium, or large) is generated by low voltage differential signaling (LVDS) drivers and digitized by time-to-digital converter (TDC).

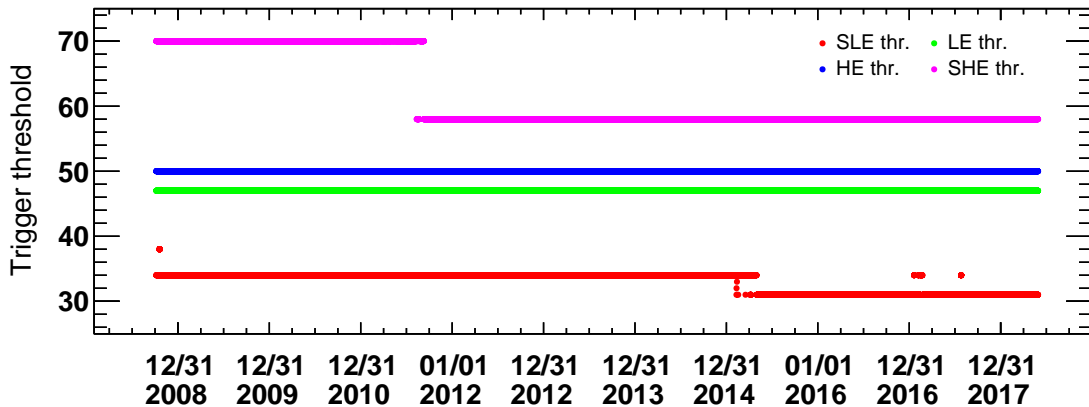


Figure 2.17: Software trigger threshold for recording PMT hits of each trigger type in SK-IV. After May 2015, SLE trigger threshold changed from 34 to 31. While, after September 2011, SHE trigger threshold changed from 70 to 58. During SK-IV, LE and HE trigger threshold was 47 and 50, respectively.

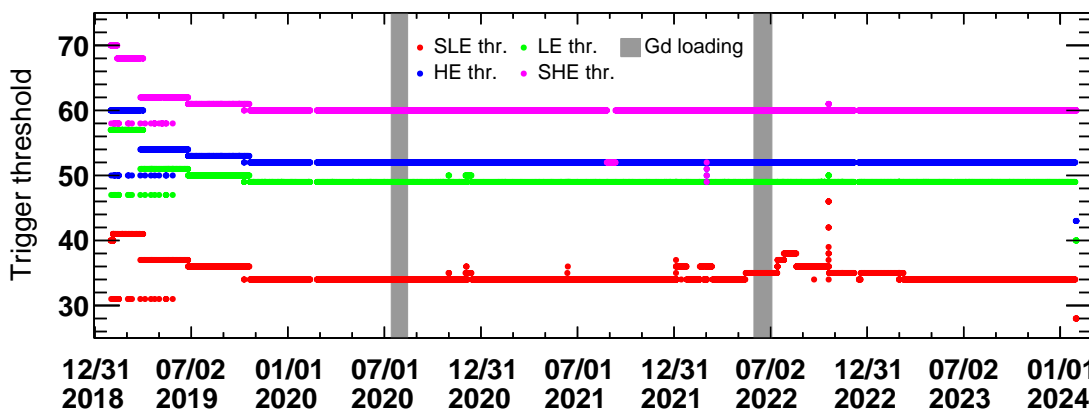


Figure 2.18: Software trigger threshold for recording PMT hits of each trigger type in SK-V, SK-VI, and SK-VII. In most periods, SLE, LE, HE, and SHE trigger threshold is 34, 49, 52, and 60, respectively.

3 Simulation

3.1 Atmospheric neutrino flux

Many hadrons like pions and kaons are generated by reactions between a cosmic ray and a nucleus in the atmosphere. The generated hadron decays into a muon and a neutrino, and the muon decays into an electron and two neutrinos. The generated neutrinos in the atmosphere are called “atmospheric neutrinos”. Figure 3.1 shows the schematic view of atmospheric neutrino production.

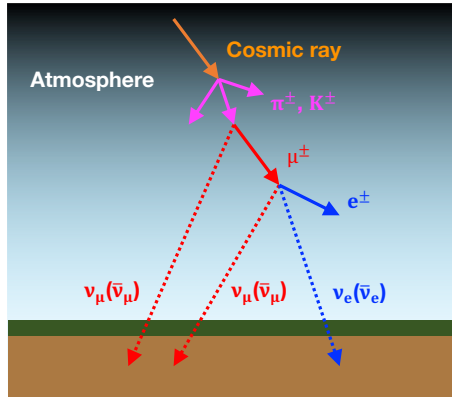


Figure 3.1: Schematic view of atmospheric neutrino production.

The atmospheric neutrino flux at the SK detector is predicted using the HKKM11 model [68]. Figure 3.2 shows the atmospheric neutrino flux predicted by the HKKM11 model for the Kamioka site [52, 68]. As shown in this figure, the predicted flux shows good agreement with the observation in SK. Atmospheric neutrino/antineutrino ratio and atmospheric neutrino flux of $\nu_e + \nu_\mu (\bar{\nu}_e + \bar{\nu}_\mu)$, $\nu_e (\bar{\nu}_e)$, and $\nu_\mu (\bar{\nu}_\mu)$ predicted by the HKKM11 model for the Kamioka site are shown in Figure 3.3 [68]. In this measurement, systematic uncertainties of atmospheric neutrino flux and atmospheric neutrino/antineutrino ratio are considered (see Section 8.2).

3.2 Neutirno interaction

Neutrino interactions are simulated using NEUT [77] (version 5.4.0.1). Figure 3.4 and Figure 3.5 show the cross sections of charged-current interactions to nucleon used in NEUT (version 5.4.0.1).

Figure 3.6 shows the schematic view of neutrino-oxygen NCQE scattering. The NCQE cross section on oxygen is based on the model using the oxygen spectral function [51, 92] with the BBBA05 vector form factor [93] and the dipole axial form factor [93].

According to Ref. [51], NCQE cross section is defined as

$$\frac{d^2\sigma_{\nu A}}{d\Omega dE'_\nu} = \sum_{N=p,n} \int d^3p dE P_N(\mathbf{p}, E) \frac{M}{E_N} \frac{d^2\sigma_{\nu N}}{d\Omega dE'_\nu}, \quad (3.1)$$

where M is the nucleon mass and $E_N = \sqrt{M^2 + \mathbf{p}^2}$. $P_N(\mathbf{p}, E)$ is the spectral function, that is, the probability of removing a nucleon of momentum \mathbf{p} from the target leaving the residual nucleus with energy

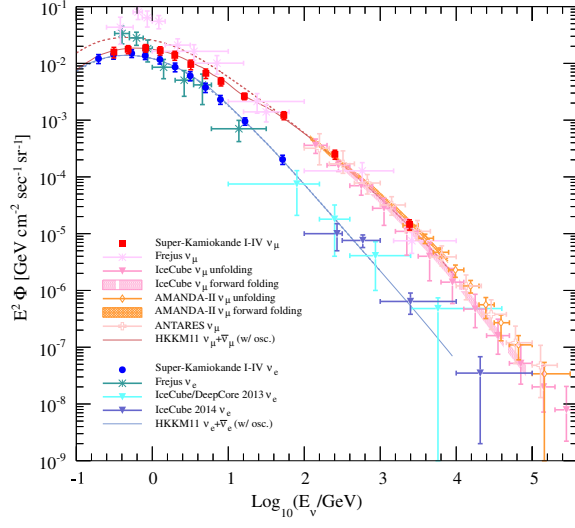


Figure 3.2: Atmospheric neutrino flux predicted by the HKKM11 model for the Kamioka site [52, 68]. Data plots are taken from the following experiments: Super-Kamiokande I-IV [52], Frejus [69], IceCube [70–73], AMANDA-II [74, 75], and ANTARES [76].

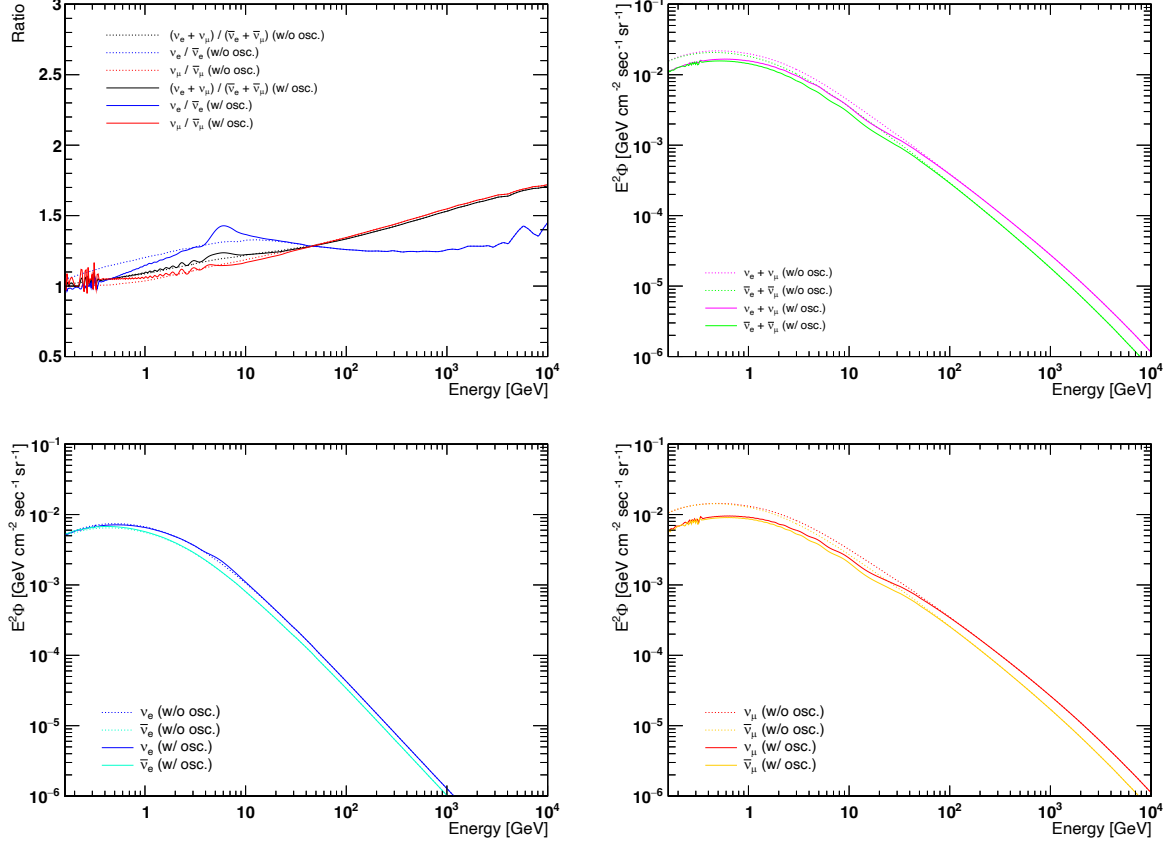


Figure 3.3: Atmospheric neutrino/antineutrino ratio (top left) and atmospheric neutrino flux of $\nu_e + \nu_\mu$ ($\bar{\nu}_e + \bar{\nu}_\mu$) (top right), ν_e ($\bar{\nu}_e$) (bottom left), and ν_μ ($\bar{\nu}_\mu$) (bottom right) predicted by the HKKM11 model for the Kamioka site [68].

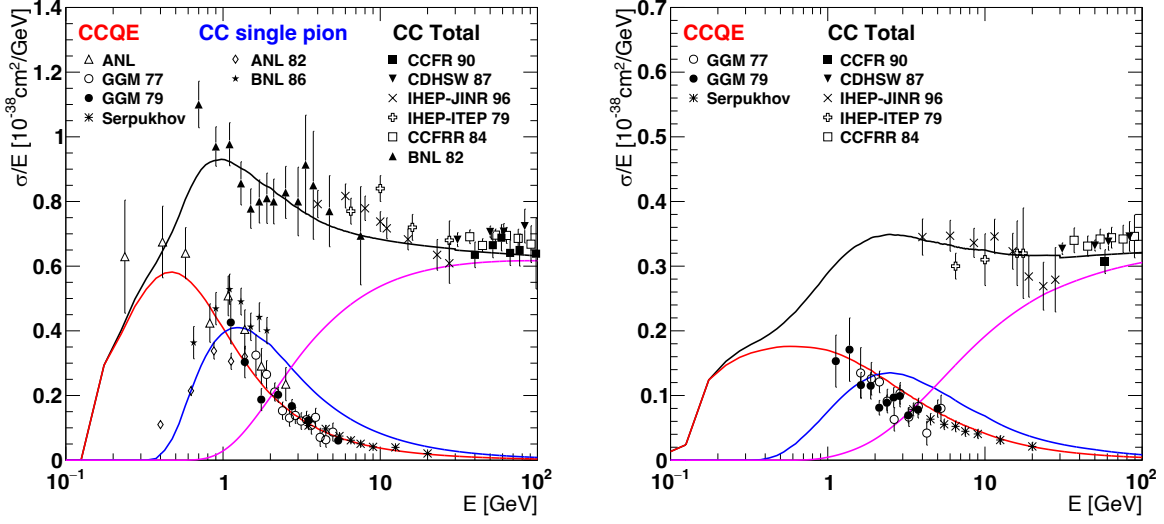


Figure 3.4: Cross sections of charged-current (CC) interactions to nucleon for ν_μ (left) and $\bar{\nu}_\mu$ (right) used in NEUT (version 5.4.0.1). These figures are based on Figure 2 in Ref. [78]. Red, blue, and magenta lines show the cross section of CC quasielastic (CCQE) scattering, CC single pion production, and CC deep inelastic scattering, respectively. Black line shows the CC total cross section. Data plots are taken from the following experiments: ANL [79], GGM 77 [80], GGM 79 (left) [81], GGM 79 (right) [82], Serpukhov [83], ANL 82 [84], BNL 86 [85], CCFR 90 [86], CDHSW 87 [87], IHEP-JINR 96 [88], IHEP-ITEP 79 [89], CCFRR 84 [90], and BNL 82 [91].

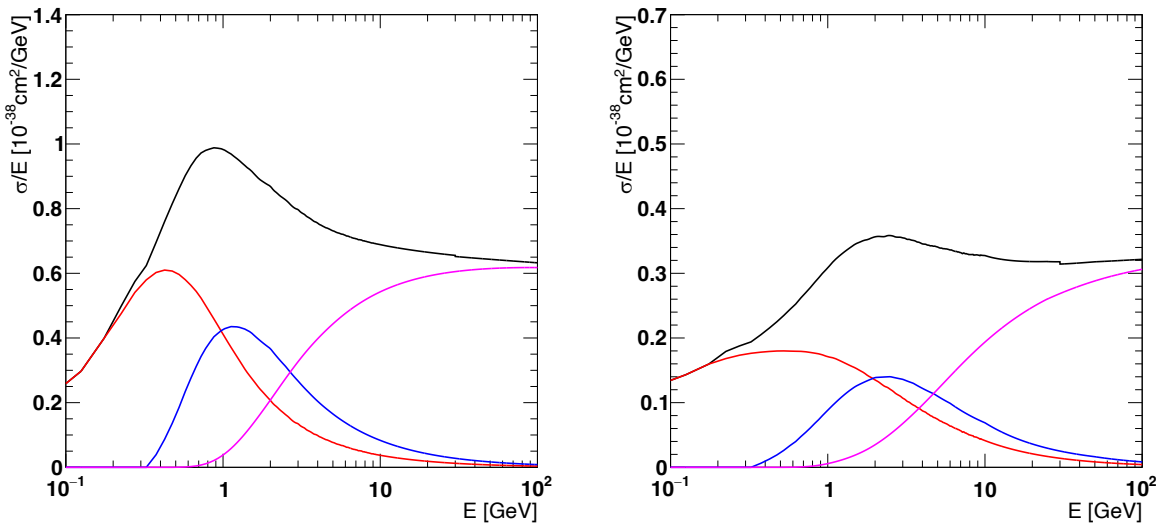


Figure 3.5: Cross sections of charged-current (CC) interactions to nucleon for ν_e (left) and $\bar{\nu}_e$ (right) used in NEUT (version 5.4.0.1). Red, blue, and magenta lines show the cross section of CC quasielastic (CCQE) scattering, CC single pion production, and CC deep inelastic scattering, respectively. Black line shows the CC total cross section.

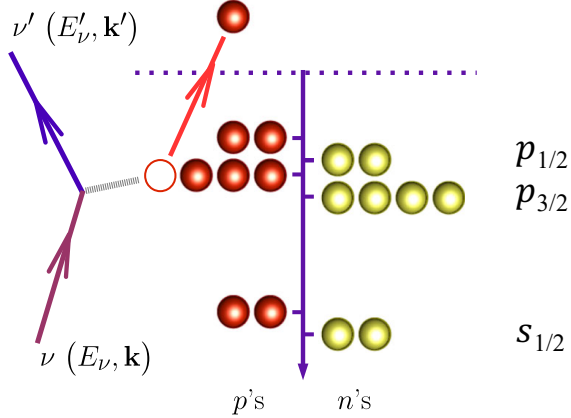


Figure 3.6: Schematic view of neutrino-oxygen NCQE scattering [51]. Dashed line represents the nucleon emission threshold. According to the shell model, protons and neutrons in the ^{16}O nucleus occupy three states ($p_{1/2}$, $p_{3/2}$, and $s_{1/2}$). The removal energy of $p_{1/2}$ state, $p_{3/2}$ state, and $s_{1/2}$ state for protons is 12.1 MeV, 18.4 MeV, and \sim 42 MeV, respectively. The removal energy for neutrons is 3.54 MeV larger than that for protons.

$E + E_0 - M$, E_0 being the target ground state energy. $d^2\sigma_{\nu N}/d\Omega dE'_\nu$ is the neutrino-nucleon cross section. In the nuclear shell model, the spectral function $P_N(\mathbf{p}, E)$ can be written in the form

$$P_N(\mathbf{p}, E) = \sum_{\alpha \in \{F\}} n_\alpha |\phi_\alpha(\mathbf{p})|^2 f_\alpha(E - E_\alpha), \quad (3.2)$$

where n_α (≤ 1) is the occupation probability of the α th state, $\phi_\alpha(\mathbf{p})$ is the momentum-space wave function associated with the α th state, $f_\alpha(E - E_\alpha)$ is the (unit-normalized) function describing the energy width of the α th state, $-E_\alpha$ ($E_\alpha > 0$) being the binding energy of the α th state, and the sum is extended to all occupied states belonging to the Fermi sea $\{F\}$. The neutrino-nucleon cross section $d^2\sigma_{\nu N}/d\Omega dE'_\nu$ can be written in the form

$$\frac{d^2\sigma_{\nu N}}{d\Omega dE'_\nu} = \frac{G_F^2}{8\pi^2} \frac{E'_\nu}{E_\nu} \frac{L_{\mu\nu} W^{\mu\nu}}{M E'_N} \delta(\tilde{\omega} + E_N - E'_N), \quad (3.3)$$

where G_F is the Fermi coupling constant and $E'_N = \sqrt{M^2 + \mathbf{p}'^2}$. The leptonic tensor $L_{\mu\nu}$ and the hadronic tensor $W^{\mu\nu}$ are given by

$$L_{\mu\nu} = 2(k'_\mu k_\nu + k'_\nu k_\mu - g_{\mu\nu} k \cdot k' - i\varepsilon_{\mu\nu\alpha\beta} k^\alpha k'^\beta), \quad (3.4)$$

$$W^{\mu\nu} = -g^{\mu\nu} M^2 W_1 + \tilde{p}^\mu \tilde{p}^\nu W_2 + i\varepsilon^{\mu\nu\alpha\beta} \tilde{p}_\alpha \tilde{q}_\beta W_3 + \tilde{q}^\mu \tilde{q}^\nu W_4 + (\tilde{p}^\mu \tilde{q}^\nu + \tilde{p}^\nu \tilde{q}^\mu) W_5, \quad (3.5)$$

where $\tilde{p} = (E_N, \mathbf{p})$ and $\tilde{q} = (\tilde{\omega}, \mathbf{k} - \mathbf{k}')$. The structure functions W_i ($i = 1, 2, 3, 4, 5$) can be written as

$$\begin{aligned} W_1 &= \tau(\mathcal{F}_1^N + \mathcal{F}_2^N)^2 + (1 + \tau)\mathcal{F}_A^2, \\ W_2 &= (\mathcal{F}_1^N)^2 + \tau(\mathcal{F}_2^N)^2 + \mathcal{F}_A^2, \\ W_3 &= (\mathcal{F}_1^N + \mathcal{F}_2^N)\mathcal{F}_A, \\ W_4 &= \frac{1}{4}[(\mathcal{F}_1^N)^2 + \tau(\mathcal{F}_2^N)^2 - (\mathcal{F}_1^N + \mathcal{F}_2^N)^2 - 4\mathcal{F}_P(\mathcal{F}_A - \tau\mathcal{F}_P)], \\ W_5 &= \frac{1}{2}W_2, \end{aligned} \quad (3.6)$$

where $\tau = -\tilde{q}^2/(4M^2)$. The nucleon form factors $\{\mathcal{F}_i^N \ (i = 1, 2), \mathcal{F}_A, \mathcal{F}_P\}$ can be written as

$$\begin{aligned}\mathcal{F}_1^N &= \pm \frac{1}{2}(F_1^p - F_1^n) - 2 \sin^2 \theta_W F_1^N, \\ \mathcal{F}_2^N &= \pm \frac{1}{2}(F_2^p - F_2^n) - 2 \sin^2 \theta_W F_2^N, \\ \mathcal{F}_A &= \frac{1}{2} \frac{\Delta s \pm g_A}{(1 - \tilde{q}^2/M_A^2)^2}, \\ \mathcal{F}_P &= \frac{2M^2 \mathcal{F}_A}{m_\pi^2 - \tilde{q}^2},\end{aligned}\tag{3.7}$$

where the upper (lower) sign corresponds to proton (neutron) form factors, θ_W is the weak mixing angle, Δs ($= -0.08$) is the strange quark contribution, $g_A = -1.2673$, M_A is the axial mass, and m_π is the pion mass. The form factors F_1^N and F_2^N can be expressed as

$$\begin{aligned}F_1^N &= \frac{G_E^N + \tau G_M^N}{1 + \tau}, \\ F_2^N &= \frac{G_M^N - G_E^N}{1 + \tau},\end{aligned}\tag{3.8}$$

where G_E^N is the electric form factors and G_M^N is the magnetic form factors. Figure 3.7 shows the NCQE cross section on nucleon and on oxygen nucleus as a function of neutrino energy. Figure 3.8 shows the ratio of the BBBA05 vector form factors to G_d (the dipole axial form factor).

The state of the residual nucleus after primary interaction (see Figure 1.8) is selected based on the probabilities computed in Ref. [51]. There are four states, $(p_{1/2})^{-1}$, $(p_{3/2})^{-1}$, $(s_{1/2})^{-1}$, and *others*, where $(\text{state})^{-1}$ shows the state of the nucleus after a nucleon initially occupying the state $(p_{1/2}, p_{3/2}, \text{ or } s_{1/2})$ is removed. The production probability of each state is 0.1580, 0.3515, 0.1055, and 0.3850, respectively. The production probabilities of $(p_{1/2})^{-1}$ state, $(p_{3/2})^{-1}$ state, and $(s_{1/2})^{-1}$ state are obtained by multiplying the spectroscopic strength by the probability that a nucleon in the state is knocked out. Spectroscopic strengths of the ^{16}O hole states and probabilities that a nucleon in the state is knocked out are summarized in Table 3.1. The production probability of *others* state is equal to $1 - 0.1580 - 0.3515 - 0.1055$.

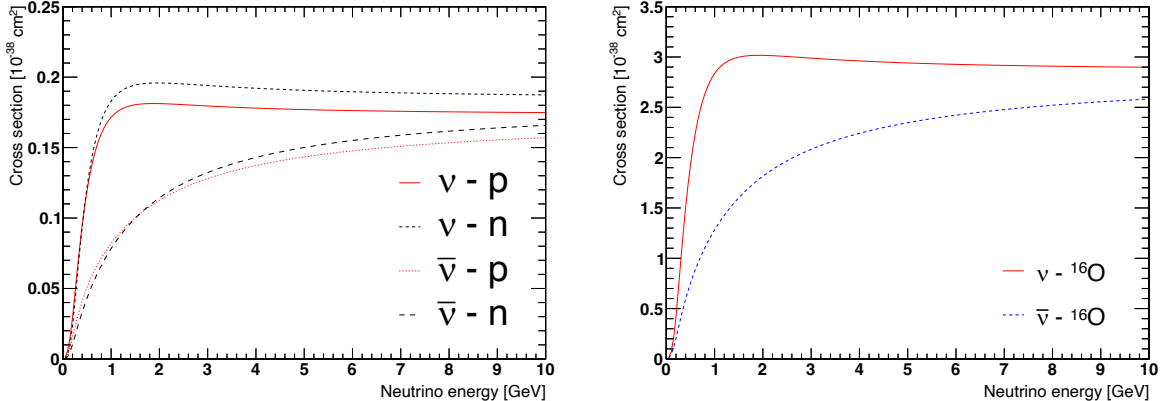


Figure 3.7: NCQE cross section on nucleon (left) and on oxygen nucleus (right) as a function of neutrino energy [51].

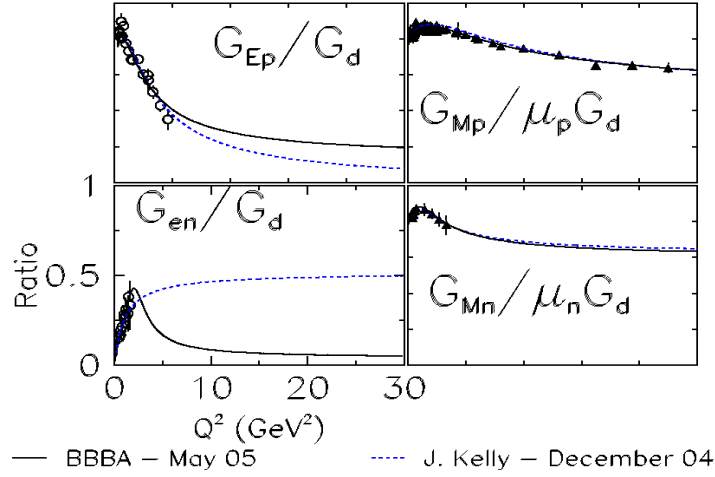


Figure 3.8: The ratio of the BBBA05 vector form factors to G_d (the dipole axial form factor) (shown in the solid black line) [93]. The dashed blue line shows the ratio of the Kelly form factors to G_d .

Table 3.1: Spectroscopic strengths of the ^{16}O hole states (S_α) and probabilities that a nucleon in the state is knocked out (P_α) [51].

α	$p_{1/2}$	$p_{3/2}$	$s_{1/2}$
S_α	0.632	0.703	0.422
P_α	2/8	4/8	2/8

$(p_{1/2})^{-1}$ state is the ground state of ^{15}O or ^{15}N , thus no gamma-ray is emitted. Mainly 6.18 MeV or 6.32 MeV gamma-rays are emitted from $(p_{3/2})^{-1}$ state of ^{15}O or ^{15}N , respectively [94, 95]. De-excitation modes of $(p_{3/2})^{-1}$ state implemented in NEUT are summarized in Table 3.2 and Table 3.3. In the case of $(s_{1/2})^{-1}$ state, nucleons and gamma-rays are emitted because the excitation energy is high. The de-excitation mode is selected based on the $^{16}\text{O}(p, 2p)$ experiment [96]. De-excitation modes of $(s_{1/2})^{-1}$ state implemented in NEUT are summarized in Table 3.4 and Table 3.5. In the case that the residual nuclei are $^{14}\text{N} + p$, kinetic energy of generated proton (E_p) is calculated by

$$E_p = \max \left[0, (39.5 \times \eta + 10.65 - E_l - E_{^{14}\text{N}+p}) \times \frac{m_{^{14}\text{N}} + E_l}{m_p + m_{^{14}\text{N}} + E_l} \right], \quad (3.9)$$

where η is a random number uniformly distributed in the range from 0 to 1, E_l is the energy level, $E_{^{14}\text{N}+p}$ (= 7.30 MeV) is the energy threshold of two-body decay from ^{15}O to $^{14}\text{N} + p$, $m_{^{14}\text{N}}$ (= 13043.78 MeV) is the mass of ^{14}N ground state, and m_p (= 938.27 MeV) is the proton mass. In the case that the residual nuclei are $^{14}\text{O} + n$, kinetic energy of generated neutron (E_n) is calculated by

$$E_n = \max \left[0, (39.5 \times \eta + 10.65 - E_l - E_{^{14}\text{O}+n}) \times \frac{m_{^{14}\text{O}} + E_l}{m_n + m_{^{14}\text{O}} + E_l} \right], \quad (3.10)$$

where $E_{^{14}\text{O}+n}$ (= 13.22 MeV) is the energy threshold of two-body decay from ^{15}O to $^{14}\text{O} + n$, $m_{^{14}\text{O}}$ (= 13048.92 MeV) is the mass of ^{14}O ground state, and m_n (= 939.56 MeV) is the neutron mass. In the

case that the residual nuclei are $^{14}\text{N} + \text{n}$, E_{n} is calculated by

$$E_{\text{n}} = \max \left[0, (39.5 \times \eta + 10.65 - E_l - E_{^{14}\text{N}+\text{n}}) \times \frac{m_{^{14}\text{N}} + E_l}{m_{\text{n}} + m_{^{14}\text{N}} + E_l} \right], \quad (3.11)$$

where $E_{^{14}\text{N}+\text{n}}$ ($= 10.83$ MeV) is the energy threshold of two-body decay from ^{15}N to $^{14}\text{N} + \text{n}$. In the case that the residual nuclei are $^{14}\text{C} + \text{p}$, E_{p} is calculated by

$$E_{\text{p}} = \max \left[0, (39.5 \times \eta + 10.65 - E_l - E_{^{14}\text{C}+\text{p}}) \times \frac{m_{^{14}\text{C}} + E_l}{m_{\text{p}} + m_{^{14}\text{C}} + E_l} \right], \quad (3.12)$$

where $E_{^{14}\text{C}+\text{p}}$ ($= 10.21$ MeV) is the energy threshold of two-body decay from ^{15}N to $^{14}\text{C} + \text{p}$ and $m_{^{14}\text{C}}$ ($= 13043.94$ MeV) is the mass of ^{14}C ground state. The *others* state includes all other possibilities that are not in $(p_{1/2})^{-1}$, $(p_{3/2})^{-1}$, and $(s_{1/2})^{-1}$ states, and there are no data nor theoretical predictions covered by this state. In our simulation, the *others* state is set to be integrated into $(s_{1/2})^{-1}$ state by default.

Other distributions related to this section are summarized in Appendix B.1.

Table 3.2: De-excitation modes of $(p_{3/2})^{-1}$ state for ^{15}O implemented in NEUT. E_{γ} and E_{p} show the (kinetic) energy of generated gamma-ray and generated proton, respectively. Probabilities that the mode is selected in NEUT are summarized in the rightmost column. Please also check Ref. [94, 95].

Residual nuclei	Energy level (MeV)	E_{γ} (MeV)	E_{p} (MeV)	Probability
^{15}O	6.18	6.18	-	86.86%
$^{14}\text{N} + \text{p}$	9.61	-	0.5	4.92%
$^{14}\text{N} + \text{p}$	10.48	-	0.5	8.22%

Table 3.3: De-excitation modes of $(p_{3/2})^{-1}$ state for ^{15}N implemented in NEUT. E_{γ} and E_{p} show the (kinetic) energy of generated gamma-rays and generated proton, respectively. Probabilities that the mode is selected in NEUT are summarized in the rightmost column. Please also check Ref. [94, 95].

Residual nuclei	Energy level (MeV)	E_{γ} (MeV)	E_{p} (MeV)	Probability
^{15}N	6.32	6.32	-	86.86%
^{15}N	9.93	9.93	-	3.82%
^{15}N	9.93	$5.30 + 4.64$	-	0.76%
^{15}N	9.93	$6.32 + 3.61$	-	0.24%
^{15}N	9.93	$7.30 + 2.63$	-	0.10%
$^{14}\text{C} + \text{p}$	10.70	-	0.5	8.22%

Table 3.4: De-excitation modes of $(s_{1/2})^{-1}$ state for ^{15}O implemented in NEUT. E_γ , E_n , and E_p show the (kinetic) energy of generated gamma-ray, generated neutron, and generated proton, respectively. Probabilities that the mode is selected in NEUT are summarized in the rightmost column. The last two rows consider the three-body decay of ^{15}O . Please also check Ref. [96].

Residual nuclei	Energy level (MeV)	E_γ (MeV)	E_n (MeV)	E_p (MeV)	Probability
$^{13}\text{N} + \text{d}$	3.09	3.09	-	-	3.00%
$^{13}\text{N} + \text{d}$	3.68	3.68	-	-	4.17%
$^{13}\text{N} + \text{d}$	3.85	3.68	-	-	1.67%
$^{13}\text{N} + \text{d}$	3.85	3.85	-	-	2.88%
$^{12}\text{N} + \text{t}$	4.44	4.44	-	-	5.80%
$^{14}\text{N} + \text{p}$	g.s.	-	-	Equation (3.9)	6.74%
$^{14}\text{N} + \text{p}$	4.92	4.92	-	Equation (3.9)	5.04%
$^{14}\text{N} + \text{p}$	5.69	3.38	-	Equation (3.9)	2.88%
$^{14}\text{N} + \text{p}$	5.69	5.69	-	Equation (3.9)	1.62%
$^{14}\text{N} + \text{p}$	5.83	5.11	-	Equation (3.9)	0.34%
$^{14}\text{N} + \text{p}$	5.83	5.83	-	Equation (3.9)	0.12%
$^{14}\text{N} + \text{p}$	6.45	5.11	-	Equation (3.9)	0.23%
$^{14}\text{N} + \text{p}$	6.45	6.44	-	Equation (3.9)	1.96%
$^{14}\text{N} + \text{p}$	7.03	7.03	-	Equation (3.9)	6.61%
$^{14}\text{O} + \text{n}$	g.s.	-	Equation (3.10)	-	1.15%
$^{14}\text{O} + \text{n}$	6.73	6.73	Equation (3.10)	-	0.41%
$^{14}\text{O} + \text{n}$	7.34	6.09	Equation (3.10)	-	2.79%
$^{14}\text{O} + \text{n}$	7.34	6.73	Equation (3.10)	-	1.96%
$^{14}\text{O} + \text{n}$	7.34	7.34	Equation (3.10)	-	0.95%
-	-	-	-	0–5	31.90%
-	-	-	0–5	-	17.78%

Table 3.5: De-excitation modes of $(s_{1/2})^{-1}$ state for ^{15}N implemented in NEUT. E_γ , E_n , and E_p show the (kinetic) energy of generated gamma-ray, generated neutron, and generated proton, respectively. Probabilities that the mode is selected in NEUT are summarized in the rightmost column. The last two rows consider the three-body decay of ^{15}N . Please also check Ref. [96].

Residual nuclei	Energy level (MeV)	E_γ (MeV)	E_n (MeV)	E_p (MeV)	Probability
$^{13}\text{C} + \text{d}$	3.09	3.09	-	-	3.00%
$^{13}\text{C} + \text{d}$	3.68	3.68	-	-	4.17%
$^{13}\text{C} + \text{d}$	3.85	3.68	-	-	1.67%
$^{13}\text{C} + \text{d}$	3.85	3.85	-	-	2.88%
$^{12}\text{C} + \text{t}$	4.44	4.44	-	-	5.80%
$^{14}\text{N} + \text{n}$	g.s.	-	Equation (3.11)	-	6.74%
$^{14}\text{N} + \text{n}$	4.92	4.92	Equation (3.11)	-	5.04%
$^{14}\text{N} + \text{n}$	5.69	3.38	Equation (3.11)	-	2.88%
$^{14}\text{N} + \text{n}$	5.69	5.69	Equation (3.11)	-	1.62%
$^{14}\text{N} + \text{n}$	5.83	5.11	Equation (3.11)	-	0.34%
$^{14}\text{N} + \text{n}$	5.83	5.83	Equation (3.11)	-	0.12%
$^{14}\text{N} + \text{n}$	6.45	5.11	Equation (3.11)	-	0.23%
$^{14}\text{N} + \text{n}$	6.45	6.44	Equation (3.11)	-	1.96%
$^{14}\text{N} + \text{n}$	7.03	7.03	Equation (3.11)	-	6.61%
$^{14}\text{C} + \text{p}$	g.s.	-	-	Equation (3.12)	1.15%
$^{14}\text{C} + \text{p}$	6.73	6.73	-	Equation (3.12)	0.41%
$^{14}\text{C} + \text{p}$	7.34	6.09	-	Equation (3.12)	2.79%
$^{14}\text{C} + \text{p}$	7.34	6.73	-	Equation (3.12)	1.96%
$^{14}\text{C} + \text{p}$	7.34	7.34	-	Equation (3.12)	0.95%
-	-	-	0–5	-	31.90%
-	-	-	-	0–5	17.78%

3.3 Simulation for the IBD-like event

Spallation events, reactor neutrino events, and DSNB events are estimated by generating one positron and one neutron isotropically over the entire ID in MC. Moreover, the positron energy is uniform. The number of events is later normalized by using neutrino flux or positron (electron) energy spectrum. Details for the normalization are summarized below.

3.3.1 Spallation events

Spallation events are decays of radioactive isotopes produced by nuclear spallation of oxygen nuclei induced by energetic cosmic ray muons. Figure 3.9 shows the schematic view of a spallation event. Some radioactive isotopes emit one electron and one neutron, mimicing the IBD events. Most of them can be ignored due to a short lifetime and a low yield, however, ${}^9\text{Li}$ cannot be ignored because of a relatively long lifetime (~ 0.26 s) and a large yield ($1.9 \times 50.8\% \times 10^{-7} \mu^{-1} \text{g}^{-1} \text{cm}^2$) [97]. Therefore, the number of events is normalized by using the energy spectrum of electrons from ${}^9\text{Li}$ decays and the measured ${}^9\text{Li}$ rate at SK ($0.86 \pm 0.12(\text{stat.}) \pm 0.15(\text{syst.}) \text{kton}^{-1} \text{day}^{-1}$) [98]. Figure 3.10 shows the energy spectrum of electrons from ${}^9\text{Li}$ decays modeled by the BESTIOLE code [99].

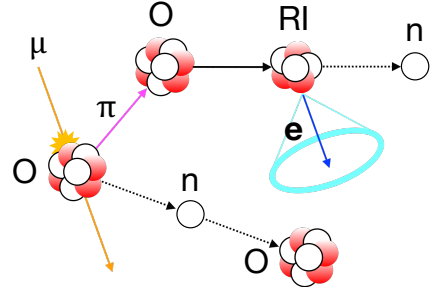


Figure 3.9: Schematic view of a spallation event. RI stands for radioactive isotope.

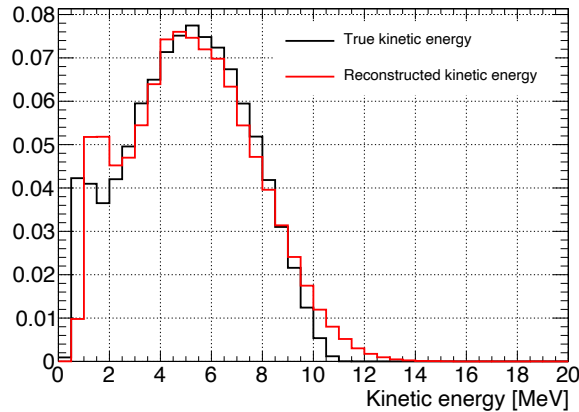


Figure 3.10: Energy spectrum of electrons from ${}^9\text{Li}$ decays modeled by the BESTIOLE code [36, 99]. Red line shows the reconstructed energy spectrum.

3.3.2 Reactor neutrino events

While reactors are operating, many electron antineutrinos are generated via beta decays. Reactor neutrino events are also the IBD events by electron antineutrinos from reactors. The reactor neutrino flux is calculated using SKReact³, which is a tool for calculating the electron antineutrino flux from reactors, considering the activity of each reactor near the SK. Figure 3.11 shows the activities of Japanese reactors from April 2018. The number of events is normalized by using the reactor neutrino flux (shown in Figure 3.12) and the IBD cross section of Strumia-Vissani model [100] (shown in Figure 3.13).

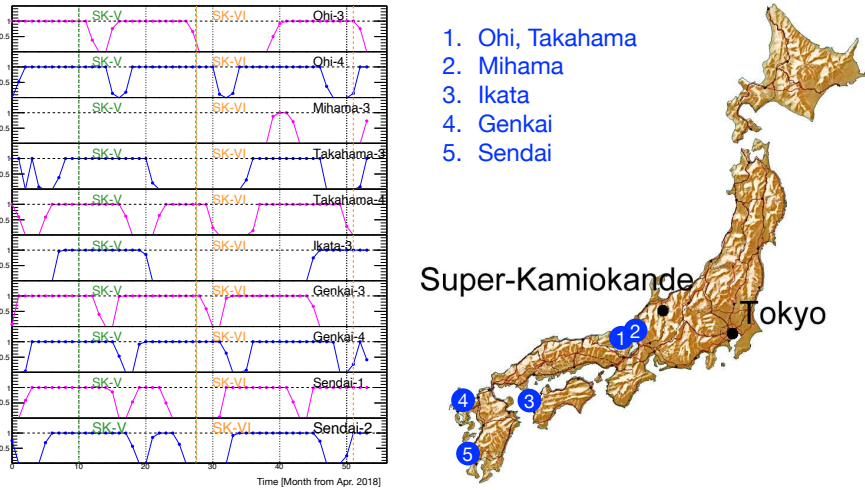


Figure 3.11: Activities of Japanese reactors from April 2018 [36,56]. Dashed line shows the 100% operation. Locations of nuclear power plants, Tokyo, and the SK are also shown in right side.

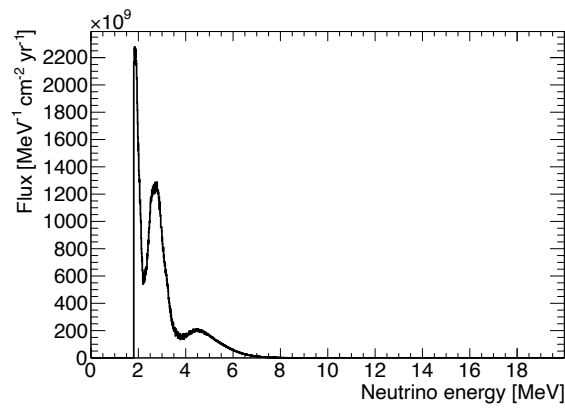


Figure 3.12: Expected reactor neutrino flux at the SK [36]. In this flux, neutrino oscillation effect is considered.

³If you would like to know how to use SKReact, please check the url (<https://github.com/Goldie643/SKReact>).

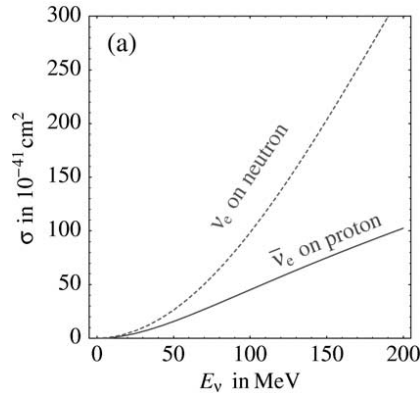


Figure 3.13: IBD cross section of Strumia-Vissani model [100].

3.3.3 DSNB events

As described in Section 1.4, DSNB events are the IBD events by electron antineutrinos. The number of events is normalized by using the DSNB electron antineutrino flux (shown in Figure 1.2) and the IBD cross section of Strumia-Vissani model [100] (shown in Figure 3.13).

3.4 Detector simulation

In the past, a GEANT3-based [101] SK detector simulation (SKDETSIM, SK Detector Simulation) where only the Bertini Cascade Model (BERT) was implemented for neutron tracking in water was used. However, a Geant4-based [102] (version 10.05.p01) SK detector simulation (SKG4, Super-Kamiokande Geant4 based Simulation) has been newly developed for the SK-Gd experiment. In this simulation, BERT (FTFP_BERT_HP physics list), the Binary Cascade Model (BIC) (QGSP_BIC_HP physics list), and the Liège Intranuclear Cascade model (INCL++) (QGSP_INCLXX_HP physics list) can be used as the secondary interaction model. Here, BERT is a traditional cascade model used in GEANT. BIC uses a large set of hadron data to choose interaction processes to improve the accuracy. INCL++ is an advanced binary cascade model including phase space and quantum mechanical processes. The features of each secondary interaction model are described in Section 7.1. In this NCQE cross section measurement, BERT is used as the baseline model.

Figure 3.14, Figure 3.15, and Figure 3.16 show the final state models of inelastic scattering for neutron, proton, and charged pion, respectively. As described in Section 1.5, knocked-out neutrons of NCQE events may have hundreds of MeV, and neutrons with hundreds of MeV follow BERT, BIC, or INCL++ model as shown in Figure 3.14. Therefore, it is important to understand the difference among these models and select an appropriate model.

As shown in Figure 3.16, when the kinetic energy (momentum) of incoming charged pion is below 379.544 (500) MeV, NEUT model is used. At the energy range, cross sections of charged pion inelastic scattering are also replaced to those of NEUT. Figure 3.17 shows the cross sections of charged pion inelastic scattering.

Gamma-rays emitted from thermal neutron capture on Gd are based on ANNRI-Gd model [103]. Here, ANNRI stands for the Accurate Neutron-Nucleus Reaction Measurement Instrument. Figure 3.18 shows the ratio of data from the ANNRI experiment to MC with the ANNRI-Gd model for the single gamma-ray

events [103]. As shown in this figure, the ANNRI-Gd model shows good agreement with the data.

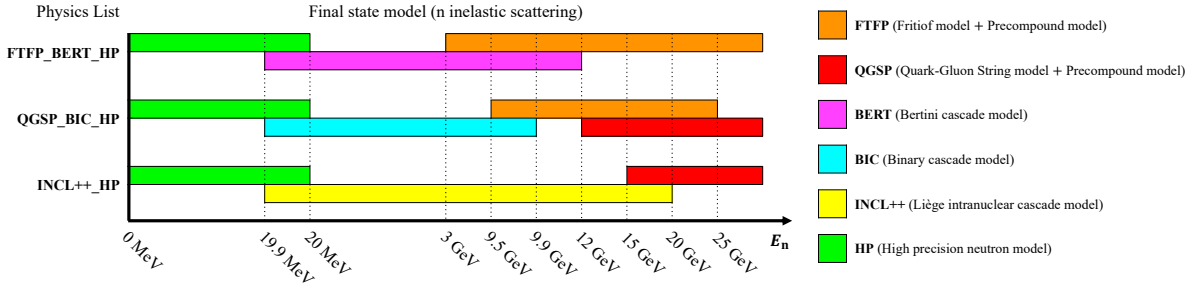


Figure 3.14: Final state models of neutron inelastic scattering. Horizontal axis represents the kinetic energy of incoming neutron.

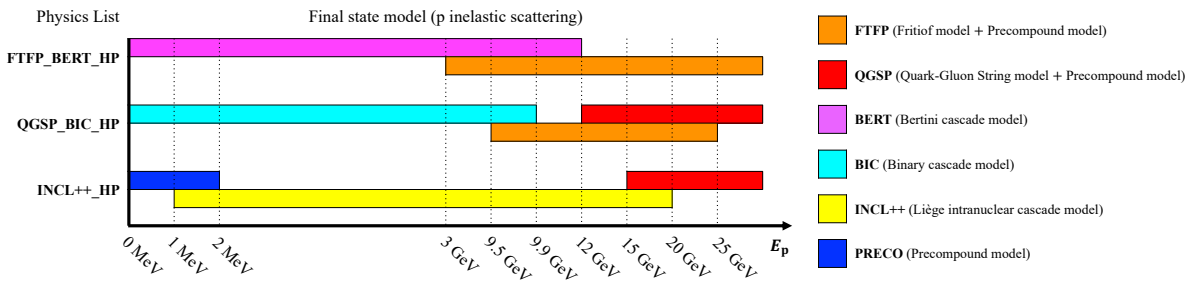


Figure 3.15: Final state models of proton inelastic scattering. Horizontal axis represents the kinetic energy of incoming proton.

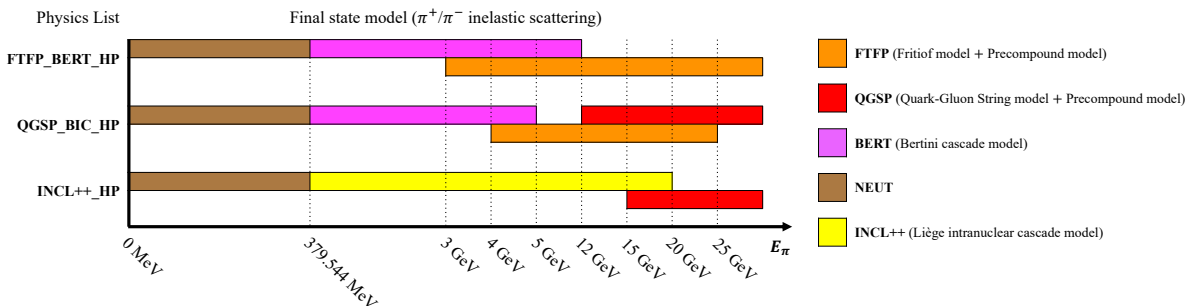


Figure 3.16: Final state models of charged pion inelastic scattering. Horizontal axis represents the kinetic energy of incoming charged pion.

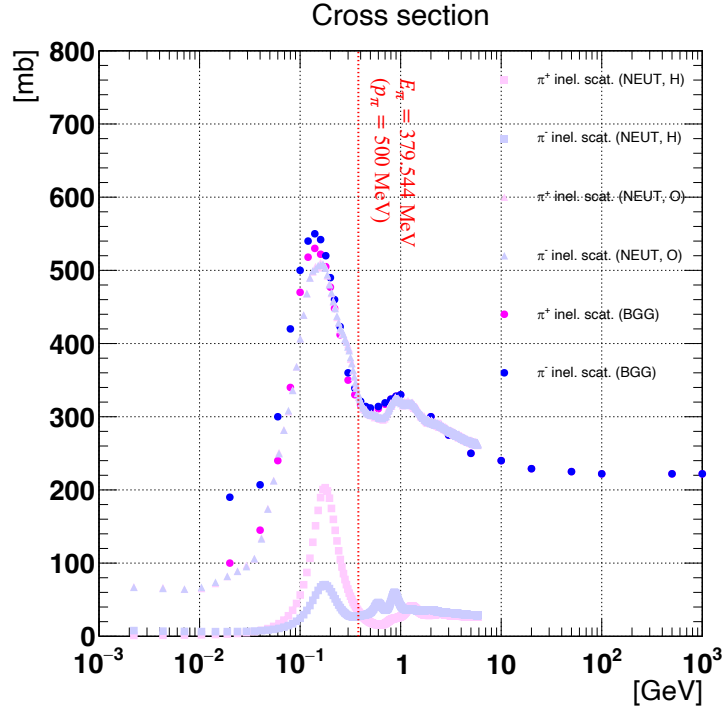


Figure 3.17: Cross sections of charged pion inelastic scattering. Horizontal axis shows the kinetic energy of incoming charged pion. BGG stands for Barashenkov-Glauber-Gribov.

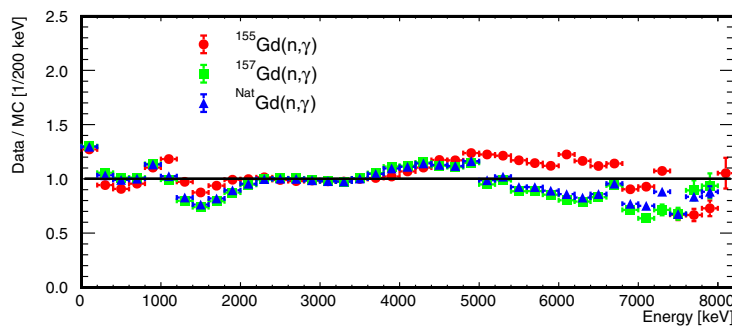


Figure 3.18: Ratio of data from the ANNRI experiment to MC with the ANNRI-Gd model for the single gamma-ray events [103].

4 Event reconstruction

4.1 Vertex reconstruction

A charged particle with the energy of $\mathcal{O}(10)$ MeV travel a few centimeters in water. Since vertex resolution is worse than track length of the charged particle due to the detector size and time resolution of PMTs, track length of the charged particle can be treated as a point. Vertex is reconstructed by using a maximum-likelihood method. The likelihood function is defined as

$$\mathcal{L}(\mathbf{x}, t_0) = \sum_{i=1}^{N_{\text{hit}}} \log P(t_{\text{res},i}), \quad (4.1)$$

$$t_{\text{res},i} = t_i - t_0 - \frac{|\mathbf{x} - \mathbf{h}_i|}{c}, \quad (4.2)$$

where $\mathbf{x} = (x, y, z)$ is the candidate vertex, t_0 is the time when a charged particle was generated, N_{hit} is the number of hit PMTs, $t_{\text{res},i}$ is the timing residual, $P(t_{\text{res},i})$ is the probability density function for $t_{\text{res},i}$, t_i is the PMT's hit time, \mathbf{h}_i is the position of hit PMT, and c is the group velocity of light in water. t_0 is fitted to minimize all $t_{\text{res},i}$. Figure 4.1 and Figure 4.2 shows the definition of the SK detector coordinate system [104] and the probability density function for $t_{\text{res},i}$ [36], respectively. Moreover, vertex resolution for SK-I, II, III, and IV is shown in Figure 4.3 [104].

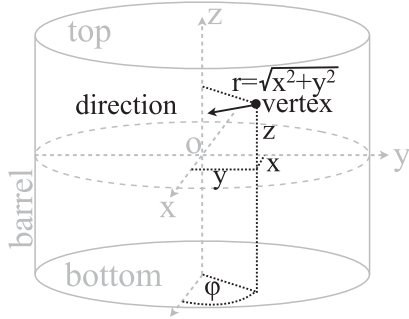


Figure 4.1: Definition of the SK detector coordinate system [104].

The vertex reconstruction goodness, which is a parameter that indicates whether the vertex reconstruction is done well or not, is defined as

$$g_{\text{vtx}} = \frac{\sum_{i=1}^{N_{\text{hit}}} \left[\exp \left\{ - \left(\frac{t_{\text{res},i}}{\sqrt{2}\omega} \right)^2 \right\} \exp \left\{ - \left(\frac{t_{\text{res},i}}{\sqrt{2}\sigma} \right)^2 \right\} \right]}{\sum_{i=1}^{N_{\text{hit}}} \exp \left\{ - \left(\frac{t_{\text{res},i}}{\sqrt{2}\omega} \right)^2 \right\}}, \quad (4.3)$$

where ω is the resolution of the $t_{\text{res},i}$ distribution and σ is the timing resolution of PMTs. The range of g_{vtx} is from 0 to 1, and the value is close to 1 when the vertex reconstruction is done well.

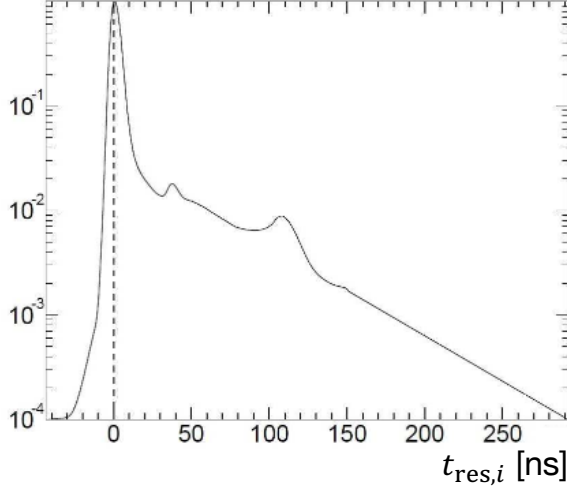


Figure 4.2: Probability density function for $t_{\text{res},i}$ [36]. Peaks around 40 ns and 110 ns come from after pulses of PMTs.

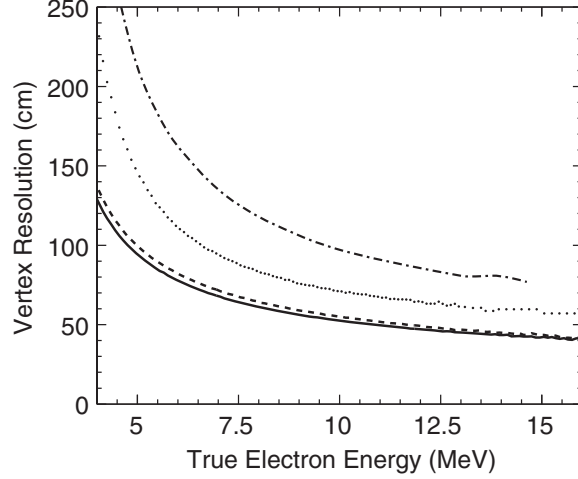


Figure 4.3: Vertex resolution for SK-I, II, III, and IV [104]. Dotted, dashed-dotted, dashed, and solid line shows that for SK-I, II, III, and IV, respectively.

4.2 Direction reconstruction

After determining the vertex, direction is reconstructed. Direction is reconstructed by using a maximum-likelihood method with hit PMTs within 20 ns. The likelihood function is defined as

$$\mathcal{L}(\mathbf{d}) = \sum_{i=1}^{N_{20}} \left[\log f(\cos \Theta_i, E) \times \frac{\cos \theta_i}{a(\theta_i)} \right], \quad (4.4)$$

where \mathbf{d} is the candidate direction, N_{20} is the number of hit PMTs within 20 ns, Θ_i is the angle between the candidate direction and the direction from the reconstructed vertex to the position of hit PMT, $f(\cos \Theta_i, E)$ is the probability density function for $\cos \Theta_i$ depending on the energy E , θ_i is the angle between the direction from the reconstructed vertex to the position of hit PMT and the direction in which the hit PMT is oriented,

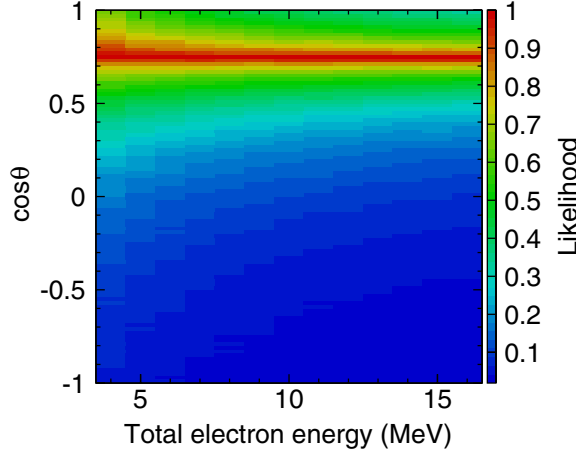


Figure 4.4: Probability density function for $\cos \Theta_i$ depending on the energy E [105].

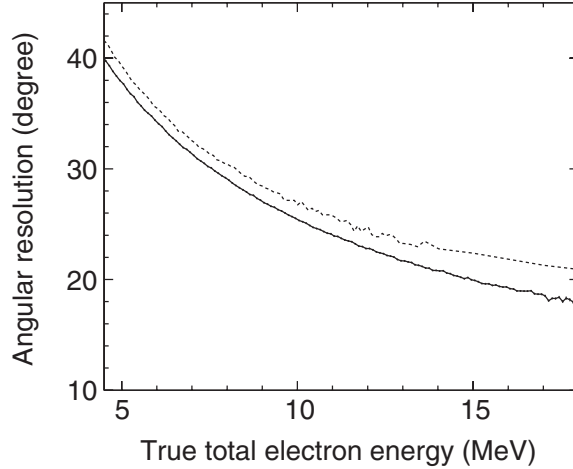


Figure 4.5: Angular resolution for SK-I and SK-III [105]. Dashed and solid line shows that for SK-I and SK-III, respectively.

and $a(\theta_i)$ is the correction function of PMT acceptance. $a(\theta_i)$ is defined as

$$a(\theta_i) = 0.205 + 0.524 \cos \theta_i + 0.390 \cos^2 \theta_i - 0.132 \cos^3 \theta_i. \quad (4.5)$$

Figure 4.4 shows the probability density function for $\cos \Theta_i$ depending on the energy E [105]. Moreover, Figure 4.5 shows the angular resolution for SK-I and SK-III [105].

The direction reconstruction goodness, which is a parameter that indicates whether the direction reconstruction is done well or not, is defined as

$$g_{\text{dir}} = \frac{1}{2\pi} \left\{ \max \left(\phi_i - \frac{2\pi \times i}{N_{\text{hit}}} \right) - \min \left(\phi_i - \frac{2\pi \times i}{N_{\text{hit}}} \right) \right\}, \quad (4.6)$$

where ϕ_i is the azimuthal angle of the i -th hit PMT. The range of g_{dir} is from 0 to 1, and the value is close to 0 when the direction reconstruction is done well.

4.3 Energy reconstruction

Energy is reconstructed by using N_{eff} , which does not depend on vertex, direction, the number of bad-channel PMTs, water transparency, and relative quantum efficiency (QE) of each PMT. N_{eff} is defined as

$$N_{\text{eff}} = \sum_{i=1}^{N_{50}} \left[(X_i + \epsilon_{\text{tail}} - \epsilon_{\text{dark}}) \times \frac{N_{\text{all}}}{N_{\text{alive}}} \times \frac{S(0, 0)}{S(\theta_i, \phi_i)} \times \exp\left(\frac{r_i}{L_{\text{eff}}^i}\right) \times \frac{1}{QE_i} \right], \quad (4.7)$$

where N_{50} is the number of hit PMTs within 50 ns. Parameters shown in Equation (4.7) is described below.

X_i : Correction for multiple hits

When an event occur at the edge of fiducial volume or an event is caused by a charged particle with high energy, multiple photons may hit a PMT nearby the vertex. The multiple hits are corrected by using X_i defined as

$$X_i = \begin{cases} \frac{\log\{1/(1 - n_i/N_i)\}}{n_i/N_i} & (n_i/N_i < 1) \\ 3.0 & (n_i/N_i = 1) \end{cases}, \quad (4.8)$$

where N_i is the number of PMTs adjacent to the hit PMT and n_i is the number of hits in the adjacent PMTs.

ϵ_{tail} : Correction for scattering and reflection

Cherenkov photons scattering in water or reflecting at the surface of PMT or black sheet may hit a PMT at time out of a time width of 50 ns. The effects of scattering and reflection are corrected by using ϵ_{tail} defined as

$$\epsilon_{\text{tail}} = \frac{N_{100} - N_{50} - N_{\text{alive}} \times R_{\text{dark}} \times 50 \text{ ns}}{N_{50}}, \quad (4.9)$$

where N_{100} is the number of hit PMTs within 100 ns, N_{alive} is the number of alive PMTs and R_{dark} (hits/ns) is the dark-noise rate at a period.

ϵ_{dark} : Correction for dark-noise hits

Hits caused by PMT dark noise may enter the time width of 50 ns. The dark-noise hits, which are not originated from Cherenkov photons, are corrected by using ϵ_{dark} defined as

$$\epsilon_{\text{dark}} = \frac{N_{\text{alive}} \times R_{\text{dark}} \times 50 \text{ ns}}{N_{50}} \times \frac{\sum_{i=1}^{N_{50}} \frac{R_{\text{dark}}^i}{N_{50}}}{\sum_{i=1}^{N_{50}} \frac{R_{\text{dark}}^i}{N_{50}}}, \quad (4.10)$$

where R_{dark}^i (hits/ns) is the dark-noise rate of the i -th hit PMT at a period.

$N_{\text{all}}/N_{\text{alive}}$: Correction for bad-channel PMTs

If there is a PMT that does not work properly, the number of hits would be underestimated and energy would not be reconstructed correctly. The effects of bad-channel PMTs are corrected by multiplying $N_{\text{all}}/N_{\text{alive}}$, where N_{all} ($= 11,129$) is the number of all PMTs.

$S(0,0)/S(\theta_i, \phi_i)$: Correction for change of photo coverage by the incident angle of photon

Photo coverage changes depending on the incident angle of a Cherenkov photon. This effect is corrected by using the correction function $S(\theta_i, \phi_i)$. Figure 4.6 and Figure 4.7 show the definition of the incident angle and distributions of correction function $S(\theta_i, \phi_i)$ for barrel PMTs and top and bottom PMTs, respectively.

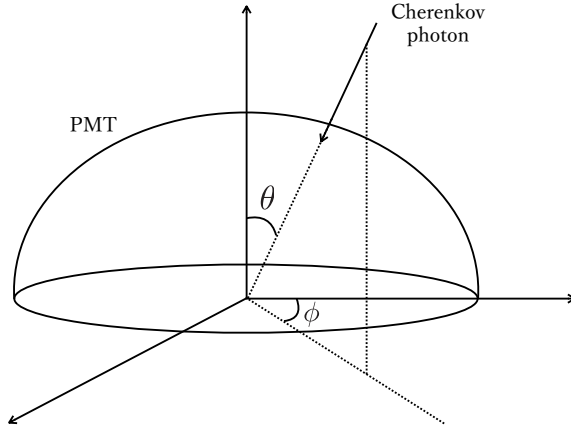


Figure 4.6: Definition of the incident angle [106].

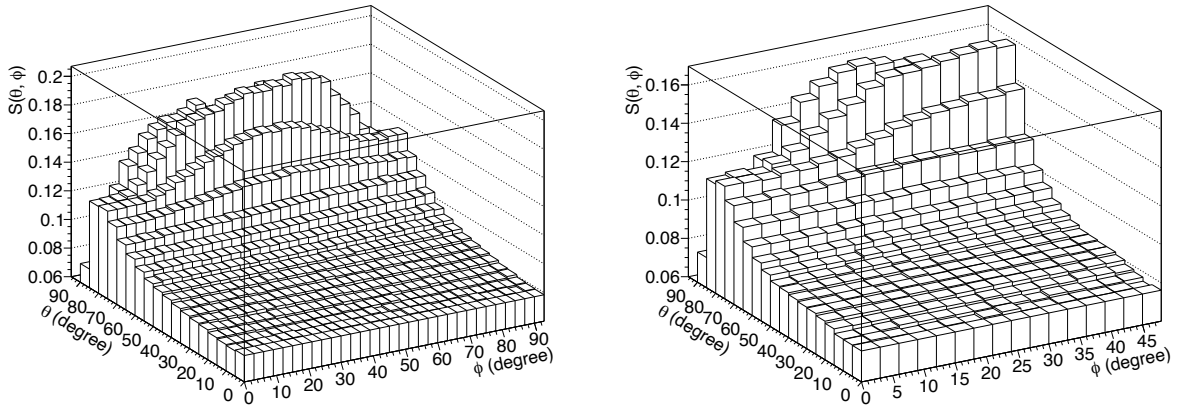


Figure 4.7: Distributions of correction function $S(\theta_i, \phi_i)$ for barrel PMTs (left) and top and bottom PMTs (right) [106].

$\exp(r_i/L_{\text{eff}}^i)$: Correction for water transparency

Cherenkov photons may be scattered or absorbed in water before arriving at a PMT. The probability that a Cherenkov photon arrives at a PMT can be written as $\exp(-r_i/L_{\text{eff}}^i)$, where r_i is the distance from the vertex to a hit PMT and L_{eff}^i is the effective attenuation length, which is described below. Therefore, the effect of water transparency is corrected by multiplying $\exp(r_i/L_{\text{eff}}^i)$.

L_{eff}^i is expressed as

$$L_{\text{eff}}^i = -\frac{r_i}{\ln \left[\int_{\lambda_{\min}}^{\lambda_{\max}} w_0(\lambda) \exp\{-\sigma_i(\lambda) \times r_i\} d\lambda \right]}, \quad (4.11)$$

where $\lambda_{\min} = 300 \text{ nm}$, $\lambda_{\max} = 650 \text{ nm}$, $w_0(\lambda)$ is the probability density function for wavelength λ of

Cherenkov photons (shown in Figure 4.8), and $\sigma_i(\lambda)$ is the cross section with water when a Cherenkov photon travels a distance r_i . $\sigma_i(\lambda)$ is expressed as

$$\sigma_i(\lambda) = \alpha_{\text{abs}}(\lambda) \left\{ 1 + \beta \left(z + \frac{1}{2} r_i \times dz_i \right) \right\} + C_{\text{sca}} \{ \alpha_{\text{sym}}(\lambda) + \alpha_{\text{asy}}(\lambda) \}, \quad (4.12)$$

where z is the z position of the vertex, dz_i is the z component of direction to the hit PMT, and $C_{\text{sca}} (\sim 0.44)$ is the correction factor of the scattering effect. C_{sca} was estimated to minimize the position dependence of N_{eff} using the SK detector simulation. $\alpha_{\text{abs}}(\lambda)$, $\alpha_{\text{sym}}(\lambda)$, and $\alpha_{\text{asy}}(\lambda)$ are the attenuation coefficients of absorption, symmetric scattering, and asymmetric scattering at wavelength λ , respectively, and β is the parameter indicating the degree of z dependence in water quality. Details about $\alpha_{\text{abs}}(\lambda)$, $\alpha_{\text{sym}}(\lambda)$, $\alpha_{\text{asy}}(\lambda)$, and β are described in Section 5.2.1.

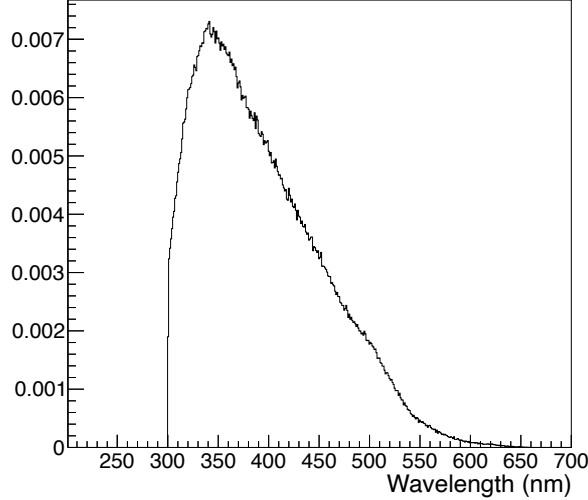


Figure 4.8: Probability density function for wavelength λ of Cherenkov photons [106].

$1/QE_i$: Correction for relative QE of each PMT

QE differs for each PMT. The effect of QE is corrected by multiplying $1/QE_i$, where QE_i is the relative QE of the hit PMT. Details about QE_i are described in Section 5.1.4.

Visible energy of the prompt signal (E_{vis}) is determined by using N_{eff} . Relation between E_{vis} and N_{eff} is expressed as

$$E_{\text{vis}} = \begin{cases} \sum_{i=0}^5 p_i (N_{\text{eff}})^i & (N_{\text{eff}} \leq N_{\text{thr}}) \\ \sum_{i=0}^5 p_i (N_{\text{thr}})^i + (N_{\text{eff}} - N_{\text{thr}}) \times \sum_{i=1}^5 i p_i (N_{\text{thr}})^{i-1} & (N_{\text{eff}} > N_{\text{thr}}) \end{cases}. \quad (4.13)$$

The values of p_i and N_{thr} are summarized in Table 4.1.

Table 4.1: Values of p_i and N_{thr} [36].

p_0	0.702
p_1	0.131
p_2	-2.35×10^{-4}
p_3	2.640×10^{-6}
p_4	-1.188×10^{-8}
p_5	1.930×10^{-11}
N_{thr}	2.202×10^2

5 Detector calibration

In physics experiments, the data reliability can be obtained by performing the detector calibration precisely. The detector calibration indicates confirming if the detector is working properly and the measurement accuracy is sufficient. If needed, it is also important to determine the parameters in MC to reproduce the experimental results. The detector calibration in SK can be largely classified as follows.

- ID detector calibration
- Photon tracking
- OD detector calibration
- Energy scale calibration

In this section, ID detector calibration, photon tracking, and energy scale calibration using the linear accelerator (LINAC) are described. The OD detector calibration is described in Ref. [58].

5.1 ID detector calibration

Before describing about each calibration, the procedure of ID detector calibration is described. First, applied voltage of each ID PMT is determined to output the similar degree of charge in all ID PMTs. This eliminates the asymmetry in the detector response and improves energy resolution. Second, we understand the individual difference of gain and quantum efficiency (QE) of ID PMTs. Here, gain is defined as the amplification factor of a photoelectron arrived to the PMT dinode. Also, QE is generally defined as the probability that a photon hitting the photocathode of a PMT is converted into a photoelectron. In SK, QE is defined also including the probability that a photoelectron arrives to the first dinode of a PMT. Signals by high energy events like cosmic ray muons largely depends on gain. While signals by low energy (DSNB and NCQE) events, which are mostly one photoelectron level, largely depends on QE. Therefore, it is crucial to understand the gain and QE of each ID PMT since the reconstructed energy depends on the gain and QE. Furthermore, the timing response of each ID PMT is calibrated to correct the deviation caused by the length of cables sending signals, the process time in electrical circuits, and the height of PMT signal waveforms.

5.1.1 High-Voltage determination

Applied voltage of each PMT (High-Voltage, HV) is determined to output the similar degree of charge in all PMTs⁴. The HV determination is conducted by setting an isotropic light source (Xe light source) at the center of the SK tank. The Xe light source consists of a Xe lamp, a UV filter, and a scintillation ball with a diameter of 5 cm. Xe lamp emits light by applying voltage inside a glass tube filled with Xe gas. Also, the scintillation ball includes 15 ppm⁵ POPOP and 2,000 ppm magnesium oxide (MgO). POPOP plays a role of converting the light wavelength, and MgO plays a role of emitting light from the scintillation ball as isotropically as possible.

⁴In SK-V, HV was retuned so that the peak of charge distribution (see Figure 5.3) obtained by using Ni-Cf source (see Figure 5.2) match in all PMTs.

⁵ppm stands for “parts per million”, and 1 ppm is equal to 0.0001%.

This measurement depends on not only the distance from the light source to a PMT, but also water transparency and photon reflectivity on the surface of PMTs. To ensure accuracy, before this measurement, 420 pre-calibrated PMTs, termed standard PMTs, with individually determined HV were installed into the SK tank. Figure 5.1 shows the location of standard PMTs in ID and schematic view of the grouping of nearby PMTs. HV of a PMT other than standard PMTs is set so that the amount of charge obtained by the PMT matches the average amount of charge obtained by standard PMTs belonging to the PMT's group. After determining the HV, the amount of charge was measured again by applying the determined HV to each PMT. As a result, the difference between the amount of charge obtained by each PMT and the average value was within 1.3% in RMS, which is consistent with the result of preliminary measurement for the standard PMTs. Note that the Xe light source is installed to monitor the long-term gain fluctuations of PMTs even after the HV is determined.

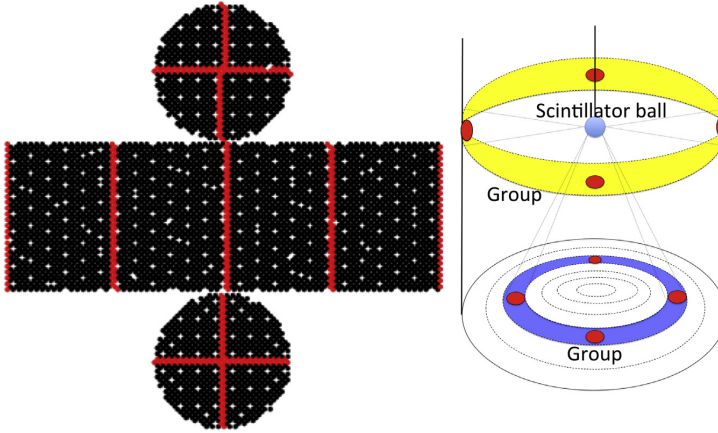


Figure 5.1: Location of standard PMTs in ID (left) and schematic view of the grouping of nearby PMTs (right) [58]. Red points show standard PMTs. There are 17 groups on barrel, and 8 groups on top and bottom.

5.1.2 Relative gain measurement

To determine the gain of each PMT, we must understand the average gain of all PMTs (absolute gain) and the deviation from the average gain of all PMTs (relative gain). To calculate this relative gain, we perform two-step measurements using an isotropic light source. First, a high intensity light is applied so that all PMTs receive a sufficient amount of light. We define the average value of the charge at the i -th PMT in this measurement as $Q_{\text{obs}}(i)$. Next, a low intensity light is applied so that PMTs receive only a small number of photons. We define the number of hits (the number of recording the amount of charge exceeding a threshold) at the i -th PMT in this measurement as $N_{\text{obs}}(i)$. By performing these two measurements using the same light source and at the same position, $Q_{\text{obs}}(i)$ and $N_{\text{obs}}(i)$ can be calculated as

$$Q_{\text{obs}}(i) \propto I_H \times a(i) \times \epsilon(i) \times G(i), \quad (5.1)$$

$$N_{\text{obs}}(i) \propto I_L \times a(i) \times \epsilon(i), \quad (5.2)$$

where I_H (I_L) shows the average amount of light of high (low) intensity, $a(i)$ shows the acceptance of the i -th PMT, $\epsilon(i)$ shows the QE of the i -th PMT, and $G(i)$ shows the gain of the i -th PMT. By taking the ratio

of Equation (5.1) and Equation (5.2), $G(i)$ can be calculated as

$$G(i) \propto \frac{Q_{\text{obs}}(i)}{N_{\text{obs}}(i)}. \quad (5.3)$$

Relative gain of each PMT can be obtained by normalizing Equation (5.3) with the average gain of all PMTs. Note that I_H/I_L can also be ignored by this normalization.

As a result of this measurement, the RMS of the relative gain distribution was found to be 5.9% [58]. Since the HV of each PMT is set so that $Q_{\text{obs}}(i)$ is the same among PMTs⁶, this difference is considered to be caused by the difference of QE for each PMT. Relative gain of each PMT is used as the correction coefficient when converting the output charge into the number of photoelectrons.

5.1.3 Absolute gain measurement

Absolute gain is used to convert the amount of charge recorded in pC to the number of photoelectrons (p.e.). Absolute gain is determined from the charge distribution of 1 p.e. signals from a Ni-Cf source, which is a gamma-ray source. Figure 5.2 shows the picture of the Ni-Cf source. The Ni-Cf source consists of a ball made from nickel oxide (NiO) and polyethylene, a brass rod, and ^{252}Cf source. ^{252}Cf source emits neutrons through spontaneous fission, and the neutrons are thermalized while repeating elastic scattering with protons. The thermalized neutron is captured on nickel nucleus, and gamma-rays are emitted isotropically. When the Ni-Cf source is placed in the center of the SK tank, more than 99% of signals are 1 p.e..



Figure 5.2: Picture of the Ni-Cf source.

Figure 5.3 shows the charge distribution of the Ni-Cf source data in SK-III. This distribution is obtained by applying the relative gain correction and adding up the charge distributions of all PMTs. Also, to minimize the influence of PMT noise hits, the charge distributions are created at the time width that does not include signals due to the Ni-Cf source (off time) and the time width that includes signals due to the Ni-Cf source (on time), and the off time distribution is subtracted from the on time distribution. Absolute gain is defined as the mean value over the full range of the distribution. The values of absolute gain is 2.055, 2.297, 2.243, 2.645, 2.460 in SK-I to SK-V, respectively. Absolute gain in SK-VI is the same as that in SK-V since HV is not changed from SK-V.

⁶As noted in the footnote of Section 5.1.1, in SK-V, HV was retuned so that the peak of charge distribution (see Figure 5.3) obtained by using Ni-Cf source (see Figure 5.2) match in all PMTs.

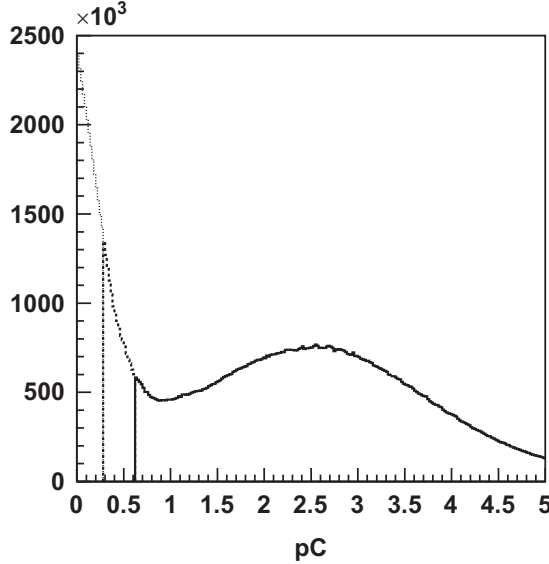


Figure 5.3: Charge distribution of the Ni-Cf source data in SK-III [58]. The dashed line shows the data with double gain and half threshold. The dotted line is linear extrapolation.

5.1.4 Relative QE measurement

Relative QE is also determined using the Ni-Cf source. First, data is obtained by setting the Ni-Cf source at the center of the SK tank. At that time, it is better to convect the ultrapure water so that the water quality is uniform. Second, "hit rate" of each PMT (R_{Data}^i) is calculated from the obtained data. R_{Data}^i is defined as

$$R_{\text{Data}}^i = \frac{N_{\text{Hit}}^i \times r_i^2 / a(\theta_i)}{\sum \{ N_{\text{Hit}}^i \times r_i^2 / a(\theta_i) \} / N_{\text{PMT}}}, \quad (5.4)$$

where N_{Hit}^i is the number of hits of i -th PMT, r_i is the distance from the Ni-Cf source position to the position of i -th PMT, $a(\theta_i)$ is the correction function of PMT acceptance, which is the same as Equation (4.5), and N_{PMT} is the number of PMTs used in this calculation. Finally, relative QE of each PMT (QE_i) is obtained by dividing R_{Data}^i by R_{MC}^i , which is the hit rate of i -th PMT obtained from MC, to cancel the effects of reflection and water quality,

$$QE_i = \frac{R_{\text{Data}}^i}{R_{\text{MC}}^i}. \quad (5.5)$$

Figure 5.4 shows the hit rate distribution of data and MC. In this figure, relative QE of each PMT is not considered in MC. While, in data, the distribution is bumpy due to the effect of relative QE of each PMT.

5.1.5 Timing response calibration

The timing response of each PMT, which is important for reconstructing the trajectory and position of charged particles, deviates depending on the length of cables sending signals and the process time in electrical circuits. Furthermore, the timing response depends on the height of PMT signal waveforms, which

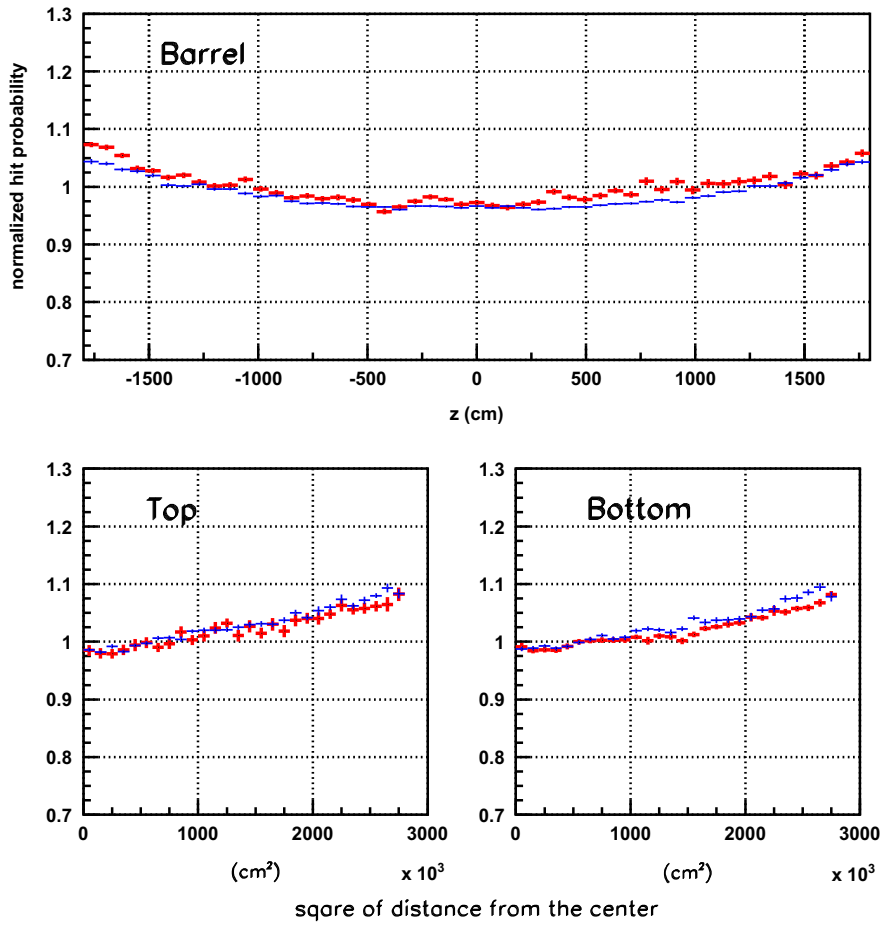


Figure 5.4: Hit rate distribution of data (red plots) and MC (blue plots) [58]. Top, bottom left, and bottom right figure shows the distribution for barrel PMTs, top PMTs, and bottom PMTs, respectively. In the distribution for barrel PMTs, horizontal axis shows the z position of barrel PMTs. In the distributions for top and bottom PMTs, horizontal axis shows $x^2 + y^2$, where x and y is the x and y position of top (bottom) PMTs, respectively. Vertical axis shows the average of R_{Data}^i or R_{MC}^i in each bin.

is known as the time walk effect. The purpose of the timing response calibration experiment is to determine the correction factor of time walk for each PMT considering the process time of entire detector.

Figure 5.5 shows the schematic view of the timing response calibration system and cross section of the diffuser ball. First, pulsed light with a wavelength of 337 nm and a full width at half maximum of 0.4 nsec is generated using a nitrogen laser. The timing at which this pulsed light is generated is determined using a 2-inch PMT with a fast timing response. After that, the wavelength of the pulsed light is shifted to 398 nm, where the QE of PMTs is high. The pulsed light then goes through the optical fiber to the diffuser ball and is emitted isotropically. Furthermore, the intensity of the pulsed light can be changed using an optical filter, and the timing response can be measured at various pulse heights. Since the pulse height is proportional to the charge, this calibration is called TQ calibration.

In this measurement, as shown in Figure 5.6, a 2D distribution of timing and charge for one readout channel can be created. This distribution is called a TQ map. The timing information on the vertical axis in Figure 5.6 is obtained by calculating the TOF (Time of Flight) from the positional relationship between the light source and the PMT and calculating $T - \text{TOF} - T_{\text{2-inch}}$, where T is the PMT hit timing and $T_{\text{2-inch}}$

is the signal transmission time of the 2-inch PMT. A total of 15 correction factors can be obtained by fitting the peak at each QBin in the TQ map with the following polynomial function depending on QBin,

$$\text{QBin} \leq 10 : F_1(x) \equiv f_3(x), \quad (5.6)$$

$$10 < \text{QBin} \leq 50 : F_2(x) \equiv F_1(10) + (x - 10)\{F'_1(10) + (x - 10)f_3(x - 10)\}, \quad (5.7)$$

$$\text{QBin} > 50 : F_3(x) \equiv F_2(50) + (x - 50)f_6(x - 50), \quad (5.8)$$

$$f_N(x) \equiv p_0 + p_1x + p_2x^2 + \dots + p_Nx^N, \quad (5.9)$$

where $F'_1(x)$ is the derivative of $F_1(x)$.

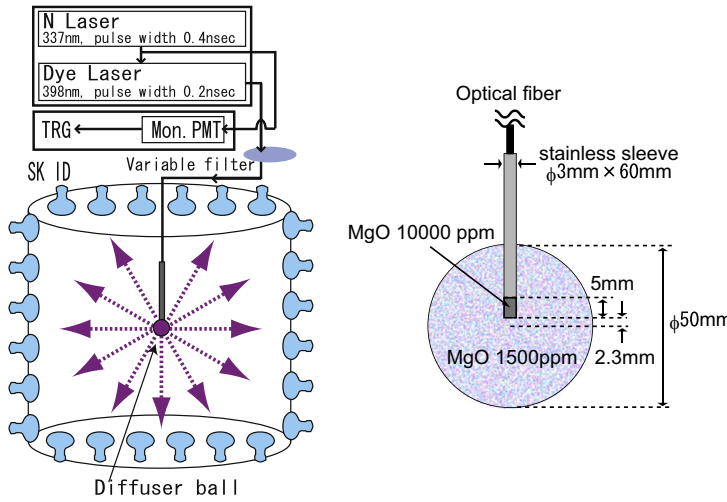


Figure 5.5: Schematic view of the timing response calibration system (left) and cross section of the diffuser ball (right) [58].

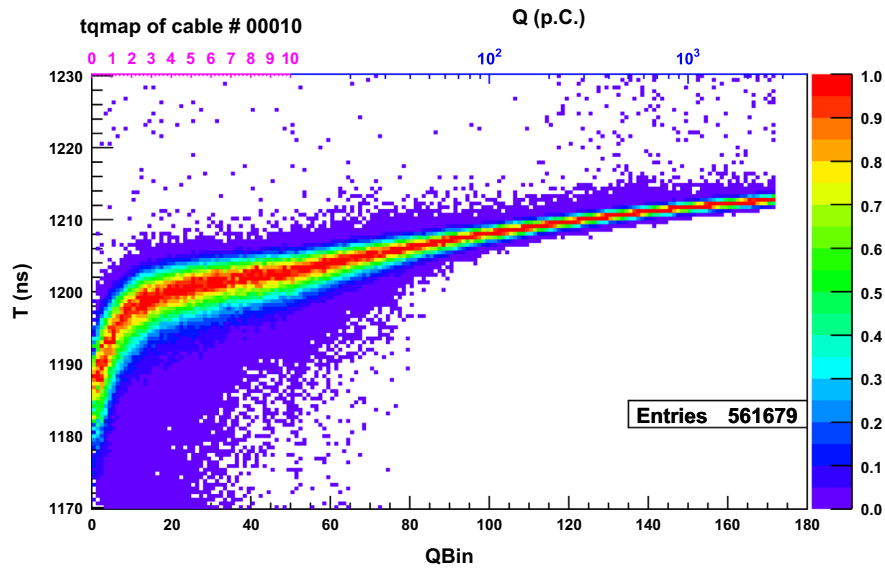


Figure 5.6: 2D distribution of timing and charge for one readout channel [58]. Horizontal axis shows charge (QBin) of each hit. Vertical axis shows TOF-corrected hit timing.

5.2 Photon tracking

5.2.1 Water transparency measurement

For photon tracking in MC, it is essential to consider the water properties like absorption and scattering. The light attenuation is expressed as $\exp\{-l/L(\lambda)\}$, where l is the light path length and $L(\lambda)$ is the attenuation length at wavelength λ . Also, in MC, $L(\lambda)$ is defined as

$$L(\lambda) = \frac{1}{\alpha_{\text{abs}}(\lambda) + \alpha_{\text{sym}}(\lambda) + \alpha_{\text{asy}}(\lambda)}, \quad (5.10)$$

where $\alpha_{\text{abs}}(\lambda)$, $\alpha_{\text{sym}}(\lambda)$, and $\alpha_{\text{asy}}(\lambda)$ are attenuation coefficients of absorption, symmetric scattering, and asymmetric scattering at wavelength λ , respectively. $\alpha_{\text{sym}}(\lambda)$ is used to consider the Rayleigh scattering and the symmetric components of Mie scattering. While $\alpha_{\text{asy}}(\lambda)$ is used to consider the forward components of Mie scattering.

To determine each attenuation coefficient, laser light of various wavelengths (337, 375, 405, 445, and 473 nm) were applied downward from the top of the SK tank, and the PMT hit timing was measured. Figure 5.7 shows the schematic view of the laser calibration system and TOF-subtracted hit timing distributions of the laser calibration data and MC. Attenuation coefficients are determined using top PMTs that are 2 m away from the laser light injector, and barrel PMTs. Barrel is separated into five regions, from B1 to B5. B3 includes PMTs for 11 lines and the others include PMTs for 10 lines. In the left side of Figure 5.7, the cyan shaded circle spot on the bottom shows the beam target used for the TOF calculation. Also, in the right side of Figure 5.7, hits between the left two blue vertical solid lines are due to scattered photons, and this region is used to determine the attenuation coefficients. The peaks in the right time region is thought to be due to photons reflected on the surface of PMT or black sheet. Each attenuation coefficient is introduced into MC using the following formula based on experiments,

$$\alpha_{\text{abs}}(\lambda) = P_0 \times \frac{P_1}{\lambda^4} + C, \quad (5.11)$$

$$C = P_0 \times P_2 \times \left(\frac{\lambda}{500} \right)^{P_3}, \quad (5.12)$$

$$\alpha_{\text{sym}}(\lambda) = \frac{P_4}{\lambda^4} \times \left(1.0 + \frac{P_5}{\lambda^2} \right), \quad (5.13)$$

$$\alpha_{\text{asy}}(\lambda) = P_6 \times \left\{ 1.0 + \frac{P_7}{\lambda^4} \times (\lambda - P_8)^2 \right\}. \quad (5.14)$$

Attenuation coefficients are determined so that χ^2 is minimized by comparing the hit timing distribution of MC created while changing the nine parameters from P_0 to P_8 with the hit timing distribution of data. Values of P_0 to P_8 are summarized in Table 5.1.

5.2.2 Top-Bottom Asymmetry

As described in Section 2.6, the ultrapure water in SK is always circulated and purified by the water purification system. The purified ultrapure water is supplied from the bottom of SK tank and collected at the top of SK tank. The water quality gradually decreases as the ultrapure water moves from the bottom to the top of SK tank. Therefore, the water transparency in the SK tank has position dependence, and it is crucial

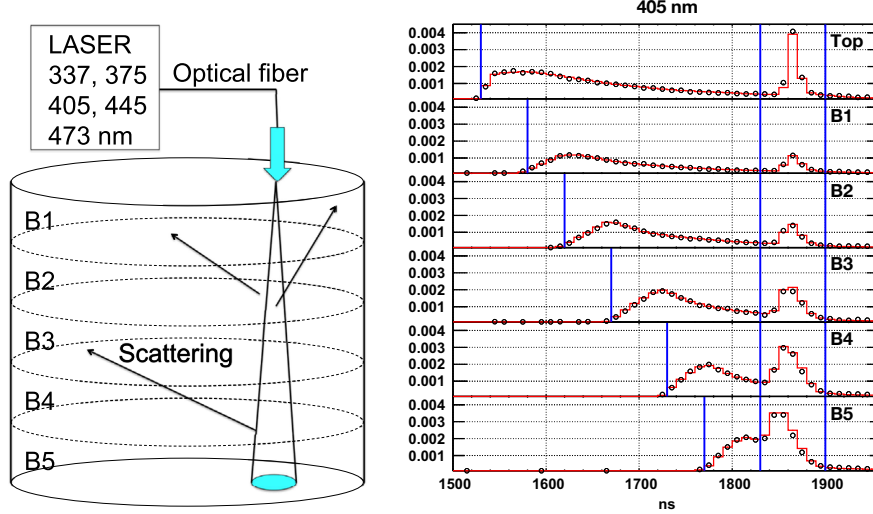


Figure 5.7: Schematic view of the laser calibration system (left) and TOF-subtracted hit timing distributions of the laser calibration data and MC (right) [58]. Water parameter tuning is performed using top PMTs that are 2 m away from the laser light injector, and barrel PMTs. Barrel is separated into five regions, from B1 to B5. B3 includes PMTs for 11 lines and the others include PMTs for 10 lines. In the left figure, the cyan shaded circle spot on the bottom shows the beam target used in the TOF calculation. In the right figure, the black circle shows data and the red histogram shows MC. Both data and MC are normalized by observed total photoelectrons. Time region between the left two blue vertical solid lines is used for the water parameter tuning. Right time region is used for the PMT reflectivity measurement.

to understand the position dependence of water transparency precisely. The vertical dependence is estimated by the Ni-Cf source data and the Xe light source data described in Section 5.1.1. The vertical asymmetry of water transparency (Top-Bottom Asymmetry, TBA) is defined as

$$TBA = \frac{N_{\text{top}} - N_{\text{bottom}}}{N_{\text{barrel}}}, \quad (5.15)$$

where N_{barrel} , N_{top} , and N_{bottom} shows the average number of ID PMT hits on the barrel, on the top, and on the bottom, respectively. Figure 5.8 shows the time variation of TBA in SK-V and SK-VI. As described above, the water quality is better in the bottom side than in the top side. Therefore, the values of TBA are negative. Also, since the time variation seen in Figure 5.8 are mainly due to the variation in absorption, the time and z-direction dependent water quality is implemented into the MC by multiplying α_{abs} by the factor $A(z, t)$. $A(z, t)$ is defined as

$$A(z, t) \equiv \begin{cases} 1 + z \times \beta(t) & (z \geq -11 \text{ m}) \\ 1 - 11 \times \beta(t) & (z < -11 \text{ m}) \end{cases}, \quad (5.16)$$

$$\beta(t) = -0.006322 \times 100 \times TBA - 0.004130, \quad (5.17)$$

where z is the z position and $\beta(t) [\text{m}^{-1}]$ is the parameter indicating the degree of z dependence in water quality as a function of t . In Equation (5.17), TBA shows the TBA calculated by using the Xe light source data, and this equation can be obtained by using all Ni-Cf source data in SK-VI.

Table 5.1: Values of P_0 to P_8 .

P_0	0.596600
P_1	5.18888×10^7
P_2	1.06522
P_3	14.1858
P_4	1.13817×10^8
P_5	5.79108×10^4
P_6	2.26159×10^{-4}
P_7	17.1260
P_8	4.48622×10^4

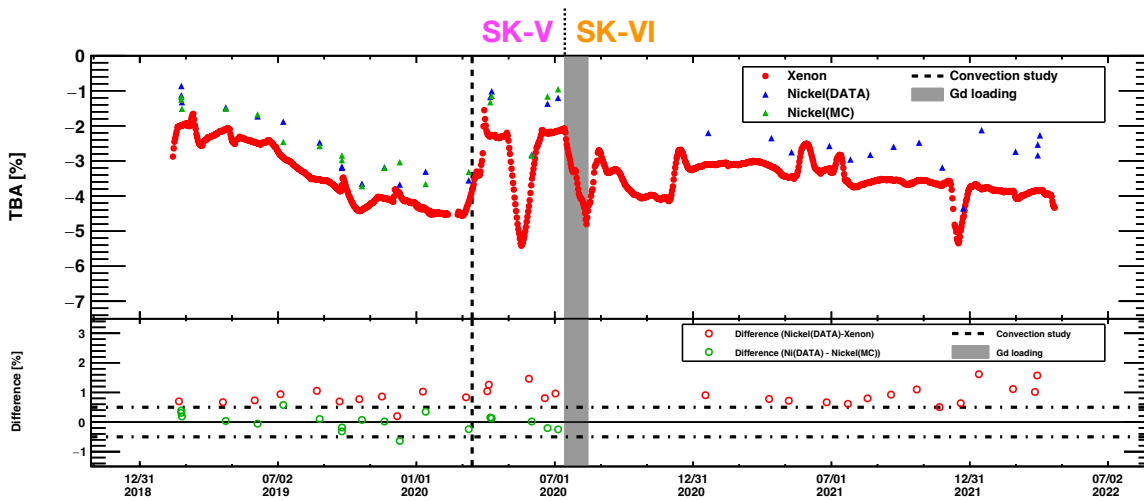


Figure 5.8: Time variation of TBA in SK-V and SK-VI [107]. The differences of TBA between Ni-Cf source data and Xe light source data and between Ni-Cf source data and MC are also shown on the bottom. The two thick horizontal dotted-dashed lines show the 0.5% difference.

5.2.3 Photon reflection on the material surface

When considering photon tracking, the photon reflection on the material surface must also be introduced into MC. In this section, reflectivity measurements of PMT and black sheet are described.

Reflection on the PMT surface

The photon reflection on the PMT surface can be estimated by comparing the time region between the right two blue vertical solid lines in Figure 5.7 between data and MC. The PMT surface consists of three layers of glass, bialkali, and vacuum. In SK, the refractive indices of the glass, bialkali, and vacuum are defined as $1.472 + 3670/\lambda^2$, $n_{\text{re}} + i \times n_{\text{im}}$, and 1.0, respectively. Here, λ [nm] is the wavelength of a photon. For bialkali, the complex refractive index is taken into account, where n_{re} and n_{im} are the real and imaginary parts of the complex refractive index, respectively. The best value of n_{re} obtained by comparing the data with MC was 2.31 at $\lambda = 337$ nm, 2.69 at $\lambda = 365$ nm, 3.06 at $\lambda = 400$ nm, and 3.24 at $\lambda = 420$ nm. While the best value of n_{im} obtained by comparing the data with MC was 1.667.

Reflection on the black sheet surface

Cherenkov photons are absorbed on the black sheet surface with high probability, but may also be reflected. The black sheet reflectivity introduced into MC is adjusted by using the results of the measurement by laser injector. Figure 5.9 shows the schematic view of the black sheet reflectivity measurement. First, laser injector is set at the center of the SK tank, laser light is injected onto a black sheet about 10 cm away, and the amount of charge by the reflected light ($Q_{\text{reflected}}$) is measured. Second, the amount of charge without black sheet (Q_{direct}) is measured. Finally, the black sheet reflectivity is adjusted by using the ratio $Q_{\text{reflected}}/Q_{\text{direct}}$. As a result of adjusting the reflectivity, the difference between data and MC is within 1%. Note that this measurement was performed at three wavelengths (337 nm, 400 nm, 420 nm) and at three reflection angles ($30^\circ, 45^\circ, 60^\circ$).

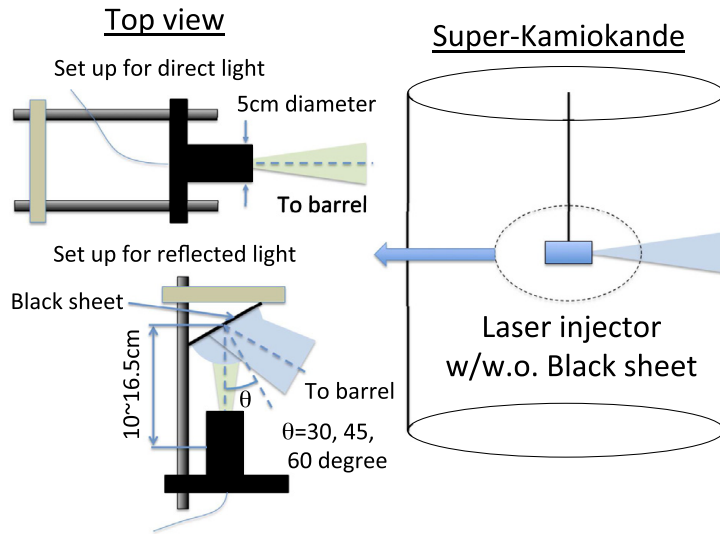


Figure 5.9: Schematic view of the black sheet reflectivity measurement [58]. Left figure shows the top view. The laser light injector is inserted from the top center of the SK tank and the reflected light is measured by ID PMTs.

5.3 LINAC

The energy scale parameter for low-energy MC simulations is determined by using the electron linear accelerator (LINAC)⁷. Figure 5.10 shows the schematic view of LINAC [108]. To suppress the effects of X-rays and gamma-rays emitted by LINAC itself, LINAC is set far from the SK detector. Electron beams generated at LINAC are sent inside the detector with stainless beam pipes and magnets. The kinetic energy of electron beams can be selected in the range of 5 to 18 MeV. Moreover, the irradiate position of electron beams can be changed by extending and taking out the beam pipes. In SK-VI, LINAC data was taken at three irradiate positions: $(-1237, -70.7, 1197)$ cm, $(-1237, -70.7, -6)$ cm, and $(-1237, -70.7, -1209)$ cm. At each position, electron beams with kinetic energies of 8 MeV, 12 MeV, and 15 MeV were irradiated. As for the position of $(-1237, -70.7, -6)$ cm, electron beams with kinetic energy of 6 MeV were also irradiated. The energy scale parameter is derived by comparing N_{eff} between LINAC data and LINAC MC. In SK-VI, the parameter was determined to be about 0.88, and this parameter is multiplied by QE of ID PMTs in MC simulations.

⁷The systematic uncertainty of energy scale is also determined by using LINAC.

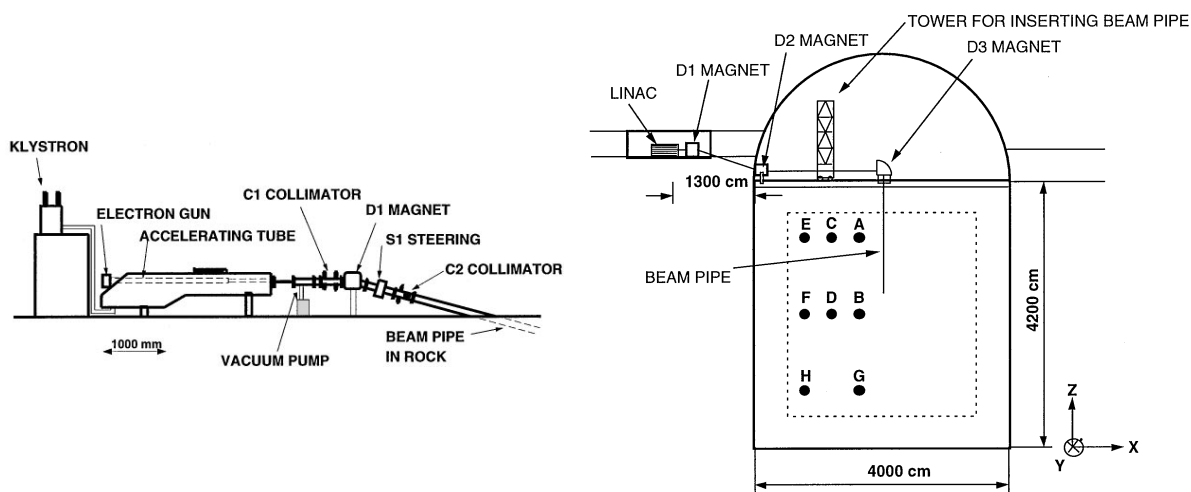


Figure 5.10: Schematic view of LINAC [108].

6 Event selection

In this study, we search for NCQE events that consist of prompt signals from de-excitation gamma-rays and delayed signals from neutrons. We select events where the visible energy of the prompt signal (E_{vis}) is between 7.49 MeV and 29.49 MeV because most NCQE events are in the E_{vis} region (see Figure 6.18). In each candidate event, delayed signals within 535 μs from the prompt signal are searched. The event reconstruction and neutron tagging method follow the DSNB search in SK-Gd phase [40, 109]. Details of the neutron tagging method are summarized in Section 6.4.2.

The data sample includes not only NCQE events but also other events such as atmospheric neutrino NC non-QE events, atmospheric neutrino charged-current (CC) events, spallation events (see Section 3.3.1), reactor neutrino events (see Section 3.3.2), and accidental coincidence events. Most of atmospheric neutrino NC non-QE events ($\sim 90.4\%$ of NC non-QE events after applying all event selections) are events with single meson, as shown in Figure 6.1. Schematic view of atmospheric neutrino CC events is shown in Figure 6.2. Muon neutrino CC events become backgrounds when the emitted muon is invisible (below Cherenkov threshold (see Section 2.5)). Accidental coincidence events are mainly pairs of a spallation event without neutrons and a neutron misidentification event. Most of these events can be removed by applying various event reductions. However, some events remain even after applying all event reductions. To determine the number of NCQE events, it is necessary to estimate the number of all those events. The methods of event reduction and event estimation are described below.

This study uses 552.2 days of data with 0.011% gadolinium-loaded water from August 2020 to June 2022. This data set is the same as the one used for the SK-Gd DSNB search [40].

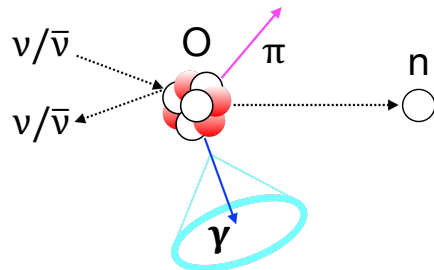


Figure 6.1: Schematic view of an atmospheric neutrino NC event with single meson.

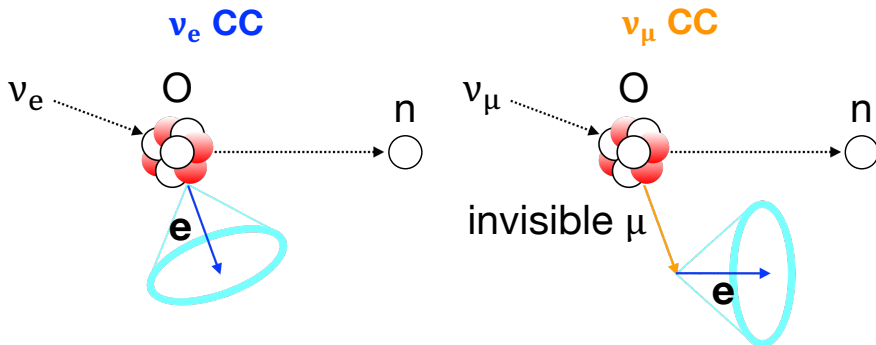


Figure 6.2: Schematic view of atmospheric neutrino CC events.

6.1 First reduction: Pre-cut

6.1.1 Non-SHE-triggered event and noise event cut

First, when a run satisfies the following conditions, events in the run are not used.

- Run time is shorter than 5 minutes
- Run started less than 15 minutes after the high-voltage was recovered
- Any hardware problem is reported
- Event distribution is unusual due to detector problems

Moreover, the following events are removed.

- Calibration trigger events
- Periodic trigger events
- T2K beam trigger events
- Pedestal events

In addition, the condition $N(Q < 0.5 \text{ p.e.})/N_{\text{total}} < 0.55$ is required to remove the events triggered by PMT noise hits, where $N(Q < 0.5 \text{ p.e.})$ is the number of hits with a charge smaller than 0.5 p.e. and N_{total} is the total number of hits.

6.1.2 Cosmic ray muon-induced event cut

Cosmic ray muons come to the SK at ~ 2 Hz, and most of these muons issue the OD trigger. To remove events induced by cosmic ray muons, events that the OD trigger is issued are not used. Moreover, some muons decay into electrons with a life time of $2.2 \mu\text{s}$, leaving hits inside the ID without an OD trigger. To remove events induced by these electrons, events within $50 \mu\text{s}$ from preceding cosmic ray muons are not used. Spallation events caused by cosmic ray muons will be described later.

6.1.3 Fiducial volume cut

Radioactive backgrounds are concentrated near the detector wall. Therefore, events within 2 m away from the ID wall are removed.

6.1.4 Fit quality cut

To remove poorly reconstructed events, events that the vertex reconstruction goodness (g_{vtx}) is less than 0.5 are removed. Details of g_{vtx} are summarized in Section 4.1.

6.1.5 Trigger requirement

To search delayed signals within $535 \mu\text{s}$ from the prompt signal, not only the SHE trigger but also the AFT trigger must be issued. However, since the AFT trigger rate was limited to once every 21 ms until the middle of SK-VI, some events did not issue the AFT trigger. Therefore, in MC, the number of events is scaled by using the AFT trigger efficiency ε_{AFT} defined as

$$\varepsilon_{\text{AFT}} = \frac{N_{\text{AFT}}}{N_{\text{SHE}}}, \quad (6.1)$$

where N_{AFT} is the number of AFT-triggered events and N_{SHE} is the number of SHE-triggered events. ε_{AFT} is summarized in Table 6.1.

Table 6.1: AFT trigger efficiency considering the whole period of SK-VI.

E_{vis} (MeV)	ε_{AFT}
7.49–9.49	85.3%
9.49–11.49	80.4%
11.49–13.49	74.3%
13.49–15.49	70.0%
15.49–17.49	67.9%
17.49–19.49	63.4%
19.49–21.49	89.7%
21.49–23.49	90.0%
23.49–25.49	90.0%
25.49–27.49	100.0%
27.49–29.49	90.5%

6.2 Second reduction: Spallation cut

Here, the spallation events, which are major backgrounds in the energy range from a few MeV to tens of MeV, are removed. As described in Section 3.3.1, some radioactive isotopes produced by cosmic-ray muon spallation of oxygen nuclei mimic the IBD and NCQE events. The spallation cut consists of five components, and these components are described in Section 6.2.1 to Section 6.2.5.

6.2.1 1 ms cut

Gamma-rays and neutrons are emitted by hadronic nuclear interactions caused by nucleons and mesons with hundreds of MeV generated by muon spallation. In some cases, the gamma-rays can issue the SHE trigger, and the neutrons can be detected as delayed signals. To remove these events, events within 1 ms from preceding cosmic ray muons are not used.

6.2.2 Multiple spallation cut

Energetic cosmic ray muons may produce multiple radioactive isotopes. When a spallation event issues the SHE trigger, other spallation events may be observed close to the event both in time and space. To remove the SHE-triggered events, low energy events with a E_{vis} of 5.49–24.49 MeV within ± 60 s from the SHE-triggered event are used. First, selection criteria of the solar neutrino analysis [104] are applied to all low energy events. Then, the distance from the SHE-triggered event to each low energy event is calculated. If there is one low energy event with a distance of less than 4.0 m, the SHE-triggered event is removed (see Figure 6.3).

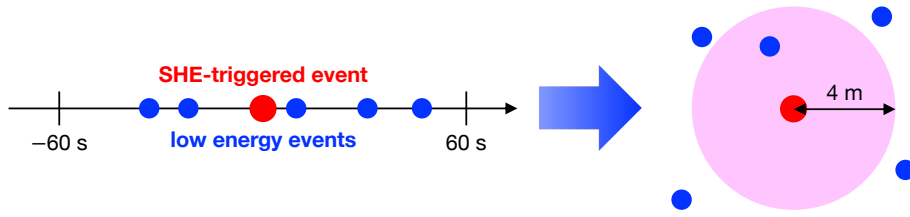


Figure 6.3: Schematic view of multiple spallation cut. In this case, the SHE-triggered event is removed.

6.2.3 Neutron cloud cut

Muon spallation produces many particles, including neutrons. These neutrons are captured on Gd, and generate neutron event clusters, named neutron cloud, near the spallation point. To remove spallation events, the information of neutron cloud is used. First, the following selection criteria are applied to neutron events after muon spallation.

- $N_{200} \geq 25$
- Timing is within $[35, 535] \mu\text{s}$ from the muon spallation
- $g_{\text{vtx}} > 0.4$ and $g_{\text{dir}} < 0.4$
- Distance from the muon track is within 5 m

Here, N_{200} is the number of hits in a TOF-subtracted 200 ns time window and g_{dir} is the direction reconstruction goodness. Details of g_{dir} are summarized in Section 4.2. These selection criteria are based on the measurement of cosmogenic neutron yield in SK-Gd [110]. If the number of neutron events that satisfied the above selection criteria (N_{cloud}) is greater or equal to 2, the muon is considered to have a neutron cloud. Then, SHE-triggered events are removed based on cut criteria summarized in Table 6.2. In Table 6.2, ΔT is the time difference between the muon and SHE-triggered event and $\Delta l (= \Delta_x^2 + \Delta_y^2 + \Delta_z^2)$ is the distance illustrated in Figure 6.4.

Table 6.2: Cut criteria of neutron cloud cut [36]. The cut criteria are based on the SK DSNB analysis [22].

	Time [s]	Spatial [cm]
$N_{\text{cloud}} \geq 2$	$\Delta T < 0.1$	$\Delta l < 1,200$
$N_{\text{cloud}} \geq 2$	$\Delta T < 1$	$\Delta l < 800$
$N_{\text{cloud}} = 2$	$\Delta T < 30$	$(\Delta_x^2 + \Delta_y^2)/200^2 + \Delta_z^2/400^2 > 1.2$
$N_{\text{cloud}} = 3$	$\Delta T < 60$	$(\Delta_x^2 + \Delta_y^2)/(6 \times 10^4) + \Delta_z^2/500^2 > 1.2$
$4 \leq N_{\text{cloud}} \leq 5$	$\Delta T < 60$	$(\Delta_x^2 + \Delta_y^2)/(1.2 \times 10^5) + \Delta_z^2/550^2 > 1.2$
$6 \leq N_{\text{cloud}} \leq 9$	$\Delta T < 60$	$(\Delta_x^2 + \Delta_y^2)/(2 \times 10^5) + \Delta_z^2/650^2 > 1.2$
$N_{\text{cloud}} \geq 10$	$\Delta T < 60$	$(\Delta_x^2 + \Delta_y^2)/500^2 + \Delta_z^2/700^2 > 1.2$

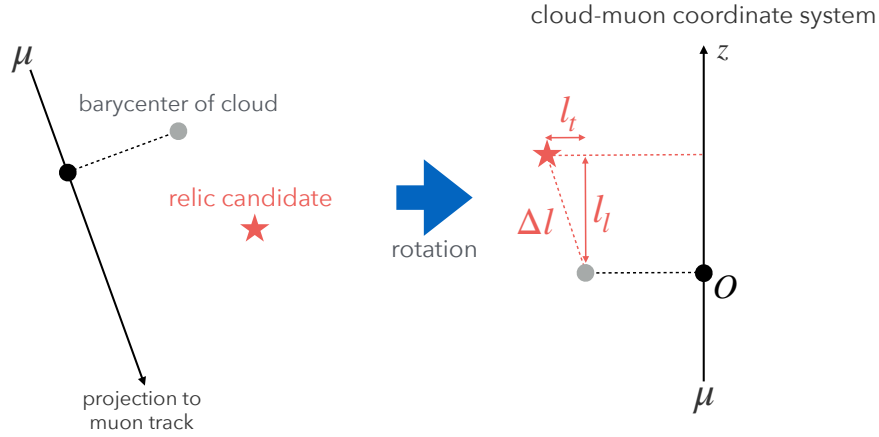


Figure 6.4: Definition of the variables used in the neutron cloud cut [36].

6.2.4 Spallation likelihood cut

To further remove spallation events, the spallation likelihood is used. The spallation likelihood $\mathcal{L}_{\text{spall}}$ is defined as

$$\mathcal{L}_{\text{spall}} = \log \prod_i \left\{ \frac{\text{PDF}_{\text{spall}}^i(x)}{\text{PDF}_{\text{random}}^i(x)} \right\}, \quad (6.2)$$

where $\text{PDF}_{\text{spall}}^i$ is the probability density function (PDF) of the muon spallation sample, $\text{PDF}_{\text{random}}^i$ is the PDF of the random sample, i is the i -th variable used in the calculation, and x is the value of the i -th variable. Definition of the muon spallation sample and the random sample is summarized in Figure 6.5 [36].

There are five variables used in the calculation as follows.

- dt : Time difference between the muon and SHE-triggered event. For spallation events, this variable should reflect lifetimes of the produced radioactive isotopes.
- l_t : Transverse distance from the muon track to SHE-triggered event. For spallation events, this variable should be within a few meters.
- l_l : Longitudinal distance from the maximum energy deposition point on the muon track to SHE-triggered event. The maximum energy deposition point is correlated to the spallation point, and this

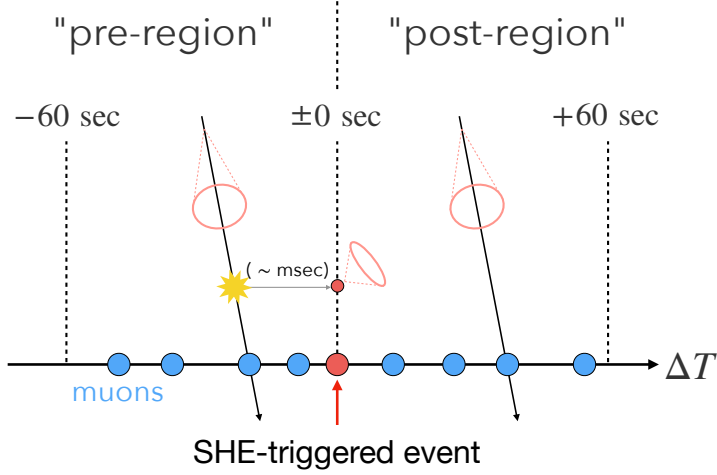


Figure 6.5: Definition of the muon spallation sample and the random sample [36]. Pre-region includes both muon spallation samples (muon events correlated with the SHE-triggered event) and random samples (muon events uncorrelated with the SHE-triggered event), while post-region includes only random samples.

variable should be within a few meters for spallation events.

- Q_μ : Total charge deposited by the muon in the ID. Q_μ of spallation events should be larger than Q_μ expected from the minimum ionization.
- Q_{res} : Difference between Q_μ and charge expected from the minimum ionization, defined as

$$Q_{\text{res}} = Q_\mu - Q_{\text{MI}} \times L, \quad (6.3)$$

where Q_{MI} is the number of photoelectrons per centimeter expected from the minimum ionization and L is the muon track length. For multiple muons, L is the sum of muon track lengths. Q_{res} indicates the probability that a muon will cause nuclear spallation.

Figure 6.6 shows the definition of l_t and l_l used in the spallation likelihood cut.

$\text{PDF}_{\text{spall}}^i$ and $\text{PDF}_{\text{random}}^i$ are made for four muon types, single-through going, stopping, multiple, and misfit muons, categorized at a muon reconstruction algorithm (Muboy) [36, 111, 112]. Figure 6.7 shows the schematic view of a single-through going muon, a stopping muon, and multiple muons. In Muboy, when the number of PMT hits is less than a certain threshold, the muon is categorized as a misfit muon. For misfit muons, only PDFs for dt are used to calculate $\mathcal{L}_{\text{spall}}$ because the number of PMT hits is small and other variables are unreliable. For single-through going, stopping, and multiple muons, PDFs for l_l , Q_μ , and Q_{res} used to calculate $\mathcal{L}_{\text{spall}}$ change depending on the values of dt (0–0.05 s, 0.05–0.5 s, 0.5–60 s) and l_t (0–300 cm, 300–1,000 cm, 1,000–5,000 cm). Figure 6.8 shows the PDFs of the muon spallation sample and the random sample for single-through going muons (dt : 0–0.05 s, l_t : 0–300 cm). These PDFs are clearly different between muon spallation samples and random samples. Details about how to make PDFs are summarized in Ref. [36].

$\mathcal{L}_{\text{spall}}$ is calculated for all muons in time region from -60 s to 60 s with the SHE-triggered event as 0 s. If just one value of $\mathcal{L}_{\text{spall}}$ exceeds the cut criterion, the SHE-triggered event is removed. Cut criteria of $\mathcal{L}_{\text{spall}}$ depend on muon type and E_{vis} . For single-through going and multiple muons, the cut criteria change depending on dt and l_t . Cut criteria of spallation likelihood cut for each muon type are summarized

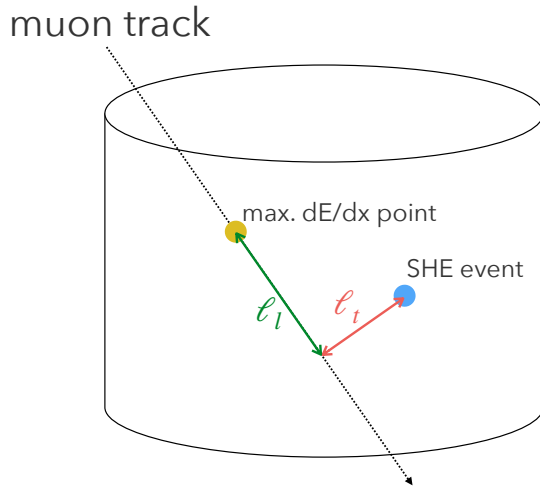


Figure 6.6: Definition of l_t and l_l used in the spallation likelihood cut [36].

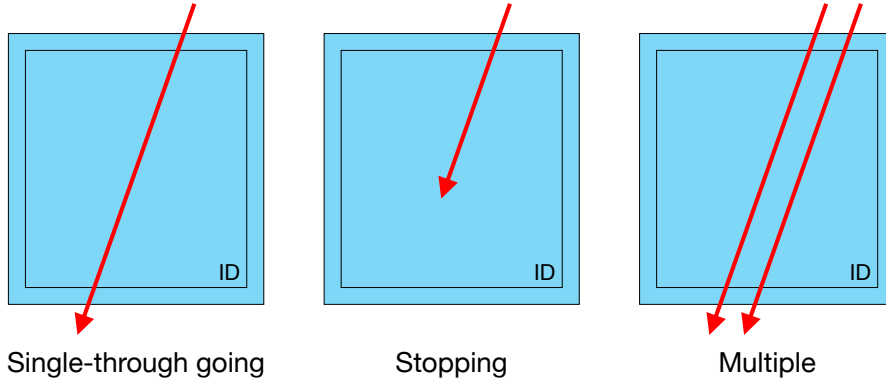


Figure 6.7: Schematic view of a single-through going muon, a stopping muon, and multiple muons.

in Table 6.3 to Table 6.6. Figure 6.9 shows the $\mathcal{L}_{\text{spall}}$ distributions when E_{vis} is between 7.49 MeV and 9.49 MeV.

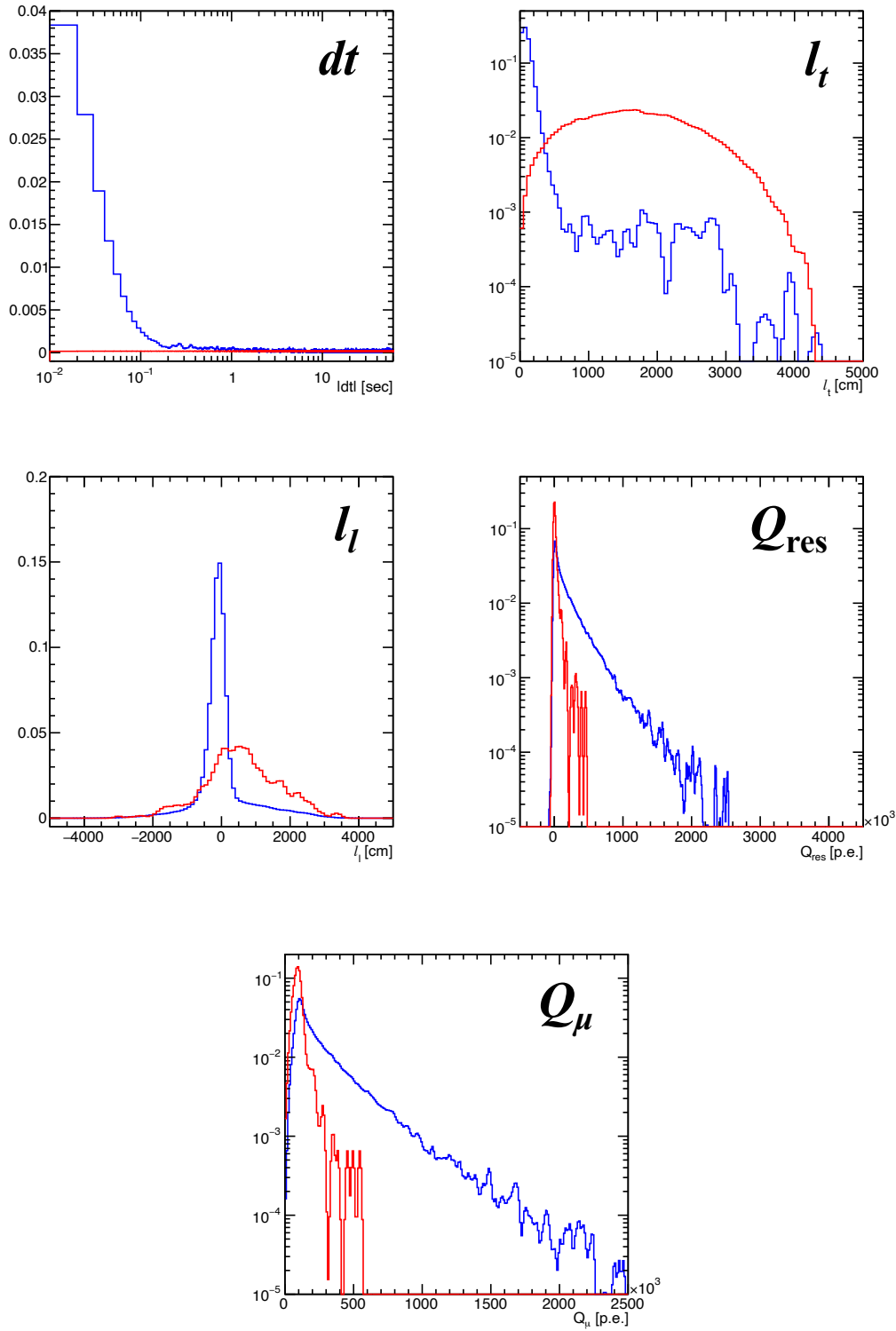


Figure 6.8: PDFs of the muon spallation sample (blue line) and the random sample (red line) for single-through going muons (dt : 0–0.05 s, l_t : 0–300 cm) [36].

Table 6.3: Cut criteria of spallation likelihood cut for single-through going muons. $\mathcal{L}_{\text{spall}}$ distributions are shown in Figure 6.9.

E_{vis} (MeV)	7.49–9.49	9.49–11.49	11.49–13.49	13.49–15.49
dt : 0–0.05 s	$\mathcal{L}_{\text{spall}} > 15.5$	$\mathcal{L}_{\text{spall}} > 18$	$\mathcal{L}_{\text{spall}} > 17.5$	$\mathcal{L}_{\text{spall}} > 17.5$
dt : 0.05–0.5 s	$\mathcal{L}_{\text{spall}} > 17$	$\mathcal{L}_{\text{spall}} > 18$	$\mathcal{L}_{\text{spall}} > 18.5$	$\mathcal{L}_{\text{spall}} > 18$
dt : 0.5–30 s	$\mathcal{L}_{\text{spall}} > 18.5$	$\mathcal{L}_{\text{spall}} > 16.5$	$\mathcal{L}_{\text{spall}} > 20.5$	$\mathcal{L}_{\text{spall}} > 23.5$
l_t : 0–200 cm	$\mathcal{L}_{\text{spall}} > 2.25$	$\mathcal{L}_{\text{spall}} > 4.5$	$\mathcal{L}_{\text{spall}} > 8.5$	$\mathcal{L}_{\text{spall}} > 12.5$
l_t : 200–300 cm	$\mathcal{L}_{\text{spall}} > 4.25$	$\mathcal{L}_{\text{spall}} > 6.5$	$\mathcal{L}_{\text{spall}} > 11$	$\mathcal{L}_{\text{spall}} > 17.5$
l_t : 300–500 cm	$\mathcal{L}_{\text{spall}} > 5.25$	$\mathcal{L}_{\text{spall}} > 7$	$\mathcal{L}_{\text{spall}} > 13.5$	$\mathcal{L}_{\text{spall}} > 18.5$
l_t : 500–1,000 cm	$\mathcal{L}_{\text{spall}} > 10.75$	$\mathcal{L}_{\text{spall}} > 10.5$	$\mathcal{L}_{\text{spall}} > 15.5$	$\mathcal{L}_{\text{spall}} > 19$
l_t : 1,000–5,000 cm	$\mathcal{L}_{\text{spall}} > 10.25$	$\mathcal{L}_{\text{spall}} > 12.5$	$\mathcal{L}_{\text{spall}} > 16$	$\mathcal{L}_{\text{spall}} > 20$

E_{vis} (MeV)	15.49–17.49	17.49–19.49	19.49–23.49
dt : 0–0.05 s	$\mathcal{L}_{\text{spall}} > 19$	$\mathcal{L}_{\text{spall}} > 19$	$\mathcal{L}_{\text{spall}} > 20.5$
dt : 0.05–0.5 s	$\mathcal{L}_{\text{spall}} > 21$	$\mathcal{L}_{\text{spall}} > 15.5$	$\mathcal{L}_{\text{spall}} > 17$
dt : 0.5–30 s	$\mathcal{L}_{\text{spall}} > 23.5$	$\mathcal{L}_{\text{spall}} > 23.5$	$\mathcal{L}_{\text{spall}} > 21.5$
l_t : 0–200 cm	$\mathcal{L}_{\text{spall}} > 12$	$\mathcal{L}_{\text{spall}} > 15.75$	$\mathcal{L}_{\text{spall}} > 18.75$
l_t : 200–300 cm	$\mathcal{L}_{\text{spall}} > 12$	$\mathcal{L}_{\text{spall}} > 13.25$	$\mathcal{L}_{\text{spall}} > 17.75$
l_t : 300–500 cm	$\mathcal{L}_{\text{spall}} > 13.5$	$\mathcal{L}_{\text{spall}} > 11.25$	$\mathcal{L}_{\text{spall}} > 15.75$
l_t : 500–1,000 cm	$\mathcal{L}_{\text{spall}} > 12.5$	$\mathcal{L}_{\text{spall}} > 14.75$	$\mathcal{L}_{\text{spall}} > 14.25$
l_t : 1,000–5,000 cm	$\mathcal{L}_{\text{spall}} > 16$	$\mathcal{L}_{\text{spall}} > 11.75$	$\mathcal{L}_{\text{spall}} > 16.75$

Table 6.4: Cut criteria of spallation likelihood cut for stopping muons. $\mathcal{L}_{\text{spall}}$ distributions are shown in Figure 6.9.

E_{vis} (MeV)	7.49–9.49	9.49–11.49	11.49–13.49	13.49–15.49
	$\mathcal{L}_{\text{spall}} > 1.5$	$\mathcal{L}_{\text{spall}} > 3.5$	$\mathcal{L}_{\text{spall}} > 2.5$	$\mathcal{L}_{\text{spall}} > 4$

E_{vis} (MeV)	15.49–17.49	17.49–19.49	19.49–23.49
	$\mathcal{L}_{\text{spall}} > 4.5$	$\mathcal{L}_{\text{spall}} > 3$	$\mathcal{L}_{\text{spall}} > 2.5$

Table 6.5: Cut criteria of spallation likelihood cut for multiple muons. $\mathcal{L}_{\text{spall}}$ distributions are shown in Figure 6.9.

E_{vis} (MeV)	7.49–9.49	9.49–11.49	11.49–13.49	13.49–15.49
dt : 0–0.05 s	$\mathcal{L}_{\text{spall}} > 13$	$\mathcal{L}_{\text{spall}} > 14$	$\mathcal{L}_{\text{spall}} > 13$	$\mathcal{L}_{\text{spall}} > 13$
dt : 0.05–0.5 s	$\mathcal{L}_{\text{spall}} > 17$	$\mathcal{L}_{\text{spall}} > 17$	$\mathcal{L}_{\text{spall}} > 18$	$\mathcal{L}_{\text{spall}} > 20$
dt : 0.5–30 s	$\mathcal{L}_{\text{spall}} > 19$	$\mathcal{L}_{\text{spall}} > 22$	$\mathcal{L}_{\text{spall}} > 24$	$\mathcal{L}_{\text{spall}} > 31$
l_t : 0–100 cm	$\mathcal{L}_{\text{spall}} > 2.25$	$\mathcal{L}_{\text{spall}} > 2.5$	$\mathcal{L}_{\text{spall}} > 8$	$\mathcal{L}_{\text{spall}} > 16$
l_t : 100–200 cm	$\mathcal{L}_{\text{spall}} > 5.25$	$\mathcal{L}_{\text{spall}} > 7$	$\mathcal{L}_{\text{spall}} > 11$	$\mathcal{L}_{\text{spall}} > 16.5$
l_t : 200–300 cm	$\mathcal{L}_{\text{spall}} > 5.75$	$\mathcal{L}_{\text{spall}} > 6.5$	$\mathcal{L}_{\text{spall}} > 13$	$\mathcal{L}_{\text{spall}} > 16.5$
l_t : 300–500 cm	$\mathcal{L}_{\text{spall}} > 4.75$	$\mathcal{L}_{\text{spall}} > 6.5$	$\mathcal{L}_{\text{spall}} > 12.5$	$\mathcal{L}_{\text{spall}} > 17$
l_t : 500–700 cm	$\mathcal{L}_{\text{spall}} > 4.75$	$\mathcal{L}_{\text{spall}} > 7$	$\mathcal{L}_{\text{spall}} > 12$	$\mathcal{L}_{\text{spall}} > 17$
l_t : 700–1,000 cm	$\mathcal{L}_{\text{spall}} > 4.75$	$\mathcal{L}_{\text{spall}} > 6.5$	$\mathcal{L}_{\text{spall}} > 11.5$	$\mathcal{L}_{\text{spall}} > 17$
l_t : 1,000–2,000 cm	$\mathcal{L}_{\text{spall}} > 6.75$	$\mathcal{L}_{\text{spall}} > 9.5$	$\mathcal{L}_{\text{spall}} > 13.5$	$\mathcal{L}_{\text{spall}} > 19$

E_{vis} (MeV)	15.49–17.49	17.49–19.49	19.49–23.49
dt : 0–0.05 s	$\mathcal{L}_{\text{spall}} > 15$	$\mathcal{L}_{\text{spall}} > 18$	$\mathcal{L}_{\text{spall}} > 23$
dt : 0.05–0.5 s	$\mathcal{L}_{\text{spall}} > 20$	$\mathcal{L}_{\text{spall}} > 23$	$\mathcal{L}_{\text{spall}} > 19$
dt : 0.5–30 s	$\mathcal{L}_{\text{spall}} > 28$	$\mathcal{L}_{\text{spall}} > 29$	$\mathcal{L}_{\text{spall}} > 26$
l_t : 0–100 cm	$\mathcal{L}_{\text{spall}} > 11$	$\mathcal{L}_{\text{spall}} > 6.75$	$\mathcal{L}_{\text{spall}} > 20.75$
l_t : 100–200 cm	$\mathcal{L}_{\text{spall}} > 14.5$	$\mathcal{L}_{\text{spall}} > 13.25$	$\mathcal{L}_{\text{spall}} > 17.75$
l_t : 200–300 cm	$\mathcal{L}_{\text{spall}} > 15.5$	$\mathcal{L}_{\text{spall}} > 8.75$	$\mathcal{L}_{\text{spall}} > 8.25$
l_t : 300–500 cm	$\mathcal{L}_{\text{spall}} > 14$	$\mathcal{L}_{\text{spall}} > 12.25$	$\mathcal{L}_{\text{spall}} > 10.25$
l_t : 500–700 cm	$\mathcal{L}_{\text{spall}} > 13$	$\mathcal{L}_{\text{spall}} > 16.75$	$\mathcal{L}_{\text{spall}} > 14.75$
l_t : 700–1,000 cm	$\mathcal{L}_{\text{spall}} > 12$	$\mathcal{L}_{\text{spall}} > 16.25$	$\mathcal{L}_{\text{spall}} > 13.25$
l_t : 1,000–2,000 cm	$\mathcal{L}_{\text{spall}} > 16.5$	$\mathcal{L}_{\text{spall}} > 13.25$	$\mathcal{L}_{\text{spall}} > 11.75$

Table 6.6: Cut criteria of spallation likelihood cut for misfit muons. $\mathcal{L}_{\text{spall}}$ distributions are shown in Figure 6.9.

E_{vis} (MeV)	7.49–9.49	9.49–11.49	11.49–13.49	13.49–15.49
	$\mathcal{L}_{\text{spall}} > 3$	$\mathcal{L}_{\text{spall}} > 3$	$\mathcal{L}_{\text{spall}} > 2.5$	$\mathcal{L}_{\text{spall}} > 2$

E_{vis} (MeV)	15.49–17.49	17.49–19.49	19.49–23.49
	$\mathcal{L}_{\text{spall}} > 3$	$\mathcal{L}_{\text{spall}} > 2$	$\mathcal{L}_{\text{spall}} > 2$

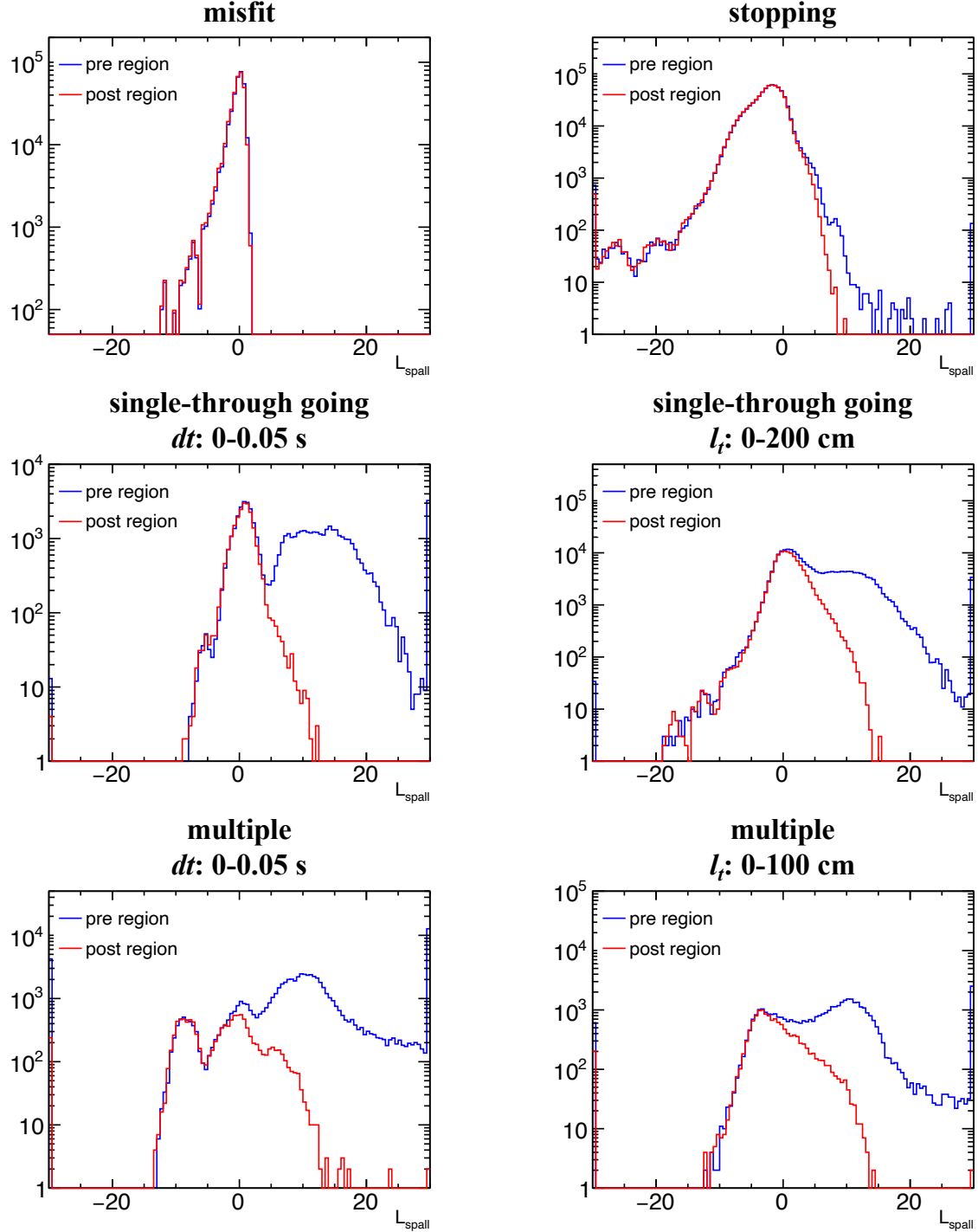


Figure 6.9: L_{spall} distributions (E_{vis} : 7.49–9.49 MeV) [36]. Blue lines show muons in pre-region (time region from -60 s to 0 s with the SHE-triggered event as 0 s). Red lines show muons in post-region (time region from 0 s to 60 s with the SHE-triggered event as 0 s).

6.2.5 Spallation box cut

When E_{vis} exceeds 15.49 MeV, it is difficult to accurately optimize the spallation likelihood cut criteria because of the small statistics of muon spallation sample. Therefore, the cut criteria summarized in Table 6.7 are applied to SHE-triggered events primarily above 15.49 MeV. In Table 6.7, g_μ is the muon reconstruction goodness. Details of the muon event reconstruction are summarized in Ref. [36].

Table 6.7: Cut criteria of spallation box cut [36].

E_{vis} (MeV)	Muon type	Cut criteria
7.49–23.49	-	$dt < 0.1 \text{ s}$ and $l_t < 400 \text{ cm}$
15.49–19.49	misfit	$dt < 1.5 \text{ s}$
15.49–17.49	single	$g_\mu \geq 0.4$ and $dt < 7 \text{ s}$ and $l_t < 150 \text{ cm}$
15.49–17.49	stopping	$g_\mu < 0.3$ and $dt < 6 \text{ s}$
15.49–19.49	stopping	$dt < 0.05 \text{ s}$
15.49–19.49	multiple	$dt < 0.05 \text{ s}$

6.2.6 Spallation cut efficiency

The expected number of events except for spallation events is scaled by using the spallation cut efficiency for random events $\varepsilon_{\text{random}}$, which is equivalent to the signal efficiency after the spallation cut. Moreover, the expected number of spallation events is scaled by using the spallation cut efficiency for ${}^9\text{Li}$ events $\varepsilon_{{}^9\text{Li}}$. Table 6.8 shows the spallation cut efficiency for random and ${}^9\text{Li}$ events. Details about how to estimate these efficiencies are summarized in Ref. [36].

Table 6.8: Spallation cut efficiency for random and ${}^9\text{Li}$ events.

E_{vis} (MeV)	$\varepsilon_{\text{random}}$	$\varepsilon_{{}^9\text{Li}}$
7.49–9.49	51.8%	3.4%
9.49–11.49	78.2%	5.0%
11.49–13.49	86.0%	5.9%
13.49–15.49	93.1%	5.5%
15.49–17.49	73.4%	0.0%
17.49–19.49	81.8%	0.0%
19.49–23.49	86.1%	0.0%
23.49–29.49	96.1%	0.0%

6.3 Third reduction

6.3.1 Effective wall distance cut

Remaining radioactive backgrounds around the detector wall are removed using the effective wall distance (d_{eff}). The definition of d_{eff} is shown in Figure 6.10, and the following cut criteria are applied to candidate events.

$$d_{\text{eff}} < \begin{cases} 500 \text{ cm} & (7.49 \text{ MeV} < E_{\text{vis}} < 15.49 \text{ MeV}) \\ 500 - 50 \times (E_{\text{vis}} - 15.49) \text{ cm} & (15.49 \text{ MeV} < E_{\text{vis}} < 19.49 \text{ MeV}) \\ 300 \text{ cm} & (19.49 \text{ MeV} < E_{\text{vis}} < 29.49 \text{ MeV}) \end{cases} \quad (6.4)$$

d_{eff} distributions are shown in Figure B.14, Figure B.15, and Figure B.16.

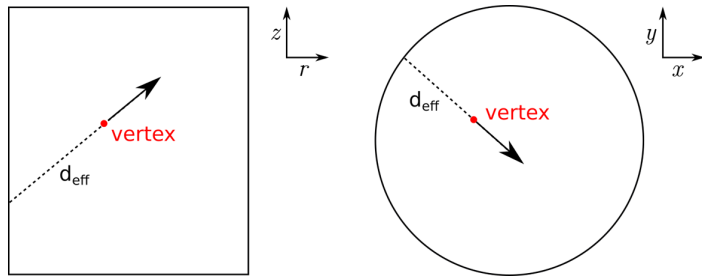


Figure 6.10: Definition of d_{eff} [22].

6.3.2 Pre-activity cut and post-activity cut

As shown in Figure 6.11, when a visible muon decays into an electron, or when de-excitation gamma-rays and an invisible muon are generated, the event may have two hit peaks within the time window of $[-5, 35] \mu\text{s}$. These events are removed by using the information of hit peaks before or after the main hit peak. To remove events with hit peaks before the main hit peak, the TOF-subtracted time window of $[-5 \mu\text{s}, -12 \text{ ns}]$ from the main peak is scanned using a TOF-subtracted 15 ns time window to search the hit clusters. When the maximal number of hits in a TOF-subtracted 15 ns time window is greater than 11, the event is removed. Moreover, to remove events with hit peaks after the main hit peak, the number of decay electrons within $35 \mu\text{s}$ from the main hit peak ($N_{\text{decay-e}}$) is searched using an algorithm used in previous SK analyses [10]. When $N_{\text{decay-e}}$ is greater or equal to 1, the event is removed. $N_{\text{decay-e}}$ distributions are shown in Figure B.17, Figure B.18, and Figure B.19.

6.3.3 Ring cleanliness cut

Cherenkov rings caused by electrons and gamma-rays become fuzzy due to the electromagnetic shower, while Cherenkov rings caused by muons and pions become clear. Events with visible muons and pions are removed by using the ring cleanliness (L_{cle}).

Here, the calculation method of L_{cle} is described. To calculate the L_{cle} , PMT hits of the main hit peak

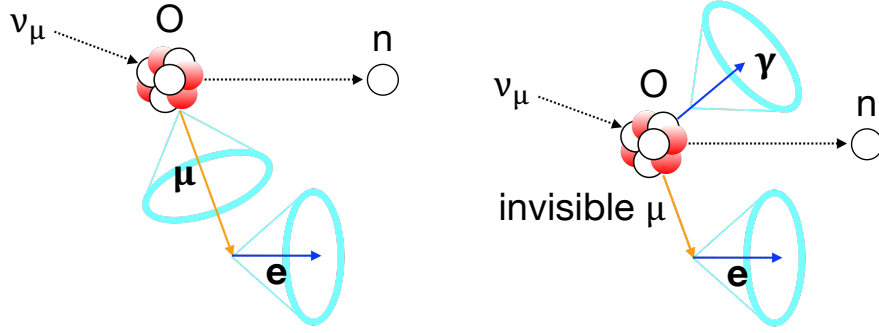


Figure 6.11: Schematic view of atmospheric neutrino events with two hit peaks.

in a TOF-subtracted 15 ns time window are used. Given a reconstructed vertex, a combination of three hits uniquely determines a cone and the opening angle θ . In Figure 6.12,

$$\begin{aligned}\sin \theta &= R \\ \theta &= \sin^{-1} R,\end{aligned}\quad (6.5)$$

and from the law of sines,

$$\begin{aligned}\frac{a}{\sin A} &= 2R \\ R &= \frac{a}{2 \sin A} \\ &= \frac{a}{2\sqrt{1 - \cos^2 A}} \\ &= \frac{a}{2\sqrt{1 - \frac{2b^2c^2 - 2a^2b^2 - 2c^2a^2 + a^4 + b^4 + c^4}{4b^2c^2}}} \left(\because \cos A = \frac{b^2 + c^2 - a^2}{2bc} \right) \\ &= \frac{abc}{\sqrt{4b^2c^2 - (2b^2c^2 - 2a^2b^2 - 2c^2a^2 + a^4 + b^4 + c^4)}} \\ &= \frac{abc}{\sqrt{2(a^2b^2 + b^2c^2 + c^2a^2) - (a^4 + b^4 + c^4)}}.\end{aligned}\quad (6.6)$$

Therefore, from Equation (6.5) and Equation (6.6), θ is

$$\theta = \sin^{-1} \left\{ \frac{abc}{\sqrt{2(a^2b^2 + b^2c^2 + c^2a^2) - (a^4 + b^4 + c^4)}} \right\}. \quad (6.7)$$

Then, θ for all combinations are filled in a histogram to determine the bin with most entries (bin_{most}). One example of the histogram of θ for all three hits combinations and the hit map is shown in Figure 6.13. Finally, L_{cle} is calculated as

$$L_{\text{cle}} = \frac{N_{5 \text{ bins}}}{N_{19 \text{ bins}}}, \quad (6.8)$$

where $N_{5 \text{ bins}}$ ($N_{19 \text{ bins}}$) shows the number of entries in five (nineteen) adjacent bins centered on bin_{most} . In Figure 6.13, filled region (dotted line region) shows the five (nineteen) adjacent bins centered on bin_{most} .

Events with visible muons and pions tend to have the large L_{cle} . In this study, events that L_{cle} is greater than 0.36 are removed. L_{cle} distributions are shown in Figure B.20, Figure B.21, and Figure B.22.

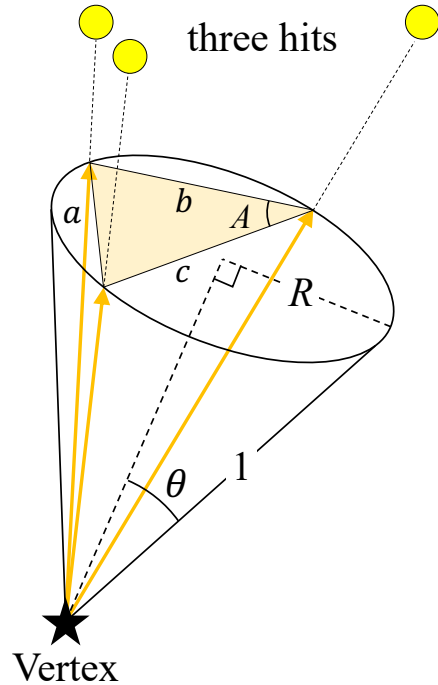


Figure 6.12: Definition of θ .

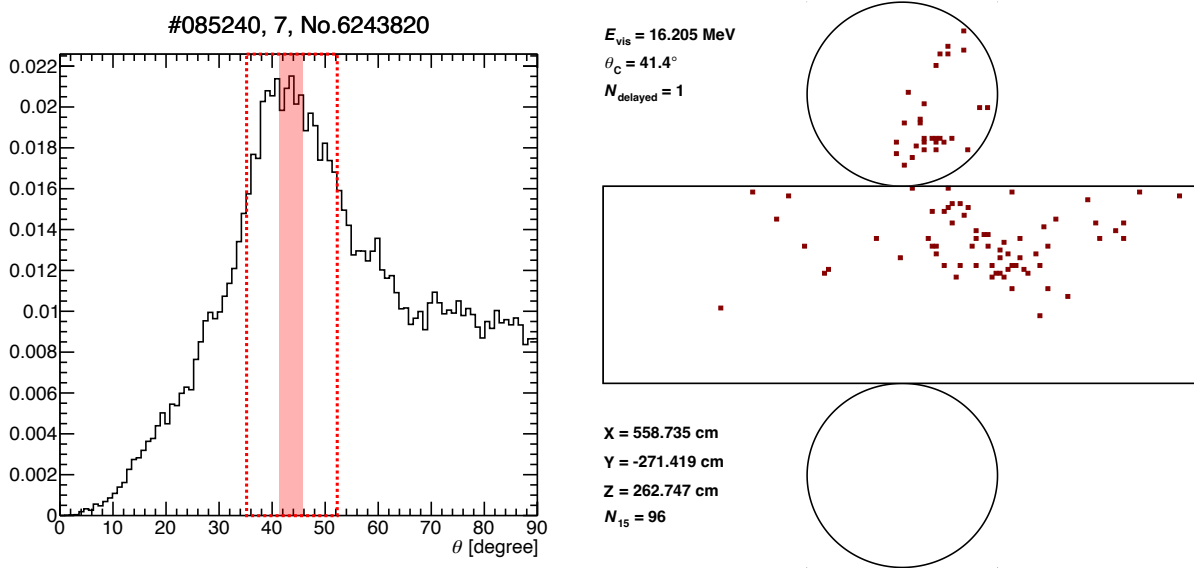


Figure 6.13: Histogram of θ for all three hits combinations (left) and the hit map (right). In the histogram, filled region (dotted line region) shows the five (nineteen) adjacent bins centered on the bin with most entries (bin_{most}). In the right figure, top circle, center rectangle, and bottom circle show the SK top, barrel, and bottom, respectively. θ_C is the reconstructed Cherenkov angle of the prompt signal (described in Section 6.4), N_{delayed} is the number of delayed signals per event (described in Section 6.4), X , Y , and Z are the reconstructed vertices, and N_{15} is the number of hits in a TOF-subtracted 15 ns time window. In this case, the total number of entries in the histogram is $N_{15} C_3 = 96 C_3 = 142,880$. Note that this histogram is normalized.

6.3.4 Charge over hit cut

As described in Section 6.3.3, Cherenkov rings caused by muons and pions become clear, and more charge is deposited on a single PMT compared to electrons. Events with visible muons and pions are further removed by using the ratio of charge to the number of hits in a TOF-subtracted 50 ns time window centered on the main hit peak (Q_{50}/N_{50}). Events with visible muons and pions tend to have the large Q_{50}/N_{50} . In this study, events that Q_{50}/N_{50} is greater than 2 are removed. Q_{50}/N_{50} distributions are shown in Figure B.23, Figure B.24, and Figure B.25.

6.4 Cherenkov angle cut and neutron tagging

Finally, we select NCQE events using the reconstructed Cherenkov angle of the prompt signal (θ_C) and the number of delayed signals per event (N_{delayed}).

6.4.1 Reconstructed Cherenkov angle of the prompt signal

θ_C is calculated using the histogram of θ for all three hits combinations described in Section 6.3.3. In the histogram, the seven adjacent bins with most entries are determined, and the upper border of the center bin is taken as θ_C (see Figure 6.14).

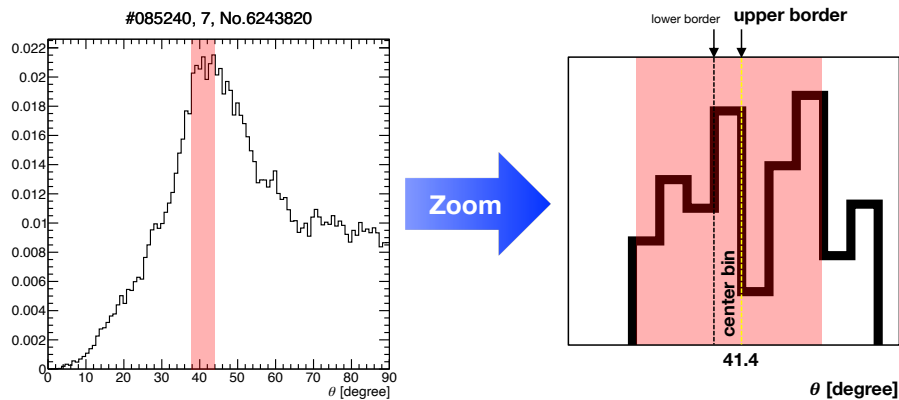


Figure 6.14: Histogram of θ for all three hits combinations. This histogram is the same as the histogram shown in Figure 6.13. Filled region shows the seven adjacent bins with most entries, and in this case θ_C is taken to be 41.4 degrees.

6.4.2 Number of delayed signals per event

Here, the neutron tagging method is explained. Figure 6.15 shows the schematic view of neutron candidate search. First, neutron candidates are searched by 25 PMT hits/200 ns trigger in the region of [4, 535] μ s from the prompt signal. Then all neutron candidates are reconstructed, and delayed signals from neutron capture on Gd are selected based on the following selection criteria.

- Distance from the ID wall is larger than 2 m

- Timing is after $4 \mu\text{s}$ from the prompt signal
- $g_{\text{vtx}} > 0.4$ and $g_{\text{dir}} < 0.4$
- $E_{\text{vis}} > 2.99 \text{ MeV}$
- Distance from the prompt vertex is smaller than 3 m

N_{delayed} is the number of delayed signals that satisfy the above selection criteria.

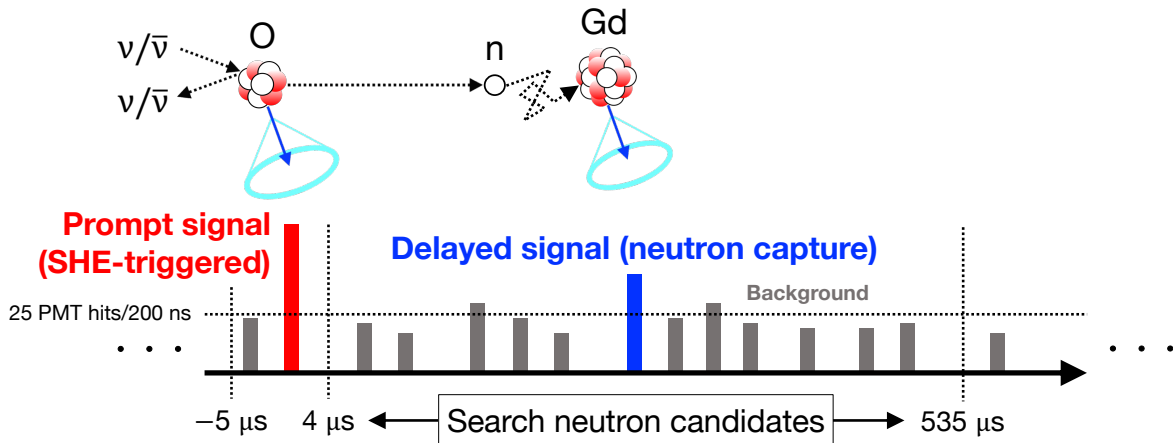


Figure 6.15: Schematic view of neutron candidate search.

6.4.3 Difference between this study and the DSNB search in SK-VI

The difference between this study and the DSNB search in SK-VI [40] is the cut criteria of θ_C and N_{delayed} . In IBD events, only one relativistic positron and one neutron are emitted (see Figure 1.6). Therefore, θ_C and N_{delayed} tend to be about 42 degrees and one, respectively. While, in an NCQE event, multiple gamma-rays and multiple neutrons are easily emitted (see Figure 1.8). When multiple gamma-rays are emitted, θ_C tends to be larger because of the uniform distribution of the hit PMTs. Therefore, in this study, we select the events that θ_C is greater than 50 degrees and N_{delayed} is greater or equal to one. The cut criteria of θ_C and N_{delayed} are the same as the study in SK pure water phase [50]. θ_C distributions are shown in Figure B.26, Figure B.27, and Figure B.28. Moreover, N_{delayed} distributions are shown in Figure B.32, Figure B.33, and Figure B.34.

6.5 Observed and expected number of events

After applying all event selections to 552.2 days of SK-VI data, 38 events remain. Figure 6.16 shows the vertex distribution of prompt signals and delayed signals for the data. From this figure, we confirmed that these events are uniformly distributed.

The expected number of events in each secondary interaction model estimated by the simulation are summarized in Table 6.9. After applying all event selections, NCQE and NC non-QE events account for about 60% and about 30% of total events, respectively. Note that the number of DSNB events predicted by the Horiuchi + 09 model [28], which is not used in this study, is 0.0854. Moreover, the number of

atmospheric neutrino events is larger in BERT than other two models. The difference of the number of atmospheric neutrino events comes from the number of de-excitation gamma-rays and neutrons by secondary interactions (see Section 7).

Figure 6.17, Figure 6.18, and Figure 6.19 show the distributions of θ_C , E_{vis} , and N_{delayed} in BERT, respectively. From these figures, we can see that the tendency of distribution is similar between NCQE and NC non-QE events.

The NCQE cumulative signal efficiencies as a function of E_{vis} are shown in Figure 6.20. Moreover, the NCQE cumulative signal efficiencies at each event reduction are summarized in Table 6.10. Signal efficiencies of θ_C cut and N_{delayed} cut increase as E_{vis} increases. This means that E_{vis} is correlated to the number of de-excitation gamma-rays and neutrons by secondary interactions. Other distributions related to this section are summarized in Appendix B.2.

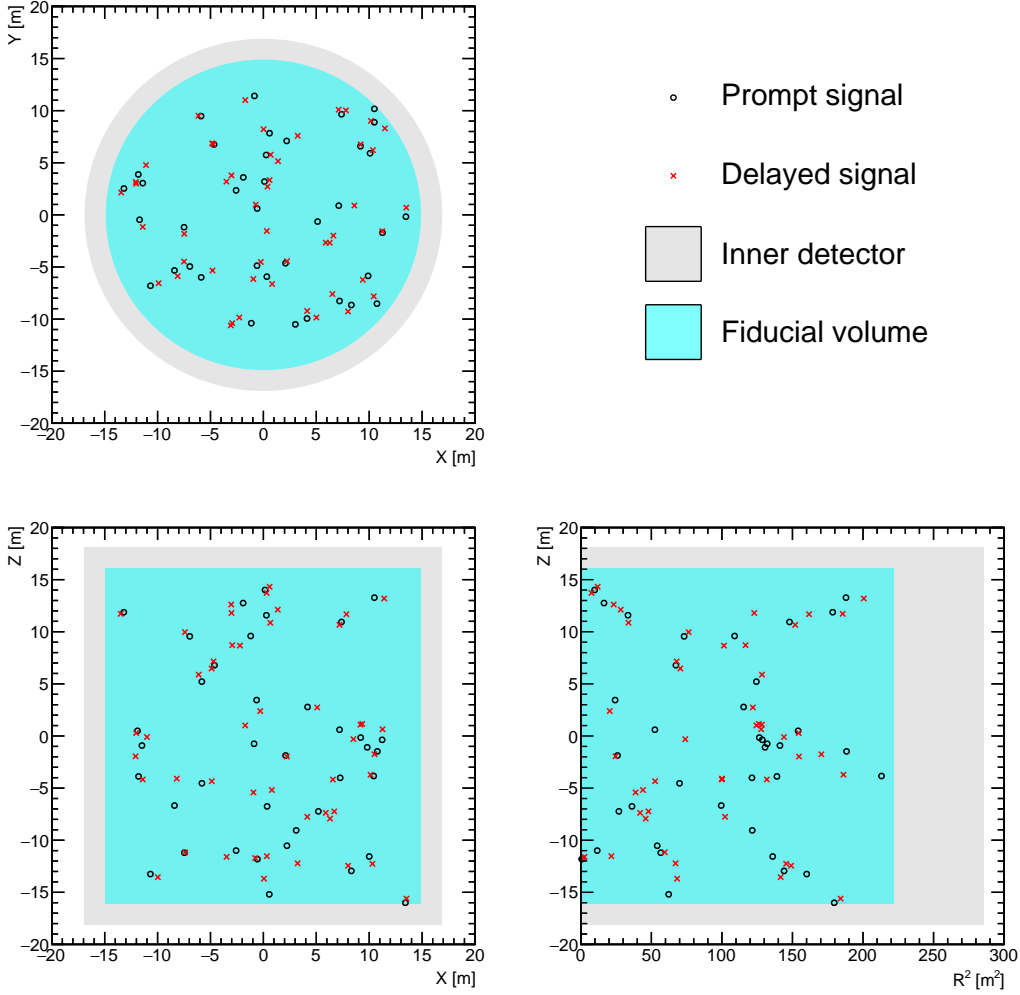


Figure 6.16: Vertex distribution of prompt signals and delayed signals for the data.

Table 6.9: The expected number of events in each secondary interaction model. The fractions are summarized in parentheses. The expected number of spallation, reactor neutrino, and accidental coincidence events, which are calculated by the same method as Ref. [40], are common to each model.

	BERT	BIC	INCL++
Total	45.8991	33.6573	33.9739
NCQE	28.7071 (62.5%)	19.8420 (59.0%)	20.2027 (59.5%)
NC non-QE	13.2721 (28.9%)	10.1887 (30.3%)	10.0517 (29.6%)
CC	1.4177 (3.1%)	1.1244 (3.3%)	1.2173 (3.6%)
Spallation	0.8879 (1.9%)	0.8879 (2.6%)	0.8879 (2.6%)
Reactor neutrino	0.0619 (0.1%)	0.0619 (0.2%)	0.0619 (0.2%)
Accidental coincidence	1.5524 (3.4%)	1.5524 (4.6%)	1.5524 (4.6%)

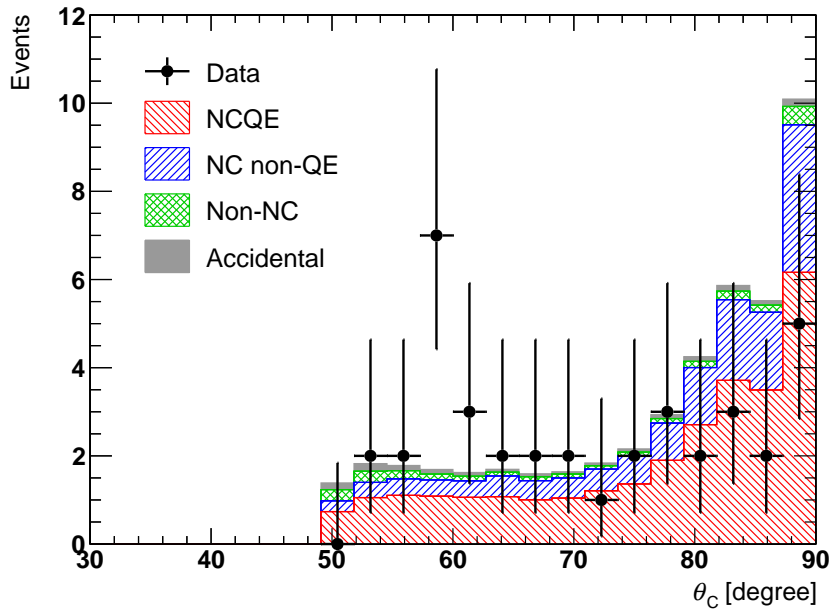


Figure 6.17: θ_C distribution in BERT. Non-NC includes CC, spallation, and reactor neutrino events. In this distribution, E_{vis} is between 7.49 MeV and 29.49 MeV and N_{delayed} is greater or equal to one.

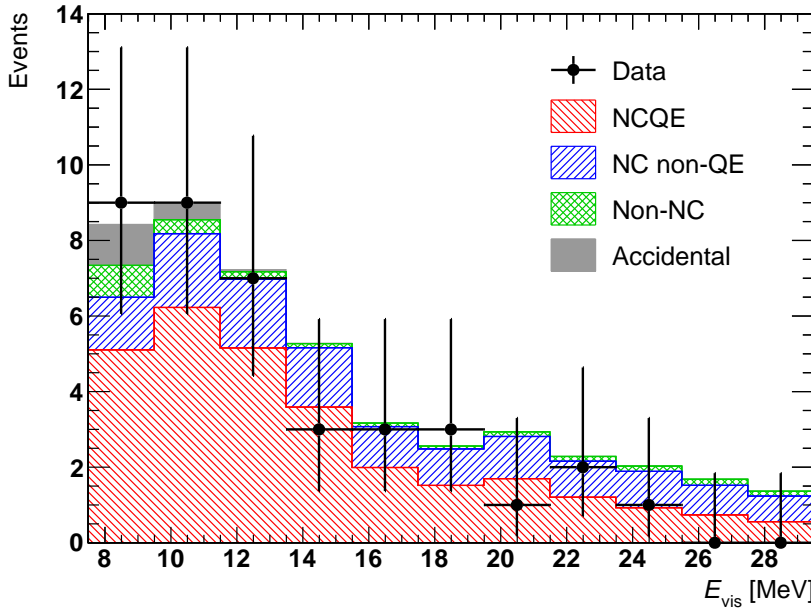


Figure 6.18: E_{vis} distribution in BERT. Non-NC includes CC, spallation, and reactor neutrino events. In this distribution, θ_C is greater than 50 degrees and N_{delayed} is greater or equal to one.

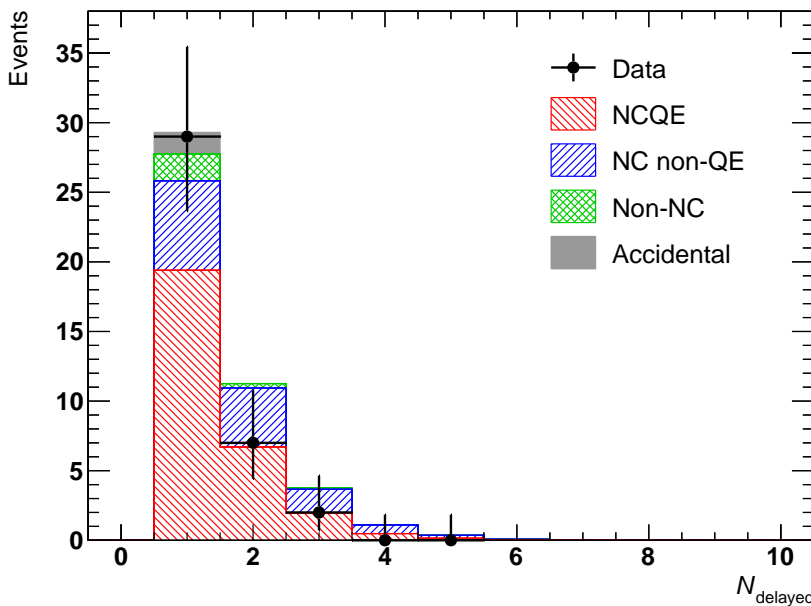


Figure 6.19: N_{delayed} distribution in BERT. Non-NC includes CC, spallation, and reactor neutrino events. In this distribution, θ_C is greater than 50 degrees and E_{vis} is between 7.49 MeV and 29.49 MeV.

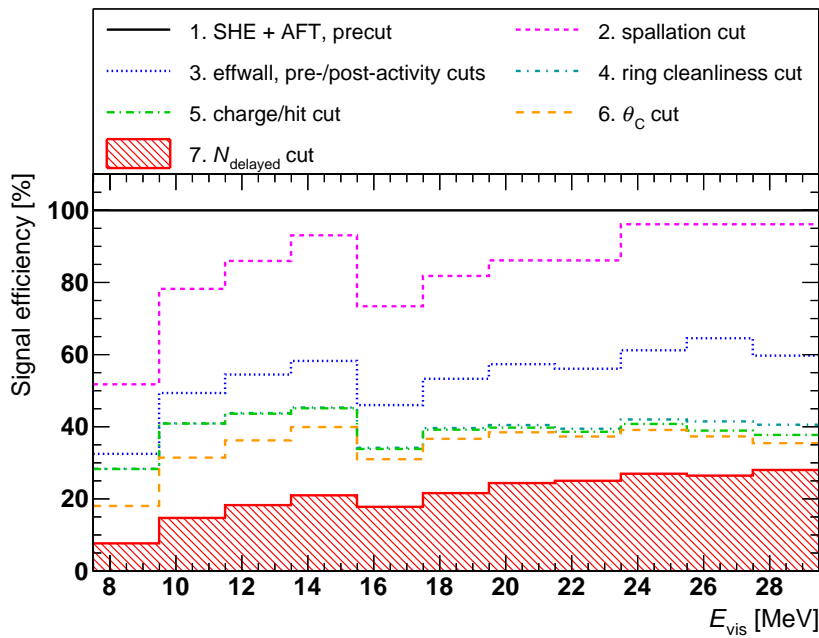


Figure 6.20: NCQE cumulative signal efficiencies as a function of E_{vis} . Event reductions are performed in the order shown in the legend, and before the reduction for spallation events is taken as 100%.

Table 6.10: NCQE cumulative signal efficiencies at each event reduction.

E_{vis} (MeV)	7.49–9.49	9.49–11.49	11.49–13.49	13.49–15.49
Spallation cut	51.8%	78.2%	86.0%	93.1%
d_{eff} cut	91.6%	92.2%	92.7%	92.4%
Pre-activity cut	99.5%	99.4%	99.2%	98.6%
Post-activity cut	68.8%	68.8%	68.9%	68.7%
L_{cle} cut	87.2%	83.0%	80.4%	77.8%
Q_{50}/N_{50} cut	99.8%	99.8%	99.6%	99.5%
θ_{C} cut	63.8%	76.9%	83.0%	88.5%
N_{delayed} cut	42.5%	46.8%	50.5%	52.6%
All cuts	7.7%	14.7%	18.3%	21.0%

E_{vis} (MeV)	15.49–17.49	17.49–19.49	19.49–21.49	21.49–23.49
Spallation cut	73.4%	81.8%	86.1%	86.1%
d_{eff} cut	93.6%	96.7%	98.6%	99.2%
Pre-activity cut	98.0%	97.2%	96.7%	95.6%
Post-activity cut	68.3%	69.3%	69.9%	68.7%
L_{cle} cut	74.3%	74.4%	70.6%	70.3%
Q_{50}/N_{50} cut	99.1%	98.9%	98.2%	97.9%
θ_{C} cut	91.6%	93.5%	96.8%	96.6%
N_{delayed} cut	57.4%	58.9%	63.4%	67.1%
All cuts	17.8%	21.6%	24.4%	25.0%

E_{vis} (MeV)	23.49–25.49	25.49–27.49	27.49–29.49	7.49–29.49
Spallation cut	96.1%	96.1%	96.1%	72.6%
d_{eff} cut	98.6%	98.7%	98.6%	93.3%
Pre-activity cut	94.8%	95.1%	91.9%	98.6%
Post-activity cut	68.1%	71.5%	68.6%	68.9%
L_{cle} cut	68.7%	64.3%	67.9%	80.2%
Q_{50}/N_{50} cut	97.0%	93.9%	93.0%	99.3%
θ_{C} cut	95.9%	95.9%	93.9%	79.3%
N_{delayed} cut	69.0%	70.9%	79.1%	51.3%
All cuts	27.0%	26.4%	28.0%	14.9%

7 Comparison of secondary interaction models

In Ref. [48, 49], it was found that agreements of the secondary interaction model based on BERT remain poor and result in significant systematic uncertainty as described in Section 1.6. Therefore, I compare the observed data with the other secondary interaction models using the newly developed Geant4-based SK detector simulation. Here, we use three secondary interaction models: BERT, BIC, and INCL++. Before showing the results of comparing the observed data with these models, features of each model are described in Section 7.1.

7.1 Features of secondary interaction models

Here, we confirmed some MC true information such as the number of neutrons, the number of gamma-rays, and energy of gamma-rays, using 500 years of atmospheric neutrino NCQE events in the SK fiducial volume. Figure 7.1 shows the number of generated neutrons per process after primary interactions (see Figure 1.8). In this figure, others include inelastic scattering reactions by the long-lived neutral kaon (K_L^0), 2H , 3H , and 3He and electron-nuclear interactions. From this figure, we can confirm that most of neutrons are generated by neutron inelastic scattering reactions. The number of neutrons generated by each process is summarized in top of Table 7.1. From this table, we can confirm that the number of neutrons generated by neutron inelastic scattering reactions is largely different among secondary interaction models. The number of neutrons is largest in BERT while smallest in INCL++.

Figure 7.2, Figure 7.3, and Figure 7.4 shows the number of neutrons generated after primary interactions, the total number of neutrons (sum of neutrons generated by primary interactions (hereafter referred to as “primary neutrons”) and neutrons generated after primary interactions), and the number of neutron captures, respectively. From these figures, we can confirm that more neutrons are generated and captured in BERT than other two models. The total number of neutrons and neutron captures are summarized in center of Table 7.1. In this table, the number of primary neutrons is common among secondary interaction models (see Figure B.4). Moreover, the number of neutron captures is smaller than the total number of neutrons. The reason is that two stable nuclei are generated by neutron inelastic scattering reaction with oxygen nucleus. For example, the following reaction is occurred,



Since 4He (α) and ${}^{13}C$ are stable, the total number of neutrons decreases when this reaction occurs.

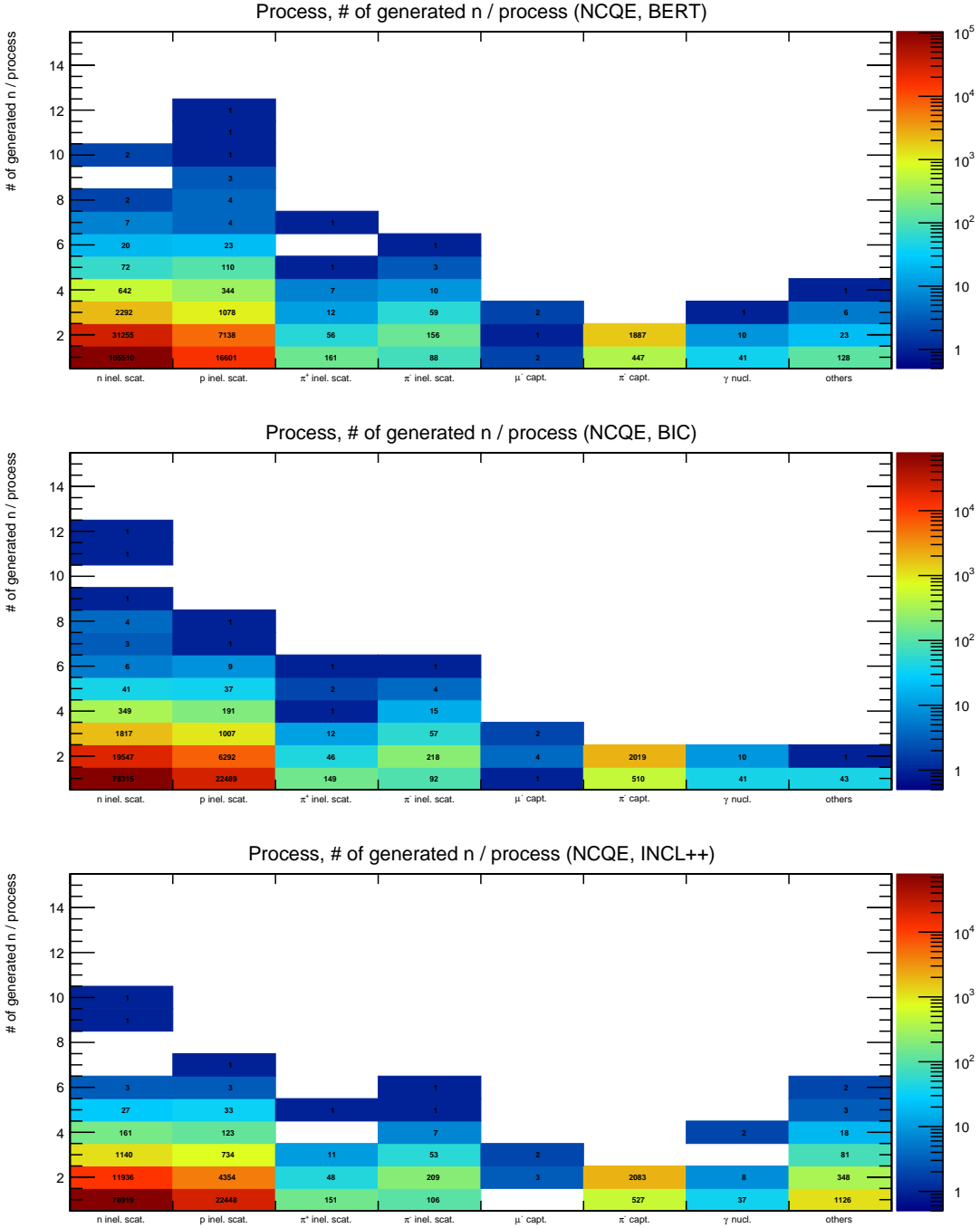


Figure 7.1: The number of generated neutrons per process after primary interactions. Top, center, and bottom figure shows the case of BERT, BIC, and INCL++, respectively. Horizontal axis shows processes that generated neutrons (neutron inelastic scattering, proton inelastic scattering, π^+ inelastic scattering, π^- inelastic scattering, μ^- capture, π^- capture, gamma-nuclear interaction, and others).

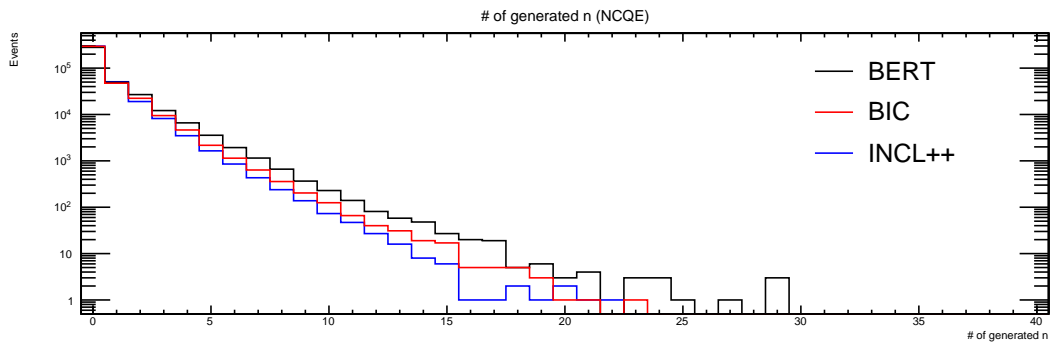


Figure 7.2: The number of neutrons generated after primary interactions. Black, red, and blue line shows the case of BERT, BIC, and INCL++, respectively.

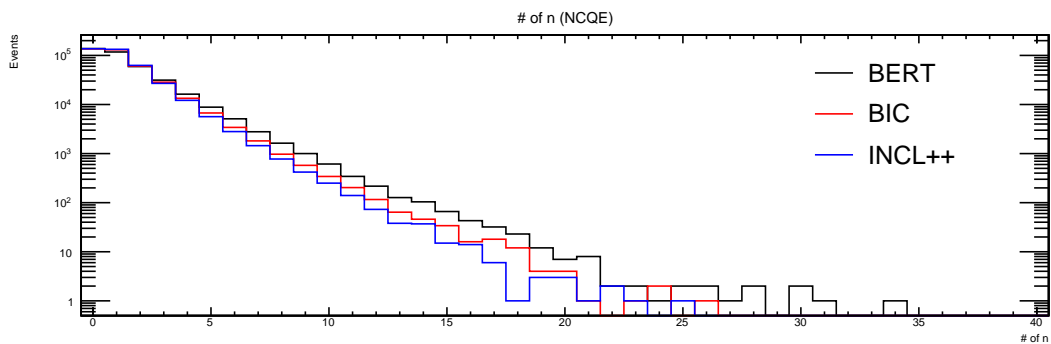


Figure 7.3: The total number of neutrons. Black, red, and blue line shows the case of BERT, BIC, and INCL++, respectively.

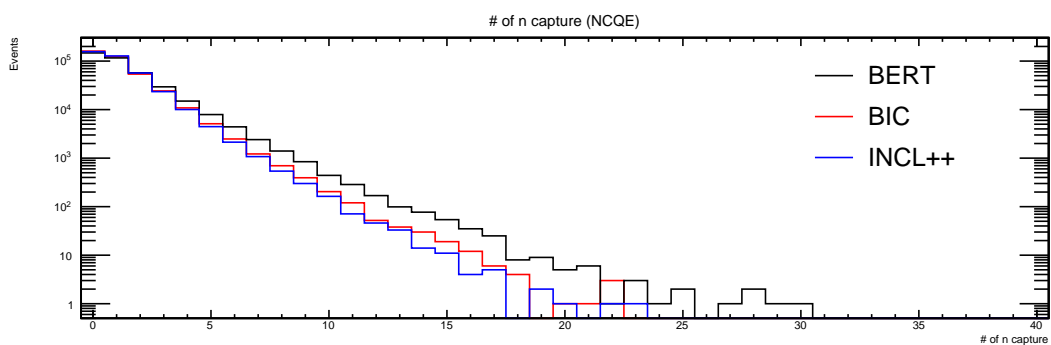


Figure 7.4: The number of neutron captures. Black, red, and blue line shows the case of BERT, BIC, and INCL++, respectively.

Next, we will focus on gamma-rays generated by neutron inelastic scattering reactions. Figure 7.5 shows the number of neutron inelastic scattering reactions. The number of neutron inelastic scattering reactions is larger in BERT than other two models but not so different, and this trend is similar to that of Figure 7.2, Figure 7.3, and Figure 7.4. However, the number of generated gamma-rays per neutron inelastic scattering reaction is largely different among secondary interaction models. In Figure 7.6, the number of generated gamma-rays per neutron inelastic scattering reaction is similar between BIC and INCL++. While, in BERT, it is apparently larger than other two models. As a result, the number of gamma-rays generated by neutron inelastic scattering reactions is largely different between BERT and other two models, as shown in Figure 7.7. Moreover, in BERT, events that the number of gamma-rays generated by neutron inelastic scattering reactions is one is small. Energy of gamma-rays generated by neutron inelastic scattering reactions is also largely different. In Figure 7.8, BERT has many continuous components in addition to peak structures of de-excitation gamma-rays, compared to other two models. Furthermore, in Figure 7.9, total energy of gamma-rays generated by neutron inelastic scattering reactions, which is related to E_{vis} , is larger in BERT than other two models. Information about the number of gamma-rays is summarized in bottom of Table 7.1. In this table, the number of primary gamma-rays is common among secondary interaction models (see Figure B.2). Moreover, the number of gamma-rays generated by neutron inelastic scattering reactions in BERT is more than twice as much as that in BIC and INCL++.

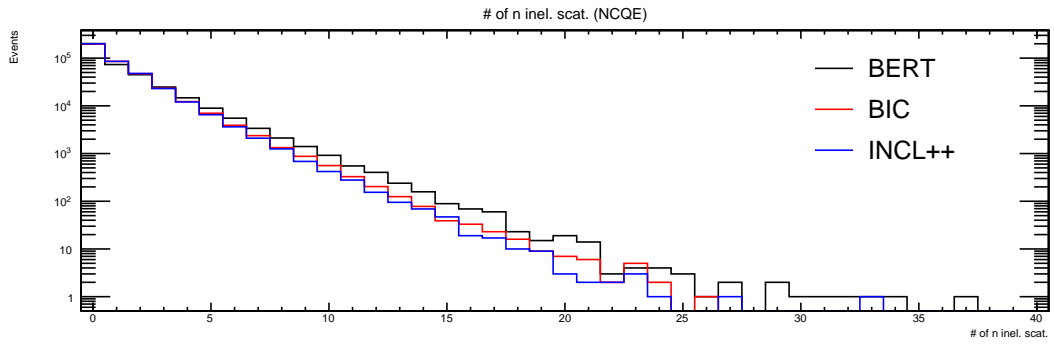


Figure 7.5: The number of neutron inelastic scattering reactions. Black, red, and blue line shows the case of BERT, BIC, and INCL++, respectively.

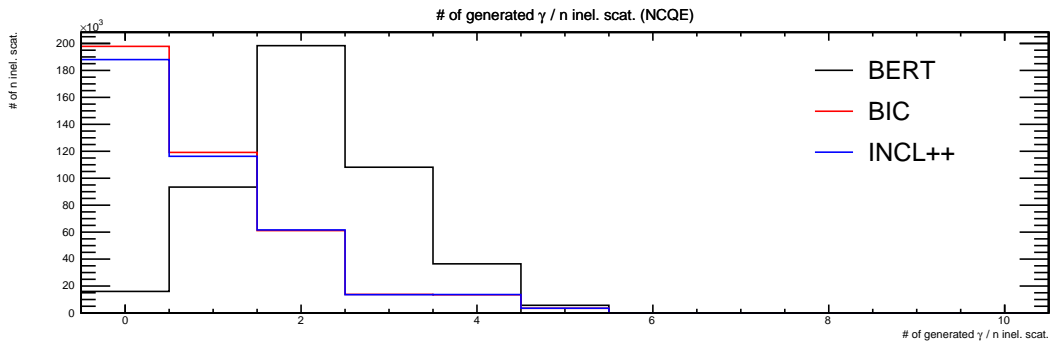


Figure 7.6: The number of generated gamma-rays per neutron inelastic scattering reaction. Black, red, and blue line shows the case of BERT, BIC, and INCL++, respectively.

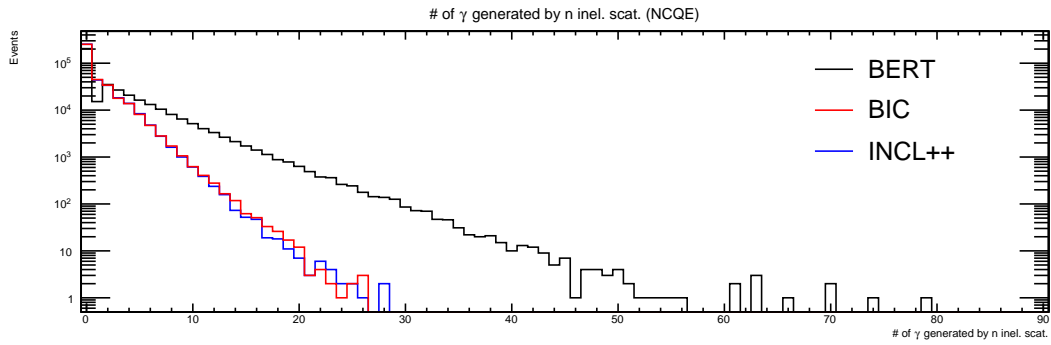


Figure 7.7: The number of gamma-rays generated by neutron inelastic scattering reactions. Black, red, and blue line shows the case of BERT, BIC, and INCL++, respectively.

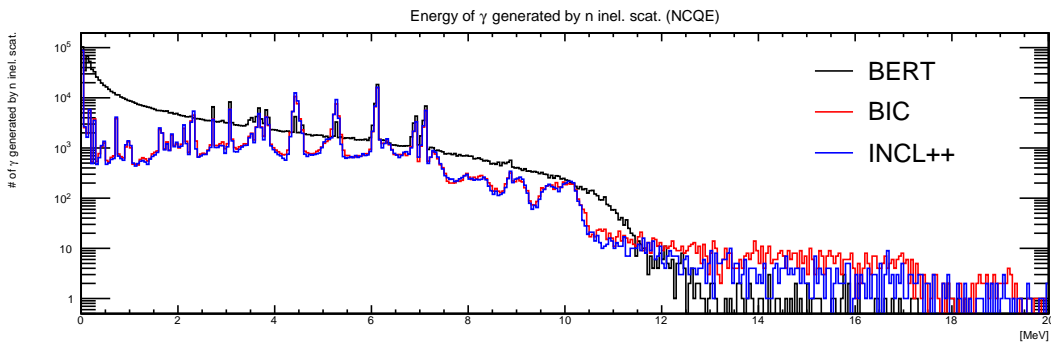


Figure 7.8: Energy of gamma-rays generated by neutron inelastic scattering reactions. Black, red, and blue line shows the case of BERT, BIC, and INCL++, respectively.

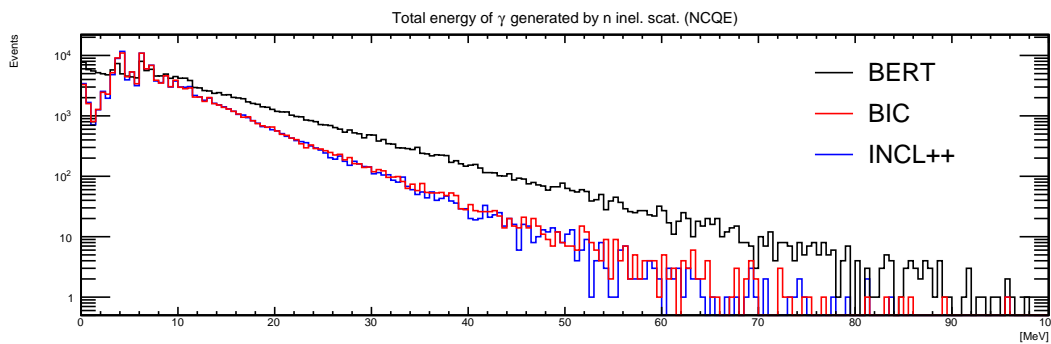


Figure 7.9: Total energy of gamma-rays generated by neutron inelastic scattering reactions. Black, red, and blue line shows the case of BERT, BIC, and INCL++, respectively.

7.2 Differences of secondary interaction models

Secondary interactions can be described by the intranuclear-cascade model embedding the pre-compound (pre-equilibrium) model and evaporation (equilibrium) model. Here, main differences of each model are described. Details of each secondary interaction model are summarized in references cited below.

7.2.1 Intranuclear-cascade model

Model category

Intranuclear-cascade models can be categorized into two types. One is a space-dependent intranuclear-cascade model, another is a time-dependent intranuclear-cascade model. BERT belongs to the space-dependent intranuclear-cascade model, while BIC and INCL++ belong to the time-dependent intranuclear-cascade model.

In space-dependent intranuclear-cascade models, a collision point between a projectile and a target nucleon is determined by using the total particle-particle cross sections and region-dependent nucleon densities [113]. According to Ref. [114], the collision point x is given by

$$\begin{aligned} x &= -\lambda \ln \xi \\ &= -\frac{1}{\rho \sigma_{NN}} \ln \xi \\ &= -\frac{A}{\rho \{Z\sigma_{Np} + (A-Z)\sigma_{Nn}\}} \ln \xi, \end{aligned} \quad (7.2)$$

where λ is the mean free path, ξ is the uniform random number between 0 and 1, ρ is the nucleon density, σ_{NN} is the nucleon-nucleon collision cross section, A is the mass number (the number of nucleons), Z is the atomic number (the number of protons), σ_{Np} is the collision cross section between the incoming particle and target proton, and σ_{Nn} is the collision cross section between the incoming particle and target neutron.

In time-dependent intranuclear-cascade models, a distance of closest approach d_i to each target nucleon i is calculated using a straight line trajectory to determine a collision point [113]. According to Ref. [113], collisions will occur when d_i satisfies the following inequality,

$$d_i < \sqrt{\frac{\sigma_i}{\pi}}, \quad (7.3)$$

where σ_i is the total cross section.

Nuclear model

Here, an oxygen nucleus (A (mass number) = 16) is taken as an example. In BERT, a nuclear model with three concentric spheres $i = \{1, 2, 3\}$ is used. According to Ref. [113], the sphere radius is defined as

$$r_i(\alpha_i) = C_2 \log \left(\frac{1 + e^{-\frac{C_1}{C_2}}}{\alpha_i} - 1 \right) + C_1 \quad (A > 11), \quad (7.4)$$

where $C_1 = 3.3836 A^{1/3}$, $C_2 = 1.7234$, and $\alpha_i = \{0.01, 0.3, 0.7\}$. Figure 7.10 shows the nucleon-density distributions of ^{65}Cu [115]. The proton density in each region is set equal to the average value of the charge distribution in the region, and the neutron-to-proton density ratio in each region is equal to the neutron-to-proton ratio in the nucleus.

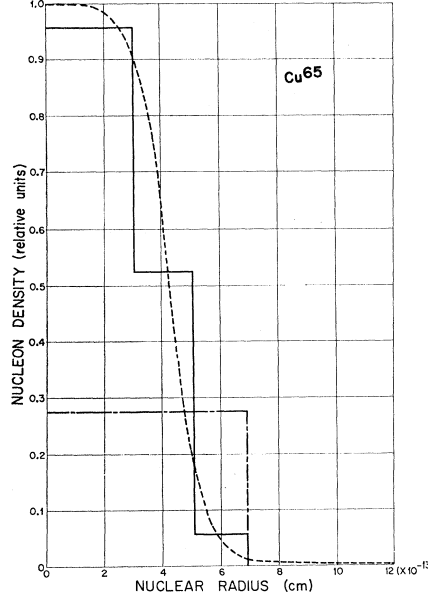


Figure 7.10: Nucleon-density distributions of ^{65}Cu [115]. Solid line, long-dash–short-dash line, and dashed line shows the standard three-region configuration, the uniform distribution, and Hofstadter’s curve [116], respectively.

In BIC [113], the nucleon radii r_i ($i = \{1, 2, \dots, A\}$) are selected randomly according to the nucleon density $\rho(r_i)$, and the nucleon density is given by

$$\rho(r_i) = (\pi R^2)^{-3/2} \exp(-r_i^2/R^2) \quad (A < 17), \quad (7.5)$$

where $R^2 = 0.8133A^{2/3} \text{ fm}^2$.

In INCL++ [117], the nucleon density is given by

$$\rho(r) = \begin{cases} \frac{\rho_0}{1 + \exp\left(\frac{r-R_0}{a}\right)} & \text{(for } r < R_{\max}) \\ 0 & \text{(for } r > R_{\max}) \end{cases}, \quad (7.6)$$

where $R_0 = (2.745 \times 10^{-4}A + 1.063)A^{1/3} \text{ fm}$, $a = 0.510 + 1.63 \times 10^{-4}A \text{ fm}$, and $R_{\max} = R_0 + 8a$. The quantity ρ_0 is like that the distribution is normalized to A .

Stopping time

In BERT and BIC [113], the cascade ends when all particles which can escape the nucleus, have done so.

While, in INCL++ [113], the cascade stopping time t_{stop} is defined as

$$t_{\text{stop}} = t_0 \left(\frac{A}{208} \right)^{0.16}, \quad (7.7)$$

where $t_0 = 70 \text{ fm}/c$. The cascade also ends if no participants are left in the nucleus. Figure 7.11 shows the time variation of four physical quantities obtained by collisions of 1-GeV protons with Pb nuclei in INCL++ [117]. In this figure, arrows show the stopping time, and the stopping time is about $70 \text{ fm}/c$ because the target nucleus is Pb ($A \sim 208$).

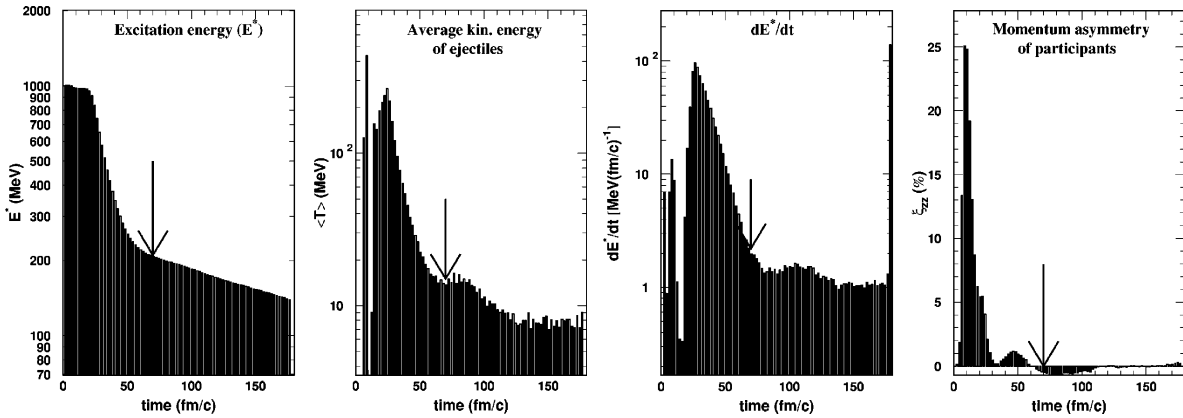


Figure 7.11: Time variation of four physical quantities obtained by collisions of 1-GeV protons with Pb nuclei in INCL++ [117]. Left, center left, center right, and right figure shows the time variation of excitation energy, average kinetic energy of ejectiles, time derivative of the excitation energy, and momentum asymmetry of participants, respectively. The arrows show the stopping time.

7.2.2 Pre-compound model and evaporation model

BERT embeds its own pre-compound and evaporation models, while BIC and INCL++ embed Geant4 native pre-compound and evaporation models [118]. However, as a option, BERT can switch to the Geant4 native pre-compound and evaporation models. Therefore, we confirmed some distributions shown in Section 7.1 using BERT embedding the Geant4 native pre-compound and evaporation models. Figure 7.12 shows the number of generated gamma-rays per neutron inelastic scattering reaction. From this figure, we can confirm that the shape of the distribution in BERT with the Geant4 pre-compound model is much closer to that in BIC and INCL++ compared to Figure 7.6. The number of gamma-rays generated by neutron inelastic scattering reactions is also close between BERT with the Geant4 pre-compound model and BIC and INCL++, as shown in Figure 7.13. Furthermore, as shown in Figure 7.14 and Figure 7.15, energy and total energy of gamma-rays generated by neutron inelastic scattering reactions are also close among these models. The numbers of neutrons, neutron captures, and gamma-rays are summarized in Table 7.1.

The main difference between models embedded in BERT and Geant4 native models seems to be the condition under which the evaporation process ends. According to Ref. [113], in evaporation model embedded in BERT, the main chain of evaporation is followed until an excitation energy falls below $E_{\text{cutoff}} = 0.1 \text{ MeV}$, and a gamma-ray emission chain continues until the excitation energy is less than $E_{\text{cutoff}}^\gamma = 10^{-15} \text{ MeV}$. By this specification, the numbers of neutrons and gamma-rays are considered to be larger in BERT that embeds its own pre-compound and evaporation models.

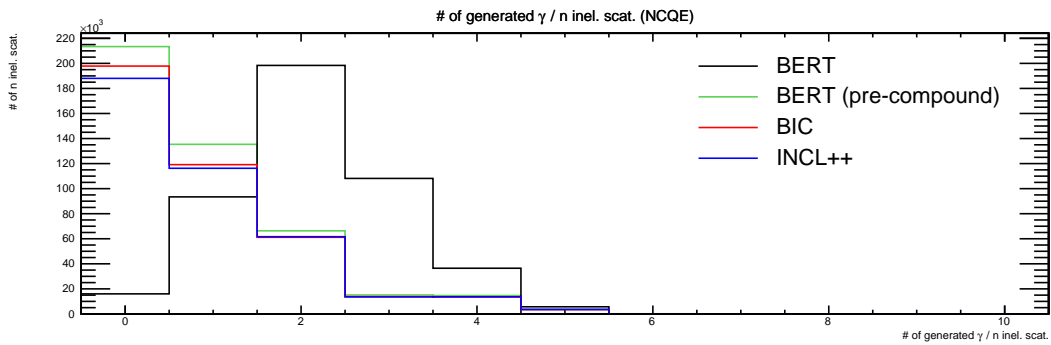


Figure 7.12: The number of generated gamma-rays per neutron inelastic scattering reaction. Black, green, red, and blue line shows the case of BERT, BERT with the Geant4 pre-compound model, BIC, and INCL++, respectively.

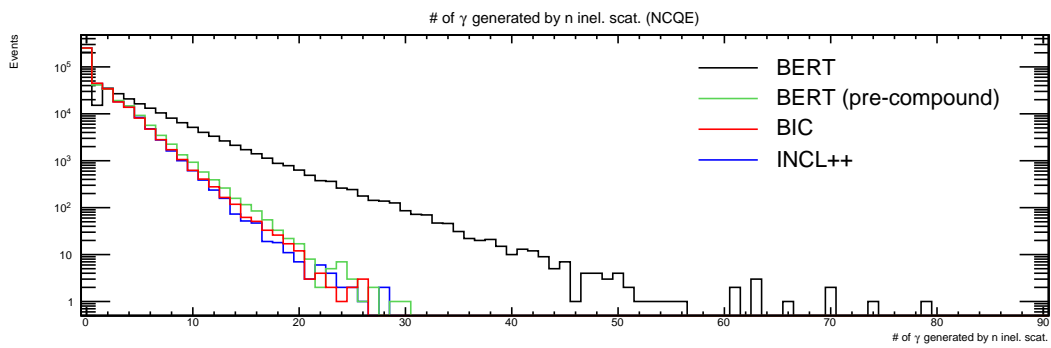


Figure 7.13: The number of gamma-rays generated by neutron inelastic scattering reactions. Black, green, red, and blue line shows the case of BERT, BERT with the Geant4 pre-compound model, BIC, and INCL++, respectively.

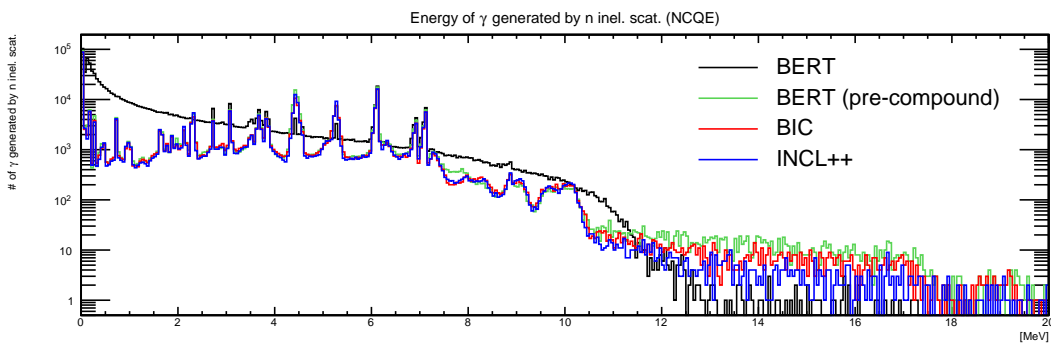


Figure 7.14: Energy of gamma-rays generated by neutron inelastic scattering reactions. Black, green, red, and blue line shows the case of BERT, BERT with the Geant4 pre-compound model, BIC, and INCL++, respectively.

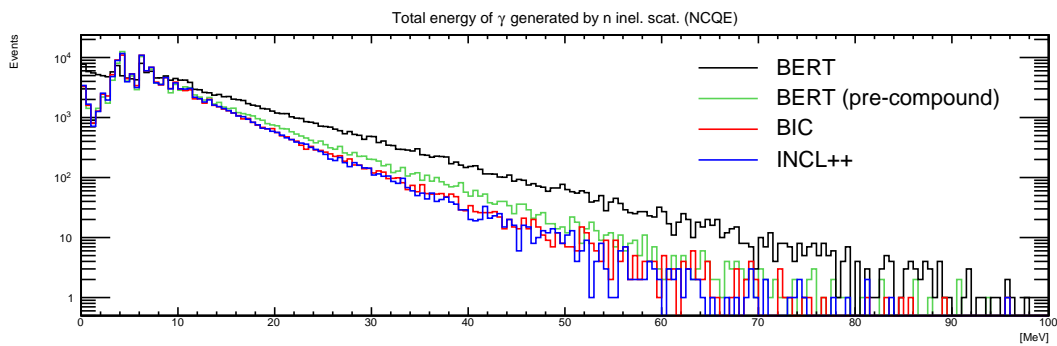


Figure 7.15: Total energy of gamma-rays generated by neutron inelastic scattering reactions. Black, green, red, and blue line shows the case of BERT, BERT with the Geant4 pre-compound model, BIC, and INCL++, respectively.

Table 7.1: The number of neutrons generated by each process (top), the total number of neutrons and neutron captures (center), and the number of gamma-rays (bottom). The numbers of primary neutrons and primary gamma-rays are common among secondary interaction models.

NCQE (383,284 events)	BERT	BERT (pre-compound)	BIC	INCL++
neutron inelastic scattering	178,029	131,337	124,582	107,027
proton inelastic scattering	36,295	29,613	39,112	34,040
π^+ inelastic scattering	349	322	297	285
π^- inelastic scattering	638	592	785	722
μ^- capture	10	9	15	12
π^- capture	4,221	4,155	4,548	4,693
gamma-nuclear interaction	64	42	61	61
others	196	169	45	2,164
The number of generated neutrons	219,802	166,239	169,445	149,004
The number of generated neutrons per event	0.5735	0.4337	0.4421	0.3888

NCQE (383,284 events)	BERT	BERT (pre-compound)	BIC	INCL++
The number of primary neutrons	310,835	310,835	310,835	310,835
The number of generated neutrons	219,802	166,239	169,445	149,004
The total number of neutrons	530,637	477,074	480,280	459,839
The number of neutron captures	495,346	425,718	411,087	405,483
The number of primary neutrons per event	0.8110	0.8110	0.8110	0.8110
The number of generated neutrons per event	0.5735	0.4337	0.4421	0.3888
The total number of neutrons per event	1.3844	1.2447	1.2531	1.1997
The number of neutron captures per event	1.2924	1.1107	1.0725	1.0579

NCQE (383,284 events)	BERT	BERT (pre-compound)	BIC	INCL++
The number of primary gamma-rays	168,060	168,060	168,060	168,060
The number of n inel. scat.	458,254	448,775	409,019	396,804
The number of gamma-rays per n inel. scat.	2.1599	0.8727	0.8677	0.8902
The number of gamma-rays by n inel. scat.	989,782	391,633	354,886	353,237
The number of primary gamma-rays per event	0.4385	0.4385	0.4385	0.4385
The number of n inel. scat. per event	1.1956	1.1709	1.0671	1.0353
The number of gamma-rays by n inel. scat. per event	2.5824	1.0218	0.9259	0.9216

7.3 Comparison with the observed data

Figure 7.16, Figure 7.17, and Figure 7.18 show the distributions of θ_C , E_{vis} , and N_{delayed} in each secondary interaction model, respectively. The distributions of θ_C , E_{vis} , and N_{delayed} strongly depend on the number of de-excitation gamma-rays and neutrons. For example, the direction of Cherenkov photons becomes more isotropic as the number of de-excitation gamma-rays is increased. Moreover, the total energy of de-excitation gamma-rays is correlated to the number of de-excitation gamma-rays. Therefore, θ_C and E_{vis} become larger as the number of de-excitation gamma-rays gets larger. Furthermore, N_{delayed} is correlated to the total number of neutrons.

In Figure 7.17 (E_{vis} distribution) and Figure 7.18 (N_{delayed} distribution), the number of events becomes larger in BERT than other two models. Furthermore, in Figure 7.16 (θ_C distribution), the differences between BERT and other two models are large in high-angle regions. These differences come from the number of de-excitation gamma-rays and neutrons by secondary interactions, which is described in Section 7.1. The number of de-excitation gamma-rays and neutrons is similar between BIC and INCL++. While, in BERT, the number of de-excitation gamma-rays and neutrons is larger than in the other two models.

We calculated the chi-square χ^2 for θ_C , E_{vis} , and N_{delayed} distributions by using the Poisson-likelihood [119]. Here, χ^2 is defined as

$$\chi^2 = 2 \sum_{i=1}^{\text{bin}} \left(N^{\text{exp},i} - N^{\text{obs},i} + N^{\text{obs},i} \ln \frac{N^{\text{obs},i}}{N^{\text{exp},i}} \right), \quad (7.8)$$

where bin is the number of bins, $N^{\text{obs},i}$ is the observed number of events of i -th bin and $N^{\text{exp},i}$ is the expected number of events of i -th bin. The derivation of Equation (7.8) is summarized in Appendix A. The values of the chi-square for θ_C , E_{vis} , and N_{delayed} distributions are summarized in Table 7.2. Due to the small statistics, the chi-square cannot give conclusive results; however, the values are smaller for BIC and INCL++ than for BERT in all distributions.

Table 7.2: Values of the chi-square for θ_C , E_{vis} , and N_{delayed} distributions.

Model	$\chi^2/\text{ndf } (\theta_C)$	$\chi^2/\text{ndf } (E_{\text{vis}})$	$\chi^2/\text{ndf } (N_{\text{delayed}})$
BERT	23.0 / 15	9.8 / 11	5.8 / 5
BIC	19.6 / 15	6.9 / 11	3.1 / 5
INCL++	19.8 / 15	6.8 / 11	2.8 / 5

As described in Section 1.6, an accelerator neutrino-oxygen NCQE cross section measurement was conducted as part of the T2K experiment [48]. The observed and expected number of events in $\theta_C \in [78, 90]$ degrees and $E_{\text{vis}} \in [7.49, 29.49]$ MeV obtained in the T2K data analysis are shown in Table 7.3. As shown in Figure 7.16, the difference between models is especially large in $\theta_C \in [78, 90]$ degrees. Therefore, using the same criteria of θ_C and E_{vis} , we have also performed an analysis of secondary interaction model comparison using atmospheric neutrinos. The results are also summarized in Table 7.3. With these selection criteria, the expected number of events in BERT is larger than the observed number of events. The similar discrepancy was observed in T2K because the secondary interaction model is based on BERT [48, 120]. In both cases, the differences of the expected and observed number of events in BERT are larger than that in BIC and INCL++, which shows similar trend as above.

Table 7.3: The observed and expected number of events in $\theta_C \in [78, 90]$ degrees and $E_{\text{vis}} \in [7.49, 29.49]$ MeV in this study and T2K [48]. In T2K, N_{delayed} (greater or equal to one) cut is not applied.

	Model	Expected	Observed
This study	BERT	26.8	
	BIC	18.4	14
	INCL++	18.9	
T2K	BERT	100.8	61

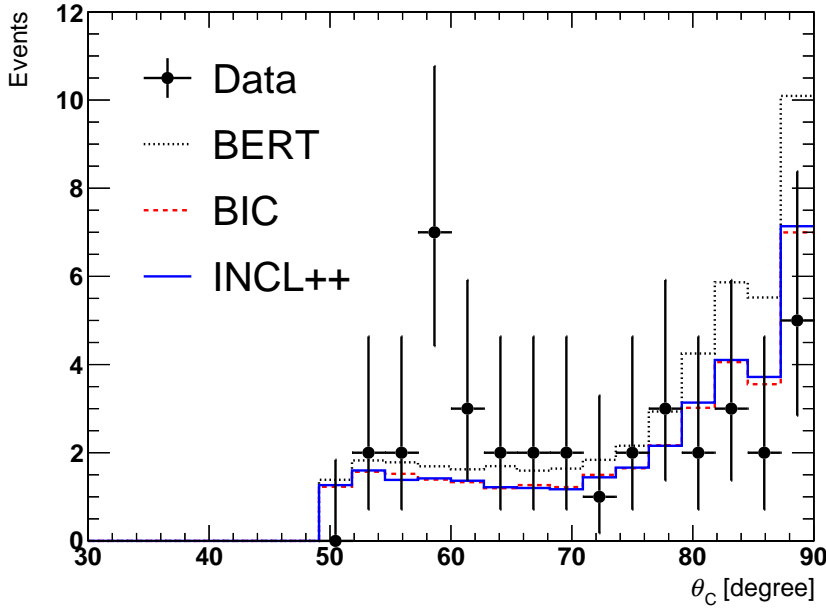


Figure 7.16: θ_C distribution. Dotted, dashed, and solid line show the total expected events in BERT, BIC, and INCL++, respectively. In BERT, the total expected events in this distribution are the same as that in Figure 6.17. In this distribution, E_{vis} is between 7.49 MeV and 29.49 MeV and N_{delayed} is greater or equal to one.

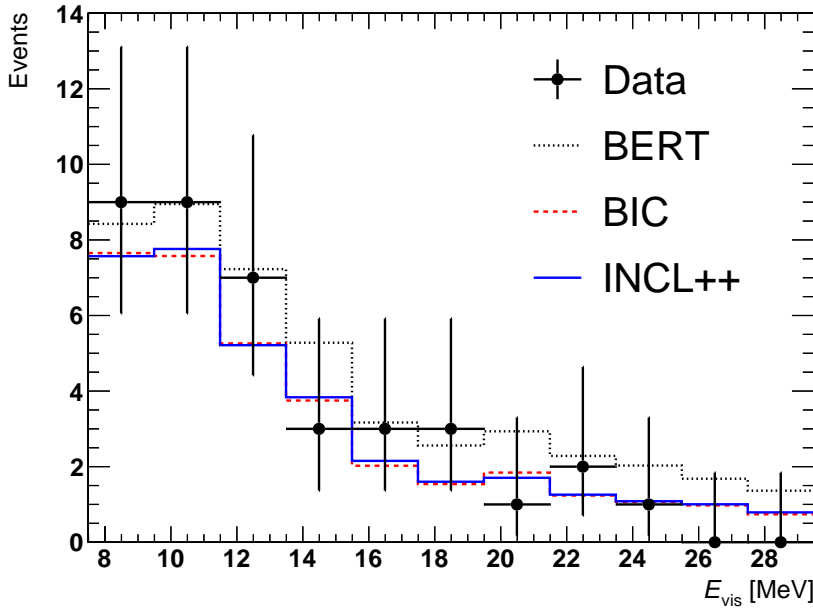


Figure 7.17: E_{vis} distribution. Dotted, dashed, and solid line show the total expected events in BERT, BIC, and INCL++, respectively. In BERT, the total expected events in this distribution are the same as that in Figure 6.18. In this distribution, θ_C is greater than 50 degrees and N_{delayed} is greater or equal to one.

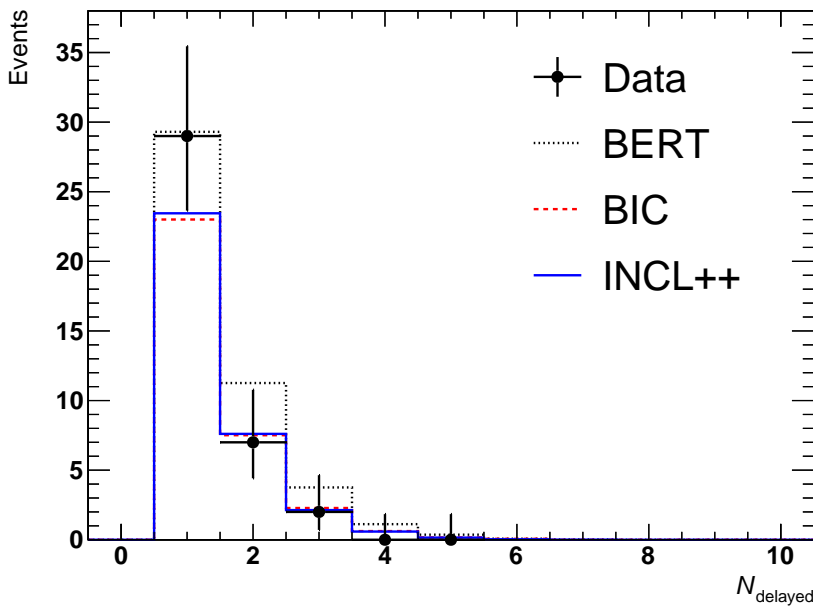


Figure 7.18: N_{delayed} distribution. Dotted, dashed, and solid line show the total expected events in BERT, BIC, and INCL++, respectively. In BERT, the total expected events in this distribution are the same as that in Figure 6.19. In this distribution, θ_C is greater than 50 degrees and E_{vis} is between 7.49 MeV and 29.49 MeV.

8 Measurement of NCQE cross section in SK-Gd

8.1 Measured NCQE cross section

The atmospheric neutrino flux-averaged theoretical neutrino-oxygen NCQE cross section is

$$\begin{aligned}\langle\sigma_{\text{NCQE}}^{\text{theory}}\rangle &= \frac{\int_{160 \text{ MeV}}^{10 \text{ GeV}} \sum_{i=\nu,\bar{\nu}} \phi_i(E) \times \sigma_i(E)^{\text{theory}}_{\text{NCQE}} dE}{\int_{160 \text{ MeV}}^{10 \text{ GeV}} \sum_{i=\nu,\bar{\nu}} \phi_i(E) dE} \\ &= 1.02 \times 10^{-38} \text{ cm}^2/\text{oxygen},\end{aligned}\quad (8.1)$$

where $\phi_i(E)$ is the atmospheric neutrino flux [68] at neutrino energy E and $\sigma_i(E)^{\text{theory}}_{\text{NCQE}}$ is the theoretical NCQE cross section [51]. The integral is performed between 160 MeV and 10 GeV because the NCQE cross section is small below 160 MeV and the atmospheric neutrino flux is small above 10 GeV (see Figure 3.2 and Figure 3.7). The systematic uncertainty by the energy cutoff is described in Section 8.2. The measured neutrino-oxygen NCQE cross section is

$$\begin{aligned}\langle\sigma_{\text{NCQE}}^{\text{measured}}\rangle &= \frac{N^{\text{obs}} - N_{\text{Non-NCQE}}^{\text{exp}}}{N_{\text{NCQE}}^{\text{exp}}} \times \langle\sigma_{\text{NCQE}}^{\text{theory}}\rangle \\ &= 0.74 \pm 0.22(\text{stat.}) \times 10^{-38} \text{ cm}^2/\text{oxygen},\end{aligned}\quad (8.2)$$

where N^{obs} ($= 38$) is the observed number of events, $N_{\text{NCQE}}^{\text{exp}}$ ($= 28.7071$) is the expected number of NCQE events, and $N_{\text{Non-NCQE}}^{\text{exp}}$ ($= 17.1920$) is the expected number of non-NCQE events, including NC non-QE, CC, spallation, reactor neutrino, and accidental coincidence. Here, the calculation of statistical uncertainty in Equation (8.2) is described. The fraction in Equation (8.2) is redefined as

$$f_{\text{NCQE}} = \frac{N^{\text{obs}} - N_{\text{Non-NCQE}}^{\text{exp}}}{N_{\text{NCQE}}^{\text{exp}}}. \quad (8.3)$$

The statistical uncertainty of numerator $\delta N^{\text{numerator}}$ is

$$\begin{aligned}\delta N^{\text{numerator}} &= \sqrt{(\delta N^{\text{obs}})^2 + (\delta N_{\text{Non-NCQE}}^{\text{exp}})^2} \\ &= \delta N^{\text{obs}} \\ &= \sqrt{N^{\text{obs}}}.\end{aligned}\quad (8.4)$$

While the statistical uncertainty of denominator $\delta N^{\text{denominator}}$ is

$$\begin{aligned}\delta N^{\text{denominator}} &= \delta N_{\text{NCQE}}^{\text{exp}} \\ &= 0.\end{aligned}\quad (8.5)$$

Therefore, the statistical uncertainty of f_{NCQE} is

$$\begin{aligned}\delta f_{\text{NCQE}} &= |f_{\text{NCQE}}| \times \sqrt{\left(\frac{\delta N^{\text{numerator}}}{N^{\text{numerator}}}\right)^2 + \left(\frac{\delta N^{\text{denominator}}}{N^{\text{denominator}}}\right)^2} \\ &= |f_{\text{NCQE}}| \times \frac{\sqrt{N^{\text{obs}}}}{N^{\text{obs}} - N_{\text{Non-NCQE}}^{\text{exp}}} \\ &= \frac{\sqrt{N^{\text{obs}}}}{N_{\text{NCQE}}^{\text{exp}}},\end{aligned}\quad (8.6)$$

and the statistical uncertainty of $\langle \sigma_{\text{NCQE}}^{\text{measured}} \rangle$ is

$$\begin{aligned}\delta \langle \sigma_{\text{NCQE}}^{\text{measured}} \rangle &= \delta f_{\text{NCQE}} \times \langle \sigma_{\text{NCQE}}^{\text{theory}} \rangle \\ &= 0.22 \times 10^{-38} \text{ cm}^2/\text{oxygen}.\end{aligned}\quad (8.7)$$

8.2 Systematic uncertainties of the expected events

Systematic uncertainties of the expected NCQE, NC non-QE, and CC events are summarized in Table 8.1. We follow the estimation methods of measurements in SK pure water phase and T2K [48–50]. The estimation of each systematic uncertainty is described below.

Table 8.1: Systematic uncertainties of the expected NCQE, NC non-QE, and CC events.

	NCQE	NC non-QE	CC
Atmospheric neutrino flux	$\pm 18.0\%$	$\pm 18.0\%$	$\pm 18.0\%$
Atmospheric neutrino/antineutrino ratio	$\pm 5.0\%$	$\pm 5.0\%$	$\pm 5.0\%$
Cross section	-	$\pm 18.0\%$	$\pm 24.0\%$
Primary interaction	$+1.5\% / -9.4\%$	$+0.0\% / -2.4\%$	$+1.2\% / -8.0\%$
Secondary interaction	$+0.0\% / -30.9\%$	$+0.0\% / -24.3\%$	$+0.0\% / -20.7\%$
Energy cutoff	$+0.0\% / -2.1\%$	$+0.0\% / -1.5\%$	$+0.0\% / -19.9\%$
Data reduction	$\pm 1.4\%$	$\pm 1.4\%$	$\pm 1.4\%$
Neutron tagging	$\pm 6.4\%$	$\pm 6.4\%$	$\pm 6.4\%$

Atmospheric neutrino flux

The uncertainty of the measured atmospheric neutrino flux in SK differs in each energy bin, as shown in Table 8.2 and Figure 8.1 [52]. From Table 8.2, atmospheric neutrino flux uncertainty $\Delta\Phi^\nu/\Phi^\nu$ is calculated by considering the weight of flux in each energy bin, as

$$\begin{aligned}\frac{\Delta\Phi^\nu}{\Phi^\nu} &= \sum_{i=1}^9 \left(\frac{\Delta\Phi_i^\nu}{\Phi_i^\nu} \times \frac{\Phi_i^\nu}{\sum_{j=1}^9 \Phi_j^\nu + \sum_{j=12}^{19} \Phi_j^\nu} \right) \\ &\quad + \sum_{i=12}^{19} \left(\frac{\Delta\Phi_i^\nu}{\Phi_i^\nu} \times \frac{\Phi_i^\nu}{\sum_{j=1}^9 \Phi_j^\nu + \sum_{j=12}^{19} \Phi_j^\nu} \right) \\ &= 17.9\%.\end{aligned}\quad (8.8)$$

In this measurement, we chose the conservative value and 18.0% in [160 MeV, 10 GeV] is applied to atmospheric neutrino flux uncertainty.

Atmospheric neutrino/antineutrino ratio

Figure 8.2 shows the ratio of atmospheric neutrino flux [121]. In the neutrino energy region below 10 GeV, the difference of atmospheric neutrino/antineutrino ratio due to the hadronic interaction models is less than 5.0%. Therefore, atmospheric neutrino/antineutrino ratio uncertainty is taken as 5.0%.

Table 8.2: Measured atmospheric neutrino flux using SK-I to SK-IV data [52]. Uncertainties are summarized in the rightmost column.

i	$\log_{10}(E/\text{GeV})$	$\log_{10}(\bar{E}_i/\text{GeV})$	$\bar{E}_i^2 \Phi_i^\nu$ ($\text{GeV}/\text{cm}^2/\text{sec}/\text{sr}$)	$\Delta \Phi_i^\nu / \Phi_i^\nu$ (%)
ν_e				
1	-0.8 to -0.6	-0.71	1.21×10^{-2}	± 18
2	-0.6 to -0.4	-0.51	1.46×10^{-2}	± 17
3	-0.4 to -0.2	-0.27	1.50×10^{-2}	± 16
4	-0.2 to 0.0	-0.09	1.37×10^{-2}	± 15
5	0.0 to 0.2	0.10	1.16×10^{-2}	± 17
6	0.2 to 0.4	0.30	8.55×10^{-3}	± 17
7	0.4 to 0.6	0.50	6.09×10^{-3}	± 18
8	0.6 to 0.8	0.70	3.73×10^{-3}	± 19
9	0.8 to 1.0	0.90	2.32×10^{-3}	± 18
10	1.0 to 1.5	1.22	9.42×10^{-4}	± 15
11	1.5 to 2.0	1.72	2.03×10^{-4}	± 18
ν_μ				
12	-0.6 to -0.4	-0.51	1.58×10^{-2}	± 21
13	-0.4 to -0.2	-0.32	1.77×10^{-2}	± 16
14	-0.2 to 0.0	-0.09	1.86×10^{-2}	± 15
15	0.0 to 0.2	0.10	1.68×10^{-2}	± 16
16	0.2 to 0.4	0.30	1.38×10^{-2}	± 18
17	0.4 to 0.6	0.51	9.59×10^{-3}	± 19
18	0.6 to 0.8	0.71	6.68×10^{-3}	± 19
19	0.8 to 1.0	0.90	4.79×10^{-3}	± 17
20	1.0 to 1.5	1.21	2.62×10^{-3}	± 13
21	1.5 to 2.0	1.73	1.20×10^{-3}	± 16
22	2.0 to 3.0	2.40	2.49×10^{-4}	± 18
23	3.0 to 4.0	3.39	1.46×10^{-5}	± 21

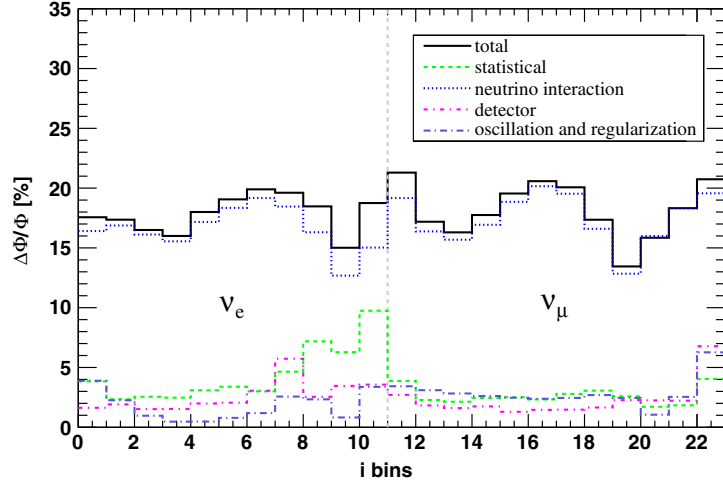


Figure 8.1: Uncertainty of the measured atmospheric neutrino flux in SK [52]. Energy region of each bin is summarized in Table 8.2. Total uncertainty consists of statistical, neutrino interaction, detector response, and neutrino oscillation and regularization uncertainties. Details of these components are summarized in Ref. [52].

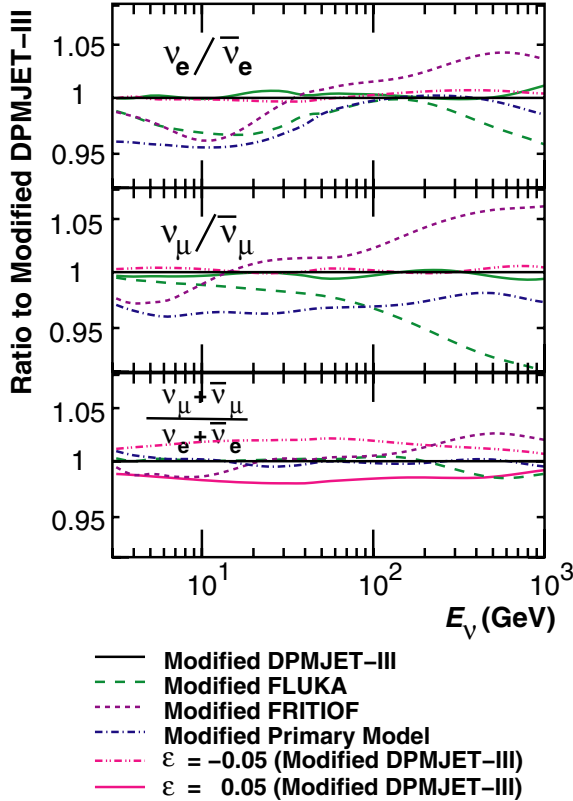


Figure 8.2: Ratio of atmospheric neutrino flux [121].

Cross section

Cross section uncertainty is taken as 18.0% for NC non-QE events and 24.0% for CC events considering the uncertainties of parameters for the cross-section models such as the axial mass, normalization parameters for each interaction, and the decay width of resonant pion production [49, 122]. Since the purpose of this study is to measure the NCQE cross section, the cross section uncertainty is not assigned for NCQE events. Details of these cross section uncertainties are summarized in Section 6.1 of Ref. [122].

Primary interaction

Primary interaction uncertainty arises from the spectroscopic strengths of the oxygen nucleus. Computation of the $p_{3/2}$ spectroscopic strength is consistent with $^{16}\text{O}(\text{e}, \text{e}'\text{p})$ experiment within 5.4% [51, 94]. Therefore, the uncertainty of $(p_{3/2})^{-1}$ state is estimated by increasing the production probabilities of this state by 5.4%. For the *others* state, there is no reliable predictions as written in Section 3.2, thus the uncertainty is conservatively estimated by comparing with an extreme case, that is the difference between the default state $((s_{1/2})^{-1})$ and the ground state $((p_{1/2})^{-1})$. The uncertainty is taken to be the difference in the expected number of events from the default condition to other conditions. Table 8.3 shows the production probabilities of $(p_{1/2})^{-1}$, $(p_{3/2})^{-1}$, and $(s_{1/2})^{-1}$ state and the expected number of NCQE, NC non-QE, and CC events in each condition of the primary interaction uncertainty estimation. From this result, the primary interaction uncertainty is taken as $+1.5\% / -9.4\%$, $+0.0\% / -2.4\%$, and $+1.2\% / -8.0\%$ for $N_{\text{NCQE}}^{\text{exp}}$, $N_{\text{NC non-QE}}^{\text{exp}}$, and $N_{\text{CC}}^{\text{exp}}$, respectively.

Table 8.3: Production probabilities of $(p_{1/2})^{-1}$, $(p_{3/2})^{-1}$, and $(s_{1/2})^{-1}$ state and the expected number of NCQE, NC non-QE, and CC events in each condition of the primary interaction uncertainty estimation. Differences of the expected number of events from the default condition are summarized in parentheses.

	$\text{others} \rightarrow (s_{1/2})^{-1}$ (Default)	$\text{others} \rightarrow (p_{1/2})^{-1}$	$(p_{3/2})^{-1} \times 1.054$
$(p_{1/2})^{-1}$	0.1580	0.5430	0.1390
$(p_{3/2})^{-1}$	0.3515	0.3515	0.3705
$(s_{1/2})^{-1}$	0.4905	0.1055	0.4905
$N_{\text{NCQE}}^{\text{exp}}$	28.7071	26.0172 (-9.4%)	29.1364 (+1.5%)
$N_{\text{NC non-QE}}^{\text{exp}}$	13.2721	12.9705 (-2.3%)	12.9520 (-2.4%)
$N_{\text{CC}}^{\text{exp}}$	1.4177	1.3042 (-8.0%)	1.4346 (+1.2%)

Secondary interaction

As described in Section 7.3, the chi-square differences were inconclusive. Therefore, the secondary interaction uncertainty is taken to be the difference in the expected number of events from BERT to BIC or INCL++. The expected number of NCQE, NC non-QE, and CC events in each condition of the secondary interaction uncertainty estimation is summarized in Table 8.4. From this result, the secondary interaction uncertainty is taken as -30.9% , -24.3% , and -20.7% for $N_{\text{NCQE}}^{\text{exp}}$, $N_{\text{NC non-QE}}^{\text{exp}}$, and $N_{\text{CC}}^{\text{exp}}$, respectively.

Energy cutoff

In Equation (8.1), the integral is performed between 160 MeV and 10 GeV, while the expected number of atmospheric neutrino events is estimated using full energy range. Energy cutoff uncertainty is estimated considering the difference of these energy range. Table 8.5 shows the expected number of NCQE, NC

Table 8.4: The expected number of NCQE, NC non-QE, and CC events in each condition of the secondary interaction uncertainty estimation. Differences of the expected number of events from the default condition are summarized in parentheses.

	BERT (Default)	BIC	INCL++
$N_{\text{NCQE}}^{\text{exp}}$	28.7071	19.8420 (-30.9%)	20.2027 (-29.6%)
$N_{\text{NC non-QE}}^{\text{exp}}$	13.2721	10.1887 (-23.2%)	10.0517 (-24.3%)
$N_{\text{CC}}^{\text{exp}}$	1.4177	1.1244 (-20.7%)	1.2173 (-14.1%)

non-QE, and CC events in each condition of the energy cutoff uncertainty estimation. Since the expected number of events decreases by the energy cutoff, only a negative direction is considered, and the energy cutoff uncertainty is taken as -2.1% , -1.5% , and -19.9% for $N_{\text{NCQE}}^{\text{exp}}$, $N_{\text{NC non-QE}}^{\text{exp}}$, and $N_{\text{CC}}^{\text{exp}}$, respectively.

Table 8.5: The expected number of NCQE, NC non-QE, and CC events in each condition of the energy cutoff uncertainty estimation. E shows the neutrino energy. Differences of the expected number of events from the default condition are summarized in parentheses.

	Full energy range (Default)	$E \in [160 \text{ MeV}, 10 \text{ GeV}]$
$N_{\text{NCQE}}^{\text{exp}}$	28.7071	28.1136 (-2.1%)
$N_{\text{NC non-QE}}^{\text{exp}}$	13.2721	13.0728 (-1.5%)
$N_{\text{CC}}^{\text{exp}}$	1.4177	1.1356 (-19.9%)

Data reduction

Table 8.6 shows the systematic uncertainties for the reduction cuts [22]. Spallation cut uncertainty is estimated by considering the dead time caused by the spallation cut. Effwall cut uncertainty is estimated from the difference in signal efficiency when the reconstructed vertex and direction are artificially shifted and not shifted. Ring cleanliness cut, charge/hit cut, and θ_C cut uncertainties are estimated from the difference in signal efficiency between LINAC data and MC. From Table 8.6, data reduction uncertainty $\delta q_{\text{reduction}} / |q_{\text{reduction}}|$ is calculated as

$$\begin{aligned} \frac{\delta q_{\text{reduction}}}{|q_{\text{reduction}}|} &= \sqrt{0.1^2 + 0.1^2 + 0.2^2 + 1.2^2 + 0.7^2} \\ &= 1.4\%. \end{aligned} \quad (8.9)$$

Details of spallation cut uncertainty and effwall cut uncertainty are described in Section 10.1.11 and Section 10.1.12 of Ref. [66], respectively. Details of ring cleanliness cut, charge/hit cut, and θ_C cut uncertainties are described in Section 3.3 of Ref. [123] and Section 8.3.6 of Ref. [36].

Neutron tagging

Neutron tagging uncertainty is estimated by using Americium-Beryllium (Am/Be) source and BGO scintillator crystals. Figure 8.3 shows the pictures and schematic views of Am/Be source and BGO scintillator

Table 8.6: Systematic uncertainties for the reduction cuts [22].

cut	systematic uncertainty
spallation cut	0.1%
effwall cut	0.1%
ring cleanliness cut	0.2%
charge/hit cut	1.2%
θ_C cut	0.7%

crystals. The main reaction process of Am/Be source is



In the calibration using Am/Be source, scintillation light caused by the 4.4 MeV gamma-ray becomes the prompt signal, and gamma-rays generated by neutron capture on Gd becomes the delayed signal. Neutron tagging uncertainty is estimated considering the uncertainties of prompt signal selection, delayed signal selection, settings of MC, position dependence of neutron tagging efficiency, and difference between data and MC for neutron tagging efficiency estimated using one BGO scintillator crystal. In this study, neutron tagging uncertainty is taken as 6.4% [40, 124]. Details of the neutron tagging uncertainty are summarized in Section 6.5 and Section 8.4.2 of Ref. [36].

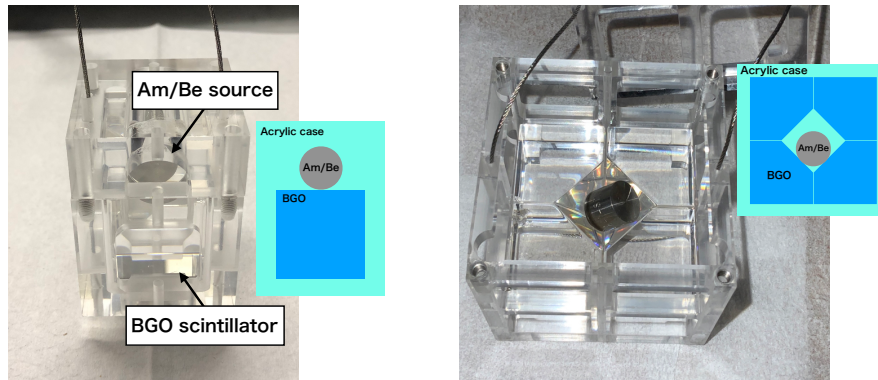


Figure 8.3: Pictures and schematic views of Am/Be source and BGO scintillator crystals [36]. Left shows the source geometry with one BGO scintillator crystal. Right shows the source geometry with eight BGO scintillator crystals.

Others

Systematic uncertainty of spallation events is estimated considering the production rate of ^9Li (see Section 3.3.1), the ^9Li energy spectrum shape (see Figure 3.10), and the reduction efficiency of ^9Li . In this study, systematic uncertainty of spallation events is taken as 60.0% [40]. Moreover, systematic uncertainty of reactor neutrino events is conservatively assigned as 100.0% [40]. Due to the small event fraction, these uncertainties are negligible. Details of these uncertainties are summarized in Section 4.3.3 and Section 4.3.4 of Ref. [123] and Section 9.2 and Section 9.3 of Ref. [36].

The expected number of accidental coincidence events is estimated by

$$N_{\text{Accidental}}^{\text{exp}} = \varepsilon_{\text{mis}} \times N_{\text{pre-ntag}}^{\text{obs}}, \quad (8.12)$$

where ε_{mis} ($= 2.85 \times 10^{-4}$) is the neutron misidentification rate [40, 124] and $N_{\text{pre-ntag}}^{\text{obs}}$ ($= 5,447$) is the observed number of events after applying all event selections except for the N_{delayed} cut (see Section 6.4.2). Systematic uncertainty of accidental coincidence events $\delta N_{\text{Accidental}}^{\text{exp}} / |N_{\text{Accidental}}^{\text{exp}}|$ is calculated by using systematic uncertainty of ε_{mis} and statistical uncertainty of $N_{\text{pre-ntag}}^{\text{obs}}$, that is,

$$\begin{aligned} \frac{\delta N_{\text{Accidental}}^{\text{exp}}}{|N_{\text{Accidental}}^{\text{exp}}|} &= \sqrt{\left(\frac{\delta \varepsilon_{\text{mis}}}{\varepsilon_{\text{mis}}}\right)^2 + \left(\frac{\delta N_{\text{pre-ntag}}^{\text{obs}}}{N_{\text{pre-ntag}}^{\text{obs}}}\right)^2} \\ &= \sqrt{4.4^2 + 1.4^2} \\ &= 4.6\%. \end{aligned} \quad (8.13)$$

Due to the small event fraction, this uncertainty is also negligible.

8.3 Systematic uncertainty of the measured NCQE cross section

Systematic uncertainty of the measured NCQE cross section is estimated by performing toy-MC considering the systematic uncertainties summarized in Section 8.2. Procedure of estimating the uncertainty is described below.

1. Make $N_{\text{NCQE}}^{\text{exp}}$, $N_{\text{NC non-QE}}^{\text{exp}}$, $N_{\text{CC}}^{\text{exp}}$, $N_{\text{Spallation}}^{\text{exp}}$, $N_{\text{Reactor}}^{\text{exp}}$, and $N_{\text{Accidental}}^{\text{exp}}$ fluctuate using Gaussian function with σ of the systematic uncertainty.
2. Calculate $\langle \sigma_{\text{NCQE}}^{\text{measured}} \rangle$ (see Equation (8.2)).
3. Repeat the above procedures for 1,000,000 times.
4. 1σ confidence level region from the nominal $\langle \sigma_{\text{NCQE}}^{\text{measured}} \rangle$ in the histogram is determined to be the systematic uncertainty.

The result of the toy-MC is shown in Figure 8.4. From this figure, the 1σ confidence level region becomes $[0.59, 1.59] \times 10^{-38} \text{ cm}^2/\text{oxygen}$, and the measured NCQE cross section is determined as

$$\langle \sigma_{\text{NCQE}}^{\text{measured}} \rangle = 0.74 \pm 0.22(\text{stat.})^{+0.85}_{-0.15}(\text{syst.}) \times 10^{-38} \text{ cm}^2/\text{oxygen}. \quad (8.14)$$

The measured NCQE cross section, the theoretical NCQE cross section [51], and the atmospheric neutrino flux predicted using the HKKM11 model [68] are shown in Figure 8.5. In this figure, the theoretical NCQE cross section $\sigma(E)_{\text{NCQE}}^{\text{theory}}$ is displayed in the form

$$\sigma(E)_{\text{NCQE}}^{\text{theory}} = \frac{\phi_\nu(E)/\phi_{\bar{\nu}}(E)}{\phi_\nu(E)/\phi_{\bar{\nu}}(E) + 1} \sigma_\nu(E)_{\text{NCQE}}^{\text{theory}} + \frac{1}{\phi_\nu(E)/\phi_{\bar{\nu}}(E) + 1} \sigma_{\bar{\nu}}(E)_{\text{NCQE}}^{\text{theory}}, \quad (8.15)$$

and the measured NCQE cross section is consistent with the flux-averaged theoretical NCQE cross section within the uncertainties.

f_{NCQE} (see Equation (8.3)) and the measured neutrino-oxygen NCQE cross section of previous studies in SK and T2K are shown in Figure 8.6 and Figure 8.7, respectively. In Figure 8.7, the measured NCQE cross section is consistent with the measurement in the SK pure water phase within the uncertainties ($1.01 \pm 0.17(\text{stat.})^{+0.78}_{-0.30}(\text{syst.}) \times 10^{-38} \text{ cm}^2/\text{oxygen}$) [50]. The systematic uncertainty of measured NCQE cross section in this study is larger than that in the measurement of the SK pure water phase. The reason is that we take the difference of secondary interaction models into consideration, conservatively estimated by the comparison among these models. The uncertainty will be reduced with better understanding of secondary interaction models in future.

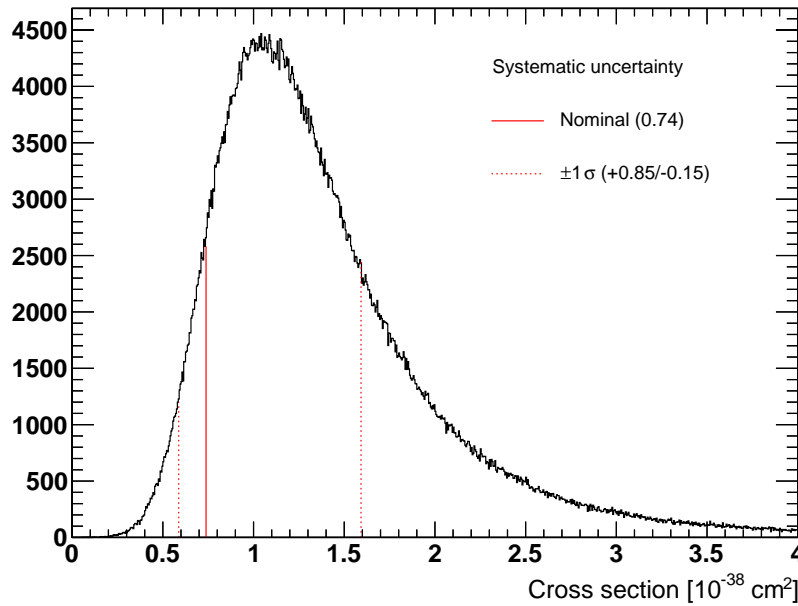


Figure 8.4: Result of the toy-MC. The 1σ confidence level region becomes $[0.59, 1.59] \times 10^{-38} \text{ cm}^2/\text{oxygen}$. Due to the secondary interaction uncertainty, the peak position is shifted right from the nominal value ($0.74 \times 10^{-38} \text{ cm}^2/\text{oxygen}$).

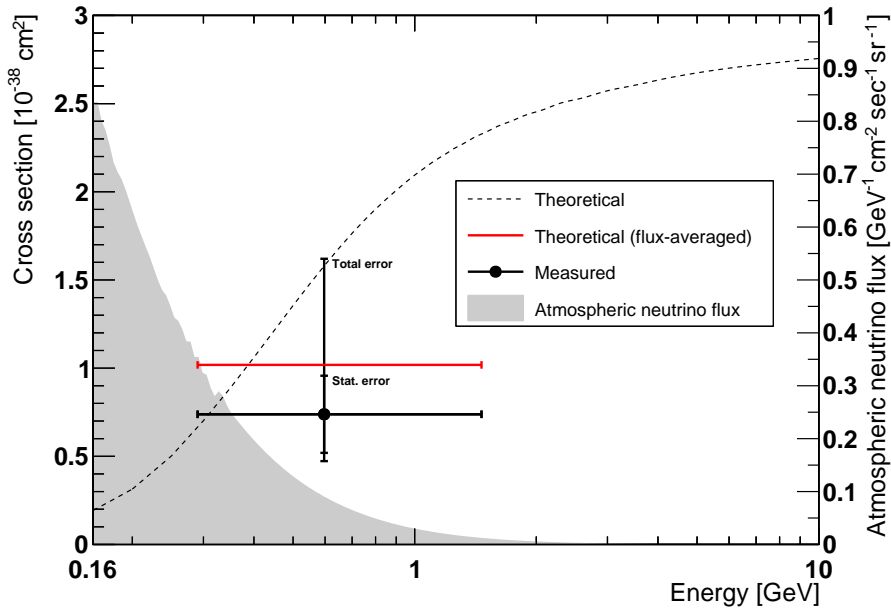


Figure 8.5: The measured neutrino-oxygen NCQE cross section, the theoretical neutrino-oxygen NCQE cross section [51], and the atmospheric neutrino flux predicted using the HKKM11 model [68]. Vertical bars show the statistical uncertainty (short bar) and the total uncertainty (long bar). Horizontal bars show the 1σ from the mean (0.60 GeV) of the theoretical NCQE cross section multiplied by the atmospheric neutrino flux.

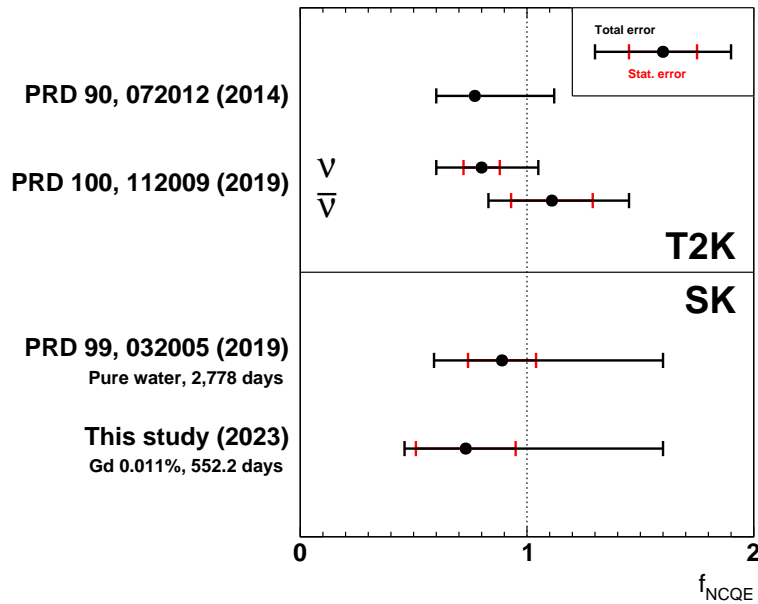


Figure 8.6: Comparison of f_{NCQE} (see Equation (8.3)) with previous measurements in SK and T2K [48–50]. Horizontal bars show the statistical uncertainty (short bar) and the total uncertainty (long bar).

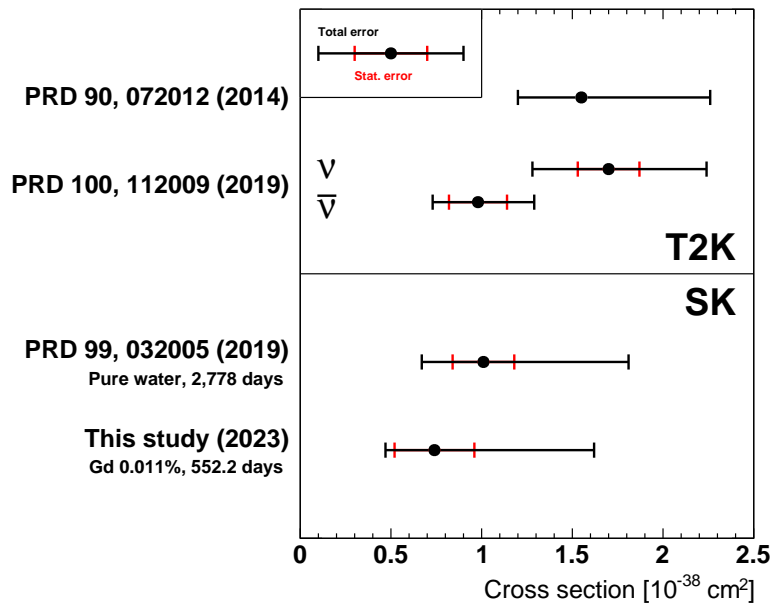


Figure 8.7: Comparison of the measured neutrino-oxygen NCQE cross section with previous measurements in SK and T2K [48–50]. Horizontal bars show the statistical uncertainty (short bar) and the total uncertainty (long bar).

9 Future prospects and conclusion

9.1 Future prospects

Now we continue the observation with a 0.03% Gd-loaded SK detector, the phase known as SK-VII. Since the neutron tagging efficiency in SK-VII is higher than that in SK-VI (35.6%) [40, 109], more delayed signals can be detected, and the observed number of events can be accumulated faster in SK-VII than in SK-VI. Figure 9.1 shows the expected N_{delayed} distributions in SK-VII. In this figure, each bin of the expected N_{delayed} distributions can be estimated as

$$(N_{\text{delayed}} = n) = \sum_{i=n} \{(N_{\text{capture}} = i) \times {}_i C_n p^n (1-p)^{i-n}\}, \quad (9.1)$$

where $(N_{\text{delayed}} = n)$ is the number of events that $N_{\text{delayed}} = n$, $(N_{\text{capture}} = i)$ is the number of events that $N_{\text{capture}} = i$, and p is the neutron tagging efficiency. Here, the neutron misidentification rate is not considered. Assuming that the neutron tagging efficiency in SK-VII is 63.0% [125], the statistics (the number of events that $N_{\text{delayed}} \geq 1$) increases by about 1.4 times with the same live time as SK-VI.

Figure 9.2 and Figure 9.3 shows the expectation of the observed number of events and the statistical uncertainty as a function of SK-VII live time, respectively. By combining about three years of data in SK-VII, the statistical uncertainty will be half of this work, and the secondary interaction models will be able to be verified more precisely.

Figure 9.4 shows the expectation of the difference between the observed and expected number of events in $\theta_C \in [78, 90]$ degrees as a function of SK-VII live time. This difference is estimated using the observed and expected number of events summarized in Table 7.3. As shown in this figure, BERT is now $\sim 2.2\sigma$ away from the data. By combining one year of data in SK-VII, BERT will be more than 3σ away from the data. Furthermore, the evaporation model can be determined at 5σ by combining about four years of data in SK-VII. Once the evaporation model is determined, the secondary interaction uncertainty is reduced, resulting that the systematic uncertainty of measured NCQE cross section is reduced.

Additional measurement using T2K's accelerator neutrino beam interactions in SK-Gd will help further refining the physics models for the secondary interactions.

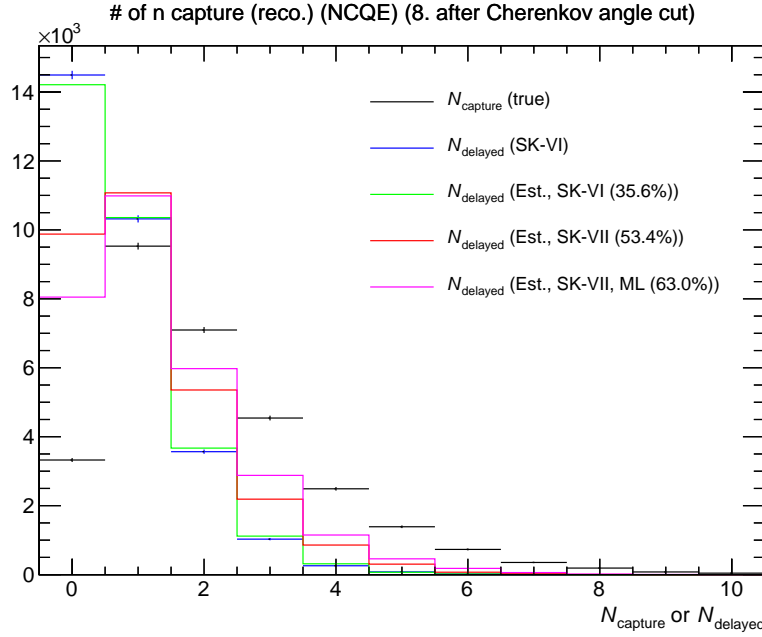


Figure 9.1: Expected N_{delayed} distributions in SK-VII. Black plots show the distribution of the number of true neutron captures (N_{capture}) before applying neutron tagging without any scalings. Blue plots show the N_{delayed} distribution after applying neutron tagging without any scalings in this study. Green line, red line, and magenta line show the N_{delayed} distribution estimated from the N_{capture} distribution assuming that neutron tagging efficiency is 35.6%, 53.4%, and 63.0%, respectively. 35.6% comes from the neutron tagging efficiency in SK-VI [40, 109]. 53.4% comes from the assumption that neutron tagging efficiency in SK-VII becomes 1.5 times higher than that in SK-VI [125]. 63.0% comes from the assumption of using the Multi-Layer (ML) neural networks in SK-VII [125].

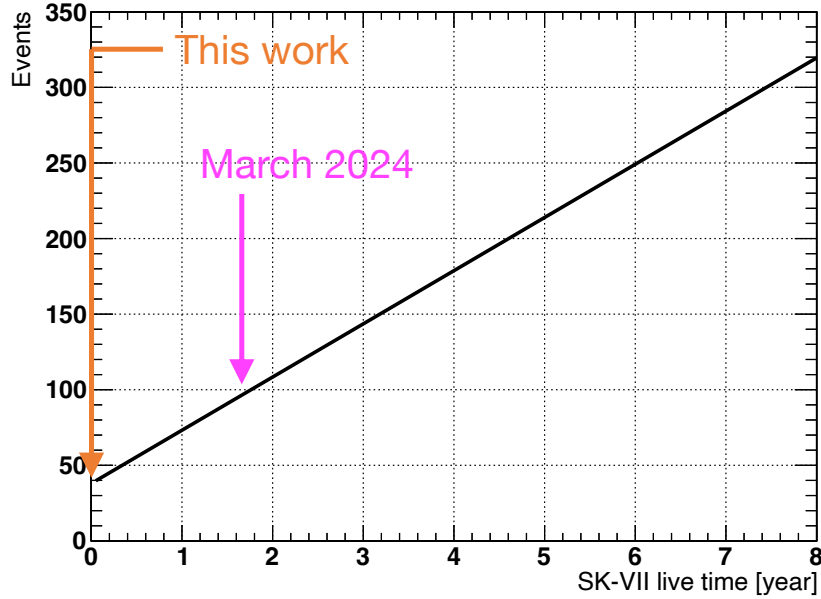


Figure 9.2: Expectation of the observed number of events as a function of SK-VII live time. Here, it is assumed that the neutron tagging efficiency in SK-VII is 63.0% [125].

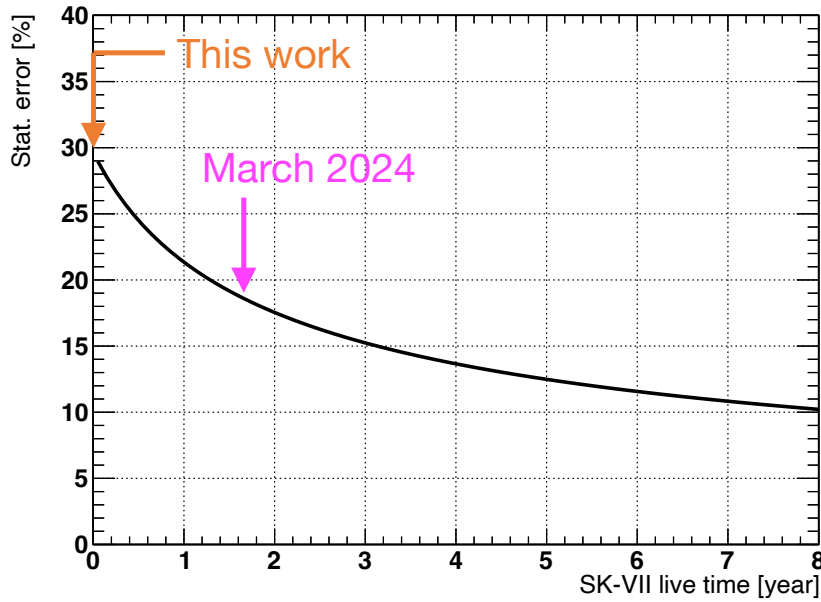


Figure 9.3: Expectation of the statistical uncertainty as a function of SK-VII live time. Here, it is assumed that the neutron tagging efficiency in SK-VII is 63.0% [125].

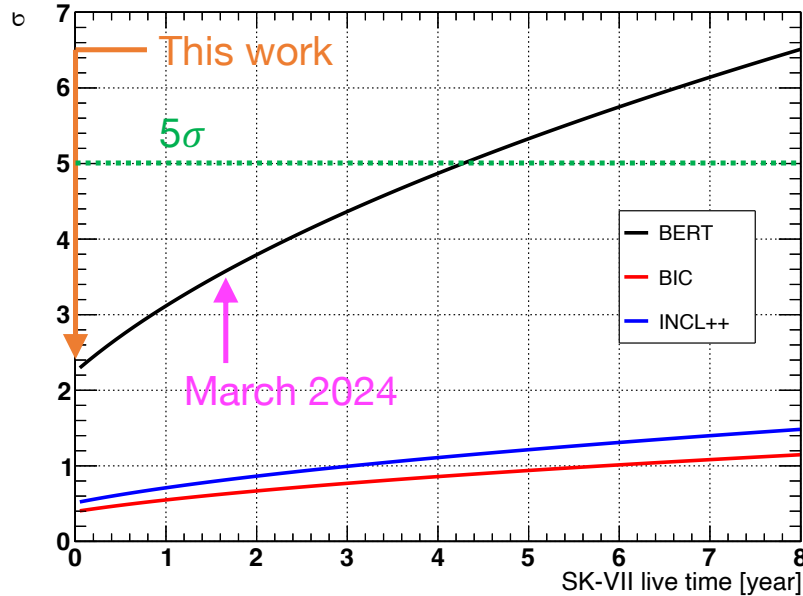


Figure 9.4: Expectation of the difference between the observed and expected number of events in $\theta_C \in [78, 90]$ degrees as a function of SK-VII live time. This difference is estimated using the observed and expected number of events summarized in Table 7.3. As for the observed number of events, statistical uncertainty is considered for this estimation. As for the expected number of events, systematic uncertainties other than secondary interaction are considered for this estimation. Here, it is assumed that the neutron tagging efficiency in SK-VII is 63.0% [125].

9.2 Conclusion

We performed the comparison of secondary interaction models using atmospheric neutrino events and the measurement of the atmospheric neutrino-oxygen NCQE cross section using 552.2 days of SK-VI data with 0.011% Gd-loaded water. Since the backgrounds in this study are the same as those in the DSNB search, event selections in the DSNB search were mainly adopted. Moreover, since multiple gamma-rays and multiple neutrons are easily emitted in NCQE events, we selected the events that θ_C is greater than 50 degrees and N_{delayed} is greater or equal to one.

After applying all event selections to 552.2 days of SK-VI data, 38 events remained. In order to understand which secondary interaction model reproduces the observed data, we calculated the chi-square for θ_C , E_{vis} , and N_{delayed} distributions using the Poisson-likelihood. As a result, due to the small statistics, the chi-square could not give conclusive results; however, the chi-square values were smaller for BIC and INCL++ than for BERT in all distributions. The results suggest that the evaporation model used in BIC and INCL++ reproduces the observed data better than that used in BERT. Furthermore, we measured the atmospheric neutrino-oxygen NCQE cross section using the atmospheric neutrino flux-averaged theoretical NCQE cross section, the observed number of events, and the expected numbers of events. As a result, the NCQE cross section was measured to be $0.74 \pm 0.22(\text{stat.})^{+0.85}_{-0.15}(\text{syst.}) \times 10^{-38} \text{ cm}^2/\text{oxygen}$ in the energy range from 160 MeV to 10 GeV, which was consistent with the atmospheric neutrino flux-averaged theoretical NCQE cross section ($1.02 \times 10^{-38} \text{ cm}^2/\text{oxygen}$) and the measured NCQE cross section in the SK pure-water phase ($1.01 \pm 0.17(\text{stat.})^{+0.78}_{-0.30}(\text{syst.}) \times 10^{-38} \text{ cm}^2/\text{oxygen}$). The large systematic uncertainty mainly comes from the difference of secondary interaction models.

Now we continue the observation with a 0.03% Gd-loaded SK detector, the phase known as SK-VII. Assuming that the neutron-tagging efficiency in SK-VII is 63.0%, the statistics increases by about 1.4 times with the same live time as SK-VI, and the statistical uncertainty will be half of this work by combining about three years of data in SK-VII. Moreover, when we focus on the observed and expected number of events in $\theta_C \in [78, 90]$ degrees, BERT is now $\sim 2.2\sigma$ away from the data. By combining about four years of data in SK-VII, the evaporation model can be determined at 5σ . Once the evaporation model is determined, the secondary interaction uncertainty is reduced, and the systematic uncertainty of measured NCQE cross section is significantly reduced.

A Chi-square using the Poisson-likelihood

$L(x, y)$ is defined as

$$L(x, y) = \prod_{i=1}^{\text{bin}} \frac{y_i^{x_i}}{x_i!} e^{-y_i}, \quad (\text{A.1})$$

where bin is the number of bins in a histogram. The chi-square using the Poisson-likelihood χ^2 is calculated as

$$\begin{aligned} \chi^2 &= -2 \ln \frac{L(n, \mu)}{L(n, n)} \\ &= -2\{\ln L(n, \mu) - \ln L(n, n)\} \\ &= -2\left\{ \ln\left(\prod_{i=1}^{\text{bin}} \frac{\mu_i^{n_i}}{n_i!} e^{-\mu_i}\right) - \ln\left(\prod_{i=1}^{\text{bin}} \frac{n_i^{n_i}}{n_i!} e^{-n_i}\right) \right\} \\ &= -2\left\{ \sum_{i=1}^{\text{bin}} \ln\left(\frac{\mu_i^{n_i}}{n_i!} e^{-\mu_i}\right) - \sum_{i=1}^{\text{bin}} \ln\left(\frac{n_i^{n_i}}{n_i!} e^{-n_i}\right) \right\} \\ &= -2\left[\sum_{i=1}^{\text{bin}} \{\ln(\mu_i^{n_i}) + \ln(e^{-\mu_i}) - \ln(n_i!)\} - \sum_{i=1}^{\text{bin}} \{\ln(n_i^{n_i}) + \ln(e^{-n_i}) - \ln(n_i!)\} \right] \\ &= -2\left[\sum_{i=1}^{\text{bin}} \{n_i \ln \mu_i - \mu_i - \ln(n_i!)\} - \sum_{i=1}^{\text{bin}} \{n_i \ln n_i - n_i - \ln(n_i!)\} \right] \\ &= -2 \sum_{i=1}^{\text{bin}} \{n_i \ln \mu_i - \mu_i - \ln(n_i!) - n_i \ln n_i + n_i + \ln(n_i!)\} \\ &= 2 \sum_{i=1}^{\text{bin}} \left(\mu_i - n_i + n_i \ln \frac{n_i}{\mu_i} \right), \end{aligned} \quad (\text{A.2})$$

where n is the observed number of events and μ is the expected number of events⁸.

⁸Even if the chi-square using the Poisson-likelihood is defined as $\chi^2 = -2 \ln L(n, \mu)$, Equation (A.2) is derived by using the Stirling's approximation ($\ln(n!) \sim n \ln n - n$).

B Other distributions

B.1 Simulation

Other distributions related to Section 3 are summarized here.

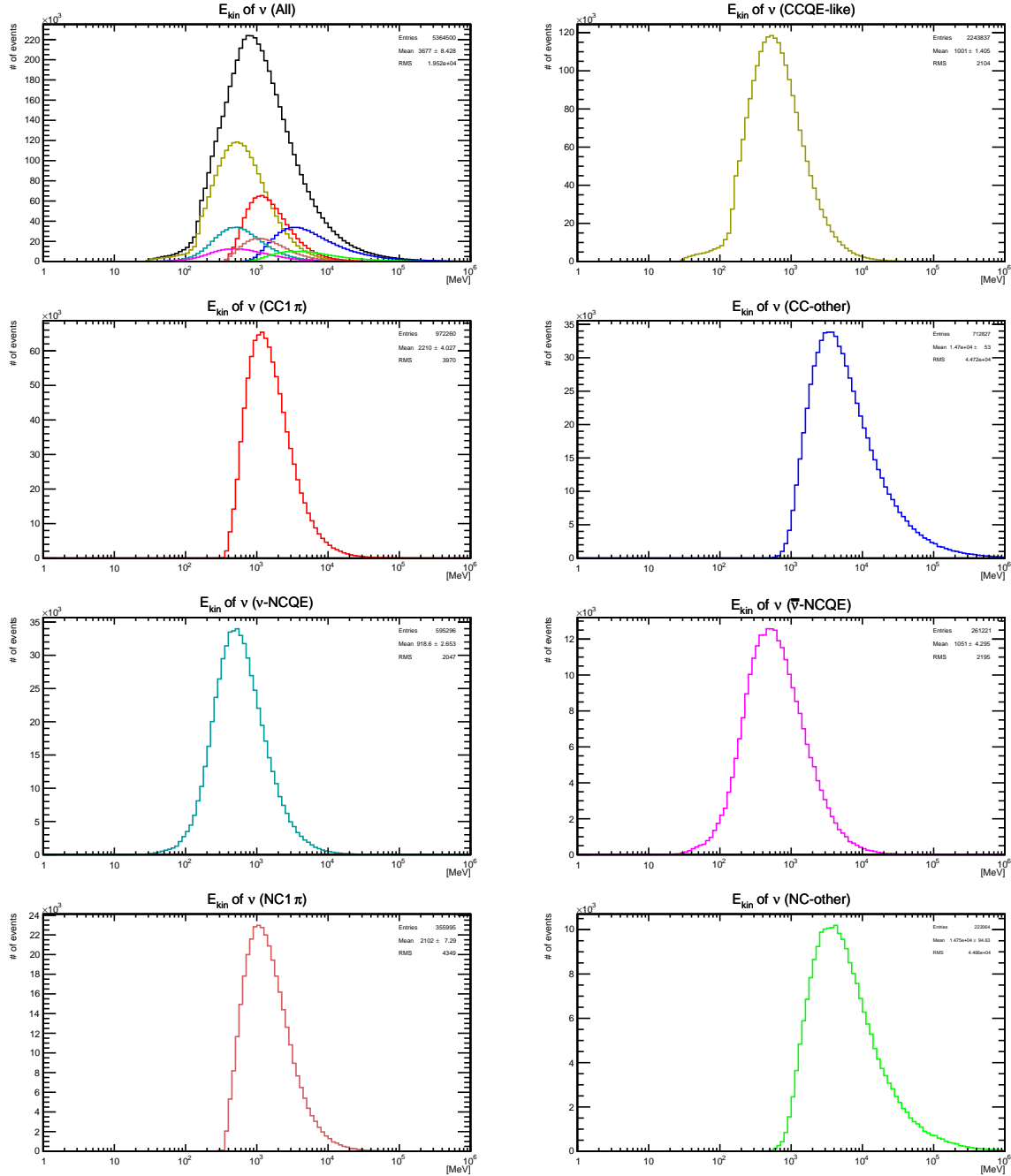


Figure B.1: Energy of atmospheric neutrinos that induced neutrino-nucleus interactions. These figures were made using 500 years' worth of atmospheric neutrino events.

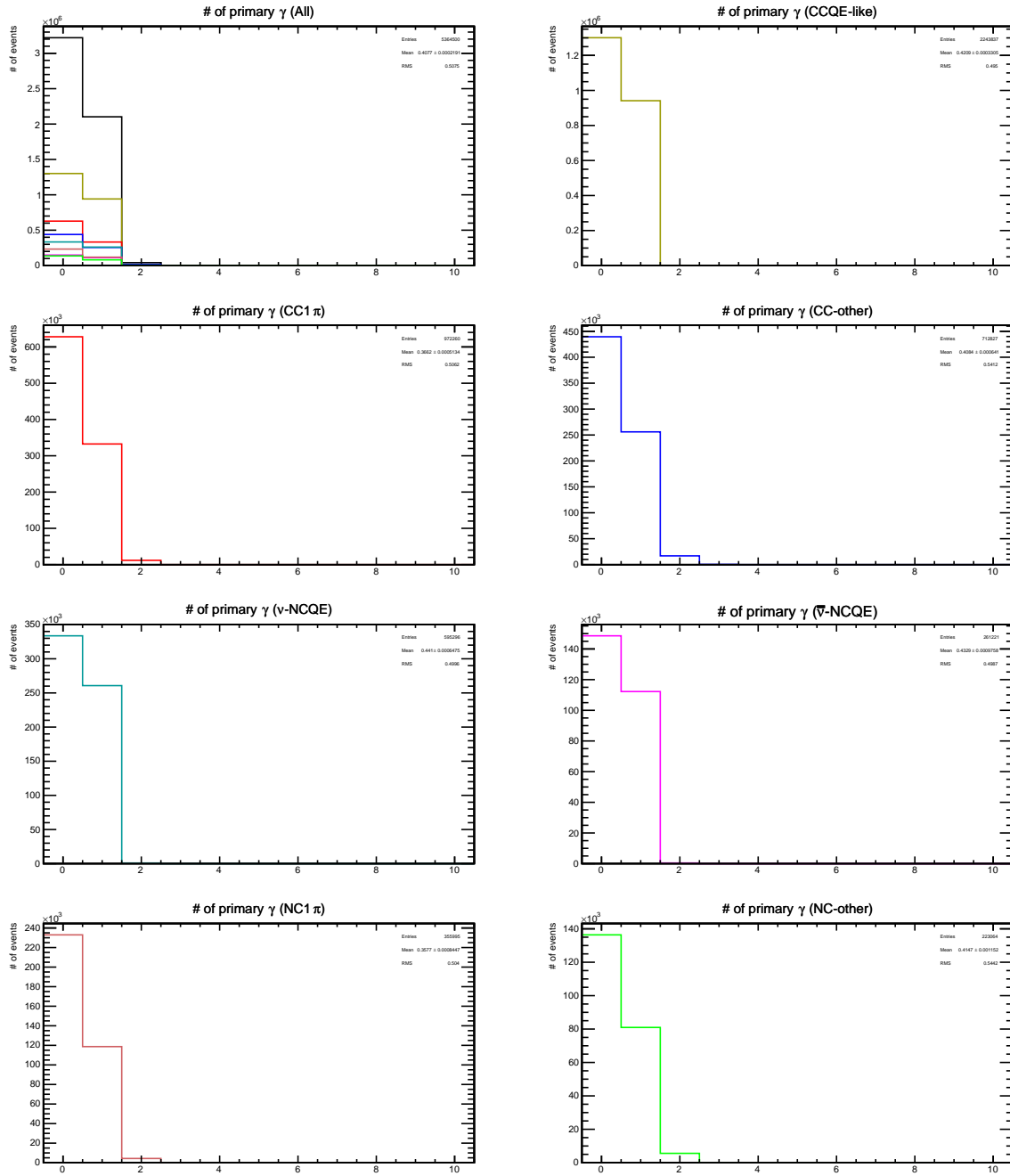


Figure B.2: The number of gamma-rays generated by neutrino-nucleus interactions. These figures were made using 500 years' worth of atmospheric neutrino events.

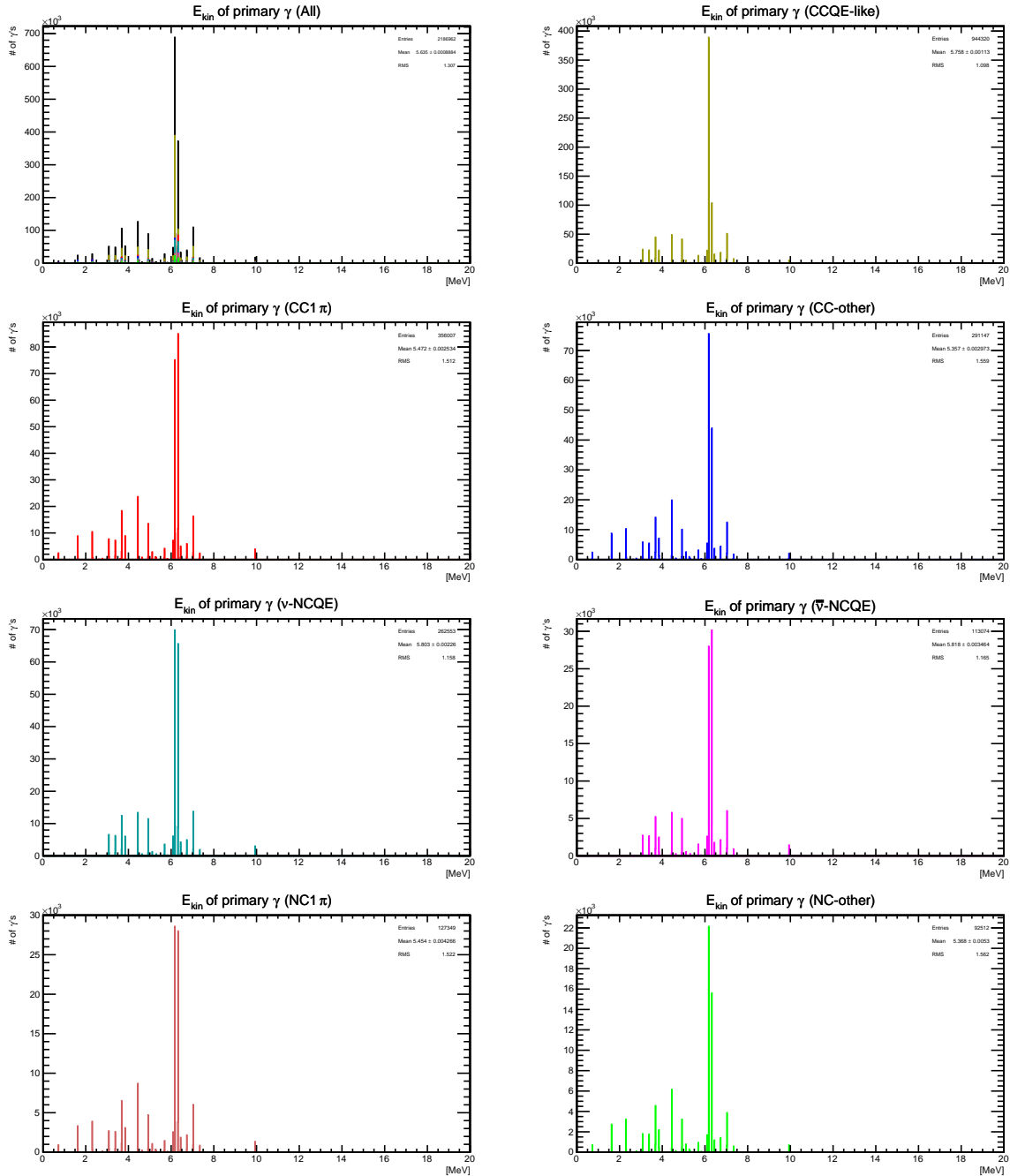


Figure B.3: Energy of gamma-rays generated by neutrino-nucleus interactions. These figures were made using 500 years' worth of atmospheric neutrino events.

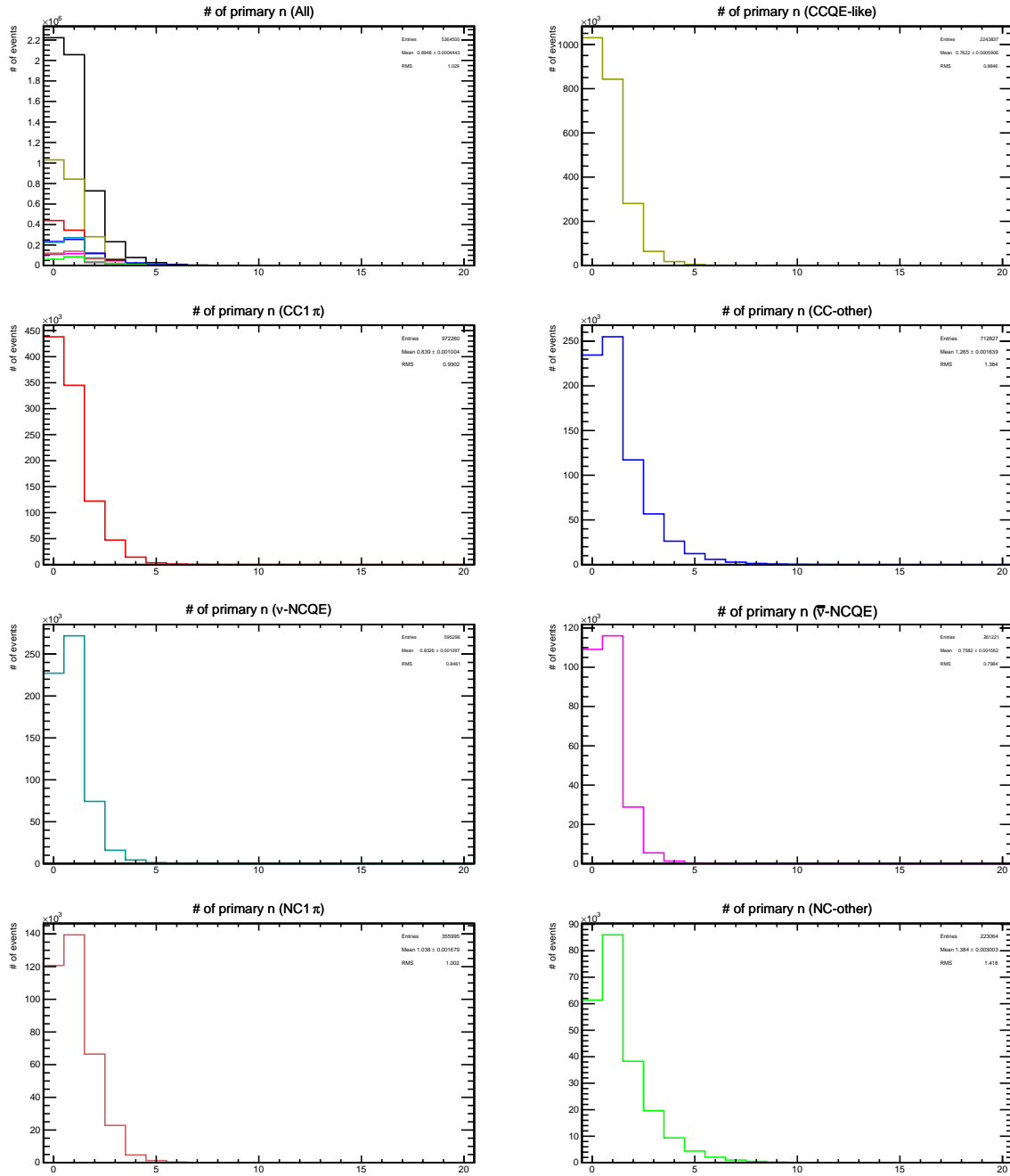


Figure B.4: The number of neutrons generated by neutrino-nucleus interactions. These figures were made using 500 years' worth of atmospheric neutrino events.

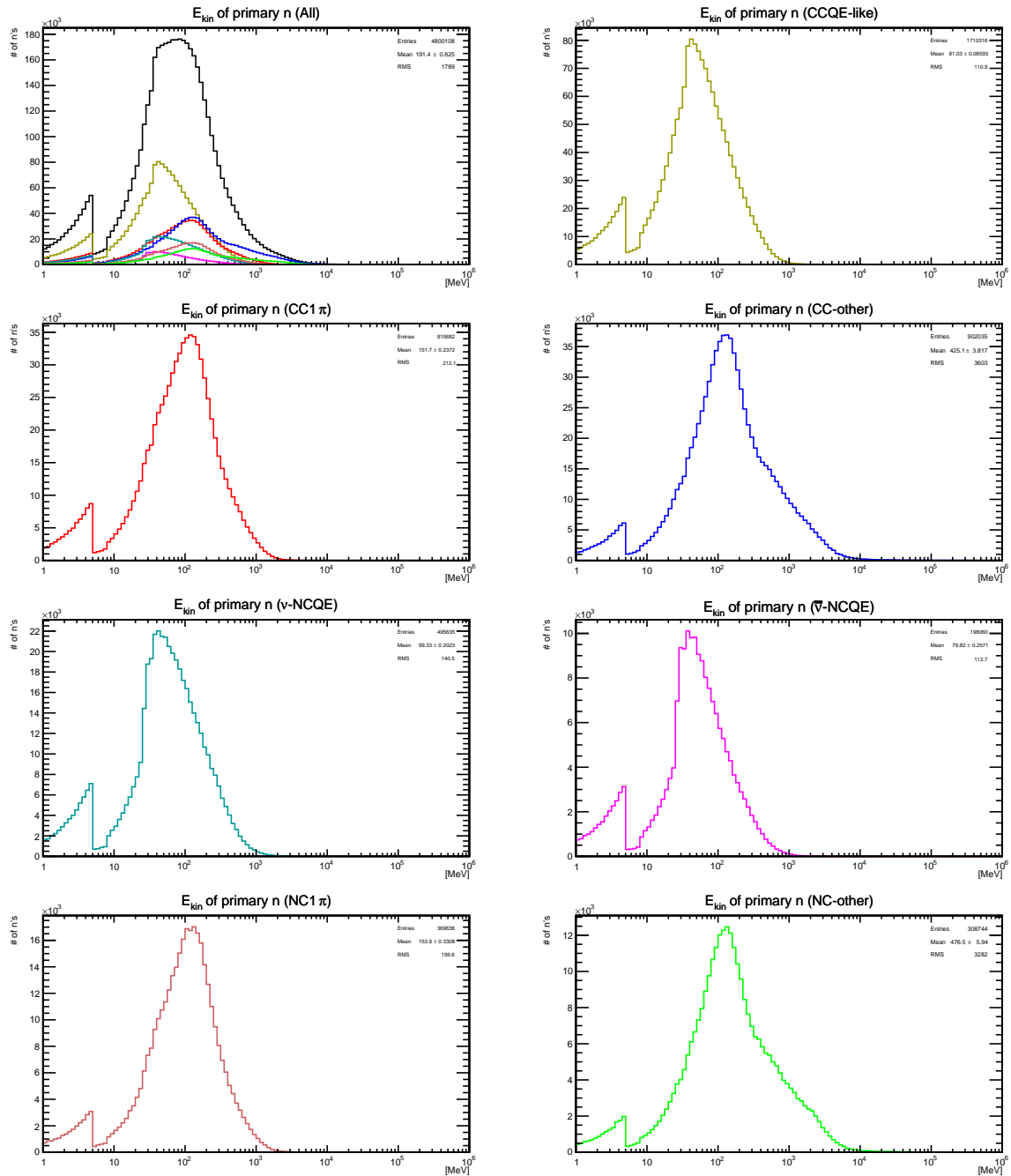


Figure B.5: Kinetic energy of neutrons generated by neutrino-nucleus interactions. These figures were made using 500 years' worth of atmospheric neutrino events.

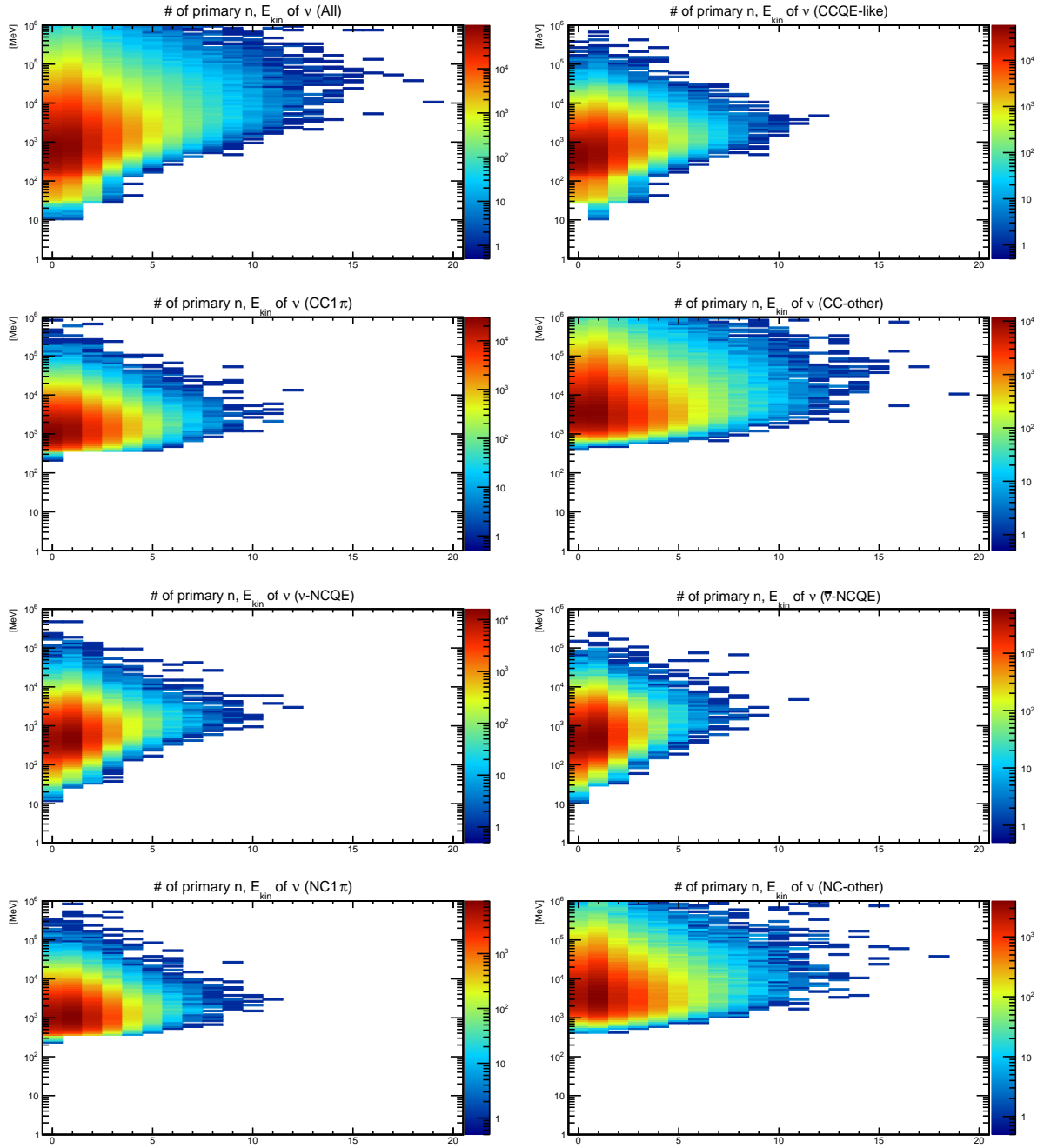


Figure B.6: 2D distribution of the number of neutrons generated by neutrino-nucleus interactions (the horizontal axis) and energy of atmospheric neutrinos that induced neutrino-nucleus interactions (the vertical axis). These figures were made using 500 years' worth of atmospheric neutrino events.

B.2 Event selection

Other distributions related to Section 6 are summarized here.

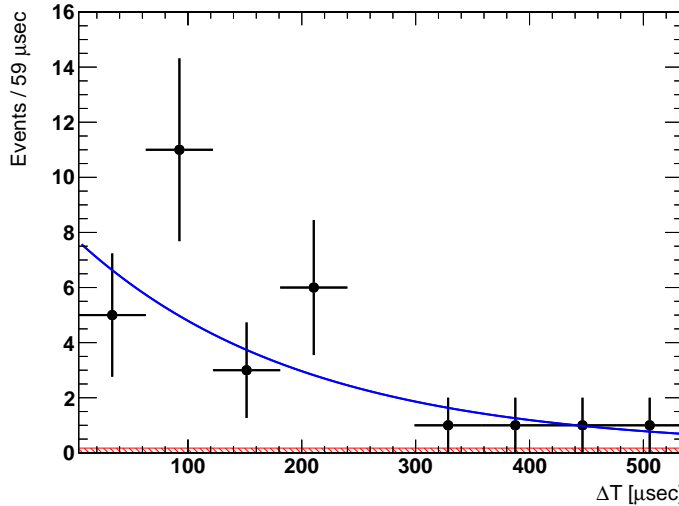


Figure B.7: Timing of delayed signals. Black plots show the data that $N_{\text{delayed}} = 1$. Red area shows the accidental coincidence events. Blue line shows the fitted exponential distribution ($p_0 \exp(-x/p_1) + p_2$). In this distribution, $p_0 = 7.646 \pm 2.470$ and $p_1 = 198.5 \pm 62.1$ [μs]. The constant term (p_2) was fixed at the number of accidental coincidence events per bin (= 1.5524/9) during the fitting.

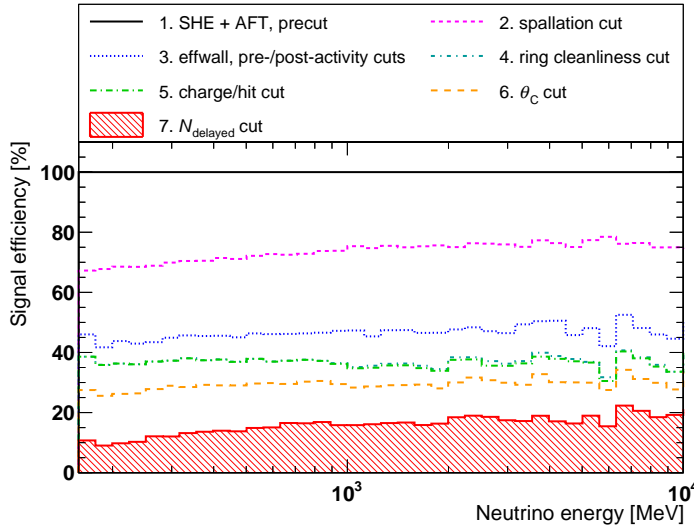


Figure B.8: NCQE cumulative signal efficiencies as a function of neutrino energy. Event reductions are performed in the order shown in the legend, and before the reduction for spallation events is taken as 100%.

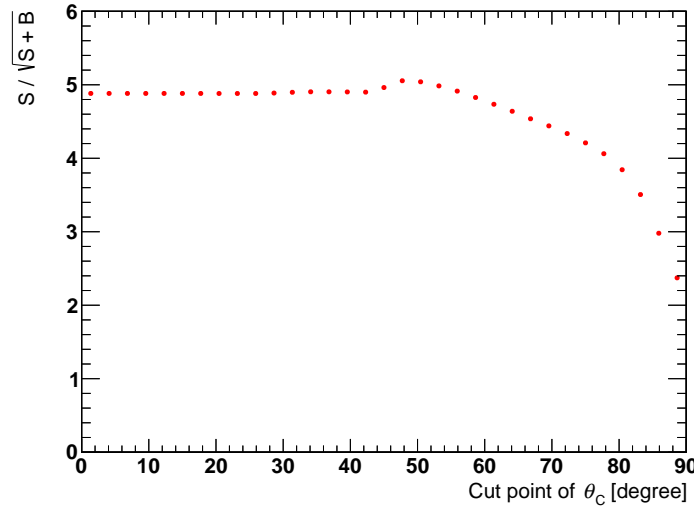


Figure B.9: Singal-to-background ratio. Horizontal axis shows the θ_C cut point. Vertical axis shows the singal-to-background ratio $S/\sqrt{S+B}$, where S is the expected number of NCQE events and B is the expected number of events, including CC, spallation, reactor neutrino, and accidental coincidence.

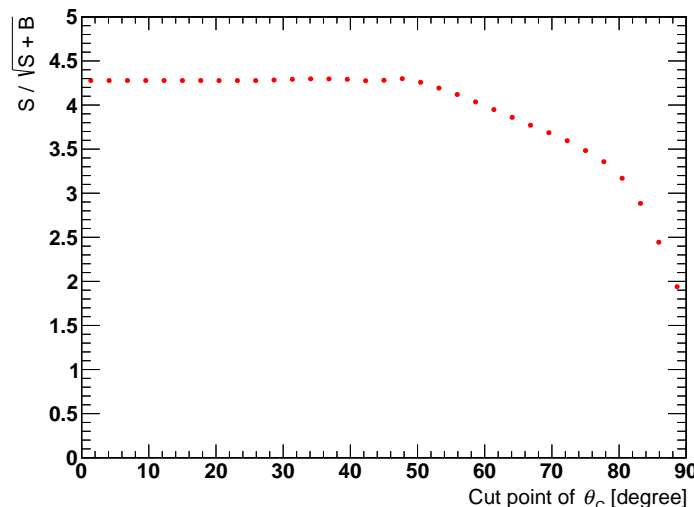


Figure B.10: Singal-to-background ratio. Horizontal axis shows the θ_C cut point. Vertical axis shows the singal-to-background ratio $S/\sqrt{S+B}$, where S is the expected number of NCQE events and B is the expected number of events, including NC non-QE, CC, spallation, reactor neutrino, and accidental coincidence.

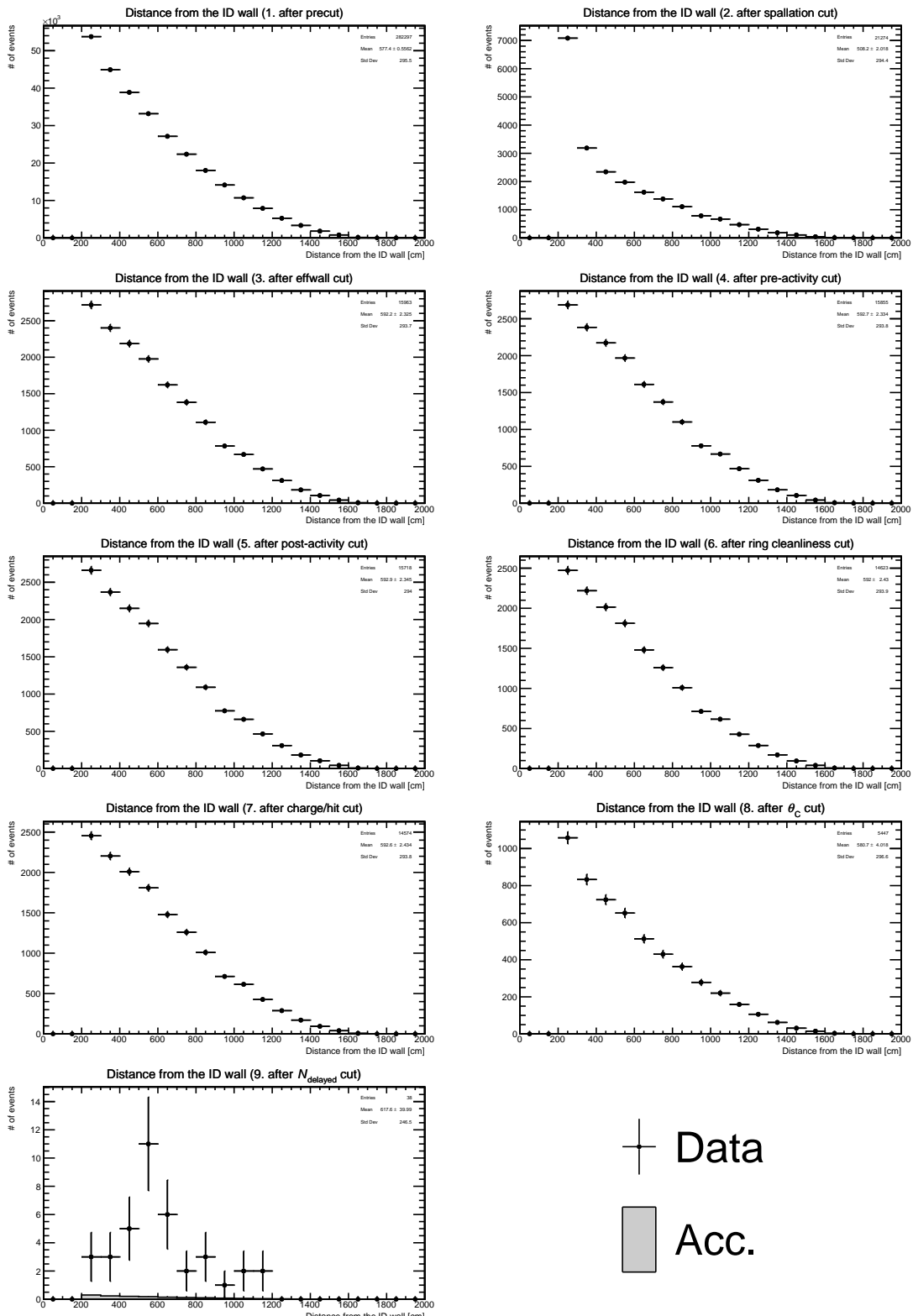


Figure B.11: Distance form the ID wall for the data and accidental coincidence events. Event reductions are performed in the order shown in the title.

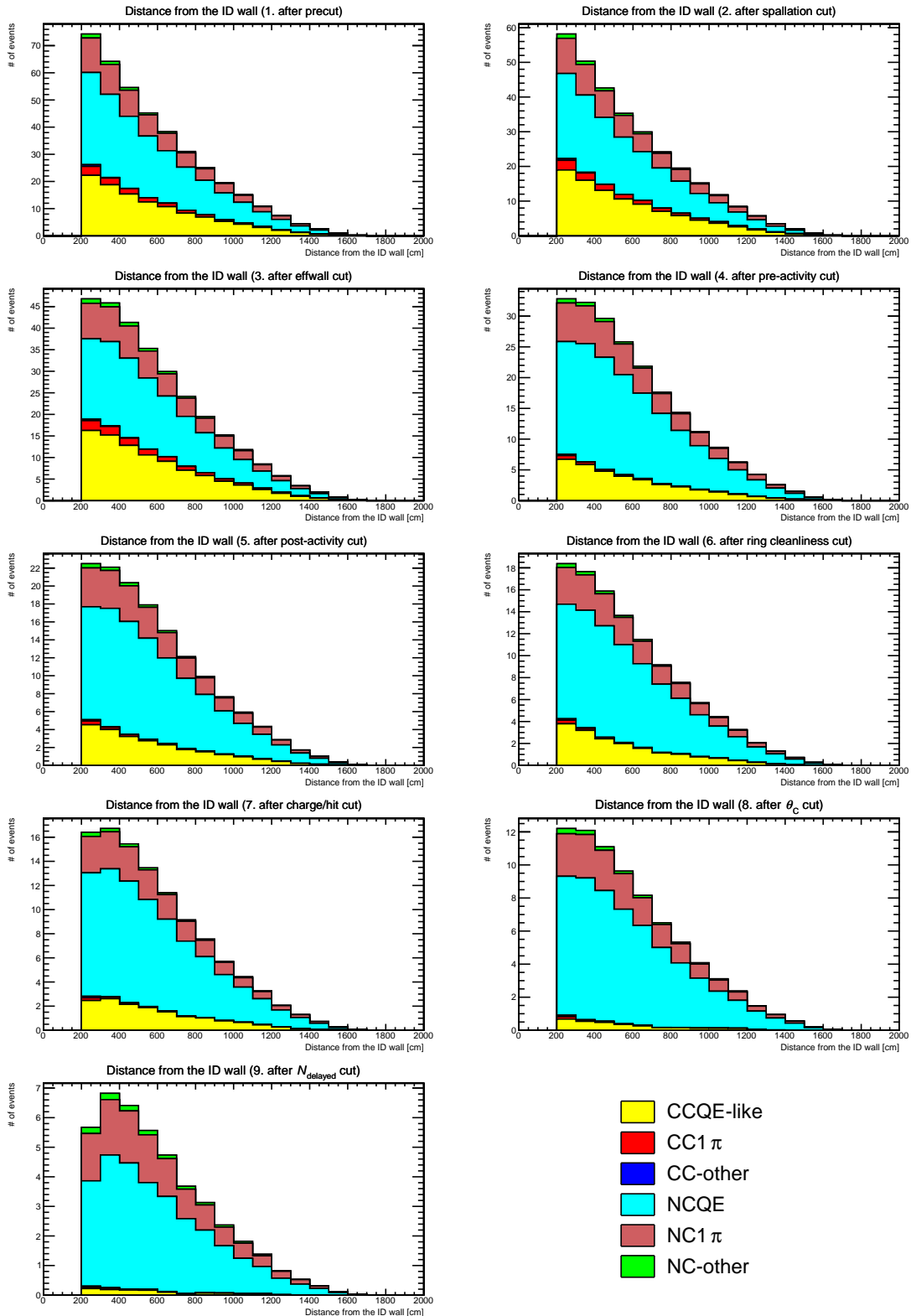


Figure B.12: Distance form the ID wall for atmospheric neutrino events. Event reductions are performed in the order shown in the title.

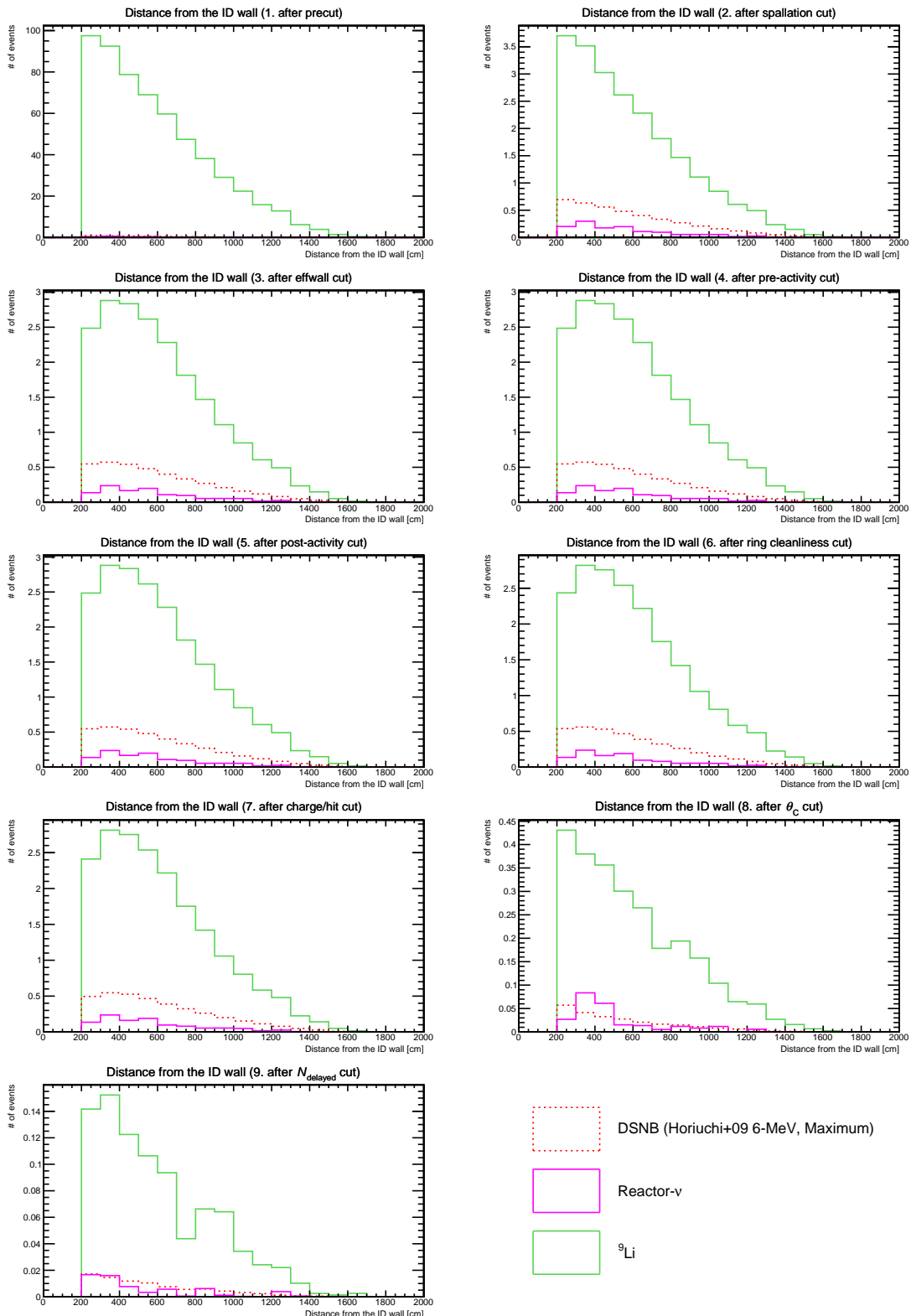


Figure B.13: Distance form the ID wall for spallation, reactor neutrino, and DSNB events. Event reductions are performed in the order shown in the title.

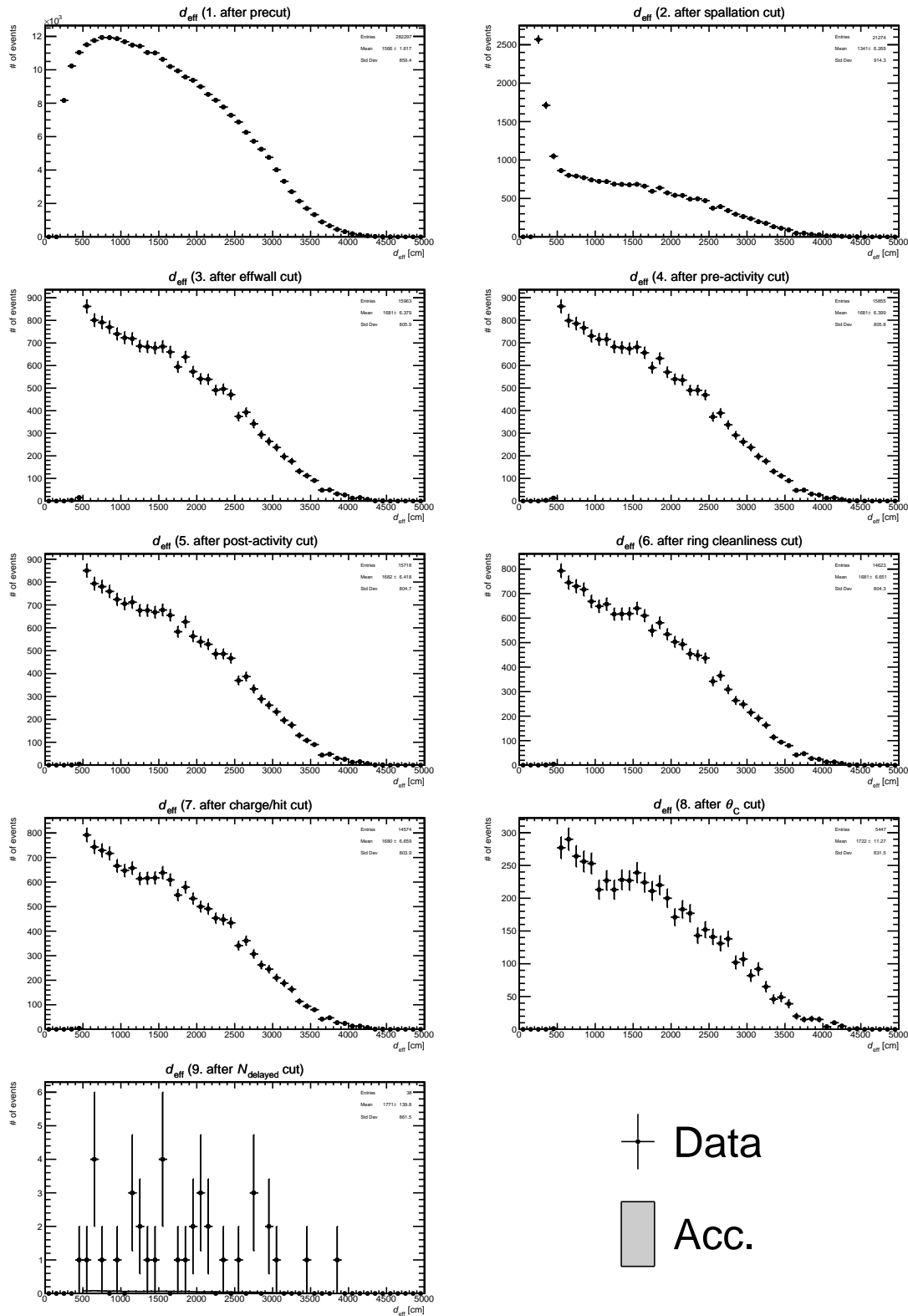


Figure B.14: d_{eff} for the data and accidental coincidence events. Event reductions are performed in the order shown in the title.

 Data
 Acc.

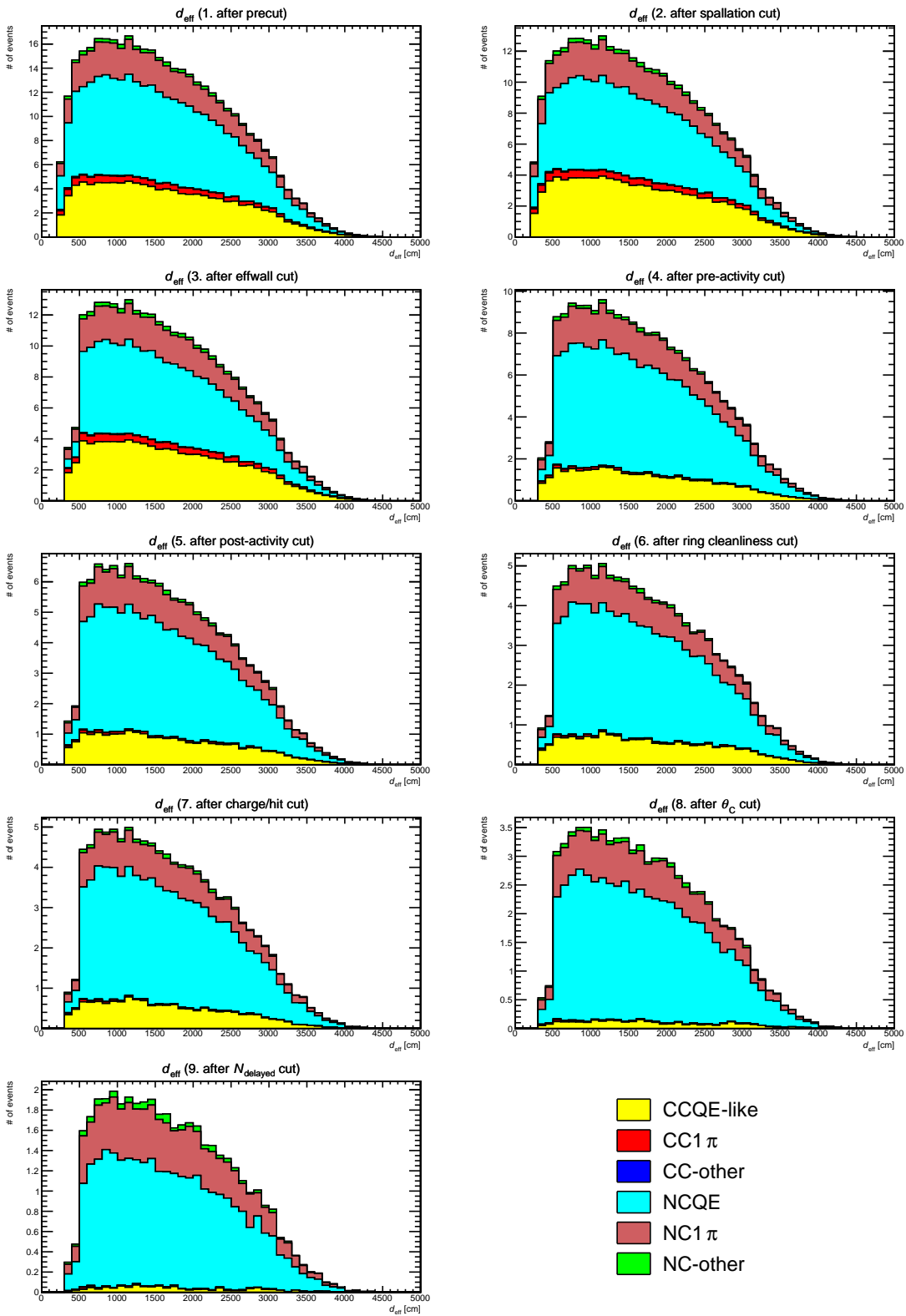


Figure B.15: d_{eff} for atmospheric neutrino events. Event reductions are performed in the order shown in the title.

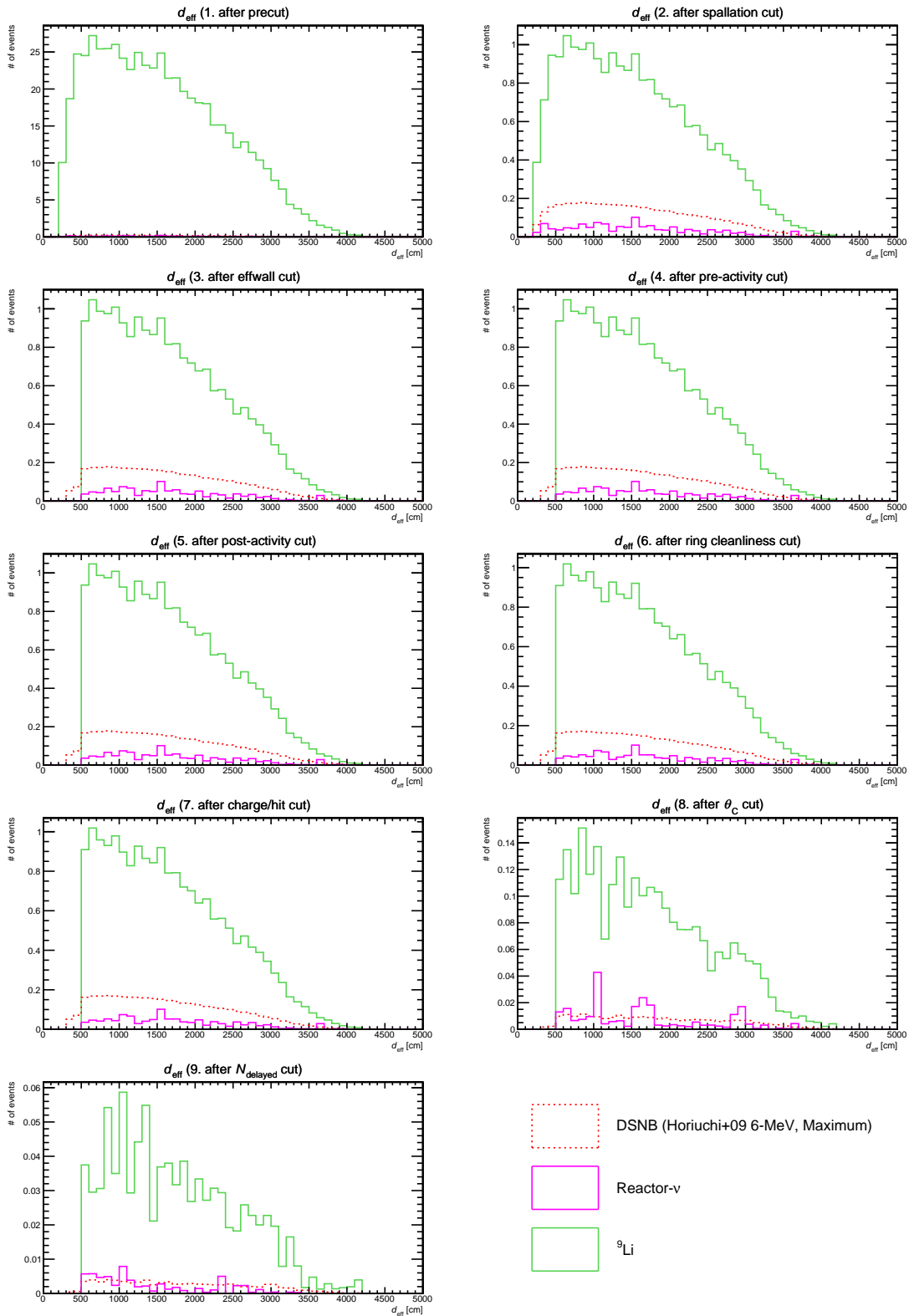
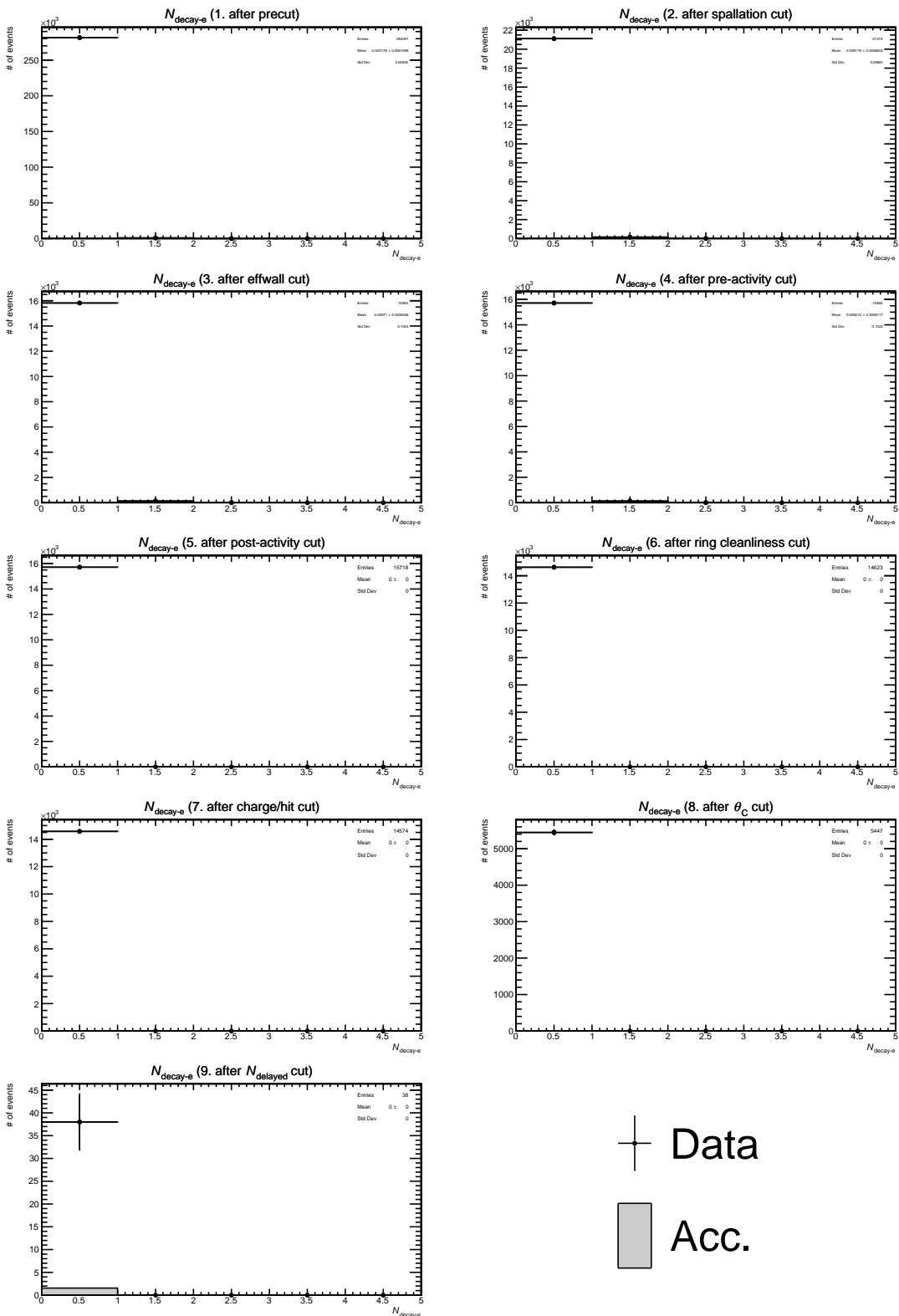


Figure B.16: d_{eff} for spallation, reactor neutrino, and DSNB events. Event reductions are performed in the order shown in the title.



 Data
 Acc.

Figure B.17: $N_{\text{decay-e}}$ for the data and accidental coincidence events. Event reductions are performed in the order shown in the title.

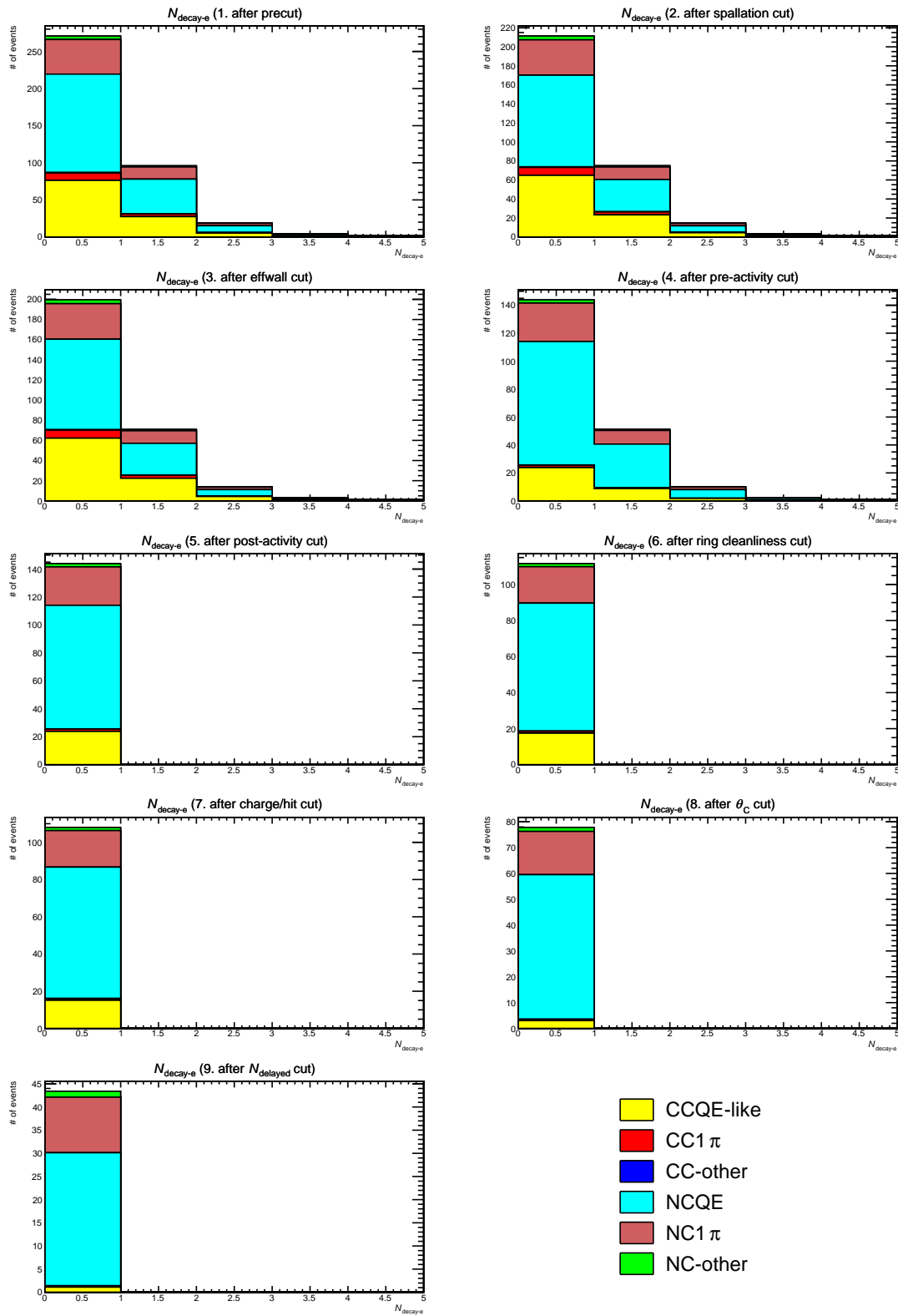


Figure B.18: $N_{\text{decay-e}}$ for atmospheric neutrino events. Event reductions are performed in the order shown in the title.

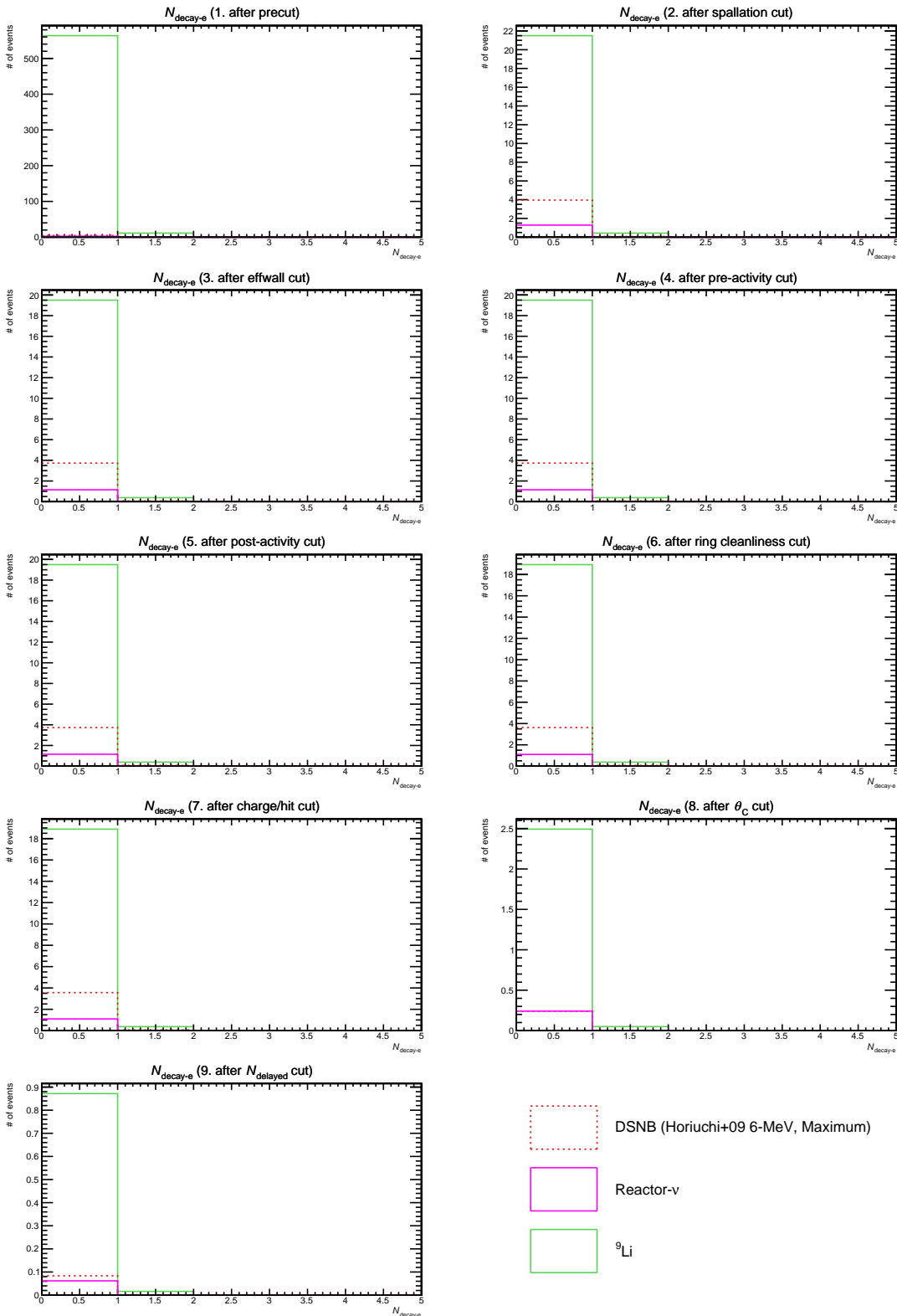
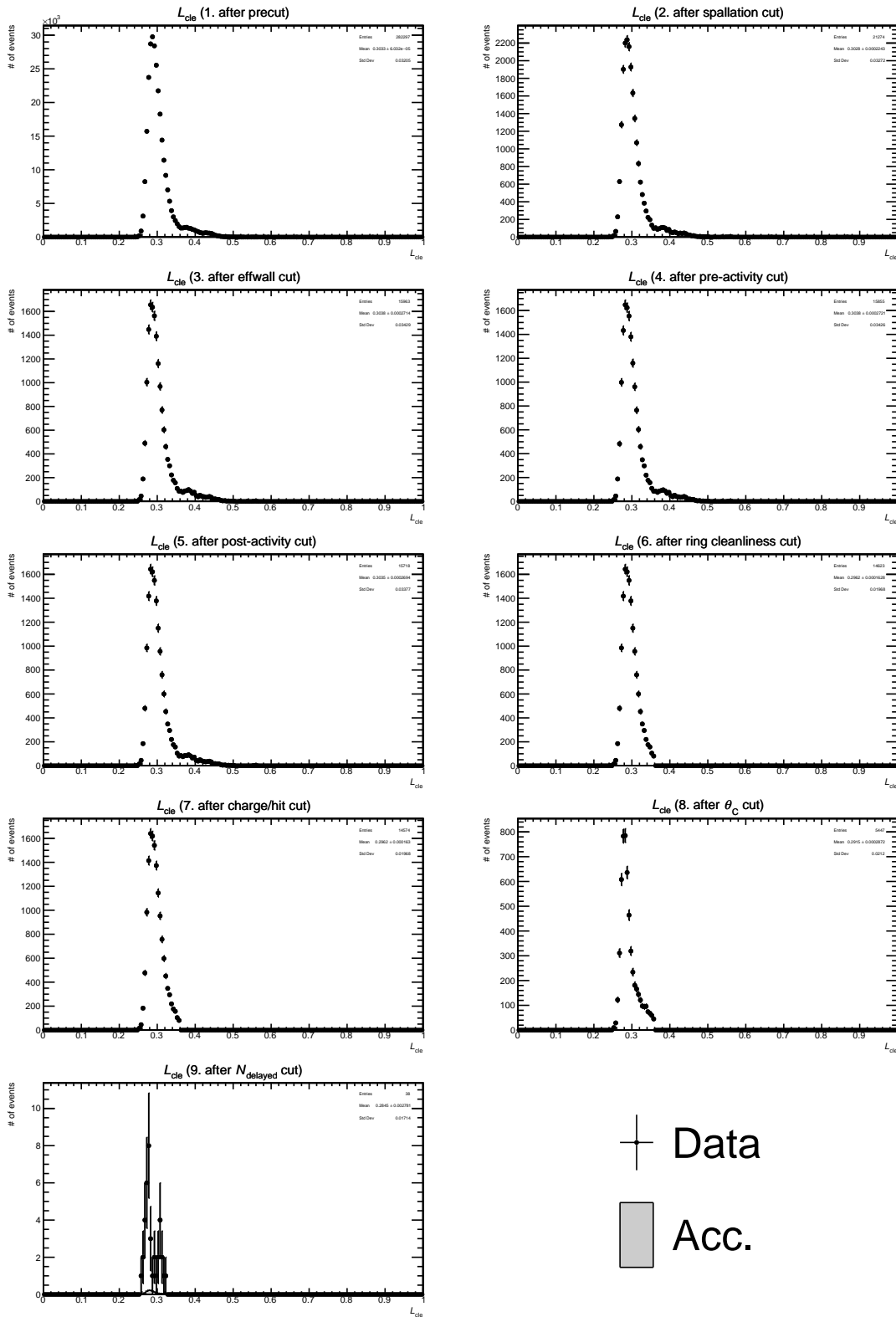


Figure B.19: $N_{\text{decay-e}}$ for spallation, reactor neutrino, and DSNB events. Event reductions are performed in the order shown in the title.



Data
 Acc.

Figure B.20: L_{cle} for the data and accidental coincidence events. Event reductions are performed in the order shown in the title.

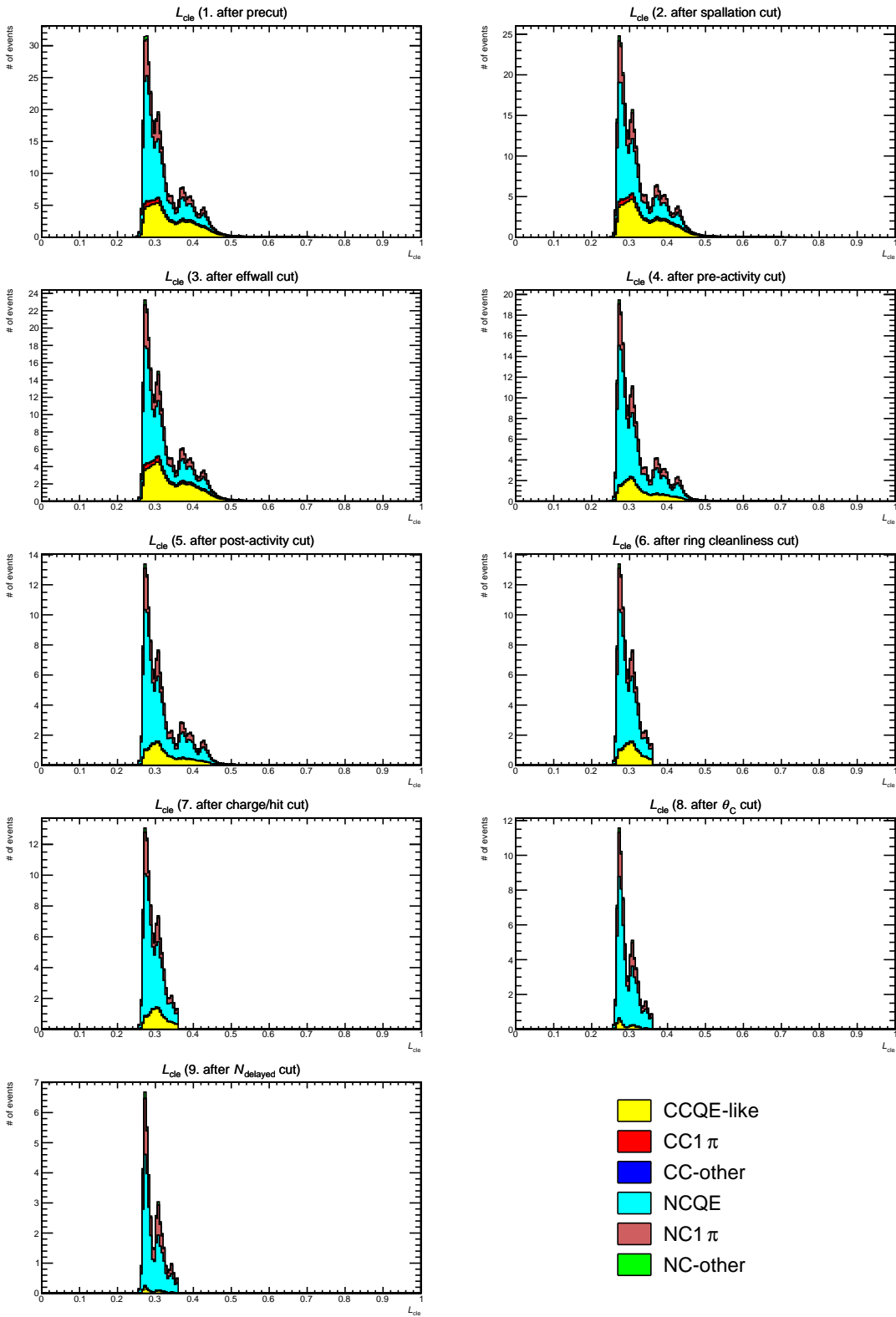


Figure B.21: L_{cle} for atmospheric neutrino events. Event reductions are performed in the order shown in the title.

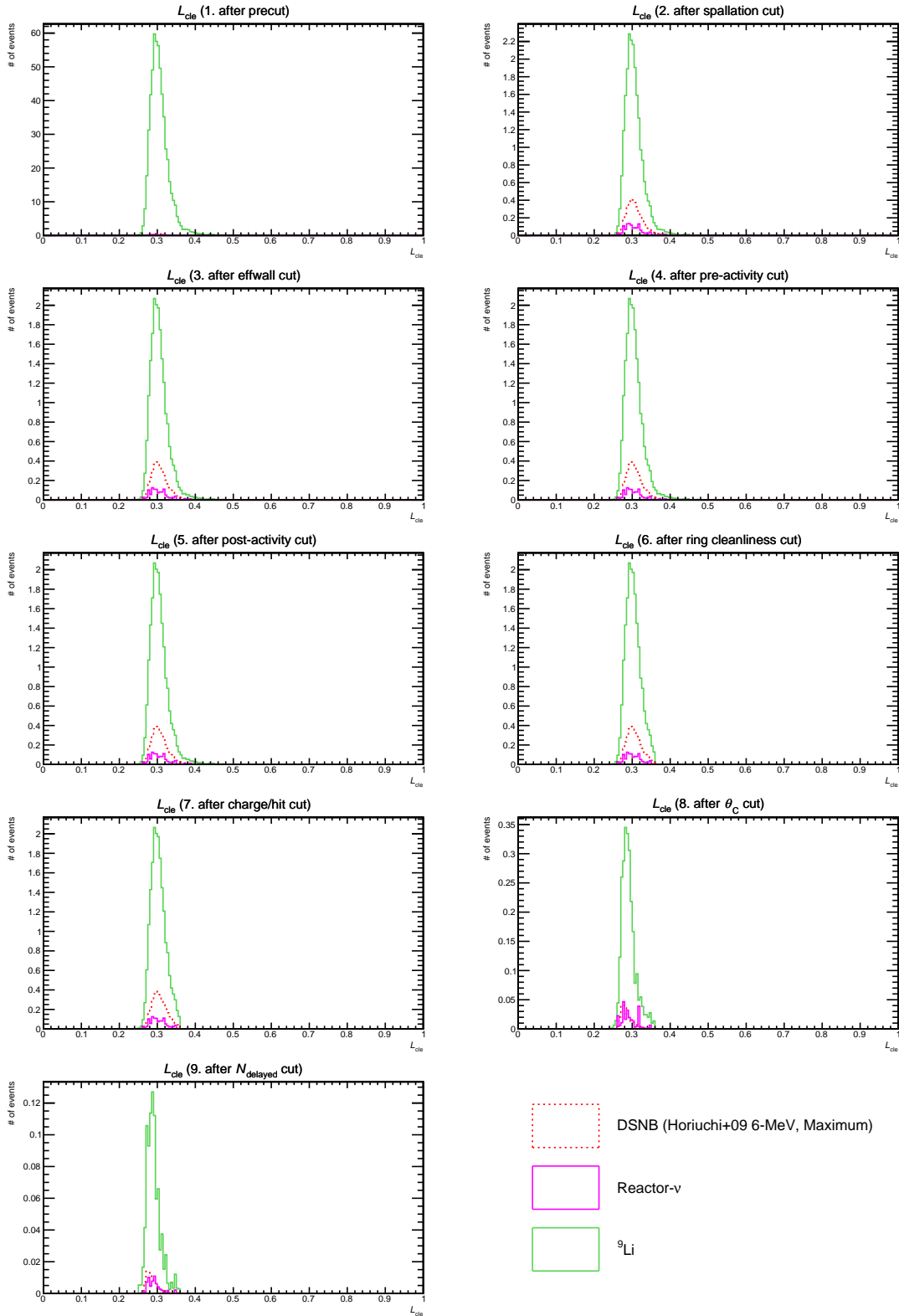


Figure B.22: L_{cle} for spallation, reactor neutrino, and DSNB events. Event reductions are performed in the order shown in the title.

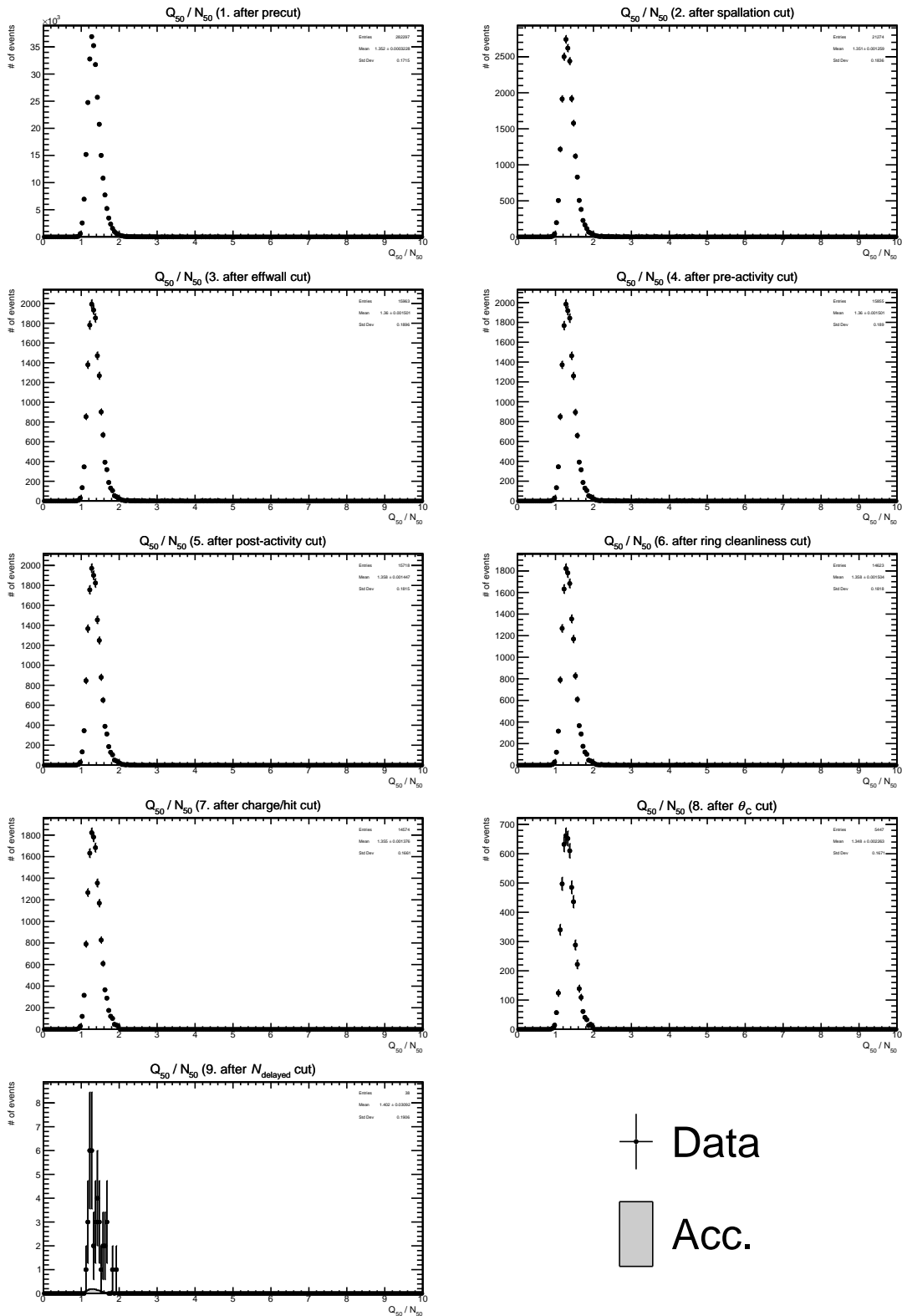


Figure B.23: Q_{50}/N_{50} for the data and accidental coincidence events. Event reductions are performed in the order shown in the title.

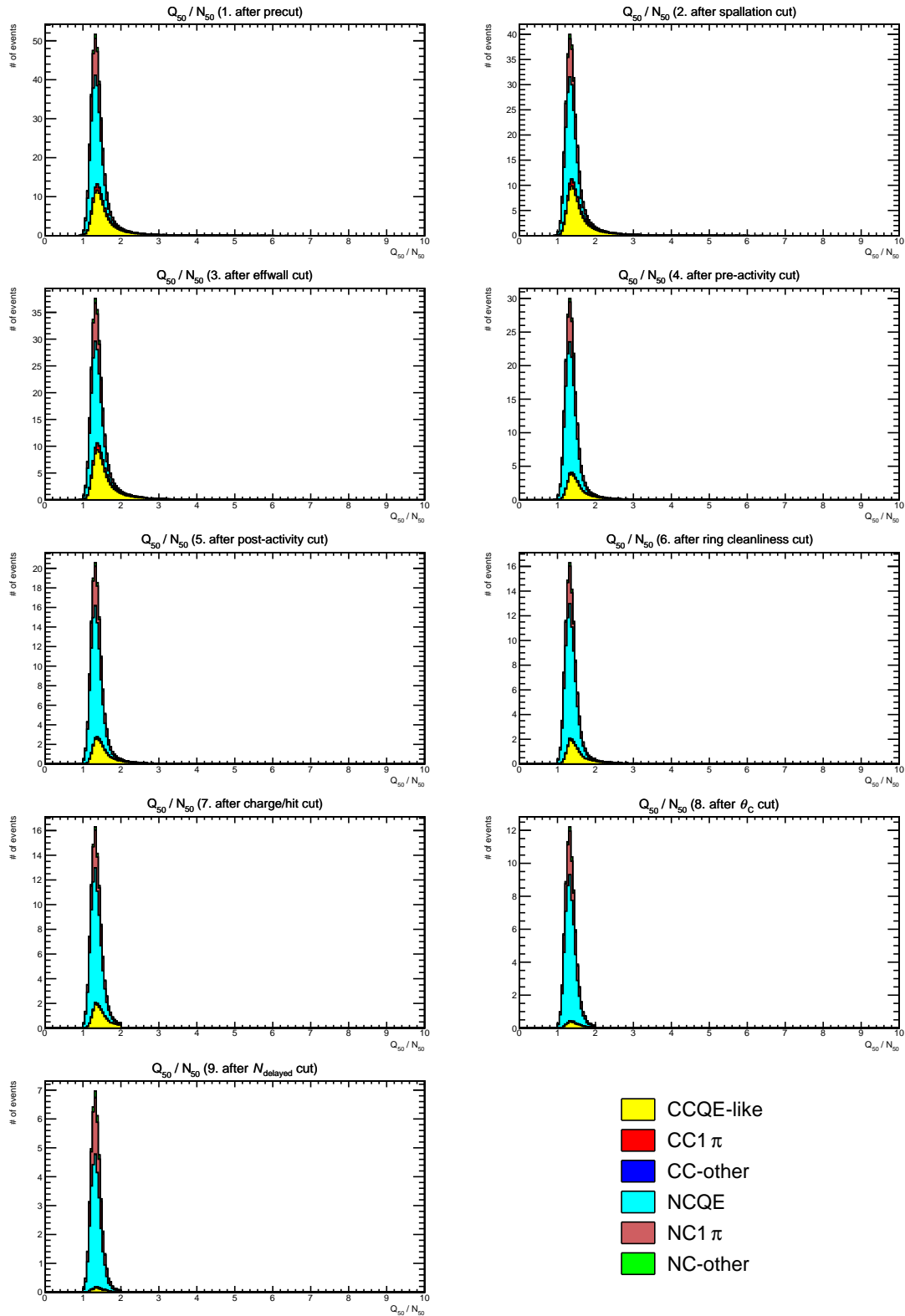


Figure B.24: Q_{50}/N_{50} for atmospheric neutrino events. Event reductions are performed in the order shown in the title.

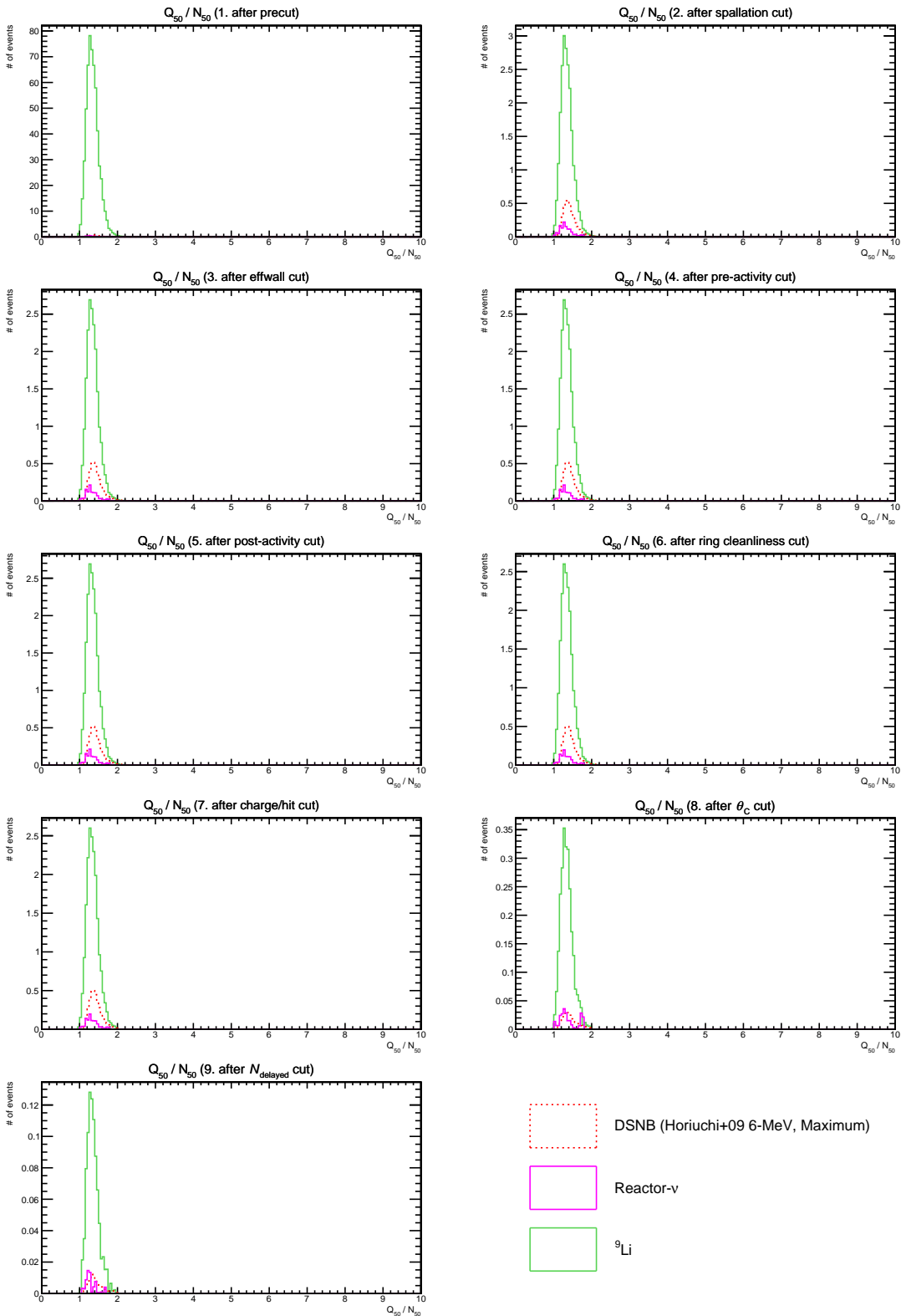


Figure B.25: Q_{50}/N_{50} for spallation, reactor neutrino, and DSNB events. Event reductions are performed in the order shown in the title.

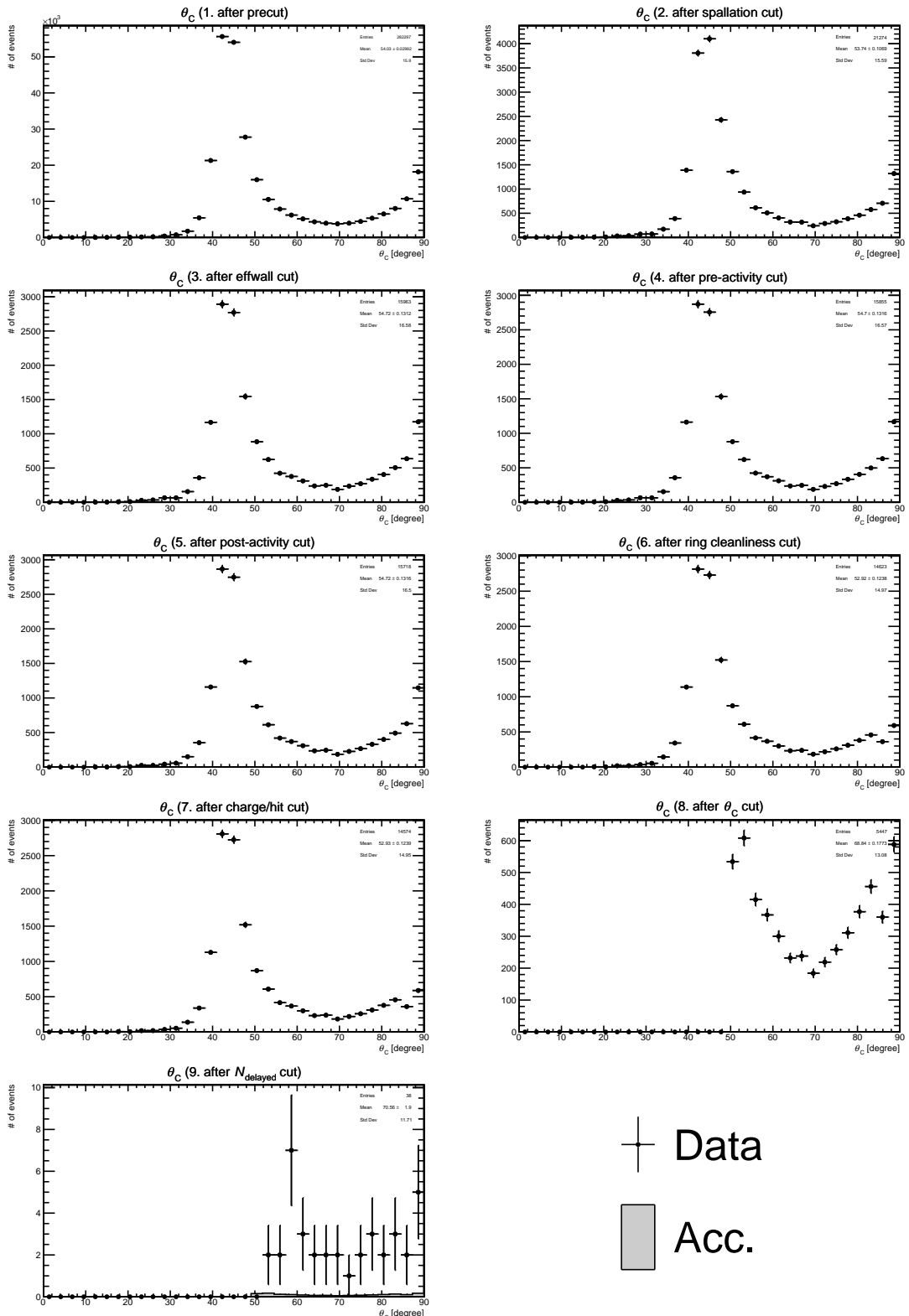


Figure B.26: θ_C for the data and accidental coincidence events. Event reductions are performed in the order shown in the title.

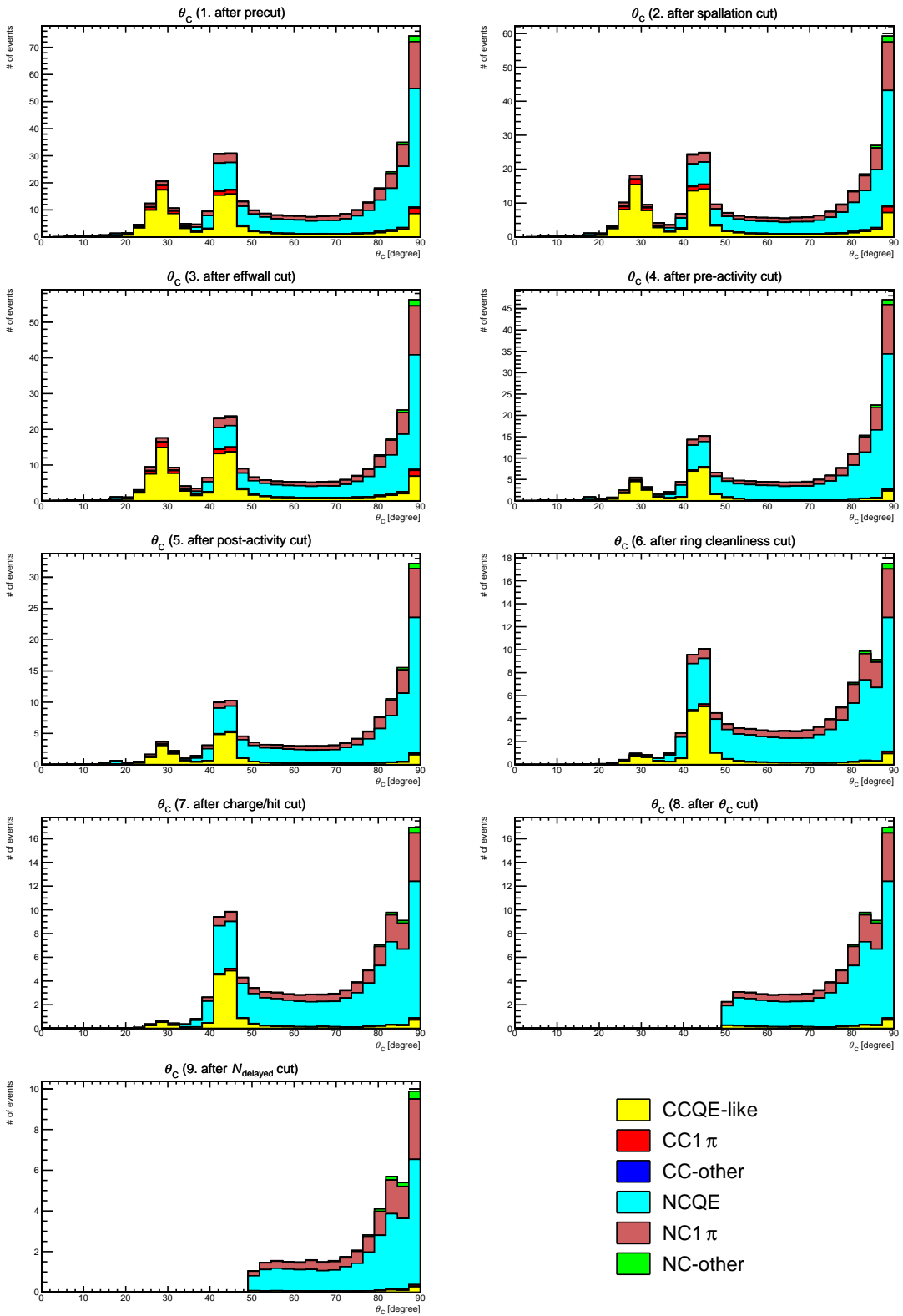


Figure B.27: θ_C for atmospheric neutrino events. Event reductions are performed in the order shown in the title.

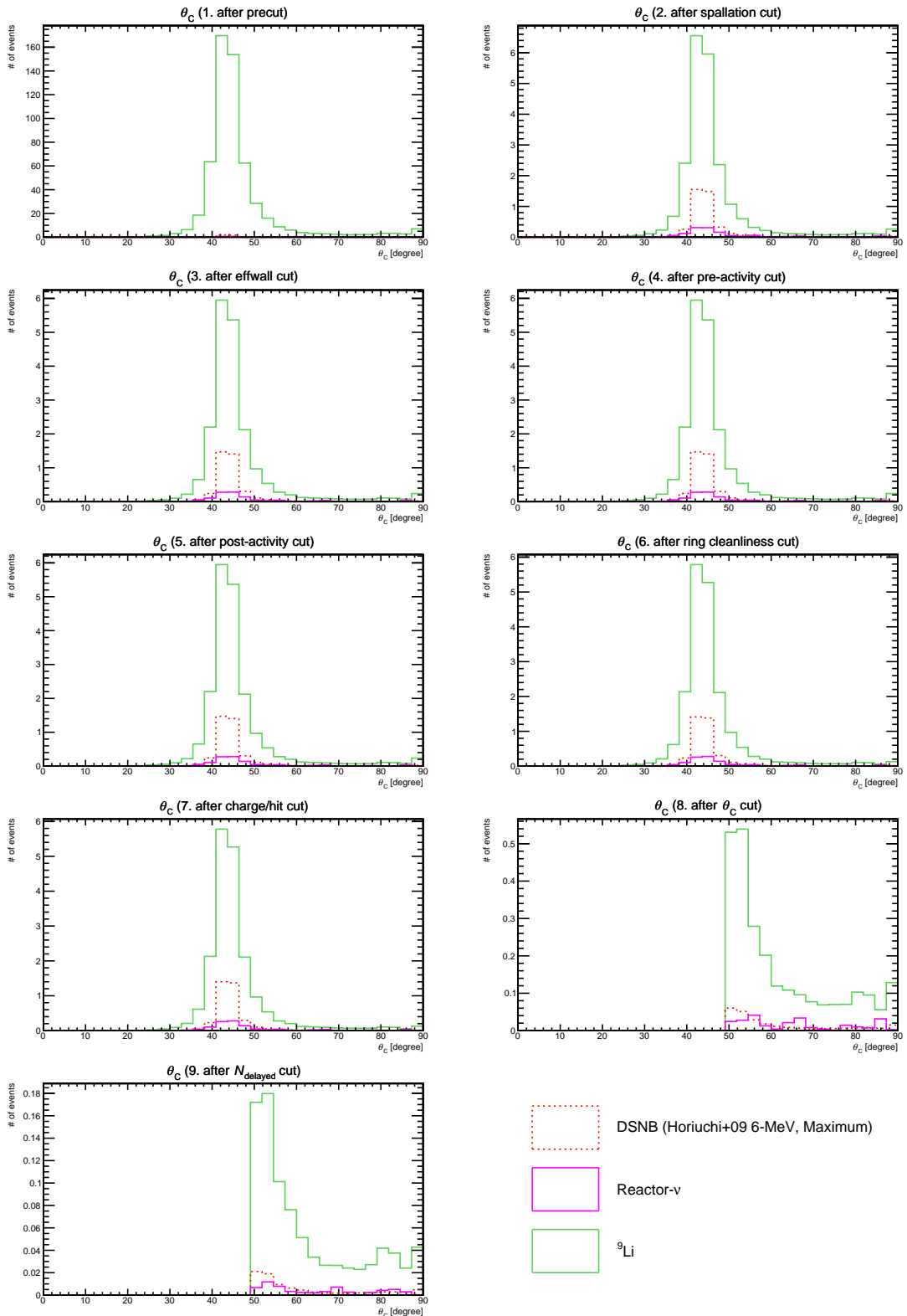


Figure B.28: θ_C for spallation, reactor neutrino, and DSNB events. Event reductions are performed in the order shown in the title.

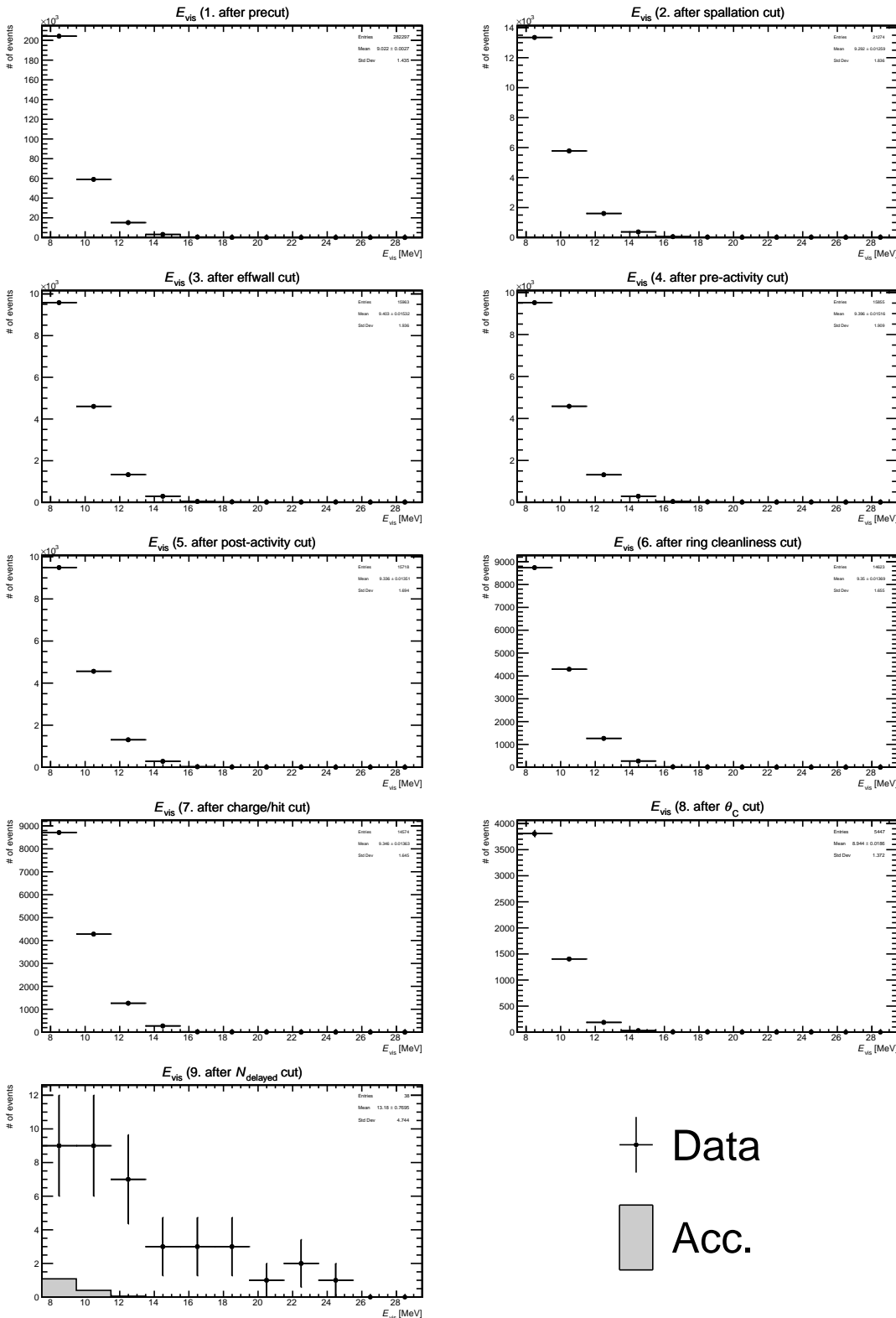


Figure B.29: E_{vis} for the data and accidental coincidence events. Event reductions are performed in the order shown in the title.

 Data
 Acc.

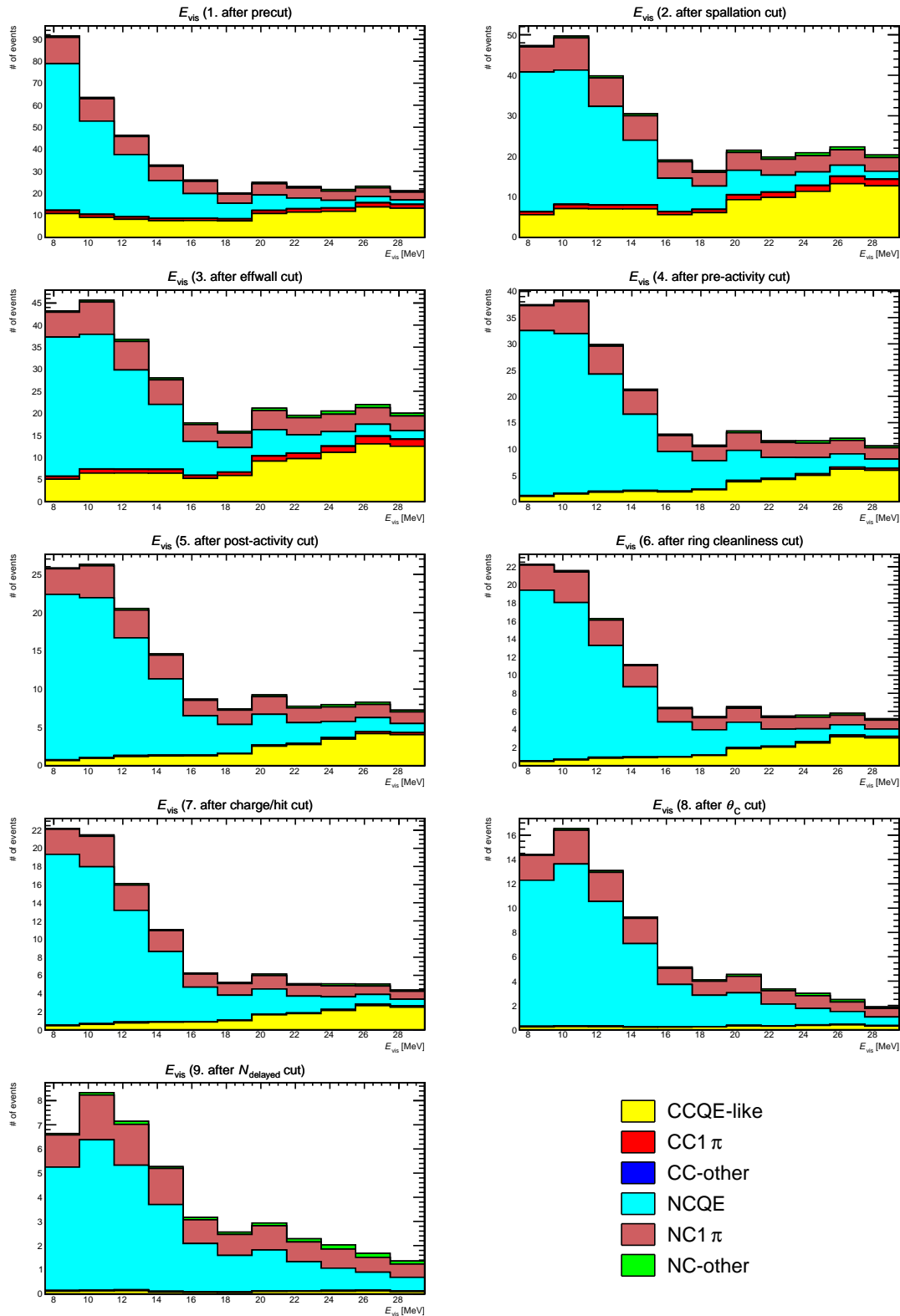


Figure B.30: E_{vis} for atmospheric neutrino events. Event reductions are performed in the order shown in the title.

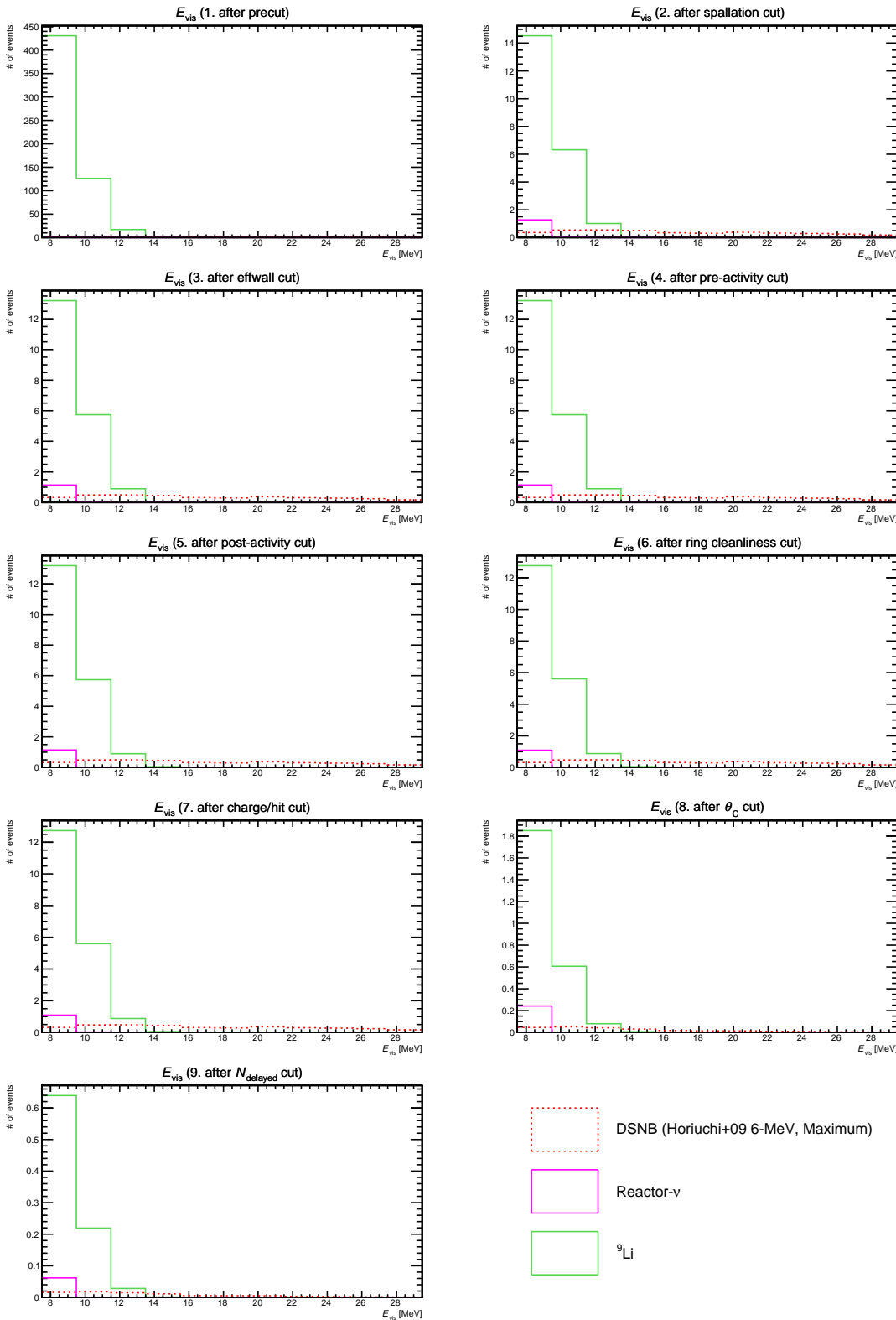
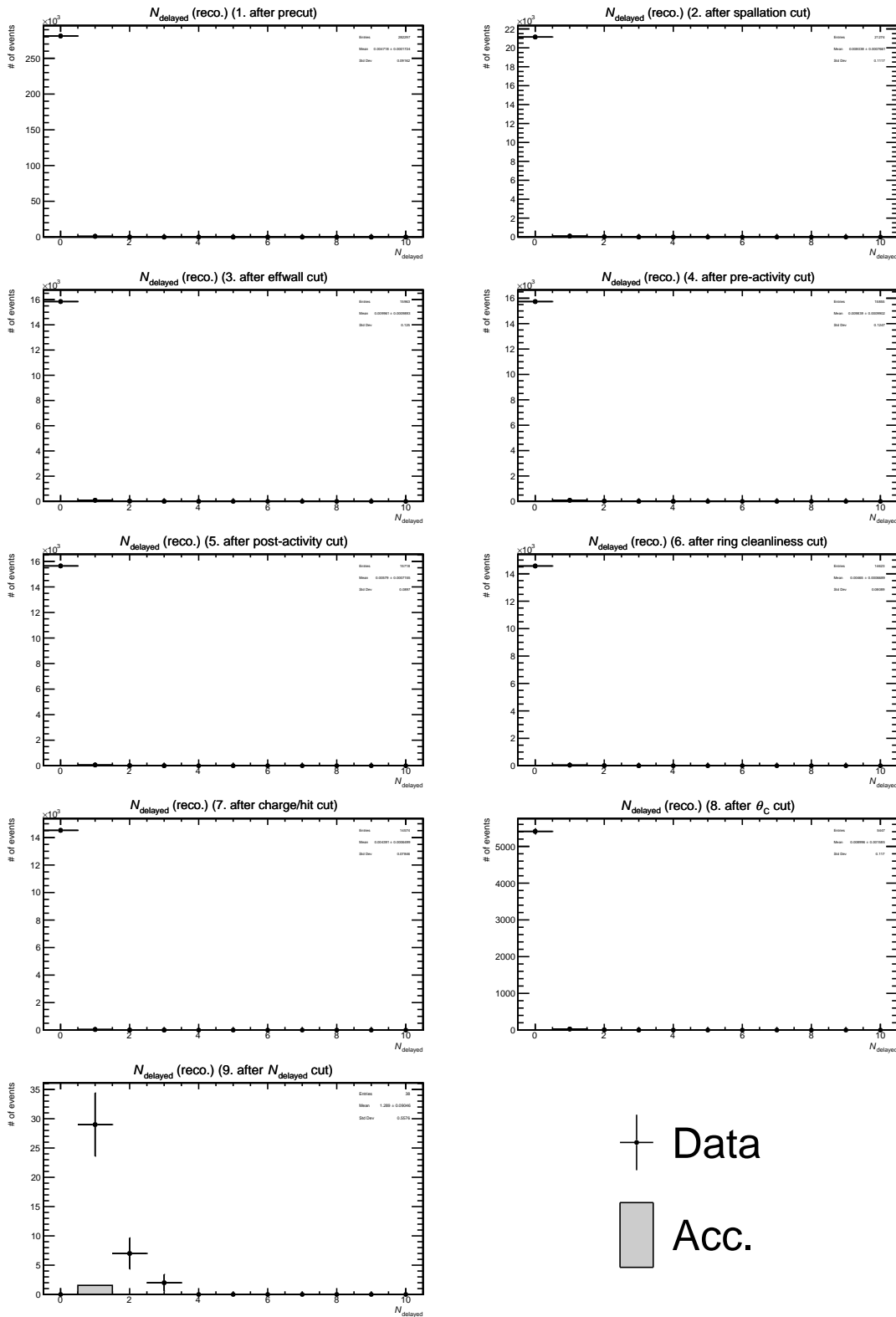


Figure B.31: E_{vis} for spallation, reactor neutrino, and DSNB events. Event reductions are performed in the order shown in the title.



 Data
 Acc.

Figure B.32: N_{delayed} for the data and accidental coincidence events. Event reductions are performed in the order shown in the title.

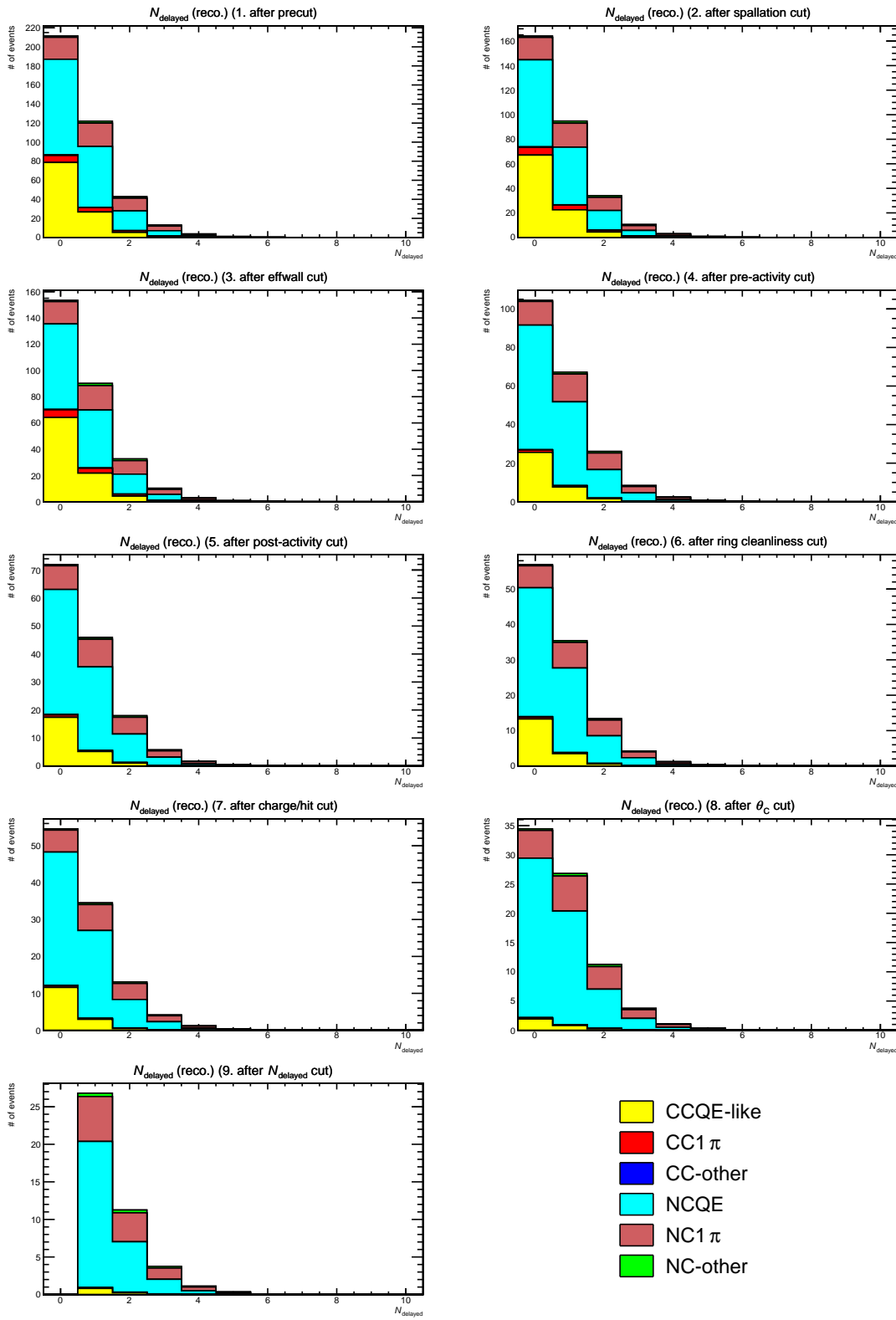


Figure B.33: N_{delayed} for atmospheric neutrino events. Event reductions are performed in the order shown in the title.

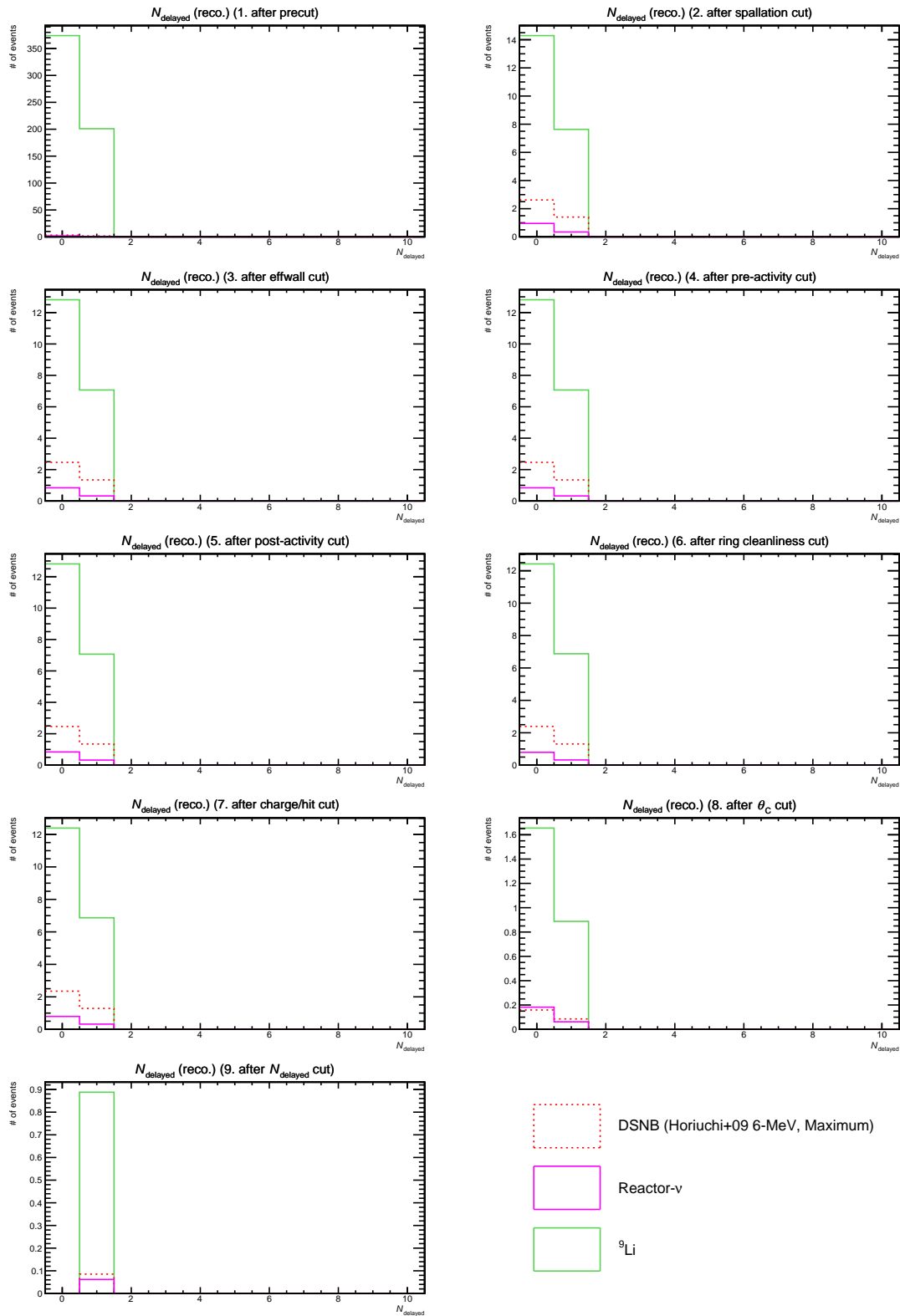


Figure B.34: N_{delayed} for spallation, reactor neutrino, and DSNB events. Event reductions are performed in the order shown in the title.

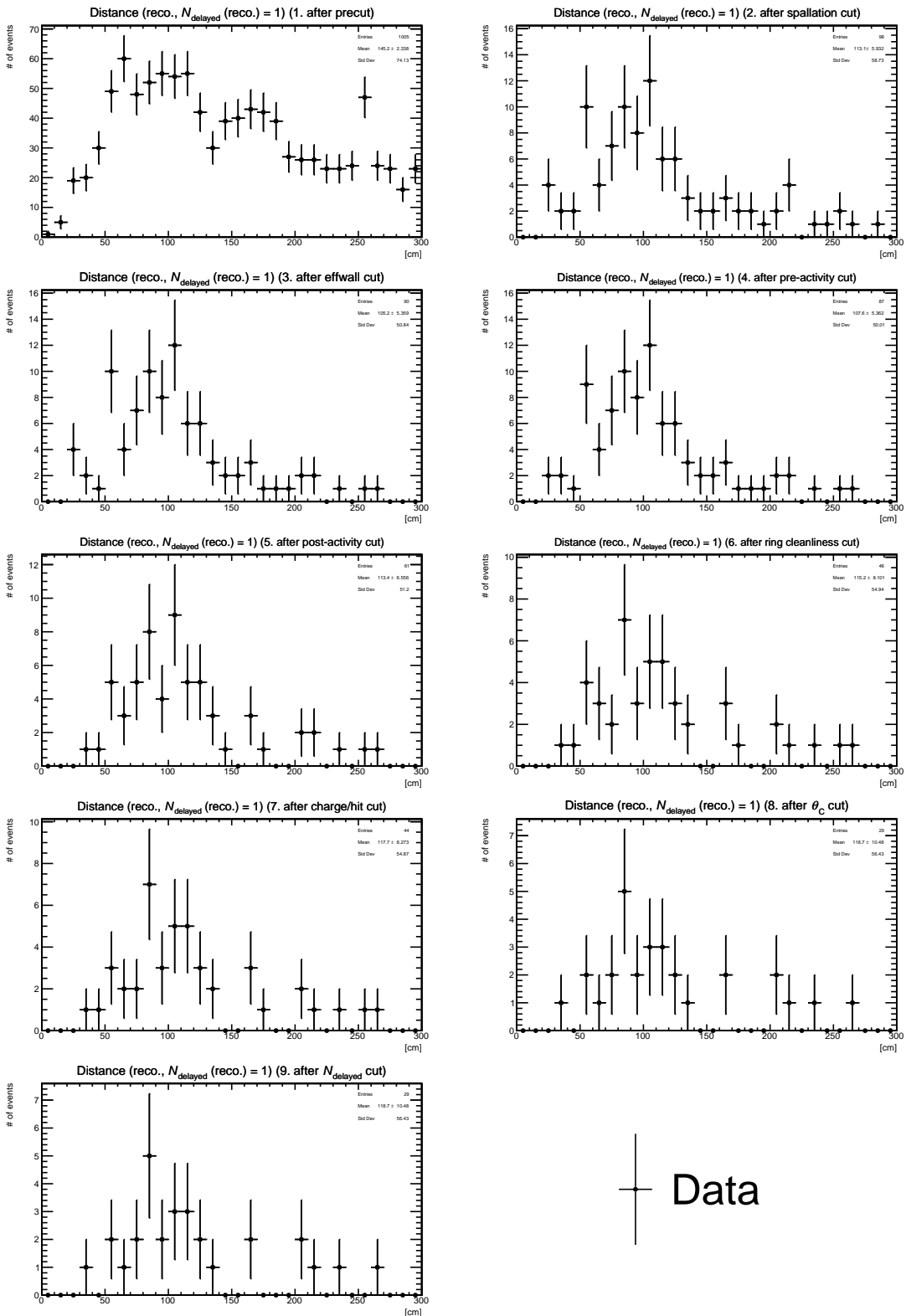


Figure B.35: Distance from prompt signal to delayed signal ($N_{\text{delayed}} = 1$) for the data and accidental coincidence events. Event reductions are performed in the order shown in the title.

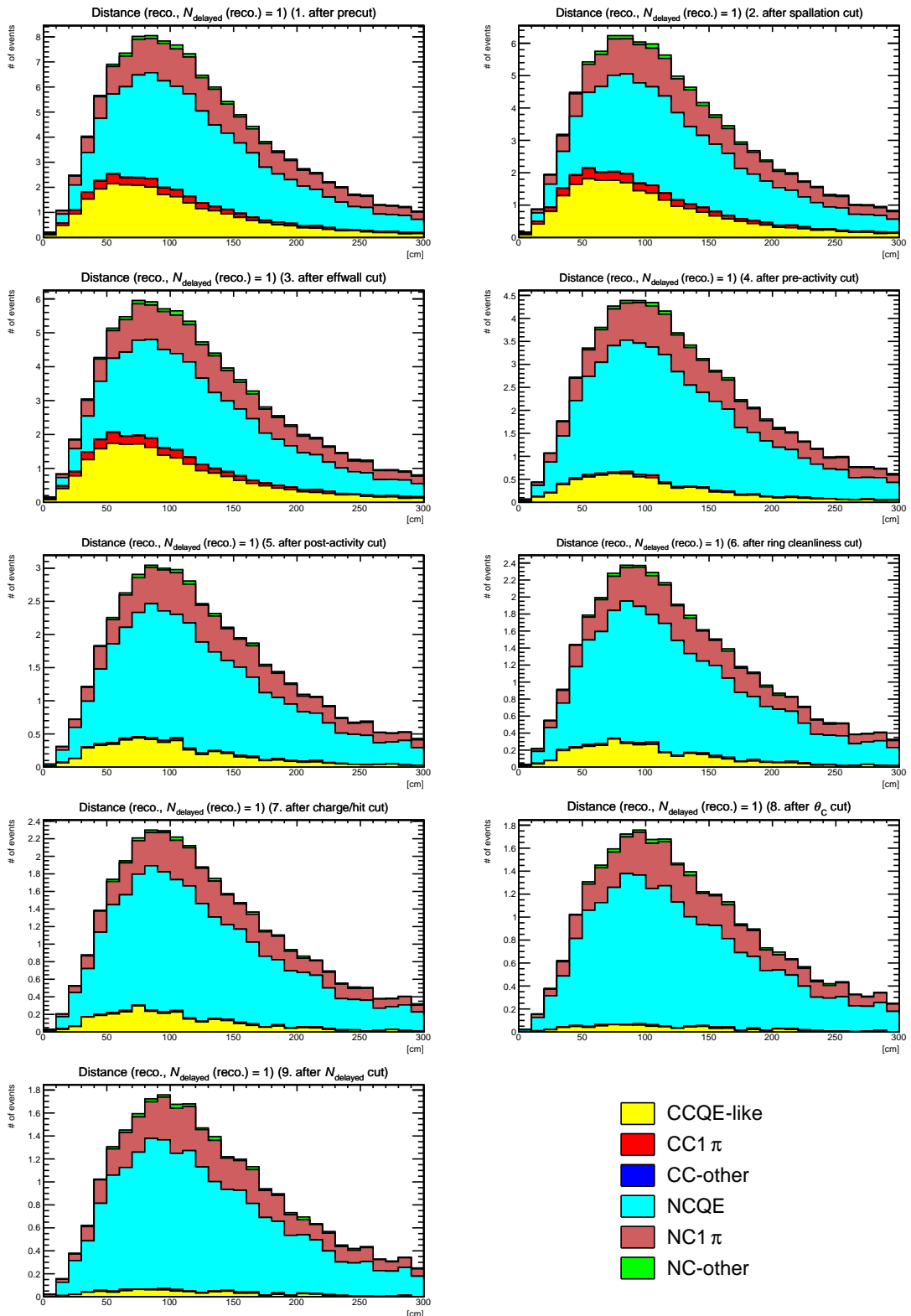


Figure B.36: Distance from prompt signal to delayed signal ($N_{\text{delayed}} = 1$) for atmospheric neutrino events. Event reductions are performed in the order shown in the title.

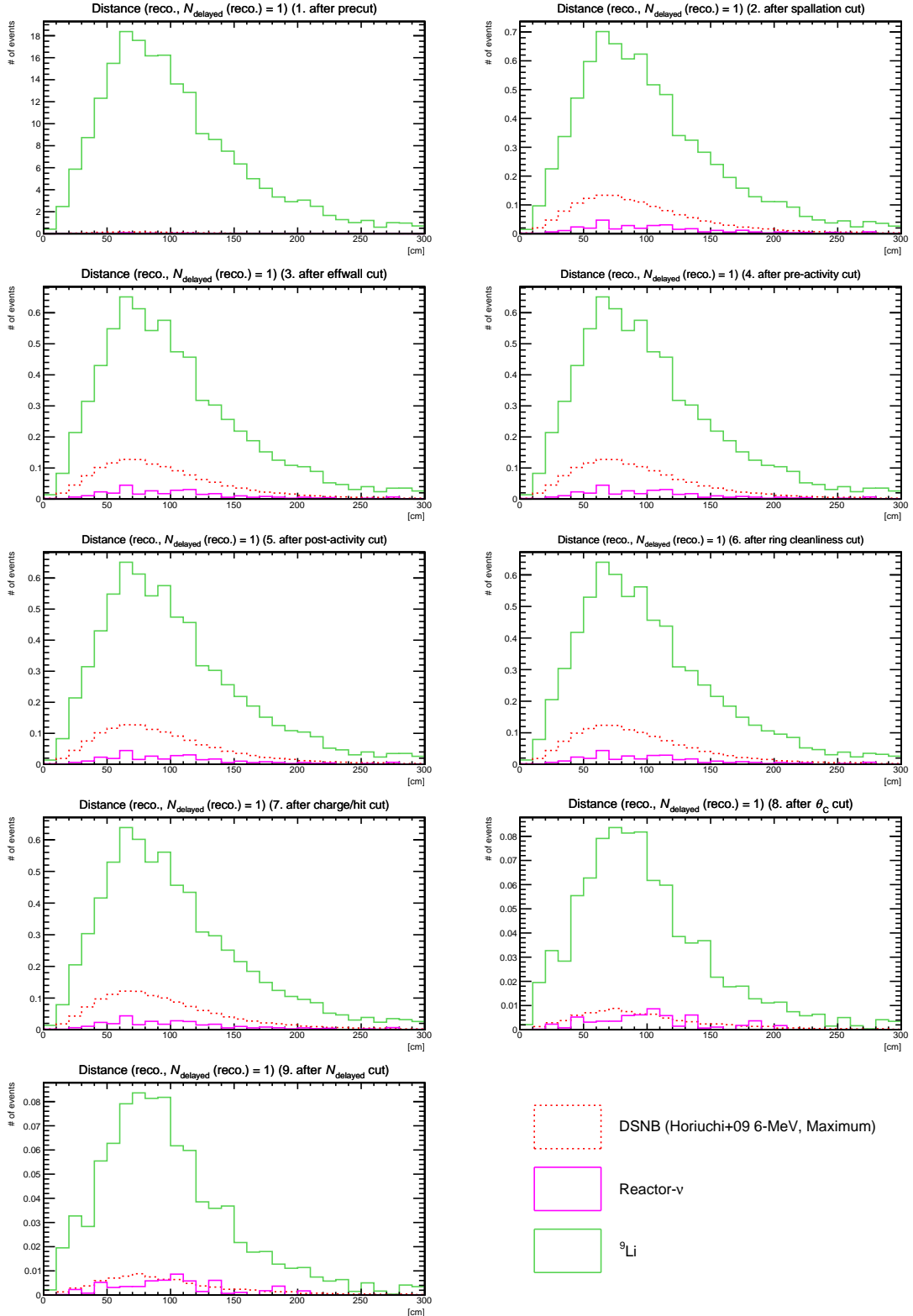


Figure B.37: Distance from prompt signal to delayed signal ($N_{\text{delayed}} = 1$) for spallation, reactor neutrino, and DSNB events. Event reductions are performed in the order shown in the title.

B.3 Comparison of secondary interaction models

Other distributions and tables related to Section 7 are summarized here.

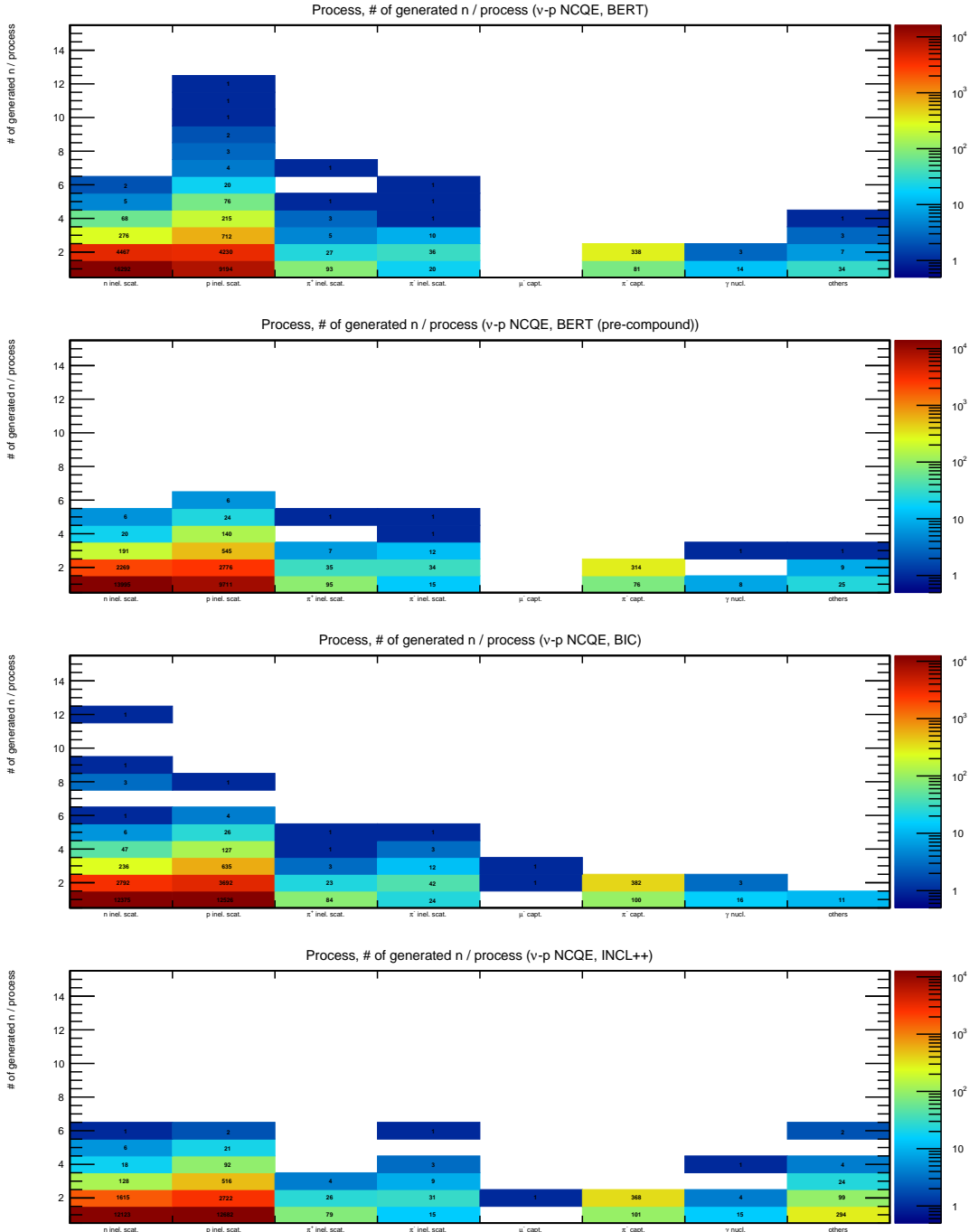


Figure B.38: The number of generated neutrons per process after neutrino-proton NCQE reactions. Top, top middle, bottom middle, and bottom figure shows the case of BERT, BERT with the Geant4 pre-compound model, BIC, and INCL++, respectively. Horizontal axis shows processes that generated neutrons (neutron inelastic scattering, proton inelastic scattering, π^+ inelastic scattering, π^- inelastic scattering, μ^- capture, π^- capture, gamma-nuclear interaction, and others).

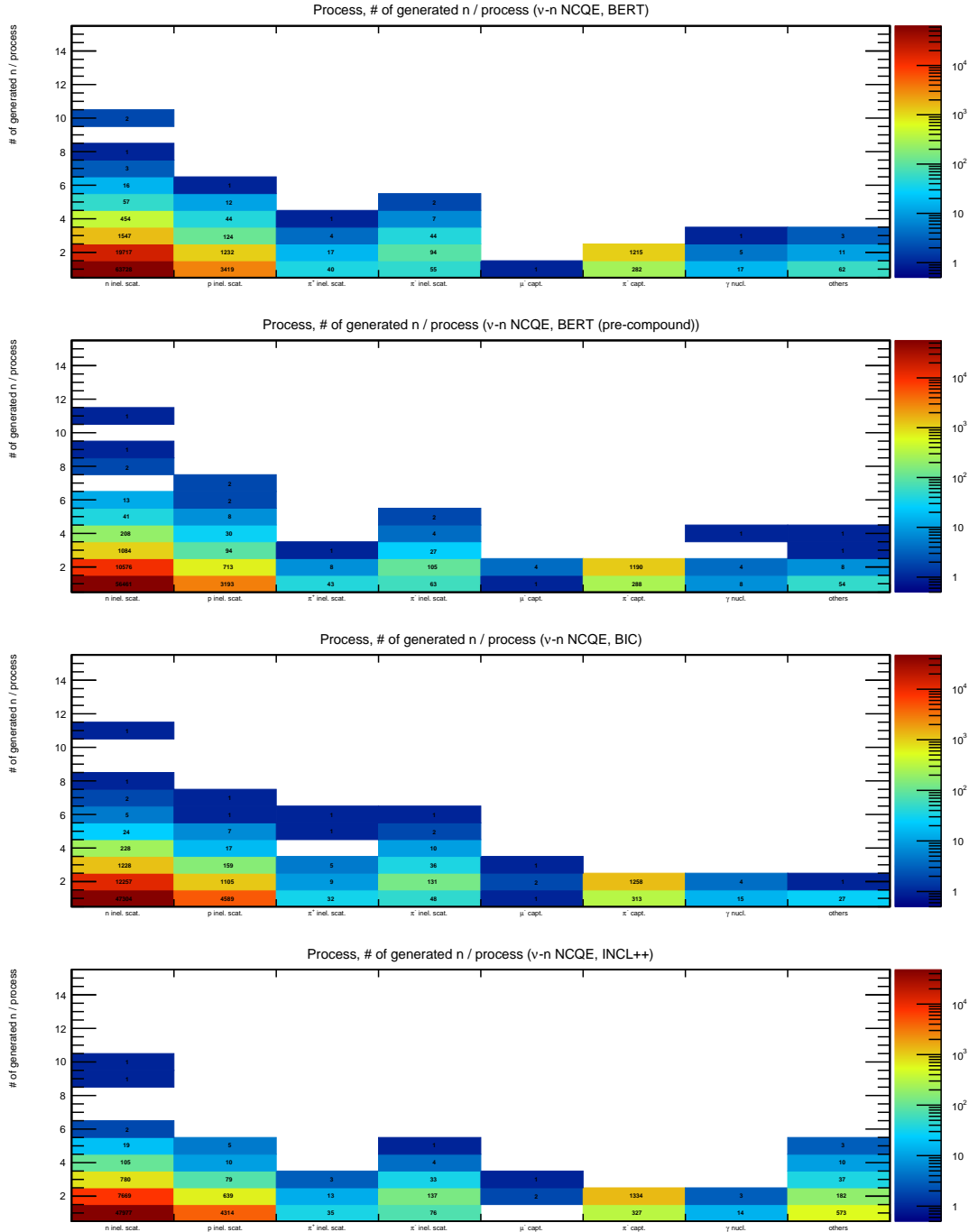


Figure B.39: The number of generated neutrons per process after neutrino-neutron NCQE reactions. Top, top middle, bottom middle, and bottom figure shows the case of BERT, BERT with the Geant4 pre-compound model, BIC, and INCL++, respectively. Horizontal axis shows processes that generated neutrons (neutron inelastic scattering, proton inelastic scattering, π^+ inelastic scattering, π^- inelastic scattering, μ^- capture, π^- capture, gamma-nuclear interaction, and others).

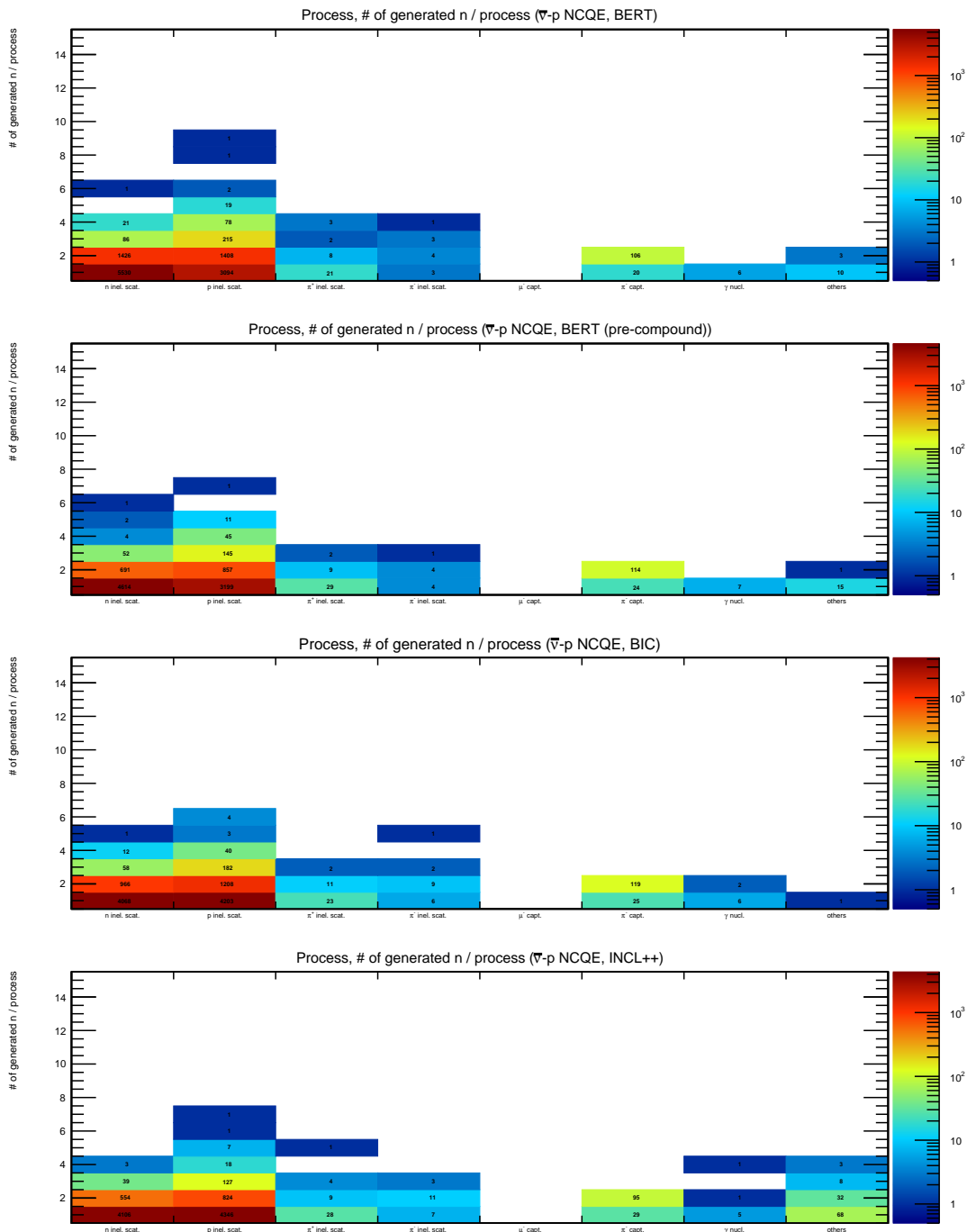


Figure B.40: The number of generated neutrons per process after antineutrino-proton NCQE reactions. Top, top middle, bottom middle, and bottom figure shows the case of BERT, BERT with the Geant4 pre-compound model, BIC, and INCL++, respectively. Horizontal axis shows processes that generated neutrons (neutron inelastic scattering, proton inelastic scattering, π^+ inelastic scattering, π^- inelastic scattering, μ^+ capture, π^+ capture, gamma-nuclear interaction, and others).

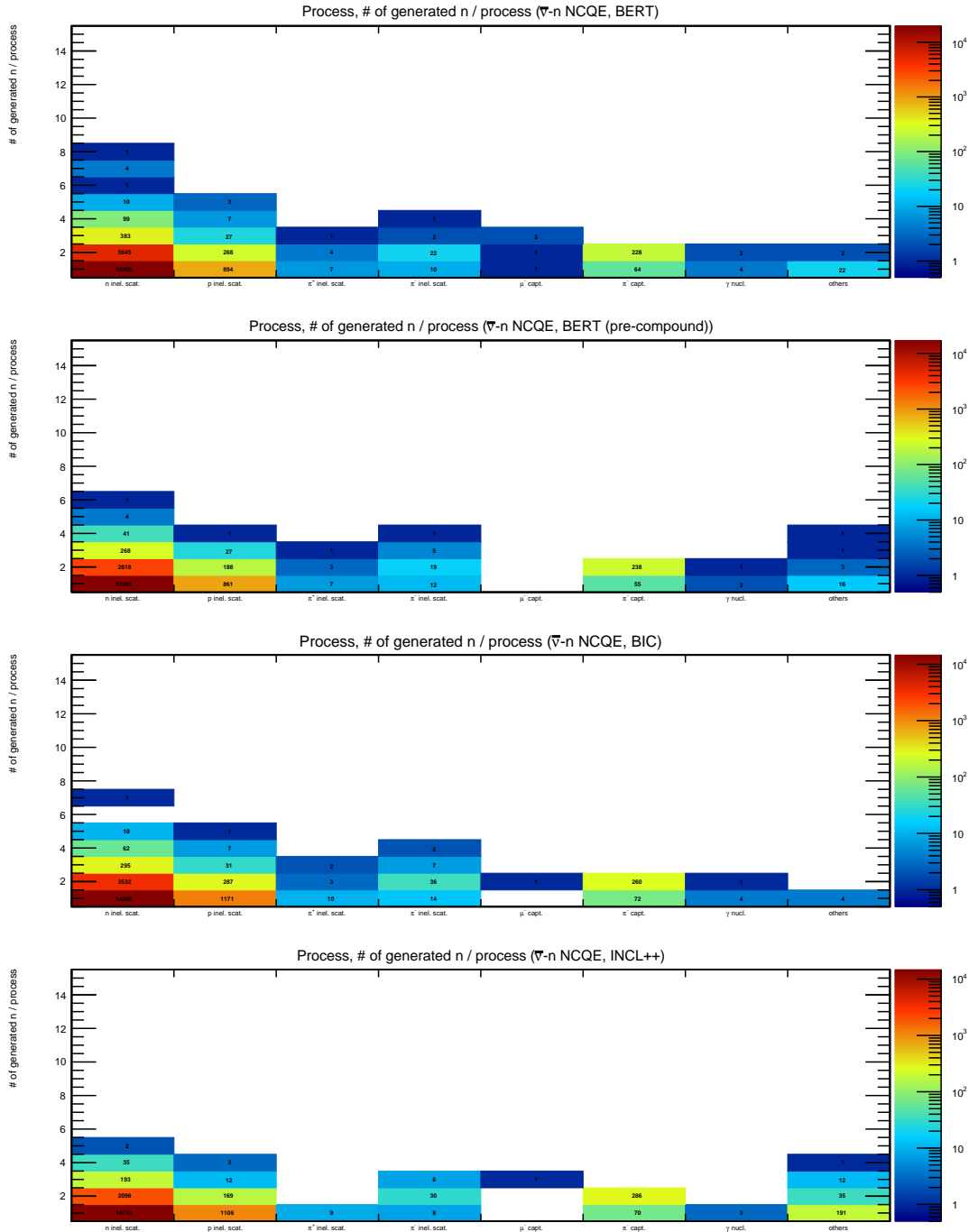


Figure B.41: The number of generated neutrons per process after antineutrino-neutron NCQE reactions. Top, top middle, bottom middle, and bottom figure shows the case of BERT, BERT with the Geant4 pre-compound model, BIC, and INCL++, respectively. Horizontal axis shows processes that generated neutrons (neutron inelastic scattering, proton inelastic scattering, π^+ inelastic scattering, π^- inelastic scattering, μ^- capture, π^- capture, gamma-nuclear interaction, and others).

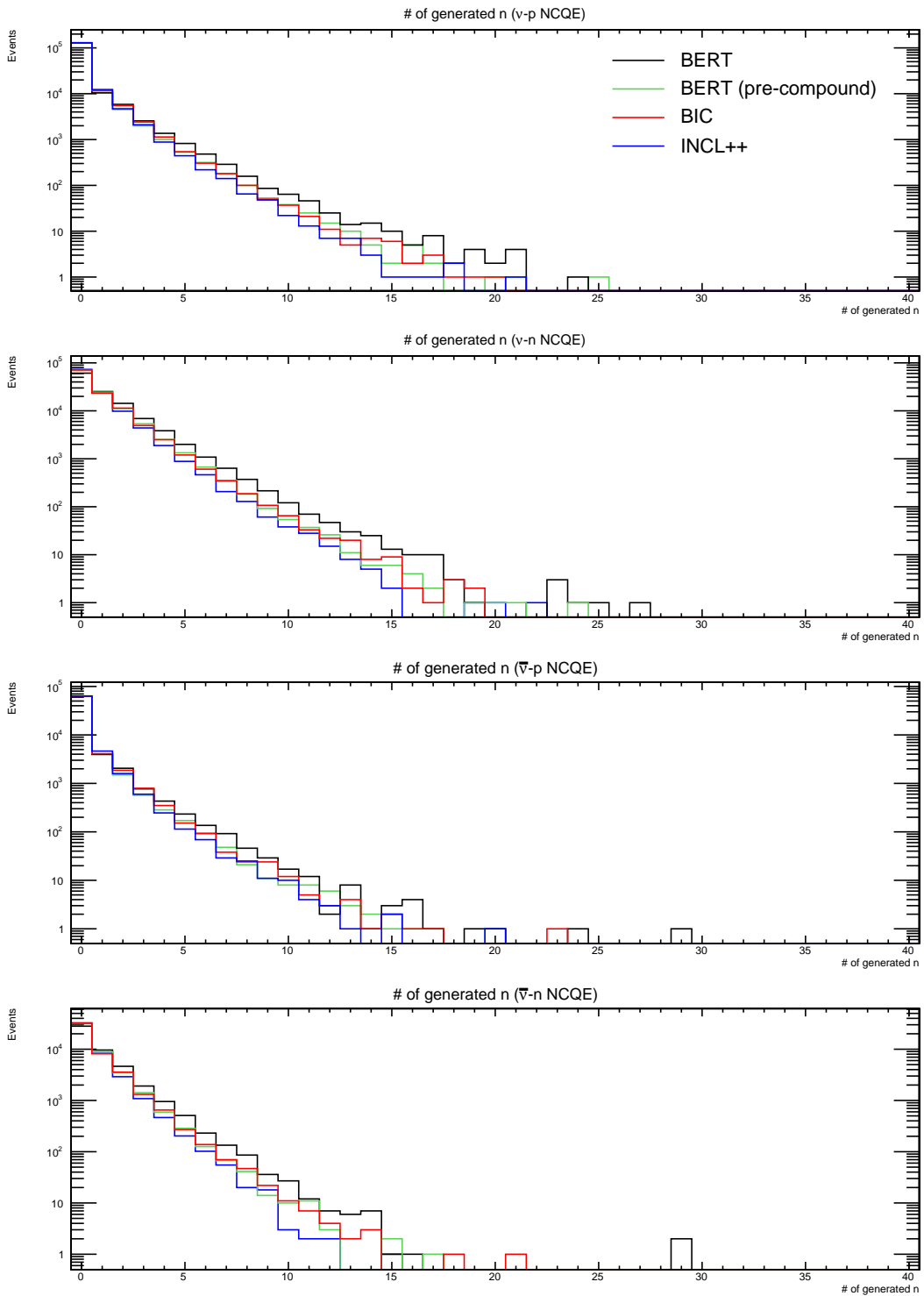


Figure B.42: The number of neutrons generated after NCQE reactions. Top, top middle, bottom middle, and bottom figure shows the case of neutrino-proton, neutrino-neutron, antineutrino-proton, and antineutrino-neutron NCQE reactions, respectively. Black, green, red, and blue line shows the case of BERT, BERT with the Geant4 pre-compound model, BIC, and INCL++, respectively.

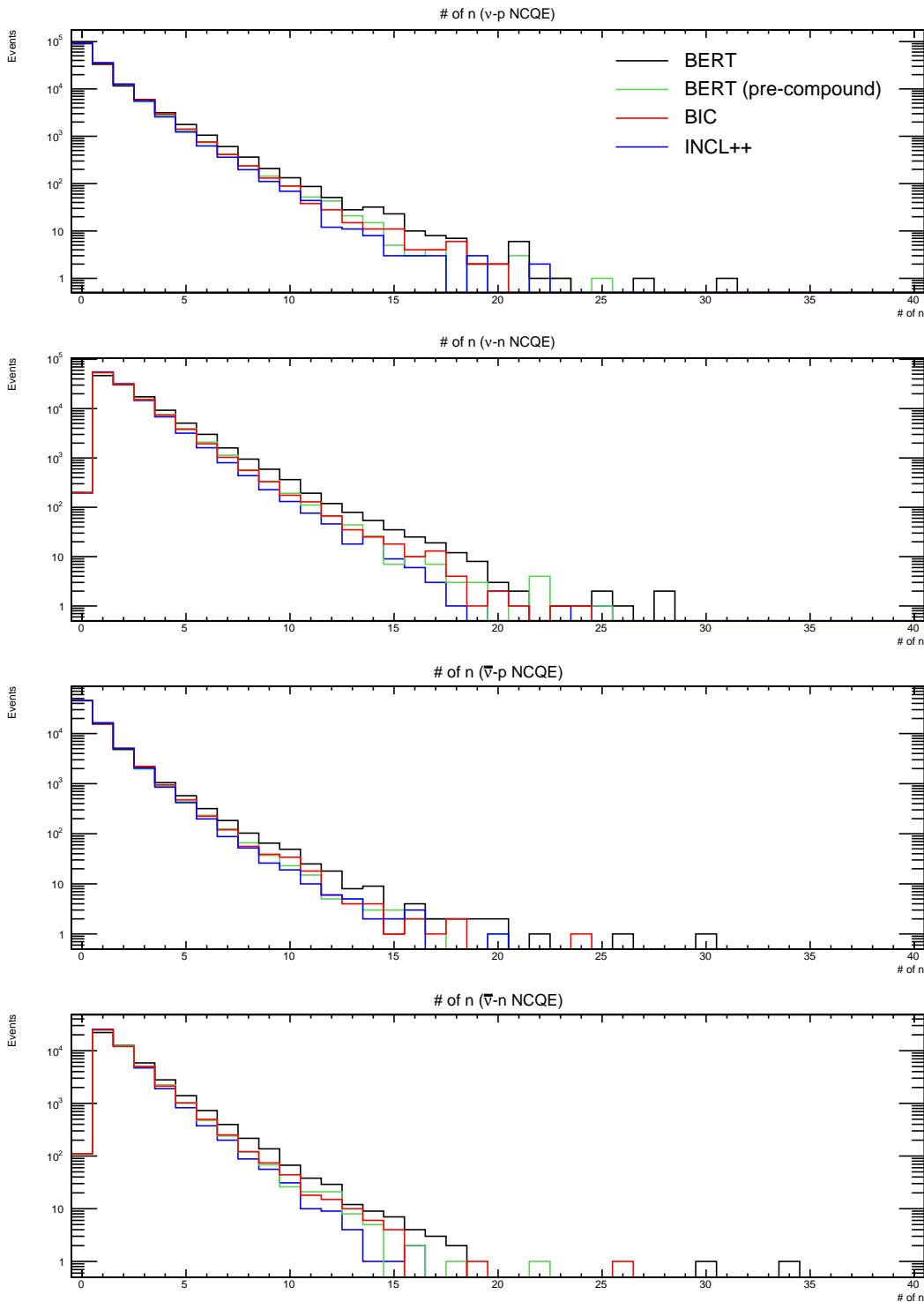


Figure B.43: The total number of neutrons. Top, top middle, bottom middle, and bottom figure shows the case of neutrino-proton, neutrino-neutron, antineutrino-proton, and antineutrino-neutron NCQE reactions, respectively. Black, green, red, and blue line shows the case of BERT, BERT with the Geant4 pre-compound model, BIC, and INCL++, respectively.

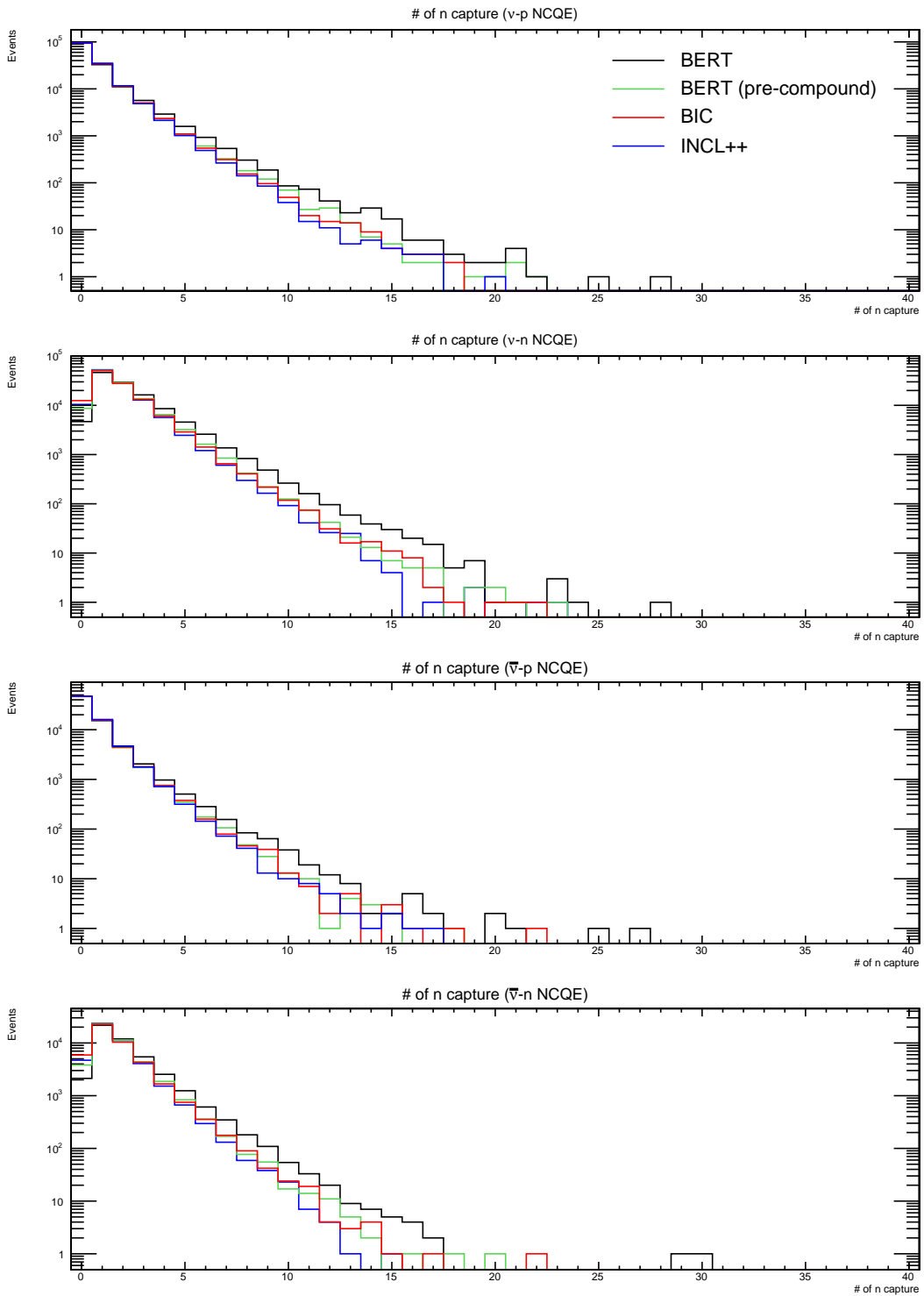


Figure B.44: The number of neutron captures. Top, top middle, bottom middle, and bottom figure shows the case of neutrino-proton, neutrino-neutron, antineutrino-proton, and antineutrino-neutron NCQE reactions, respectively. Black, green, red, and blue line shows the case of BERT, BERT with the Geant4 pre-compound model, BIC, and INCL++, respectively.

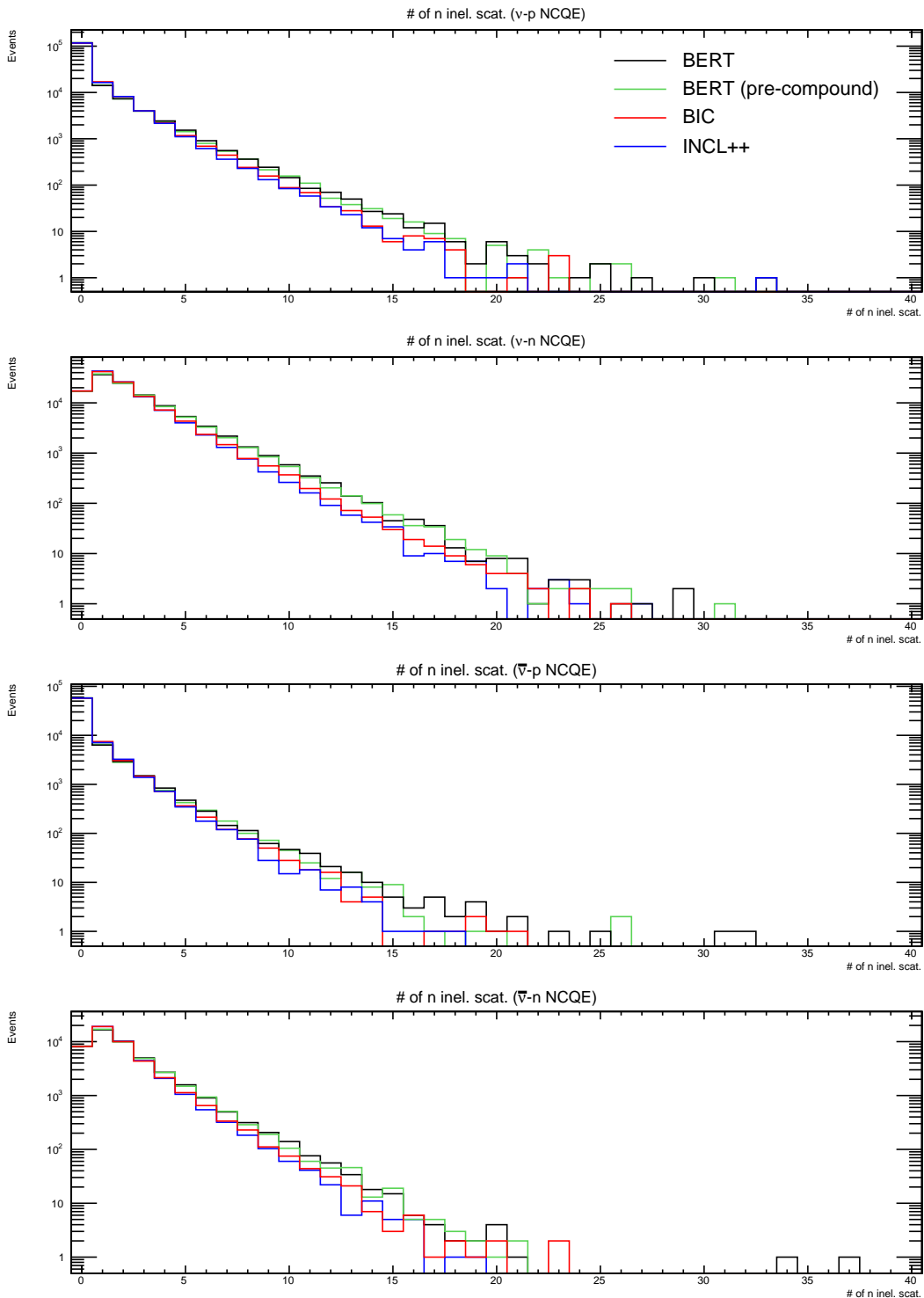


Figure B.45: The number of neutron inelastic scattering reactions. Top, top middle, bottom middle, and bottom figure shows the case of neutrino-proton, neutrino-neutron, antineutrino-proton, and antineutrino-neutron NCQE reactions, respectively. Black, green, red, and blue line shows the case of BERT, BERT with the Geant4 pre-compound model, BIC, and INCL++, respectively.

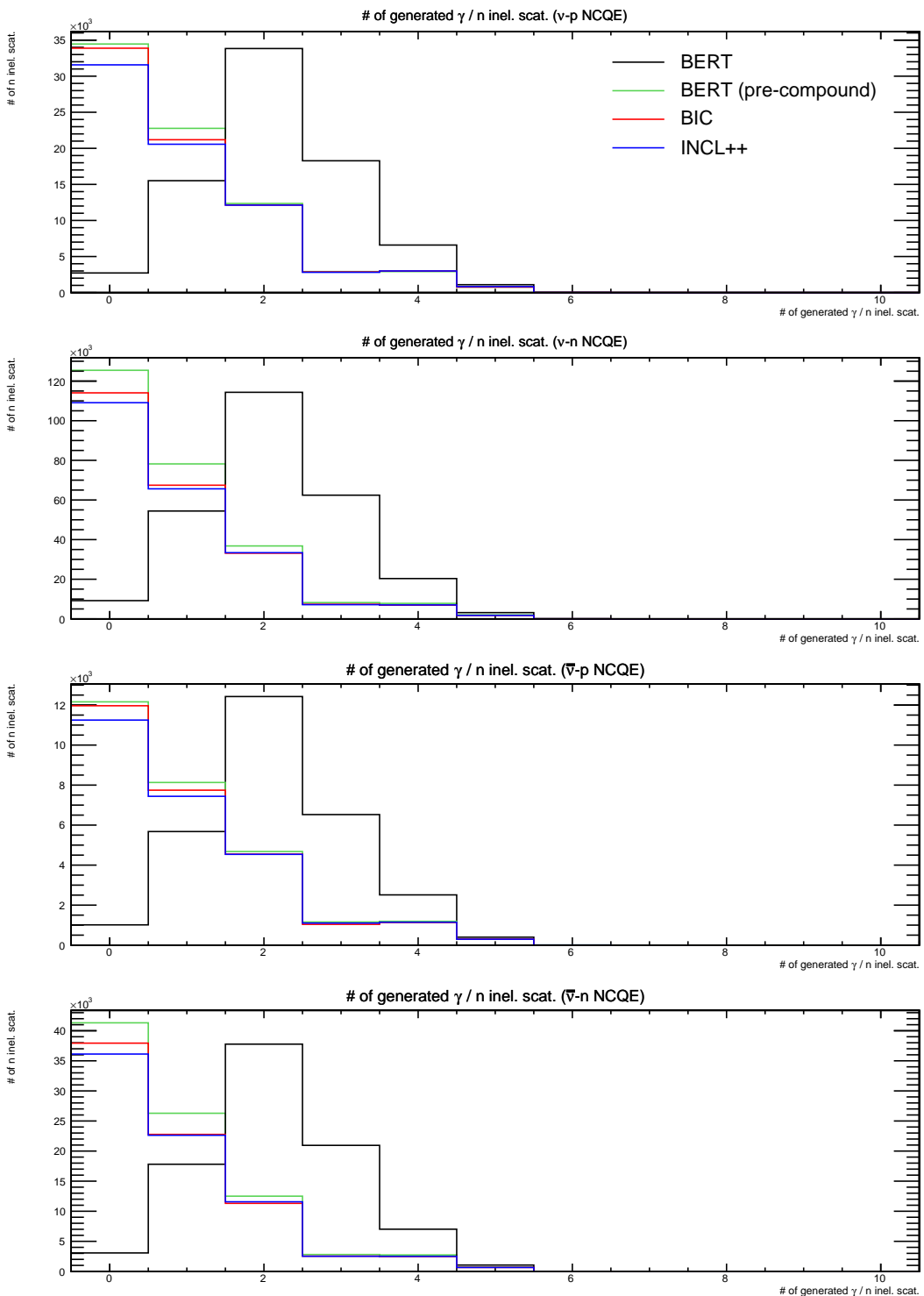


Figure B.46: The number of generated gamma-rays per neutron inelastic scattering reaction. Top, top middle, bottom middle, and bottom figure shows the case of neutrino-proton, neutrino-neutron, antineutrino-proton, and antineutrino-neutron NCQE reactions, respectively. Black, green, red, and blue line shows the case of BERT, BERT with the Geant4 pre-compound model, BIC, and INCL++, respectively.

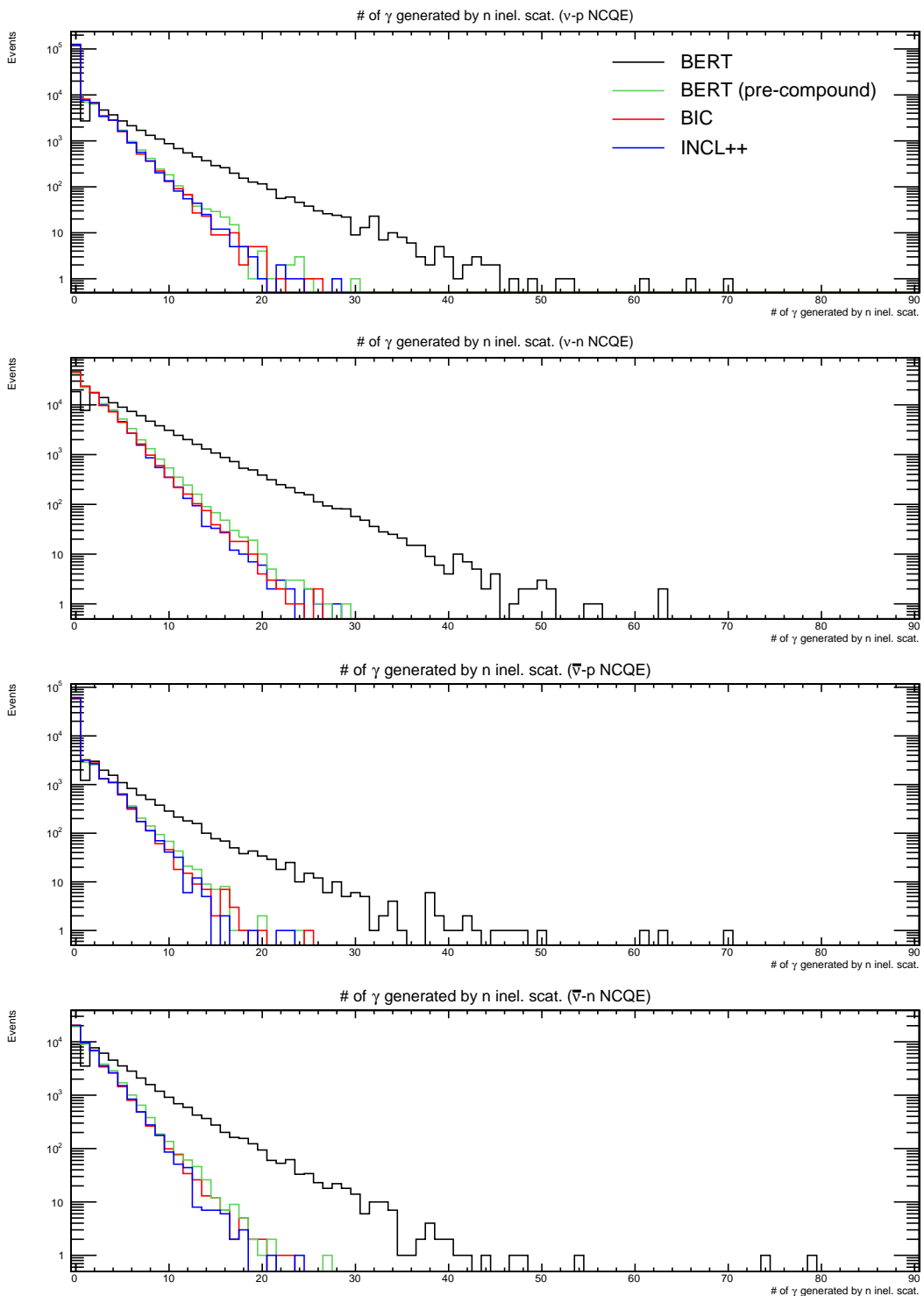


Figure B.47: The number of gamma-rays generated by neutron inelastic scattering reactions. Top, top middle, bottom middle, and bottom figure shows the case of neutrino-proton, neutrino-neutron, antineutrino-proton, and antineutrino-neutron NCQE reactions, respectively. Black, green, red, and blue line shows the case of BERT, BERT with the Geant4 pre-compound model, BIC, and INCL++, respectively.

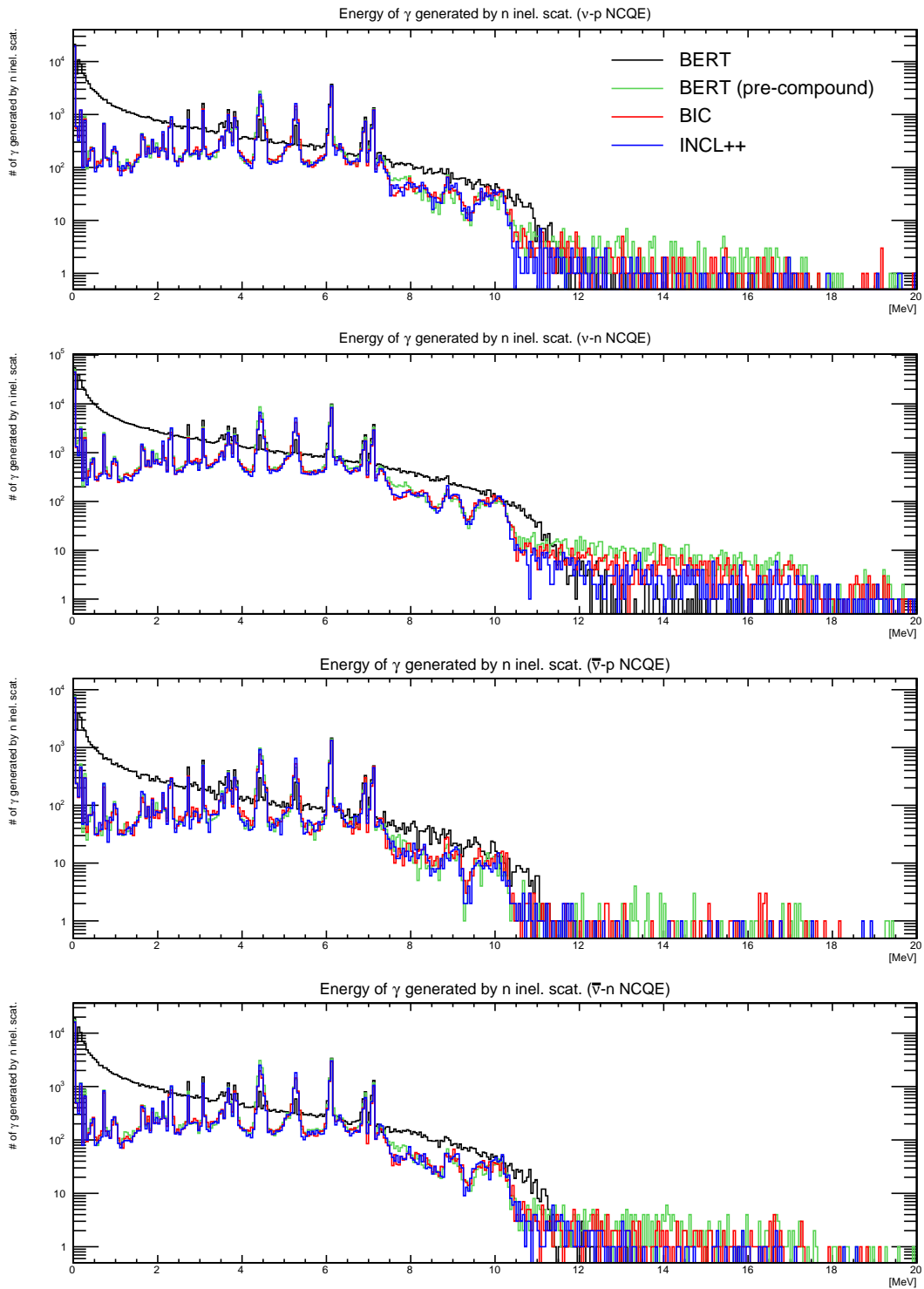


Figure B.48: Energy of gamma-rays generated by neutron inelastic scattering reactions. Top, top middle, bottom middle, and bottom figure shows the case of neutrino-proton, neutrino-neutron, antineutrino-proton, and antineutrino-neutron NCQE reactions, respectively. Black, green, red, and blue line shows the case of BERT, BERT with the Geant4 pre-compound model, BIC, and INCL++, respectively.

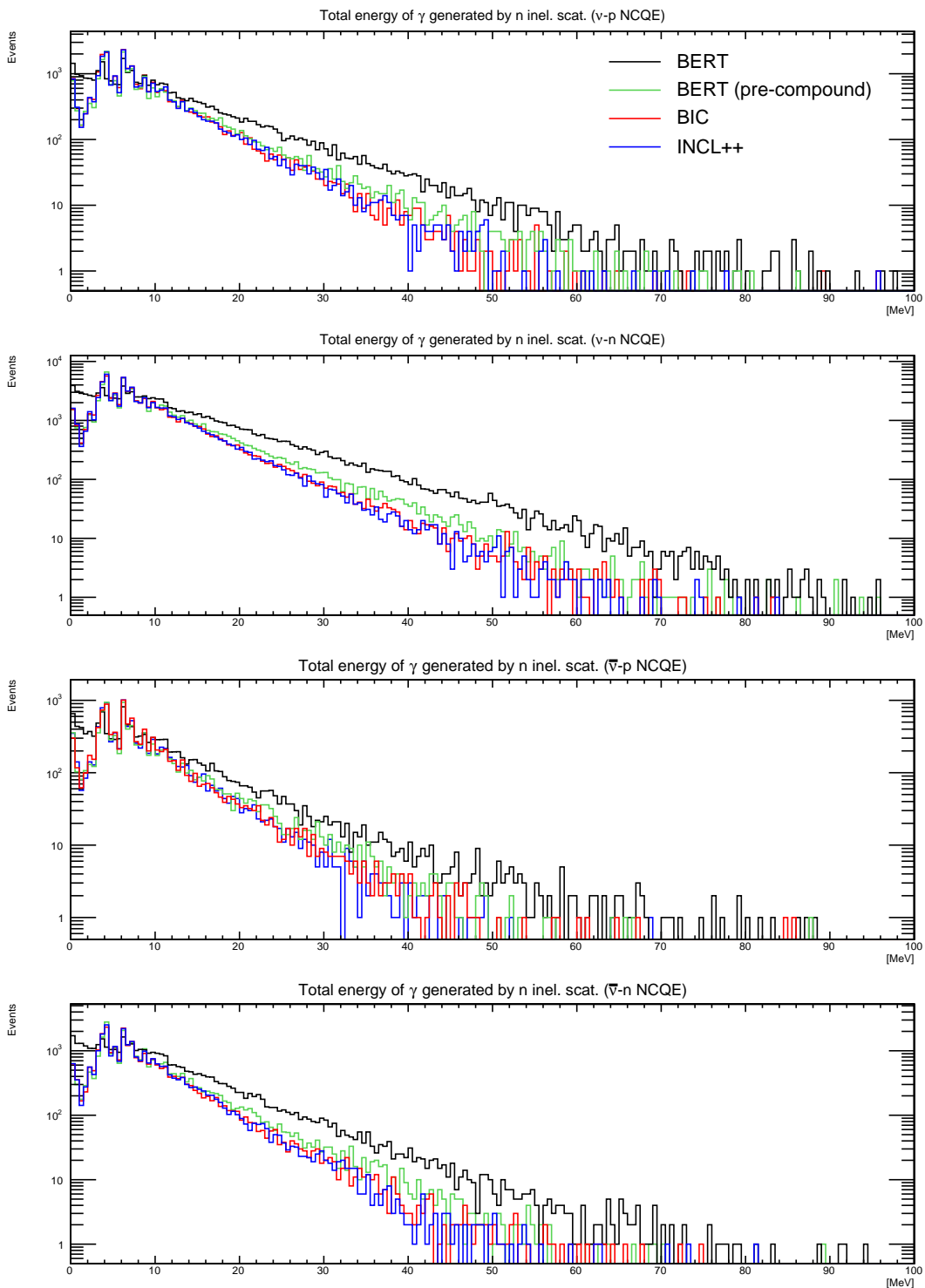


Figure B.49: Total energy of gamma-rays generated by neutron inelastic scattering reactions. Top, top middle, bottom middle, and bottom figure shows the case of neutrino-proton, neutrino-neutron, antineutrino-proton, and antineutrino-neutron NCQE reactions, respectively. Black, green, red, and blue line shows the case of BERT, BERT with the Geant4 pre-compound model, BIC, and INCL++, respectively.

Table B.1: The number of neutrons generated by each process (top), the total number of neutrons and neutron captures (center), and the number of gamma-rays (bottom) in the case of neutrino-proton NCQE reactions. The numbers of primary neutrons and primary gamma-rays are common among secondary interaction models.

ν -p NCQE (150,214 events)	BERT	BERT (pre-compound)	BIC	INCL++
neutron inelastic scattering	26,363	19,216	18,936	15,845
proton inelastic scattering	21,253	17,614	22,485	20,159
π^+ inelastic scattering	186	191	148	143
π^- inelastic scattering	137	128	161	122
μ^- capture	0	0	5	2
π^- capture	757	704	864	837
gamma-nuclear interaction	20	11	22	27
others	61	46	11	592
The number of generated neutrons	48,777	37,910	42,632	37,727
The number of generated neutrons per event	0.3247	0.2524	0.2838	0.2512

ν -p NCQE (150,214 events)	BERT	BERT (pre-compound)	BIC	INCL++
The number of primary neutrons	67,105	67,105	67,105	67,105
The number of generated neutrons	48,777	37,910	42,632	37,727
The total number of neutrons	115,882	105,015	109,737	104,832
The number of neutron captures	108,839	95,445	95,764	94,176
The number of primary neutrons per event	0.4467	0.4467	0.4467	0.4467
The number of generated neutrons per event	0.3247	0.2524	0.2838	0.2512
The total number of neutrons per event	0.7714	0.6991	0.7305	0.6979
The number of neutron captures per event	0.7246	0.6354	0.6375	0.6269

ν -p NCQE (150,214 events)	BERT	BERT (pre-compound)	BIC	INCL++
The number of primary gamma-rays	57,996	57,996	57,996	57,996
The number of n inel. scat.	78,045	76,194	73,851	70,923
The number of gamma-rays per n inel. scat.	2.1776	0.9422	0.9477	0.9803
The number of gamma-rays by n inel. scat.	169,947	71,788	69,987	69,524
The number of primary gamma-rays per event	0.3861	0.3861	0.3861	0.3861
The number of n inel. scat. per event	0.5196	0.5072	0.4916	0.4721
The number of gamma-rays by n inel. scat. per event	1.1314	0.4779	0.4659	0.4628

Table B.2: The number of neutrons generated by each process (top), the total number of neutrons and neutron captures (center), and the number of gamma-rays (bottom) in the case of neutrino-neutron NCQE reactions. The numbers of primary neutrons and primary gamma-rays are common among secondary interaction models.

ν -n NCQE (116,031 events)	BERT	BERT (pre-compound)	BIC	INCL++
neutron inelastic scattering	110,049	82,016	76,597	66,201
proton inelastic scattering	6,497	5,087	7,392	5,894
π^+ inelastic scattering	90	62	76	70
π^- inelastic scattering	413	380	474	470
μ^- capture	1	9	8	7
π^- capture	2,712	2,668	2,829	2,995
gamma-nuclear interaction	30	20	23	20
others	93	77	29	1,103
The number of generated neutrons	119,885	90,319	87,428	76,760
The number of generated neutrons per event	1.0332	0.7784	0.7535	0.6615

ν -n NCQE (116,031 events)	BERT	BERT (pre-compound)	BIC	INCL++
The number of primary neutrons	154,978	154,978	154,978	154,978
The number of generated neutrons	119,885	90,319	87,428	76,760
The total number of neutrons	274,863	245,297	242,406	231,738
The number of neutron captures	255,807	217,113	205,968	202,607
The number of primary neutrons per event	1.3357	1.3357	1.3357	1.3357
The number of generated neutrons per event	1.0332	0.7784	0.7535	0.6615
The total number of neutrons per event	2.3689	2.1141	2.0891	1.9972
The number of neutron captures per event	2.2046	1.8712	1.7751	1.7461

ν -n NCQE (116,031 events)	BERT	BERT (pre-compound)	BIC	INCL++
The number of primary gamma-rays	59,612	59,612	59,612	59,612
The number of n inel. scat.	263,957	258,553	230,736	224,076
The number of gamma-rays per n inel. scat.	2.1518	0.8437	0.8348	0.8524
The number of gamma-rays by n inel. scat.	567,986	218,135	192,614	191,012
The number of primary gamma-rays per event	0.5138	0.5138	0.5138	0.5138
The number of n inel. scat. per event	2.2749	2.2283	1.9886	1.9312
The number of gamma-rays by n inel. scat. per event	4.8951	1.8800	1.6600	1.6462

Table B.3: The number of neutrons generated by each process (top), the total number of neutrons and neutron captures (center), and the number of gamma-rays (bottom) in the case of antineutrino-proton NCQE reactions. The numbers of primary neutrons and primary gamma-rays are common among secondary interaction models.

$\bar{\nu}$ -p NCQE (70,695 events)	BERT	BERT (pre-compound)	BIC	INCL++
neutron inelastic scattering	8,730	6,184	6,227	5,343
proton inelastic scattering	6,991	5,590	7,364	6,495
π^+ inelastic scattering	55	53	51	63
π^- inelastic scattering	24	15	35	38
μ^- capture	0	0	0	0
π^- capture	232	252	263	219
gamma-nuclear interaction	6	7	10	11
others	16	17	1	168
The number of generated neutrons	16,054	12,118	13,951	12,337
The number of generated neutrons per event	0.2271	0.1714	0.1973	0.1745

$\bar{\nu}$ -p NCQE (70,695 events)	BERT	BERT (pre-compound)	BIC	INCL++
The number of primary neutrons	28,958	28,958	28,958	28,958
The number of generated neutrons	16,054	12,118	13,951	12,337
The total number of neutrons	45,012	41,076	42,909	41,295
The number of neutron captures	42,327	37,208	37,587	37,208
The number of primary neutrons per event	0.4096	0.4096	0.4096	0.4096
The number of generated neutrons per event	0.2271	0.1714	0.1973	0.1745
The total number of neutrons per event	0.6367	0.5810	0.6070	0.5841
The number of neutron captures per event	0.5987	0.5263	0.5317	0.5263

$\bar{\nu}$ -p NCQE (70,695 events)	BERT	BERT (pre-compound)	BIC	INCL++
The number of primary gamma-rays	26,774	26,774	26,774	26,774
The number of n inel. scat.	28,557	27,634	26,734	25,778
The number of gamma-rays per n inel. scat.	2.1770	0.9886	0.9731	1.0061
The number of gamma-rays by n inel. scat.	62,170	27,319	26,014	25,936
The number of primary gamma-rays per event	0.3787	0.3787	0.3787	0.3787
The number of n inel. scat. per event	0.4039	0.3909	0.3782	0.3646
The number of gamma-rays by n inel. scat. per event	0.8794	0.3864	0.3680	0.3669

Table B.4: The number of neutrons generated by each process (top), the total number of neutrons and neutron captures (center), and the number of gamma-rays (bottom) in the case of antineutrino-neutron NCQE reactions. The numbers of primary neutrons and primary gamma-rays are common among secondary interaction models.

$\bar{\nu}$ -n NCQE (46,344 events)	BERT	BERT (pre-compound)	BIC	INCL++
neutron inelastic scattering	32,887	23,921	22,822	19,638
proton inelastic scattering	1,554	1,322	1,871	1,492
π^+ inelastic scattering	18	16	22	9
π^- inelastic scattering	64	69	115	92
μ^- capture	9	0	2	3
π^- capture	520	531	592	642
gamma-nuclear interaction	8	4	6	3
others	26	29	4	301
The number of generated neutrons	35,086	25,892	25,434	22,180
The number of generated neutrons per event	0.7571	0.5587	0.5488	0.4786

$\bar{\nu}$ -n NCQE (46,344 events)	BERT	BERT (pre-compound)	BIC	INCL++
The number of primary neutrons	59,794	59,794	59,794	59,794
The number of generated neutrons	35,086	25,892	25,434	22,180
The total number of neutrons	94,880	85,686	85,228	81,974
The number of neutron captures	88,373	75,952	71,768	71,492
The number of primary neutrons per event	1.2902	1.2902	1.2902	1.2902
The number of generated neutrons per event	0.7571	0.5587	0.5488	0.4786
The total number of neutrons per event	2.0473	1.8489	1.8390	1.7688
The number of neutron captures per event	1.9069	1.6389	1.5486	1.5426

$\bar{\nu}$ -n NCQE (46,344 events)	BERT	BERT (pre-compound)	BIC	INCL++
The number of primary gamma-rays	23,678	23,678	23,678	23,678
The number of n inel. scat.	87,695	86,394	77,698	76,027
The number of gamma-rays per n inel. scat.	2.1629	0.8611	0.8529	0.8782
The number of gamma-rays by n inel. scat.	189,679	74,391	66,271	66,765
The number of primary gamma-rays per event	0.5109	0.5109	0.5109	0.5109
The number of n inel. scat. per event	1.8923	1.8642	1.6765	1.6405
The number of gamma-rays by n inel. scat. per event	4.0928	1.6052	1.4300	1.4406

B.4 Measurement of NCQE cross section in SK-Gd

Other distributions related to Section 8 are summarized here.

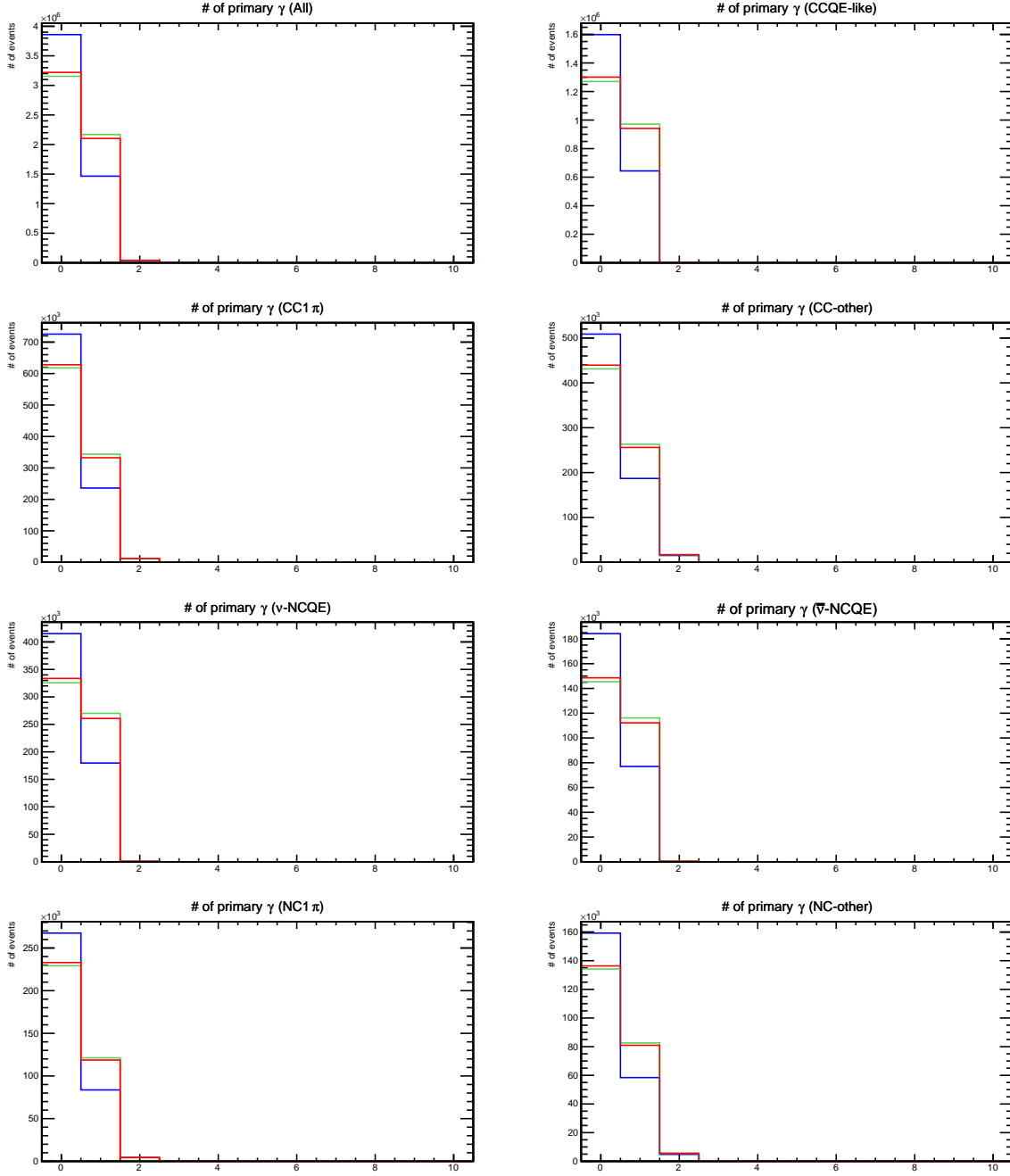


Figure B.50: The comparison of the number of gamma-rays generated by neutrino-nucleus interaction. The red line shows the case of including *others* state into $(s_{1/2})^{-1}$ state. The blue line shows the case of including *others* state into $(p_{1/2})^{-1}$ state. The green line shows the case of increasing $(p_{3/2})^{-1}$ state by 5.4%. These figures were made using 500 years' worth of atmospheric neutrino events.

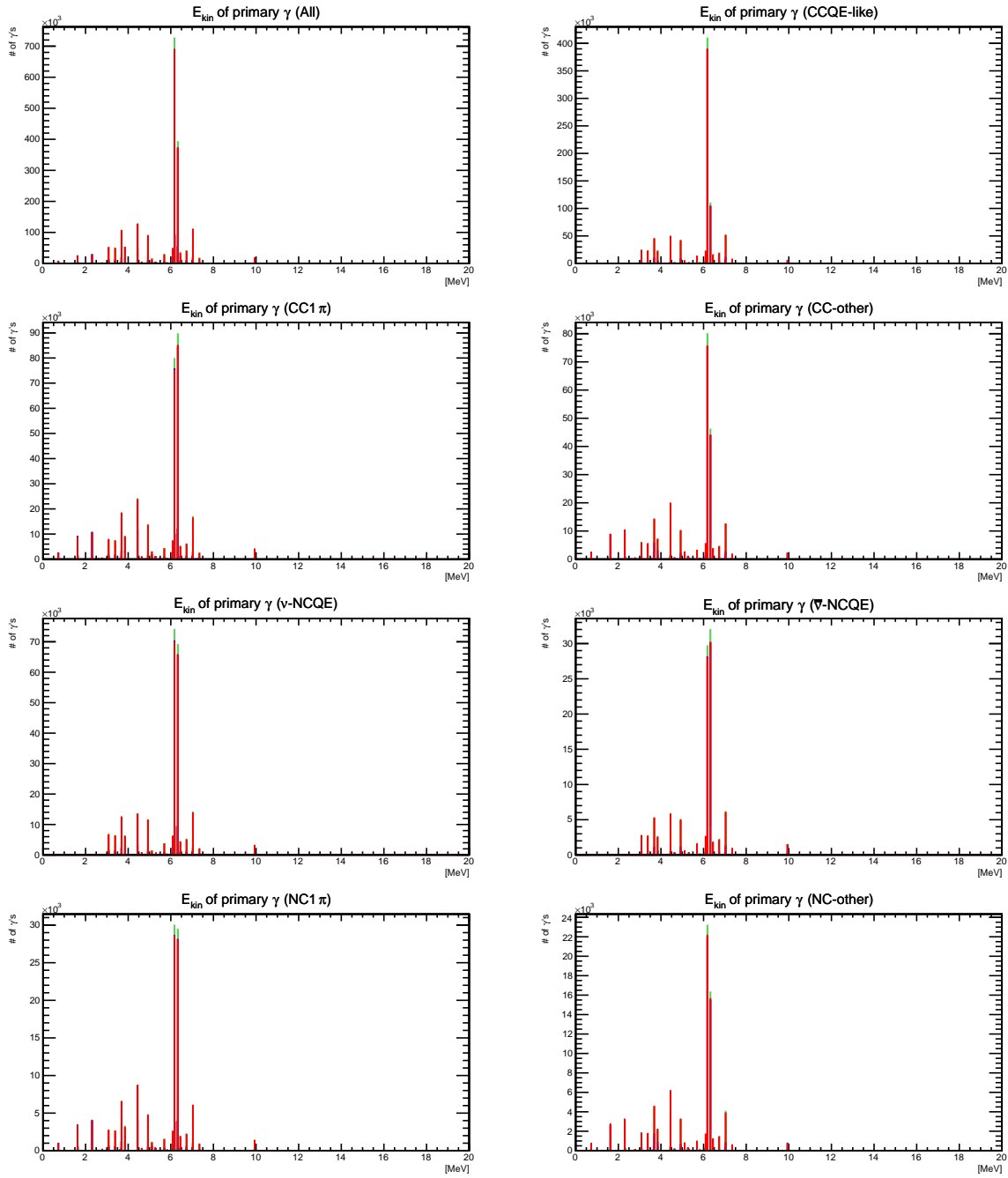


Figure B.51: The comparison of energy of gamma-rays generated by neutrino-nucleus interaction. The red line shows the case of including *others* state into $(s_{1/2})^{-1}$ state. The blue line shows the case of including *others* state into $(p_{1/2})^{-1}$ state. The green line shows the case of increasing $(p_{3/2})^{-1}$ state by 5.4%. These figures were made using 500 years' worth of atmospheric neutrino events.

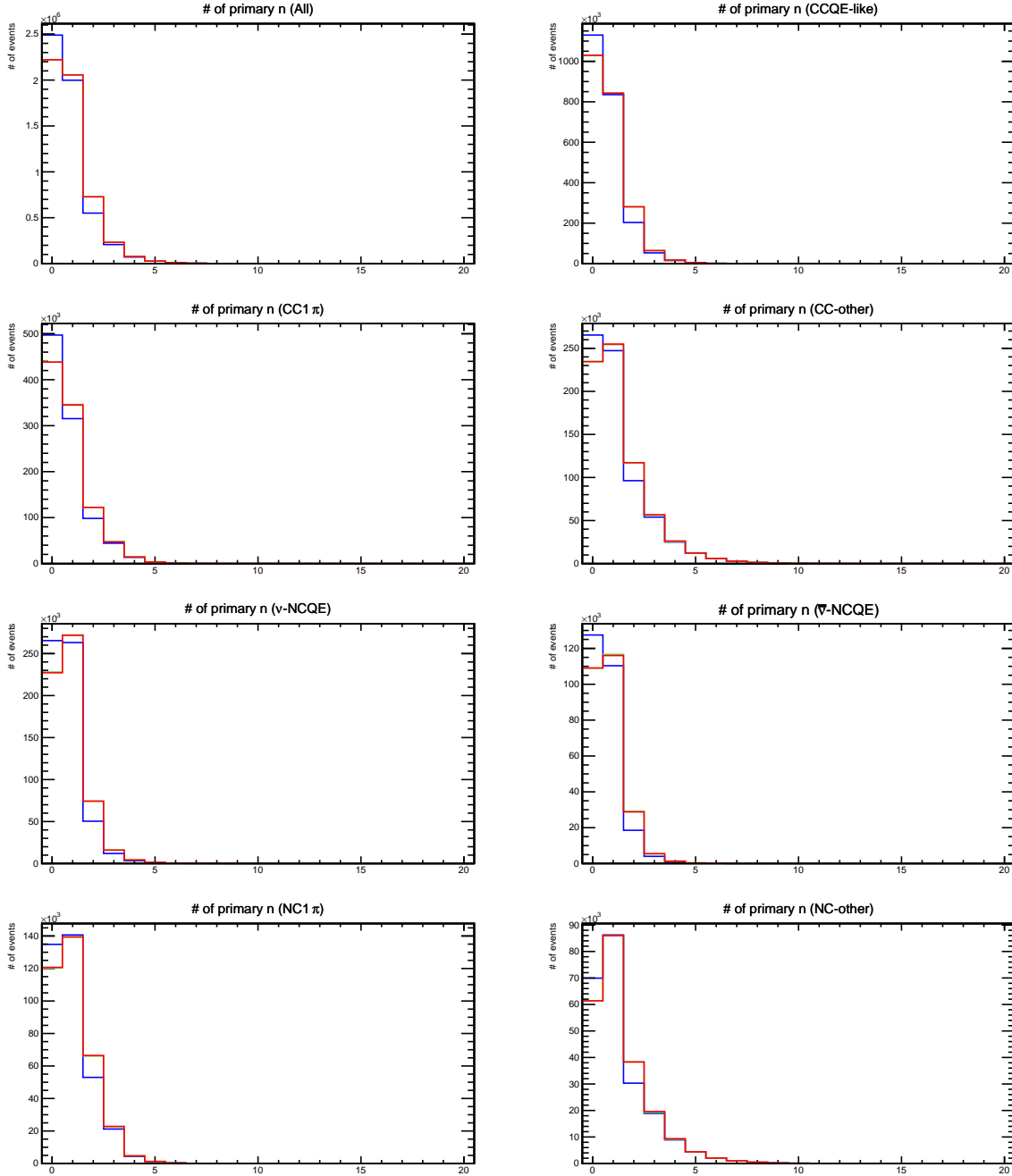


Figure B.52: The comparison of the number of neutrons generated by neutrino-nucleus interaction. The red line shows the case of including *others* state into $(s_{1/2})^{-1}$ state. The blue line shows the case of including *others* state into $(p_{1/2})^{-1}$ state. The green line shows the case of increasing $(p_{3/2})^{-1}$ state by 5.4%. These figures were made using 500 years' worth of atmospheric neutrino events.

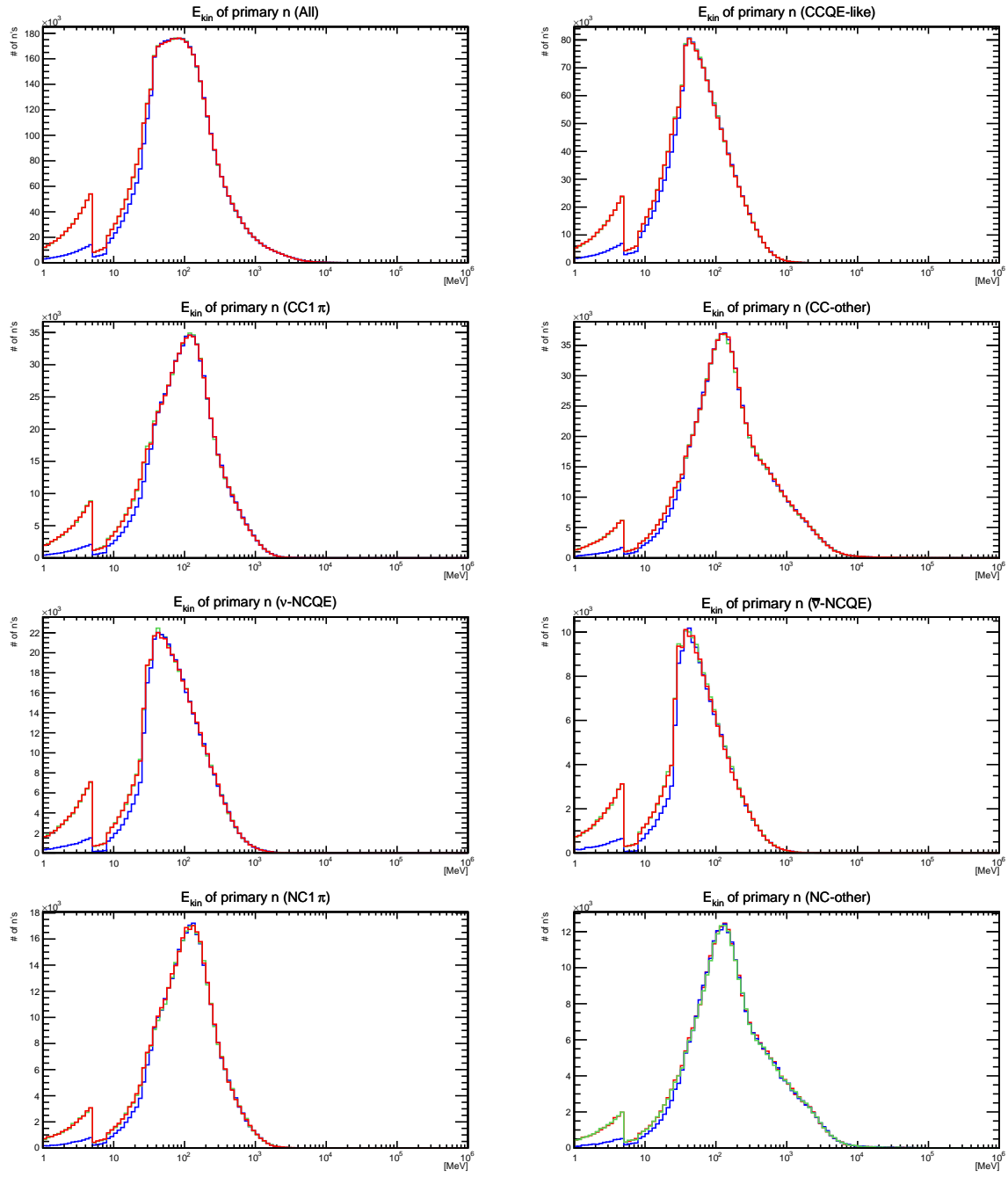


Figure B.53: The comparison of energy of neutrons generated by neutrino-nucleus interaction. The red line shows the case of including *others* state into $(s_{1/2})^{-1}$ state. The blue line shows the case of including *others* state into $(p_{1/2})^{-1}$ state. The green line shows the case of increasing $(p_{3/2})^{-1}$ state by 5.4%. These figures were made using 500 years' worth of atmospheric neutrino events.

References

- [1] R. L. Workman *et al.*, Prog. Theor. Exp. Phys. **2022**, 083C01 (2022).
- [2] “History of Neutrino”, <https://www-sk.icrr.u-tokyo.ac.jp/en/sk/neutrino/history/>.
- [3] J. Chadwick, Verh. Phys. Gesell. **16**, 383 (1914).
- [4] F. Reines, C. L. Cowan, Nature **178**, 446 (1956).
- [5] G. Danby *et al.*, Phys. Rev. Lett. **9**, 36 (1962).
- [6] K. Kodama *et al.*, Phys. Lett. B **504**, 218 (2001).
- [7] Y. Fukuda *et al.*, Phys. Rev. Lett. **81**, 1562 (1998).
- [8] T. K. Kuo, J. Pantaleone, Rev. Mod. Phys. **61**, 937 (1989).
- [9] “Particle Data Group”, <https://pdg.lbl.gov/> (2023).
- [10] K. Abe *et al.*, Phys. Rev. D **96**, 092006 (2017).
- [11] K. Abe *et al.*, Nature **580**, 339 (2020).
- [12] K. S. Hirata *et al.*, Phys. Rev. D **38**, 448 (1988).
- [13] A. Burrows, Rev. Mod. Phys. **85**, 245 (2013).
- [14] A. S. Burrows, Springer, ISBN 978-1-4612-3286-5 (1990).
- [15] H. A. Bethe, Rev. Mod. Phys. **62**, 801 (1990).
- [16] K. Hirata *et al.*, Phys. Rev. Lett. **58**, 1490 (1987).
- [17] R. M. Bionta *et al.*, Phys. Rev. Lett. **58**, 1494 (1987).
- [18] E. N. Alekseev *et al.*, JETP Lett. **45**, 589 (1987).
- [19] S. M. Adams *et al.*, Astrophys. J. **778**, 164 (2013).
- [20] J. F. Beacom, Annu. Rev. Nucl. Part. Sci. **60**, 439 (2010).
- [21] K. Nakazato *et al.*, Astrophys. J. **804**, 75 (2015).
- [22] K. Abe *et al.*, Phys. Rev. D **104**, 122002 (2021).
- [23] S. Horiuchi *et al.*, Phys. Rev. D **103**, 043003 (2021).
- [24] Z. Tabrizi, S. Horiuchi, J. Cosmol. Astropart. Phys. 05 (2021) 011.
- [25] D. Kresse, T. Ertl, H.-T. Janka, Astrophys. J. **909**, 169 (2021).
- [26] S. Horiuchi *et al.*, Mon. Not. R. Astron. Soc. **475**, 1363 (2018).
- [27] S. Galais *et al.*, Phys. Rev. D **81**, 053002 (2010).

- [28] S. Horiuchi, J. F. Beacom, E. Dwek, Phys. Rev. D **79**, 083013 (2009).
- [29] C. Lunardini, Phys. Rev. Lett. **102**, 231101 (2009).
- [30] S. Ando, K. Sato, T. Totani, Astropart. Phys. **18**, 307 (2003).
- [31] M. Kaplinghat, G. Steigman, T. P. Walker, Phys. Rev. D **62**, 043001 (2000).
- [32] R. Malaney, Astropart. Phys. **7**, 125 (1997).
- [33] D. Hartmann, S. Woosley, Astropart. Phys. **7**, 137 (1997).
- [34] T. Totani, K. Sato, Astropart. Phys. **3**, 367 (1995).
- [35] S. I. Ando, *Proceedings of the Next Generation of Nucleon Decay and Neutrino Detectors, Aussois, Savoie, France, 2005*, edited by J. Dumarchez (2005).
- [36] M. Harada, “Development of Neutron Tagging Algorithm and Search for Supernova Relic Neutrino in SK-Gd Experiment”, Ph.D. Thesis, Okayama University (2023).
- [37] F. Nakanishi, “Developing a novel analysis method for supernova neutrino observations in Super-Kamiokande”, Master’s Thesis, Okayama University (2023).
- [38] S. Ando *et al.*, Proc. Jpn. Acad., Ser. B **99**, 460 (2023).
- [39] K. Bays *et al.*, Phys. Rev. D **85**, 052007 (2012).
- [40] M. Harada *et al.*, Astrophys. J. Lett. **951**, L27 (2023).
- [41] S. Abe *et al.*, Astrophys. J. **925**, 14 (2022).
- [42] M. Agostini *et al.*, Astropart. Phys. **125**, 102509 (2021).
- [43] K. Nakazato *et al.*, Astrophys. J. Suppl. **205**, 2 (2013).
- [44] A. Burrows, D. Vartanyan, Nature **589**, 29 (2021).
- [45] H. Nagakura, A. Burrows, D. Vartanyan, Mon. Not. R. Astron. Soc. **506**, 1462 (2021).
- [46] K. Abe *et al.*, Nucl. Instrum. Methods Phys. Res., Sect. A **1027**, 166248 (2022).
- [47] J. F. Beacom, M. R. Vagins, Phys. Rev. Lett. **93**, 171101 (2004).
- [48] K. Abe *et al.*, Phys. Rev. D **100**, 112009 (2019).
- [49] K. Abe *et al.*, Phys. Rev. D **90**, 072012 (2014).
- [50] L. Wan *et al.*, Phys. Rev. D **99**, 032005 (2019).
- [51] A. M. Ankowski *et al.*, Phys. Rev. Lett. **108**, 052505 (2012).
- [52] E. Richard *et al.*, Phys. Rev. D **94**, 052001 (2016).
- [53] D. Wright, M. Kelsey, Nucl. Instrum. Methods Phys. Res., Sect. A **804**, 175 (2015).

- [54] G. Folger, V. N. Ivanchenko, J. P. Wellisch, Eur. Phys. J. A **21**, 407 (2004).
- [55] A. Boudard *et al.*, Phys. Rev. C **87**, 014606 (2013).
- [56] S. Fukuda *et al.*, Nucl. Instrum. Methods Phys. Res., Sect. A **501**, 418 (2003).
- [57] Z. Conner, “A STUDY OF SOLAR NEUTRINOS USING THE SUPER-KAMIOKANDE DETECTOR”, Ph.D. Thesis, University of Maryland (1997).
- [58] K. Abe *et al.*, Nucl. Instrum. Methods Phys. Res., Sect. A **737**, 253 (2014).
- [59] T. Yamaguchi, “Observation of ${}^8\text{B}$ Solar Neutrinos from 300-day data at Super-Kamiokande”, Ph.D. Thesis, University of Osaka (1998).
- [60] “Report from cause committee”, <https://www-sk.icrr.u-tokyo.ac.jp/cause-committee/> (2003).
- [61] H. Nishino *et al.*, Nucl. Instrum. Methods Phys. Res., Sect. A **610**, 710 (2009).
- [62] H. Watanabe *et al.*, Astropart. Phys. **31**, 320 (2009).
- [63] M. Vagins, “A Gadolinium-loaded Super-Kamiokande”, <https://indico.kps.or.kr/event/30/contributions/930/attachments/229/455/Mark%20Vagins.pdf> (2022).
- [64] L. Marti *et al.*, Nucl. Instrum. Methods Phys. Res., Sect. A **959**, 163549 (2020).
- [65] K. Yamamoto *et al.*, “Application of Cherenkov Light Observation to Reactor Measurements (1) - Estimation of Reactor Power from Cherenkov Light Intensity -”, JAEA-Technology 2014-028 (2015).
- [66] Y. Nakano, “ ${}^8\text{B}$ solar neutrino spectrum maesurement using Super-Kamiokande IV”, Ph.D. Thesis, University of Tokyo (2015).
- [67] S. Yamada *et al.*, IEEE Trans. Nucl. Sci. **57**, 428 (2010).
- [68] M. Honda *et al.*, Phys. Rev. D **83**, 123001 (2011).
- [69] K. Daum *et al.*, Z. Phys. C **66**, 417 (1995).
- [70] R. Abbasi *et al.*, Phys. Rev. D **83**, 012001 (2011).
- [71] R. Abbasi *et al.*, Phys. Rev. D **84**, 082001 (2011).
- [72] M. G. Aartsen *et al.*, Phys. Rev. Lett. **110**, 151105 (2013).
- [73] M. G. Aartsen *et al.*, Phys. Rev. D **91**, 122004 (2015).
- [74] R. Abbasi *et al.*, Phys. Rev. D **79**, 102005 (2009).
- [75] R. Abbasi *et al.*, Astropart. Phys. **34**, 48 (2010).
- [76] S. Adrián-Martínez *et al.*, Eur. Phys. J. C **73**, 2606 (2013).
- [77] Y. Hayato, L. Pickering, Eur. Phys. J. Spec. Top. **230**, 4469 (2021).
- [78] Y. Koshio, Universe **6**, 80 (2020).

- [79] S. J. Barish *et al.*, Phys. Rev. D **16**, 3103 (1977).
- [80] S. Bonetti *et al.*, Nuovo Cimento A **38**, 260 (1977).
- [81] S. Ciampolillo *et al.*, Phys. Lett. B **84**, 281 (1979).
- [82] N. Armenise *et al.*, Nucl. Phys. B **152**, 365 (1979).
- [83] S. V. Belikov *et al.*, Z. Phys. A **320**, 625 (1985).
- [84] G. M. Radecky *et al.*, Phys. Rev. D **25**, 1161 (1982).
- [85] T. Kitagaki *et al.*, Phys. Rev. D **34**, 2554 (1986).
- [86] P. S. Auchincloss *et al.*, Z. Phys. C **48**, 411 (1990).
- [87] P. Berge *et al.*, Z. Phys. C **35**, 443 (1987).
- [88] V. B. Anikeev *et al.*, Z. Phys. C **70**, 39 (1996).
- [89] A. I. Mukhin *et al.*, Sov. J. Nucl. Phys. **30**, 528 (1979).
- [90] D. B. MacFarlane *et al.*, Z. Phys. C **26**, 1 (1984).
- [91] N. J. Baker *et al.*, Phys. Rev. D **25**, 617 (1982).
- [92] O. Benhar *et al.*, Phys. Rev. D **72**, 053005 (2005).
- [93] R. Bradford *et al.*, Nucl. Phys. B, Proc. Suppl. **159**, 127 (2006).
- [94] M. Leuschner *et al.*, Phys. Rev. C **49**, 955 (1994).
- [95] F. Ajzenberg-Selove, Nucl. Phys. A **523**, 1 (1991).
- [96] K. Kobayashi *et al.*, arXiv:nucl-ex/0604006 (2006).
- [97] G. Battistoni *et al.*, AIP Conf. Proc. **896**, 31 (2007).
- [98] H. Zhang *et al.*, Astropart. Phys. **60**, 41 (2015).
- [99] T. Mueller, “Expérience Double Chooz : simulation des spectres antineutrinos issus de réacteurs”, Ph.D. Thesis, Paris-Sud University (2010).
- [100] A. Strumia, F. Vissani, Phys. Lett. B **564**, 42 (2003).
- [101] R. Brun *et al.*, CERN, Report No. CERNW5013 (1994).
- [102] J. Allison *et al.*, Nucl. Instrum. Methods Phys. Res., Sect. A **835**, 186 (2016).
- [103] T. Tanaka *et al.*, Prog. Theor. Exp. Phys. **2020**, 043D02 (2020).
- [104] K. Abe *et al.*, Phys. Rev. D **94**, 052010 (2016).
- [105] K. Abe *et al.*, Phys. Rev. D **83**, 052010 (2011).

- [106] M. Shinoki, “スーパーカミオカンデ-ガドリニウム実験による宇宙線ミューオン核破碎反応に由来する中性子生成率の測定”, Master’s Thesis, Tokyo University of Science (2021).
- [107] Y. Nakano, K. Ieki, N. Shigeta, “SK-VI low-energy data quality”, https://indico-sk.icrr.u-tokyo.ac.jp/event/7212/contributions/22289/attachments/20777/26579/quality_20220520.pdf (2022).
- [108] M. Nakahata *et al.*, Nucl. Instrum. Methods Phys. Res., Sect. A **421**, 113 (1999).
- [109] M. Harada, Proc. Sci., ICHEP2022 (**2022**) 1178.
- [110] M. Shinoki *et al.*, Phys. Rev. D **107**, 092009 (2023).
- [111] Z. Conner, “A STUDY OF SOLAR NEUTRINOS USING THE SUPER-KAMIONADE DETECTOR”, Ph.D. Thesis, University of Maryland (1997).
- [112] S. Desai, “HIGH ENERGY NEUTRINO ASTROPHYSICS WITH SUPER-KAMIOKANDE”, Ph.D. Thesis, Boston University (2004).
- [113] “Physics Reference Manual”, <https://geant4-userdoc.web.cern.ch/UsersGuides/PhysicsReferenceManual/BackupVersions/V10.5-2.0/html/index.html> (2018).
- [114] M. J. Kobra, “Intranuclear Cascade Model for Deuteron- and Alpha-induced Reactions at Intermediate Energies”, Ph.D. Thesis, Kyushu University (2017).
- [115] H. W. Bertini, Phys. Rev. **131**, 1801 (1963).
- [116] R. Hofstadter, Rev. Mod. Phys. **28**, 214 (1956).
- [117] A. Boudard *et al.*, Phys. Rev. C **66**, 044615 (2002).
- [118] J. M. Quesada *et al.*, Prog. Nucl. Sci. Tech. **2**, 936 (2011).
- [119] X. Ji *et al.*, Nucl. Instrum. Methods Phys. Res., Sect. A **961**, 163677 (2020).
- [120] W. A. Coleman, T. W. Armstrong, ORNL, Report No. ORNL-4606 (1970).
- [121] M. Honda *et al.*, Phys. Rev. D **75**, 043006 (2007).
- [122] H. Kunxian, “Measurement of the Neutrino-Oxygen Neutral Current Quasi-elastic Interaction Cross-section by Observing Nuclear De-excitation γ -rays in the T2K Experiment”, Ph.D. Thesis, Kyoto University (2015).
- [123] S. E. Hedri *et al.*, “The Diffuse Supernova Neutrino Background in Super-Kamiokande IV”, https://kmcvs.icrr.u-tokyo.ac.jp/svn/rep/skdoc/technote/2004_DSNB-sk4/DSNB_technical_note.pdf (2020).
- [124] M. Harada, “SK-VI DSNB analysis Cut-based neutron tagging + Spectrum-independent analysis”, https://indico-sk.icrr.u-tokyo.ac.jp/event/7834/contributions/24494/attachments/22339/29106/20221202_limit.pdf (2022).
- [125] Y. Kanemura, “Improvement of neural network analysis in SK-VII”, https://indico-sk.icrr.u-tokyo.ac.jp/event/8192/contributions/25926/attachments/23284/30695/2023summerSKCM_kanemura.pdf (2023).